

Improving the use of eclogitic garnet as a diamond indicator mineral, and constraining the origin
of eclogites in the subcontinental lithospheric mantle

by

Matthew Fraser Hardman

A thesis submitted in partial fulfillment of the requirements for the degree of

Doctor of Philosophy

Department of Earth and Atmospheric Sciences

University of Alberta

© Matthew Fraser Hardman, 2020

Abstract

Diamond occurs in the subcontinental lithospheric mantle (SCLM) and is transported to the surface by kimberlite-lamproite volcanism and other deeply-derived volcanic rocks. In the SCLM diamond is often hosted by peridotitic or eclogitic substrates and is a highly sought-after mineral. Even when it occurs in economic abundances in a kimberlite deposit, diamond is extremely scarce, typically below the parts per million level. Therefore, diamond exploration practices often seek out “diamond indicator minerals,” silicate or oxide minerals that may have co-existed with diamond or equilibrated under conditions where diamond may have been stable. These minerals are typically much more abundant than diamond, and the more resistant minerals may be transported by mechanical processes on the surface. By utilising the compositions of diamond indicator minerals recovered in concentrate during kimberlite exploration, it is possible to locate a diamondiferous kimberlite deposit. Diamond exploration practices often employ garnet geochemistry, as garnet is a silicate mineral present in almost all the major diamond-host lithologies in the SCLM. The exploration practices that use high-Cr garnets to locate diamondiferous deposits hosted by peridotitic substrates are robust. Some practices that employ low-Cr garnets to identify diamondiferous deposits hosted by eclogitic substrates, however, are susceptible to error: one of the causes of this is that there is significant compositional overlap between low-Cr garnets from mantle eclogites – which may be diamondiferous – and garnets from lower crustal granulites, which are barren.

One existing methods for the discrimination of crustal- and mantle-derived garnets is the Mg# ($Mg/[Mg+Fe]$) versus Ca# ($Ca/[Ca+Mg]$) method of Schulze (2003). To determine if the Schulze (2003) method can successfully discriminate garnets derived from granulites from those derived

from mantle eclogites, I determined the major- and trace-element compositions of garnets from 190 new lower crustal granulite and 529 new mantle eclogite xenoliths, from a variety of kimberlites globally. These data are combined with the major-element compositions of 2977 garnets from published literature. When this combined dataset is applied to the Schulze (2003) method, the full error rate is 17.1 ± 2.1 %, with a misclassification rate of garnets from lower crustal granulites of 39.2 %. One consequence of this for diamond exploration is the possibility of “false positive” signals – crustal garnets classified incorrectly as mantle-derived – which may lead to an erroneous impression of the expected amount of mantle material present in a deposit, if the kimberlite sampled garnet granulite during eruption, or if garnet granulite is also present in till-derived indicator mineral samples. To remedy this situation, in Chapter 2 I derive new probabilistic single-grain discriminants for crustal and mantle garnets using major-element compositions. These discriminants are based on two multivariate statistical methods, namely linear discriminant analysis and logistic regression. The cross-validated error rate of the logistic regression method is 7.5 ± 1.9 %. This error rate is the lowest overall in published literature for the classification of low-Cr garnets derived from crustal and mantle low-Cr garnets. This approach reduces the error rate of garnets from granulites to ~ 7.6 % using the available dataset. These new statistical methods can be applied to single garnets with known major-element compositions and can assign a probability of certainty to every classification.

However, even using these new methods the error rates for classification of garnets from granulites and mantle eclogites are non-negligible; major-element geochemical overlap is still present between some low-Cr garnets from crustal and mantle rocks and cannot be resolved even using eight major-elements. Therefore, in Chapter 3, I assess the value of garnet trace-element data in improving classification error rates during diamond exploration. Using a combined

dataset of garnet trace-element compositions from new xenoliths in this study and data in the published literature, I find that classification error rates for garnets from crustal granulites and mantle eclogites are improved by adding tracing element data as classifiers. I present a new trace-element classifier system using the statistical method Classification and Regression Trees (CART). This CART classifier is additive to the outputs of the major-element method in Chapter 2, and adds garnet Eu-anomalies and Sr concentrations as variables. The combination of the trace-element CART method and the major-element logistic regression method results in an error rate as low as 4.7 % on calibration data. Based on these results, an explorationist can weigh the value of acquiring trace-element data at an additional cost, based on its improvement to classification success rates.

Finally, in Chapter 4 I undertake a study of eclogite xenoliths from the former Roberts Victor diamond mine, South Africa. Eclogite xenoliths from the Roberts Victor kimberlite have long yielded fundamental insights into the origins of eclogites and deep cratonic roots. I analysed a new suite of 65 eclogite xenoliths from Roberts Victor for their major- and trace-element compositions. In addition to a new dataset of 34 oxygen isotope analyses by SIMS, I report the first triple oxygen isotope data ($\delta^{17}\text{O}$, $\delta^{18}\text{O}$) for eight kimberlite-derived eclogites. Eight new samples in the dataset have sub-chondritic whole-rock LREE abundances and are low in Sr, HFSE, sodium-in-garnet, potassium-in-clinopyroxene, Zr/Hf, and $\delta^{18}\text{O}$ (< 4.0 ‰). These samples classify as Group II eclogites, based on textural equilibrium exemplified by interlocking grains with straight grain boundaries. For the larger sample set of Group I eclogites from Roberts Victor, based on their major- and trace-element characteristics, I concur with previous authors that they are metamorphosed basaltic-picritic lavas or gabbroic cumulates from oceanic crust, crystallised from melts of depleted MORB mantle. For the Group II eclogites, however, I

propose formation as cumulates in deep oceanic crust from melts that were chemically less-enriched than N-MORB due to derivation from a residual mantle source. Previous melting of this depleted mantle source at garnet- ± spinel-facies preferentially extracted incompatible elements and fractionated Zr-Hf in the residue. Cumulates precipitated from the second-stage melts inherited the residual chemical signature of their mantle sources. Coupling the low $\delta^{18}\text{O}$ values of the Group II eclogites, which fall outside of the canonical mantle range, with their variable europium anomalies, indicates that they crystallised in plagioclase-facies oceanic crust. The Group II protoliths were altered by seawater at high temperatures ($> 350\text{ }^{\circ}\text{C}$), possibly at greater stratigraphic depths than the Group I eclogite protoliths, consistent with the presumed location at depth of their proposed cumulate protoliths.

Preface

This thesis is an original work prepared by Matthew F Hardman and contains the findings of his PhD research supervised by D. Graham Pearson and Thomas Stachel. Samples described in Chapters 2 and 3 were provided by Rio Tinto, De Beers Canada, Peregrine Diamonds Ltd., Jon Carlson (Dominion Diamond Mines), Star Diamond Corp. (formerly Shore Gold Inc.), Slava Spetsius (Alrosa), Juanita Bellinger, D. Graham Pearson, and Thomas Stachel. Sets of major-element data included in Chapter 2 were provided by Daniel Schulze, Thomas Chacko, and Larry Taylor. Samples described in Chapter 4 were provided by Thomas Stachel.

A modified version of Chapter 2 has been published as *Hardman MF, Pearson DG, Stachel T, Sweeney RJ (2018) Statistical approaches to the discrimination of crust- and mantle-derived low-Cr garnet – Major-element-based methods and their application in diamond exploration. Journal of Geochemical Exploration 186:24-35*. I completed all sample preparation and analysis and wrote the manuscript. Andrew Locock assisted in determination of major-element compositions of garnets by electron probe microanalysis. D. Graham Pearson and Thomas Stachel assisted with data interpretation and preparation of the manuscript. Russell Sweeney assisted with the application of multivariate statistical techniques.

A modified version of Chapter 3 has been published as *Hardman MF, Pearson DG, Stachel T, Sweeney RJ (2018) Statistical approaches to the discrimination of mantle- and crust-derived low-Cr garnets using major and trace element data. Mineralogy and Petrology 112:697-706*. I completed all sample preparation and analysis and prepared the manuscript. Yan Luo assisted in determination of trace-element compositions of garnets by laser-ablation ICP-MS. D. Graham Pearson and Thomas Stachel provided substantial assistance in preparation of the manuscript

through discussion and editorial oversight. Russell Sweeney provided important background on the application of statistical techniques and aided in discussion in the manuscript.

Chapter 4 constitutes a study on eclogite xenoliths from the former Roberts Victor diamond mine, which has not yet been submitted to a journal for publication. I conducted the major- and trace-element analyses of garnet and clinopyroxene with the assistance of Andrew Locoock and Yan Luo. Chiranjeeb Sarkar assisted with strontium isotope analysis. Oxygen isotope analysis of garnets by SIMS was completed at the University of Alberta under the direction of Richard Stern and assistance in sample preparation and imaging by Robert Dokken. Oxygen isotope compositions for select garnet and clinopyroxene were determined by laser fluorination at the Center for Stable Isotopes at the University of New Mexico by Zachary Sharp and Erick Cano. Thomas Stachel, D. Graham Pearson, Herman Grütter, and Gerhard Brey provided substantial input on the content and composition of the chapter.

Acknowledgements

I would firstly like to thank my supervisors Thomas Stachel and D. Graham Pearson for being exceptionally supportive mentors during my graduate studies. Both were always available when I needed advice, a question answered, or simply a chance to chat. Thomas, thank you for the group lunches and Graham, I apologise very much for having Folger's coffee on-hand that one time – it never happened again, I promise (by the same token, thanks for converting me to Starbucks).

I am very grateful to my candidacy and defense committee members Herman Grütter, Thomas Chacko, Robert Luth, and external examiner Fanus Viljoen. Your comments and insight have each helped me grow as a scientist and improved the quality of this final product.

This research has benefited from the assistance of many individuals in the Earth and Atmospheric Sciences Department, and beyond. I gratefully acknowledge the continued assistance of Andrew Locock, Martin von Dollen, Mark Labbe, Yan Luo, Chiranjeeb Sarkar, Richard Stern, Robert Dokken, Gerhard Brey, Tom McCandless, and Walter Hartley. I thank Yuri Kinakin and Juanita Bellinger for their continued support of this project. I am grateful to Daniel Schulze, Thomas Chacko, and Larry Taylor for provision of major-element data for this study. Samples were provided by Rio Tinto, De Beers Canada Ltd., Star Diamond Ltd (Shore Gold), Slava Spetsius (Alrosa), Juanita Bellinger, and Dominion Diamond Mines. Parts of this research were funded by Diavik Diamond Mines (2012) Inc., an NSERC CRD grant in partnership with Diavik Diamond Mines (2012) to Thomas Stachel and D. Graham Pearson (grant number CRDPJ 476392), and a CERC award to D. Graham Pearson. Without this support, this research would not have been possible.

I extend heartfelt thanks and appreciation to my friends and colleagues. Thank you Nicole, Mike, Mandy, Alix, Stéphane, Garrett, Denny, Matt, Janina, Margo, Theetso, and Ben, for making the last few years a wonderful experience. Thank you Kyle and Sean for all the Halo and Smash Bros. Finally, thank you to my family and to Elaine, for helping me during this journey. Your support has been invaluable, and I will always be grateful. As Bilbo Baggins once said, “I think I’m quite ready for another adventure.”

Contents

Abstract.....	ii
Preface	vi
Acknowledgements.....	viii
List of Tables	xv
List of Figures.....	xvii
List of abbreviations and symbols.....	xx
Chapter 1 Introduction and Background	1
1.1 Introduction	1
1.2 Existing classification methods for garnets from crustal and mantle rocks.....	3
1.3. Group I and II eclogites from the former Roberts Victor diamond mine.....	8
1.4 Objectives	11
Chapter 2 Statistical approaches to the discrimination of crust- and mantle-derived low-Cr garnet – Major-element-based methods and their application in diamond exploration.....	12
2.1 Introduction	12
2.1.1 Overview.....	12
2.1.2 Goals and definitions	16
2.2 Background.....	17
2.2.1 Garnet compositional variation.....	17

2.2.2 Historical graphical discrimination techniques	17
2.2.3 Statistical discrimination methods.....	19
2.3 Dataset.....	22
2.3.1 Overview.....	22
2.3.2 Data quality control and analytical methods for new and literature data.....	23
2.4 Classification methodology.....	25
2.4.1 Geochemical variables and dealing with compositional data.....	25
2.4.2 Derivation of a classification scheme: Graphical discrimination.....	29
2.4.3 Derivation of a classification scheme: Statistical discrimination.....	33
2.4.4 Probabilities, error quantification, and quality of success	34
2.5 Results – Comparison of new graphical and statistical schemes.....	36
2.5.1 Graphical methods.....	36
2.5.2 Statistical methods.....	37
2.5.3 Low-Cr megacryst discrimination.....	38
2.6 Final discussion and conclusions.....	39
2.6.1 Graphical methods.....	39
2.6.2 Statistical methods.....	41
2.6.3 Quality assessment/valuation.....	44
2.6.4 Summary.....	45

Chapter 3 Statistical approaches to the discrimination of mantle- and crust-derived low-Cr garnets using major and trace element data	46
3.1 Introduction	46
3.2 Dataset and analytical method	49
3.3 Results: Trace elements in garnet	51
3.3.1 Rare earth elements and europium anomalies	51
3.3.2 Strontium	55
3.3.3 Zirconium, Hf, and Nb.....	57
3.4 Discussion.....	58
3.4.1 General remarks.....	58
3.4.2 Trace element systematics in garnet related to petrogenesis	59
3.4.3 New trace element classification method for crustal and mantle garnets	64
3.4.4 Outcomes	65
3.5 Conclusions and implications for garnet-based exploration	68
Chapter 4 Tracing the crustal and mantle sources of Roberts Victor eclogites.....	70
4.1 Introduction	70
4.2 Geologic setting	73
4.3 Sample set and Petrography	75
4.4 Analytical Methods	80
4.4.1 Major elements.....	80

4.4.2 Trace-elements	80
4.4.3 Oxygen isotopes.....	81
4.4.4 Strontium isotopes	84
4.5 Results	85
4.5.1 Overview.....	85
4.5.2 Sample texture and mineral chemistry.....	85
4.5.3 REE-based groups and extended trace-element patterns	86
4.5.4 Oxygen isotope compositions ($\delta^{18}\text{O}$, $\delta^{17}\text{O}$).....	93
4.5.5 Strontium isotopes	96
4.5.6 Equilibration pressures and temperatures.....	97
4.6 Discussion.....	99
4.6.1 Oxygen isotope systematics	99
4.6.2 Radiogenic isotope systematics	104
4.6.3 Existing models for the origin of Group II eclogites	106
4.6.4 Chemical characteristics of the Roberts Victor eclogite protoliths.....	117
4.6.5 HFSE and REE systematics during melting of depleted MORB mantle	132
4.6.6 Possible settings for magmas less-enriched than MORB in oceanic crust	145
4.7 Summary and Conclusions	150
Chapter 5 Conclusions	153
5.1 Major element discrimination of crust-mantle garnets using statistical methods	153

5.2 Trace-element discrimination of crust-mantle garnets using statistical methods.....	155
5.3 The protoliths of Group II eclogites at Roberts Victor	157
References	158
Appendix A	177
Appendix B	188
Appendix C	192

List of Tables

Appendix A	177
Table A.1	Commonly substituting cations in garnet chemical formula..... 178
Table A.2	Analytical conditions for determination of major-element compositions in garnet and clinopyroxene by electron probe microanalysis. 179
Table A.3	Factors for calculation of geochemical variables using garnet data as either cations or oxide wt% 180
Table A.4	Formulae for boundaries in new $\ln(\text{Mg}/\text{Fe})$ versus $\ln(\text{Ti}/\text{Si})$ graphical method in this study 181
Table A.5	Coefficient of determination (R^2) and variance inflation factor (VIF) values for geochemical variables used in this study 182
Table A.6	R runstreams for derivation of linear discriminant analysis (LDA) and logistic regression (LR) solutions 183
Table A.7	Classification error (CE) of low-Cr crust-mantle garnet classification methods in this study and the literature 184
Table A.8	K-fold cross-validated error rates for low-Cr crust-mantle garnet classification methods in this study and the literature..... 185
Table A.9	CE for low-Cr mantle-megacryst garnet classification methods in the literature 187
Appendix B	188
Table B.1	R runstream for derivation of Classification and Regression Trees (CART) solution 189

Table B.2	CE for methods in this study and the literature for classification of low-Cr garnets	190
Table B.3	K-fold cross-validated error rate for CART-based trace-element method.....	191
Appendix C	192
Table C.1	Petrographic and geochemical features of Roberts Victor Group I and Group II eclogites from published literature	193
Table C.2	Roberts Victor eclogite hand sample petrography	194
Table C.3	Roberts Victor eclogite thin section petrography.....	196
Table C.4	References for Roberts Victor data from published literature	201
Table C.5	Oxygen isotope compositions for garnet and clinopyroxene from Roberts Victor eclogites in this study	202
Table C.6	Garnet major-element compositions from Roberts Victor eclogites in this study	203
Table C.7	Clinopyroxene major-element compositions from Roberts Victor eclogites in this study	208
Table C.8	Garnet trace-element compositions from Roberts Victor eclogites in this study	213
Table C.9	Clinopyroxene trace-element compositions from Roberts Victor eclogites in this study	217
Table C.10	Average garnet $\delta^{18}\text{O}$ and whole-rock trace-element compositions for Roberts Victor Group I, II _{No} , II _F , II _L , and II _H eclogites	221
Table C.11	Strontium isotope compositions for garnet and clinopyroxene from Roberts Victor eclogites in this study	223

List of Figures

Figure 1.1	Schulze (2003) Mg# versus Ca# plot with the compositions of garnets from crustal rocks.....	6
Figure 1.2	Schulze (1997) TiO ₂ versus Na ₂ O plot for classification of mantle versus megacryst garnets.....	8
Figure 1.3	Simplified map of the Kaapvaal craton.....	9
Figure 2.1	Grütter <i>et al.</i> (2004) Cr ₂ O ₃ versus CaO plot with compositions of low-Cr garnets from crustal and mantle rocks.....	14
Figure 2.2	Schulze (2003) Mg# versus Ca# plot with compositions of low-Cr garnets from crustal and mantle rocks.....	15
Figure 2.3	Schulze (1997) TiO ₂ versus Na ₂ O plot with compositions of low-Cr garnet megacrysts and low-Cr garnets from mantle rocks.....	16
Figure 2.4	Distribution of Na ₂ O contents in garnets from crustal and mantle rocks.....	28
Figure 2.5	New graphical method for classification of crustal and mantle garnet compositions using the variables ln(Ti/Si) versus ln(Mg/Fe).....	30
Figure 2.6	Histogram of the probability values (0 = crustal to 1 = mantle) assigned to low-Cr garnets using the new major-element logistic regression method.....	38
Figure 3.1	Median REE _N and interquartile ranges for low-Cr garnets from crustal and mantle rocks.....	52
Figure 3.2	Median REE _N curves for low-Cr garnets from crustal and mantle rocks, subdivided by garnet Eu-anomaly (Eu/Eu*).....	53
Figure 3.3	Box and whisker plots for Eu/Eu*, Sr, Hf, Nb, and Zr in low-Cr garnets from crustal and mantle rocks.....	54

Figure 3.4	Median REE _N and interquartile ranges for low-Cr garnets previously classified using major-element methods	56
Figure 3.5	Schematic CART flowchart for classification of low-Cr garnets using trace-element data.....	66
Figure 4.1	Simplified map of the Kaapvaal craton.....	74
Figure 4.2	Backscattered electron (BSE) images of Roberts Victor eclogite thin sections ...	79
Figure 4.3	Garnet compositions from Roberts Victor eclogites in Mg-Ca-Fe space	87
Figure 4.4	Schematic flowchart summarising the classification of Roberts Victor eclogites into Groups I, II _{No} , II _F , II _L , and II _H	88
Figure 4.5	Whole-rock REE _N compositions of Roberts Victor eclogites.....	90
Figure 4.6	Whole-rock extended trace-element compositions of Roberts Victor eclogites ...	91
Figure 4.7	Whole-rock Zr, Zr/Hf, and Zr/Y compositions of Roberts Victor eclogites.....	92
Figure 4.8	Distribution of garnet δ ¹⁸ O from Roberts Victor eclogites	94
Figure 4.9	Δ ¹⁷ O versus δ ¹⁸ O plot for Roberts Victor eclogites in this study	95
Figure 4.10	Comparison of garnet and clinopyroxene δ ¹⁸ O for Roberts Victor eclogites	96
Figure 4.11	Calculated equilibration pressure-temperature conditions of Roberts Victor eclogites.....	98
Figure 4.12	REE _N and HFSE compositions of residues modeled during melt extraction from N-MORB.....	110
Figure 4.13	Whole-rock Sr/Sr* versus Nd and Mg# versus Ni for Roberts Victor eclogites	113
Figure 4.14	Whole-rock ΣHREE versus Eu/Eu* for Roberts Victor eclogites.....	114
Figure 4.15	Whole-rock Na ₂ O versus MgO and Al ₂ O ₃ versus MgO for Roberts Victor eclogites.....	118

Figure 4.16	Whole-rock Na ₂ O, Zr/Hf, Mg# and Ca# of Roberts Victor eclogites.....	119
Figure 4.17	Whole-rock FeO/MgO versus TiO ₂ for Roberts Victor eclogites.....	120
Figure 4.18	Shervais (1982) V versus Ti/1000 plot with compositions of whole-rock Roberts Victor eclogites	121
Figure 4.19	Whole-rock FeO/MgO versus Zr/Hf for Roberts Victor eclogites	123
Figure 4.20	Whole-rock FeO/MgO versus SiO ₂ for Roberts Victor eclogites.....	125
Figure 4.21	Whole-rock MgO versus FeO for Roberts Victor eclogites.....	126
Figure 4.22	Schematic phase diagrams for crystallisation of basaltic-picritic magma at 1 atm and 7 kbar	130
Figure 4.23	Schematic overview of mid ocean ridge basalt (MORB) formation from depleted MORB mantle (DMM), as well as slab melting during subduction	135
Figure 4.24	Compositions of modeled residues, fractional melts, and equilibrium clinopyroxene during melting of DMM in the garnet- or spinel-facies	137
Figure 4.25	REE _N compositions of residues during fractional melting of DMM in the garnet- or spinel-facies	139
Figure 4.26	REE _N compositions, Zr abundances, and Zr/Hf ratios of modeled residues, fractional melts, and equilibrium clinopyroxene during polybaric melting of DMM.....	141
Figure 4.27	Zr abundances and Zr/Hf ratios of ophiolite-hosted lavas, tholeiites, and gabbros in the published literature.....	149

List of abbreviations and symbols

‰	Parts per thousand; per mil
~	Approximately
°C	Degrees Celsius
Amph	Amphibole
apfu	Atoms per formula unit
atm	Atmosphere
atomic%	Atomic percent
BAB	Back-arc basin
bdl	Below detection limit
BSE	Backscattered electrons
CA	Cluster analysis
Ca#	Molar calcium number, $Ca/(Ca+Mg)$
CARP	Cluster Analysis by Recursive Partitioning
CART	Classification and Regression Trees
CCIM	Canadian Centre for Isotopic Microanalysis
CE	Classification error
CI	Confidence interval
Cpx	Clinopyroxene
d, d_{CM-LR} , d_{CM-LDA}	Discriminant value
D	Partition coefficient

DMM	Depleted MORB-source mantle
e.g.	For example
EPMA	Electron probe microanalyser
Eu/Eu*	Europium anomaly, $2 \times \text{Eu}_N / (\text{Sm}_N + \text{Gd}_N)$
G0, G1, G3, G4	G classifications for garnet, from Grütter <i>et al.</i> (2004)
Ga	Giga-annum; billion years
GPa	Gigapascal
Grt	Garnet
HFSE	High field strength element
HREE	Heavy rare earth element
Hz	Hertz
i.e.	That is, in other words
Ilm	Ilmenite
IQR	Interquartile range
J/cm ²	Fluence, joules per square centimetre
kbar	Kilobar
keV	Kiloelectronvolt
km	Kilometre
kV	Kilovolt
Ky	Kyanite
LA-ICP-MS	Laser-ablation inductively-coupled plasma mass spectrometry

LDA	Linear discriminant analysis
LF	Laser fluorination
Lhz	Lherzolite
LILE	Large ion lithophile element
LLD	Lower limit of detection
LOQ	Limit of quantitation
LR	Logistic regression
LREE	Light rare earth element
LSE	Least squares estimation
Ma	Mega-annum; million years
mbar	Millibar
mg	Milligram
Mg#	Molar magnesium number; $Mg/(Mg+Fe)$
ml	Millilitre
MLE	Maximum likelihood estimators
mol%	Mole percent
MORB	Mid-ocean ridge basalt
MQ	Milli-Q water
MREE	Middle rare earth element
mW/m^2	Milliwatt per square metre
N	Subscript denoting normalisation of value

N	Abundance, number
N-MORB	Normal-type mid ocean ridge basalt
na	Not analysed
nA	Nanoampere
ng	Nanogram
p	Probability
P-T	Pressure-temperature (also separately as P or T)
PCA	Principal component analysis
Plag	Plagioclase
ppb	Parts per billion
ppm	Parts per million
R ²	Coefficient of determination
REE	Rare earth element
Rut	Rutile
s	Second
San	Sanidine
SCLM	Subcontinental lithospheric mantle
SIMS	Secondary ion mass spectrometry
Spl	Spinel
Sr/Sr*	Strontium anomaly, $2 \times \text{Sr}_N / (\text{Pr}_N + \text{Nd}_N)$
T _{DM}	Depleted mantle model age

Ti/Ti*	Titanium anomaly, $2 \times \text{Ti}_N / (\text{Eu}_N + \text{Dy}_N)$
TIMS	Thermal ionization mass spectrometry
T _{Krogh88}	Temperatures determined using Krogh (1988) Fe-Mg geothermometer
VIF	Variation inflation factor
VSMOW	Vienna standard mean ocean water
W	Watt
wt%	Weight percent
$\delta^{17}\text{O}$	Oxygen isotope composition ($^{17}\text{O}/^{16}\text{O}$) normalised to VSMOW
$\delta'^{17}\text{O}$	$\delta^{17}\text{O}$ recast as $1000 \times \ln(1 + \delta^{17}\text{O}/1000)$
$\delta^{18}\text{O}$	Oxygen isotope composition ($^{18}\text{O}/^{16}\text{O}$) normalised to VSMOW
$\delta'^{18}\text{O}$	$\delta^{18}\text{O}$ recast as $1000 \times \ln(1 + \delta^{18}\text{O}/1000)$
$\Delta^{17}\text{O}$	Departure from terrestrial fraction line in a $\delta'^{17}\text{O}$ versus plot $\delta'^{18}\text{O}$
$\theta_{\text{Grt-Cpx}}$	Garnet-clinopyroxene variations for $\delta'^{17}\text{O}$ and $\delta'^{18}\text{O}$
μL	Microlitre
μm	Micrometer
σ	Sigma, one standard deviation of the mean
Σ	Sum

Chapter 1 Introduction and Background

1.1 Introduction

The rigid subcontinental lithospheric mantle (SCLM) underlies and stabilizes cratons (Heaman and Pearson 2010). Within these roots, pressure-temperature conditions permit the formation and storage of diamond (Boyd and Gurney 1986). Diamond is dominantly associated with peridotite, websterite, or eclogite substrates, which together comprise the bulk of the SCLM (e.g., Meyer and Boyd 1972; Sobolev 1977). From there, diamond is transported to the surface rapidly by kimberlite-lamproite volcanism. Even when present in economic abundances, diamond is still exceptionally rare. Thus, diamond prospecting makes use of much more abundant minerals whose chemistry may indicate the presence of diamond (“diamond indicator minerals”), and thereby can be traced back to their original volcanic source more easily. Garnet is a particularly potent indicator mineral because it is a constituent of most diamond-bearing lithologies in the SCLM, both the high- and low-Cr assemblages. Its geochemical characteristics often reflect the host rock in Earth’s mantle from which it is derived (Dawson and Stephens 1975; Nowicki *et al.* 2007). Further, garnet is metastable at surface temperatures and pressures, and some garnet compositions are resilient against alteration.

Exploration practices for peridotite-sourced diamonds are relatively robust. In these peridotites, high-Cr, low-Ca garnets are associated with highly-depleted harzburgitic lithosphere in which diamond formation may be favourable (Gurney and Switzer 1973; Gurney 1984). During exploration for peridotite-sourced diamonds several options exist for single-grain thermometry and even thermobarometry, allowing for the confident identification of grains derived from diamond-facies conditions.

While approximately one-third of all minerals included in diamond are eclogitic (Stachel and Harris 2008), eclogite only comprises between one and five volumetric percent of the SCLM (Dawson and Stephens 1975; Schulze 1989). This affords targets with a large proportion of eclogite high economic potential during diamond exploration, highlighting the importance of accurately identifying eclogite-associated deposits. By IUGS definition, eclogite is a plagioclase-free biminerale assemblage of garnet and omphacite (clinopyroxene with jadeite > 20 mol%; Desmons and Smulikowski 2007). Garnet and omphacite together comprise > 75 % of the rock, with neither mineral being > 75 %. Omphacite distinguishes eclogite *sensu stricto* from garnet-pyroxenite, which contains low-jadeite clinopyroxene. Mantle pyroxenite, however, is not a significant diamond host rock (Stachel and Harris 2008), and therefore during exploration it is important to distinguish pyroxenite from eclogite. When garnet and clinopyroxene are found together in a xenolith the distinction between eclogite and pyroxenite is straightforward. However, indicator mineral samples obtained during diamond exploration programs typically provide only single garnet grains, meaning that paired clinopyroxene compositions cannot be used for source rock identification. Current classifications using garnet chemistry lack the power to discriminate effectively between some low-Cr garnets derived from mantle eclogite and pyroxenite (e.g., Grütter *et al.* 2004), that is, garnets in the “G4” category derive from a mixture of host rocks including eclogite, pyroxenite, and websterite. Likewise, garnets in lower crustal rocks such as granulites typically are in equilibrium with plagioclase and low-jadeite clinopyroxene, but single low-Cr garnets derived from these granulites are compositionally similar to many of those derived from mantle eclogites. As a result, single garnets from some crustal rocks will classify as high-Ca eclogitic (G3) or pyroxenitic/low-Ca eclogitic (G4) using the Grütter *et al.* (2004) methodology. In this thesis I develop new geochemical discriminants for

low-Cr garnets from lower crustal rocks, such as granulites, and garnets from mantle rocks such as eclogites. The outcome is refined exploration practices for kimberlites using geochemistry of single garnets in concentrate.

One of the key aspects in development of chemical classification methods using garnet is a representative calibration database, so that the full range of unknown garnet compositions can be confidently assessed. However, even within the broad rock types granulite and eclogite, there is significant chemical variability. This is especially apparent within the eclogite suite from the former Roberts Victor diamond mine, South Africa. A subset of eclogites from the locality – the so-called Group II eclogites, characterised by equilibrium-type textures – contain garnets with significant incompatible element depletion relative to garnets from Group I eclogites. Group I and II eclogites are generally inferred to both have originated as oceanic crust that was subducted and metamorphosed to eclogite, based partially on their broadly basaltic chemistry and oxygen isotope compositions that mimic the distribution seen in Cretaceous ophiolites (Jacob 2004). The Group II eclogites, which are characterised by significantly lower whole-rock LREE, HFSE, Sr, and TiO₂ abundances than Group I eclogites, have been inferred by many studies to be residues of significant partial melt extraction during subduction. In this study I combine new elemental and oxygen isotope data with literature data to propose a new model specific to the formation of the Group II eclogites, to partially reconcile their complex, multistage histories.

1.2 Existing classification methods for garnets from crustal and mantle rocks

Extensive solid solution in garnet permits a wide range of chemical compositions, which makes it a potent chemical tool in assessing mantle source regions. The Cr content of garnet has a predictable effect on its colour (e.g., McLean *et al.* 2007). Garnet geochemistry can be leveraged

to discriminate many mantle lithologies in kimberlitic xenocryst assemblages (Grütter *et al.* 2004). However, single garnets cannot always fully replace the need for a whole-rock in determination of source lithology. A xenolith derived from the lower crust may be easily distinguished from a mantle rock based on mineralogy, for example, by the occurrence of plagioclase. The presence of omphacite (jadeite > 20 mol%) differentiates eclogite *sensu stricto* from garnet-pyroxenite but when only the garnet is available, low-Cr garnets from both rock types may classify as “G4” (low-Ca eclogite or pyroxenite; Grütter *et al.* 2004). For instances when only garnet is available, Schulze (2003) used Mg# ($Mg/[Mg+Fe]$) versus Ca# ($Ca/[Ca+Mg]$) to discriminate crust and mantle samples.

One of the fundamental issues for the correct classification of a single low-Cr garnet as being derived from either a crustal rock – such as a granulite – or from a mantle rock – such as an eclogite is that low-Cr garnets derived from lithologies in the crust and mantle are often very similar geochemically (Schulze 2003). The occurrence of garnets from crustal rocks such as garnet granulites indicates that a kimberlite may have sampled at least some portion of the crust during ascent. Their occurrence in till may indicate that the source region contained granulite-facies crustal outcrops, relatively common in cratonic regions, in addition to undiscovered kimberlites or related rocks. Since crustal rocks are derived from graphite-facies conditions, crustal garnets must be separated from potentially diamond-associated mantle garnets for exploration purposes. Misclassification of garnets from mantle eclogites as having derived from a crustal rock represents a “false negative” scenario, while misclassification of a crustal-derived garnets as having derived from a mantle rock is a “false positive” scenario. Both scenarios are undesirable during exploration, as both will give an incorrect impression of the amount of mantle material present at a locality.

Many chemistry-based exploration methods currently in usage leverage the association between specific garnet compositions and their host lithology (e.g., Grütter *et al.* 2004). The Grütter *et al.* (2004) classification method is not calibrated to crustal garnets and therefore does not distinguish pyrope-rich ($> \sim 30$ mol%) crustal garnets from a subset of eclogite- and pyroxenite-derived mantle garnets. Therefore, application of crustal garnets to the method – outside of its calibrated compositional range – might lead a user to infer that the garnets instead derive from low-Cr mantle rocks such as mantle eclogite. As such misclassification may lead to a substantial overestimation of the proportion of mantle eclogite in a deposit, it is first important to properly classify single low-Cr garnets as crust- or mantle-derived. The classification method of Schulze (2003) is calibrated to discriminate garnets from crustal and low-Cr mantle rocks using molar Mg# and Ca# (Figure 1.1). Schulze (2003) derived a boundary between “crust” and “mantle” garnet compositions based on the goal of correctly identifying all garnets from mantle rocks, thereby accepting that some crust-derived garnets misclassified as mantle-derived. This is problematic because there is substantial chemical overlap between garnets from granulites and from mantle eclogites that is documented by a significant compositional range for garnets from lower crustal rocks, which extends into the “mantle” field (Figure 1.1). The calibration dataset for the Schulze (2003) method contained a very small proportion of garnets from lower crustal granulites. This may be remedied by deriving a classification method using a dataset containing a “representative” suite of garnet chemical compositions.

Suggate and Hall (2013) and Krippner *et al.* (2014) evaluated the classification of garnet compositions using a variety of existing graphical discrimination diagrams. However, even upon expanding the number of assessed compositional variables to three, compositional overlap between garnets from some rock types is still apparent. To further address compositional overlap

between garnets from some rock types, Krippner *et al.* (2014) applied principal component analysis (PCA) to the discrimination of garnet compositions which resulted in better classification success for some garnet compositions, but could not resolve all overlap. Those authors concluded that multivariate statistics represents the likeliest means of improving classification success for garnet compositions. Other applications of statistics to garnet classification in the literature include cluster analysis, which Dawson and Stephens (1975) applied to garnets hosted by kimberlite.

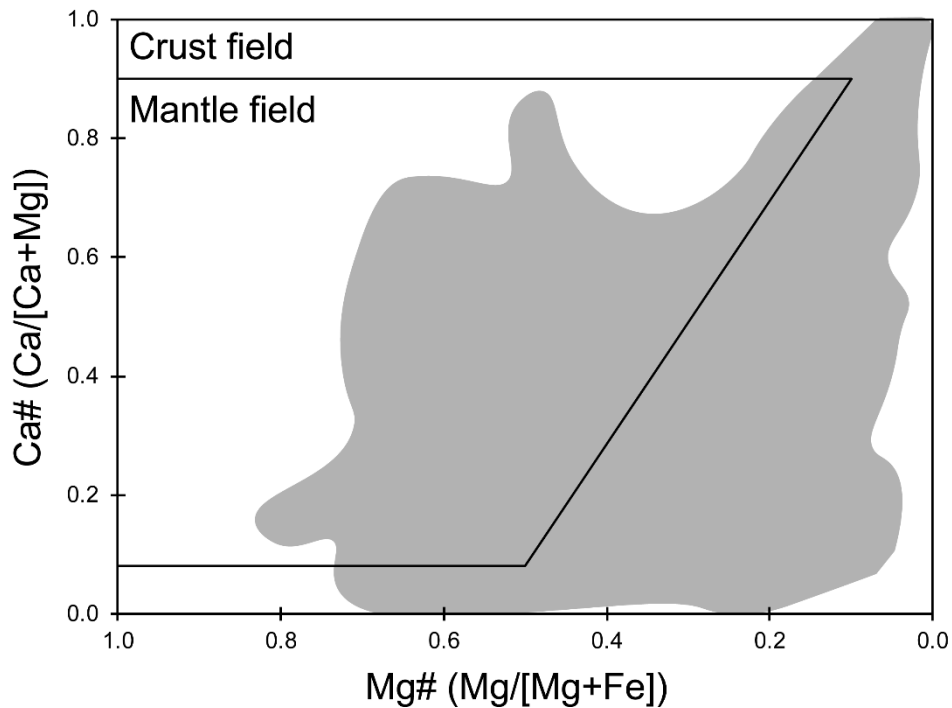


Figure 1.1 Schulze (2003) Mg# versus Ca# method for classification of crust- and mantle-derived garnets. Grey field indicates the compositional range of low-Cr garnets from crustal rocks. Garnet compositions are from new lower crustal xenoliths analysed in this study (N = 190) and compiled from the literature (N = 1386).

Those authors calibrated a method using 352 garnet compositions, resulting in 12 chemical classes. The Dawson and Stephens (1975) method is a demonstration of the successful application of statistics to geological classification problems but it was not calibrated including

garnets from lower crustal lithologies. The problem of determining a crustal- or mantle-provenance for single garnets can be addressed by expanding the calibration dataset to include those garnet compositions. Additional discriminatory power may also be added by reducing the number of rock types that are the focus of discrimination – i.e., by limiting the calibration dataset to only the most intractable rock types, such as garnets from lower crustal granulites and from mantle eclogites. The results of Schulze (2003), Suggate and Hall (2013) and Krippner *et al.* (2014) demonstrate that some crustal lithologies are effectively identified using existing chemical classification methods. Therefore, one option may be to limit calibration datasets to only the most intractable garnet compositions – garnets from granulites and mantle eclogites – so that the sensitivity of the method is not reduced by garnet compositions that can already be classified by other means. Classification methods may also be refined with the application of trace-elements, which have been applied comparatively rarely in the literature due to their relative paucity (Krippner *et al.* 2014). Finally, while the principal focus in diamond exploration is the proper classification of garnets from crustal versus mantle rocks, similar attention may need to be directed to garnet compositions from other rock types that may “dilute” an economic deposit. For example, low-Cr garnet megacrysts may occur in concentrate but have an origin cognate with kimberlite and other mantle-derived alkaline magmas, and may also be misclassified as mantle xenocrysts. Existing methods for classification of megacrystic garnets are based on cluster analysis (Dawson and Stephens 1975; Danchin and Wyatt 1979) and graphical classifiers (e.g., Figure 1.2; Schulze 1997; Grütter *et al.* 2004; Rogers and Grütter 2009).

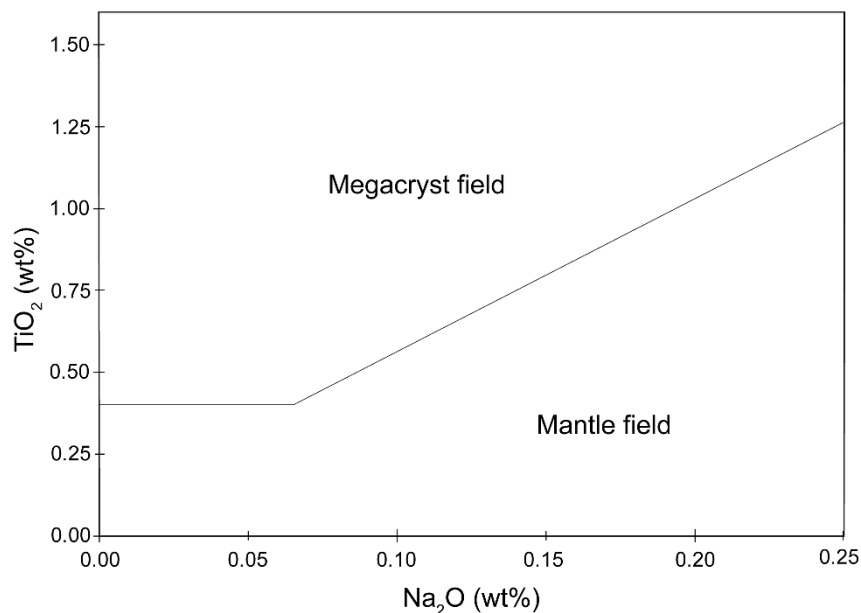


Figure 1.2 Schulze (1997) Na₂O versus TiO₂ (wt%) method for classification of single megacrystic and mantle garnets.

1.3. Group I and II eclogites from the former Roberts Victor diamond mine

The Roberts Victor pipe is a Group II kimberlite (carbonate-rich lamproite in the nomenclature of Pearson *et al.* 2019) that erupted through the Kaapvaal craton, South Africa, $\sim 128 \pm 15$ Ma (Smith *et al.* 1985). The pipe is situated on the Colesberg Lineament which marks the suturing of the Kimberley (West) and Witwatersrand (East) blocks at 2.88 to 2.93 Ga (Figure 1.3; Schmitz *et al.* 2004; Shirey *et al.* 2004, and references therein). Eclogite comprises the majority of the mantle xenolith population encountered at surface at the Roberts Victor kimberlite (> 90 %; Gréau *et al.* 2011), far in excess of the one to five percent eclogite estimated to comprise the SCLM globally (Dawson and Stephens 1975; Schulze 1989). Thus the Roberts Victor locality represents a unique opportunity to investigate the geochemical, petrographic, and petrogenetic characteristics of mantle eclogites, particularly since Roberts Victor is the type locality for the textural division of eclogites into Groups I and II.

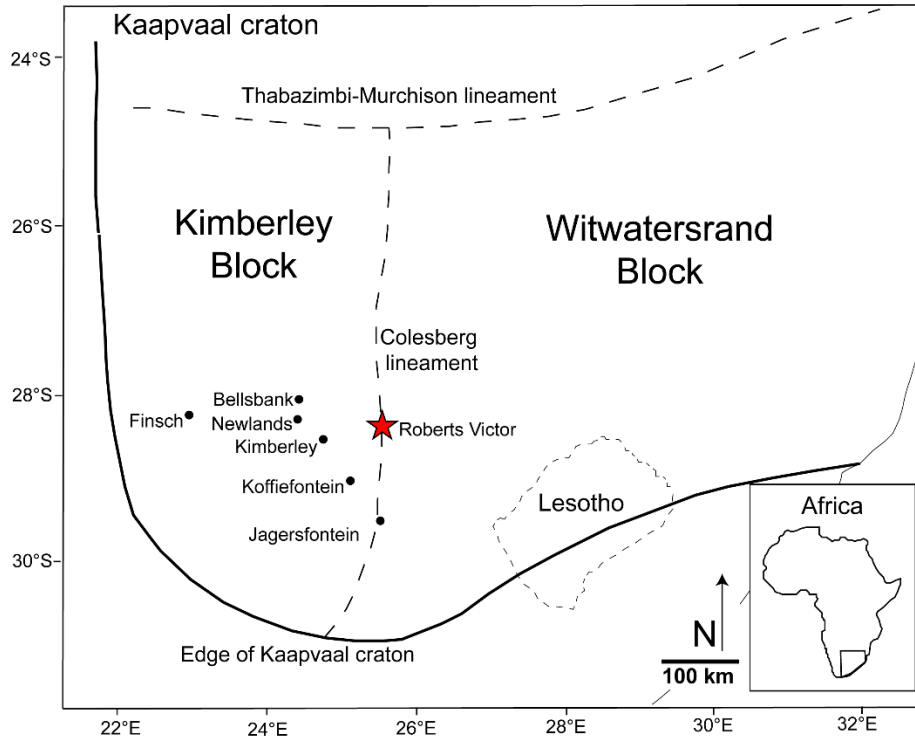


Figure 1.3 Geological map of the Kaapvaal craton, simplified after Schmitz *et al.* (2004). The locations of Roberts Victor and several other kimberlites are indicated.

Group I eclogites have anhedral to subhedral garnets within a matrix of interstitial clinopyroxene, and Group II eclogites have equilibrium-type microstructures characterised by straight grain boundaries and inter-mineral triple junctions (MacGregor and Carter 1970). With advancements in analytical methodologies and observation, it was shown that Group II eclogites have significantly lower contents of highly to mildly incompatible elements (LREE, HFSE, TiO_2 , Sr), lower Na_2O -in-garnet, lower K_2O -in-clinopyroxene, and $\delta^{18}\text{O}$ values much lower than Group I eclogites (Garlick *et al.* 1971; MacGregor and Manton 1986; McCandless and Gurney 1989).

Many studies link the basaltic to picritic bulk composition of eclogite, their sometimes prominent positive or negative Eu-anomalies, and $\delta^{18}\text{O}$ values outside of the canonical mantle range, to an

origin of eclogite as subducted and metamorphosed oceanic crust (Helmstaedt and Doig 1975; Gregory and Taylor 1981; MacGregor and Manton 1986; Shervais *et al.* 1988; Shu *et al.* 2016). The alternative model is that eclogites crystallised from mantle melts at high pressures (Hatton 1978; Caporuscio and Smyth 1990; Caporuscio 1990). Oxygen isotope compositions have been decisive in resolving the ultimately oceanic-crustal origin of mantle eclogites, as the range of $\delta^{18}\text{O}$ in eclogite xenolith suites globally is similar to that of modern ophiolite sequences (Jacob 2004; Ickert *et al.* 2013; Korolev *et al.* 2018). Values of $\delta^{18}\text{O}$ outside the mantle range in oceanic basalt, for example, must be the result of low-temperature seawater alteration processes in oceanic crust sequences (Muehlenbachs and Clayton 1972a, 1972b), compared to oxygen isotope fractionation in the mantle which is minimal ($< 1 \text{ ‰}$; Eiler 2001; Riches *et al.* 2016). However, while both Group I and II eclogites with $\delta^{18}\text{O}$ values outside of the canonical mantle range are generally inferred to have had crustal protoliths that were altered by seawater, the relative differences in elemental chemistry between Group I and II eclogites have been the focus of speculation and debate. Some studies suggest that Group II eclogites experienced significant melt extraction during subduction, which resulted in a reduction of their highly to mildly incompatible element contents relative to the Group I eclogites (e.g., Radu *et al.* 2019).

In this study, I combine new-acquired elemental and oxygen isotope analyses from Roberts Victor eclogites with data available in published literature and propose a new model for the Group II eclogites from Roberts Victor. This new model places less emphasis on partial melting during subduction as the cause of incompatible element depletions in the Group II eclogites, and instead proposes that the low incompatible element contents primarily relate to melting of a residual previously-depleted mantle source, prior to cumulate precipitation as oceanic crust. This study of the Roberts Victor eclogites provides a unique opportunity to investigate the effects of

petrogenesis on garnet chemistry, since during the trace-element analysis of garnets derived from 571 new xenoliths for Chapter 3, it was only the garnets from Roberts Victor Group II eclogites that showed such uniquely low incompatible element contents.

1.4 Objectives

The objectives of this PhD thesis are summarised as follows:

- i. The compilation of a new, expanded and more representative garnet geochemical database. This database is a combination of new high-quality major- and trace-element compositions of garnets from xenoliths with known paragenesis. These data are combined with high quality data from published literature.
- ii. The derivation of new single-grain chemical discriminants for garnets from lithologies hosted in the crust- and mantle, transported by kimberlite. These methods are derived by applying multivariate statistical methods to major- and trace-element compositions of garnets. These methods will reduce the number of crustal garnets that incorrectly classify as mantle-derived and vice-versa, improving the accuracy of exploration practices for kimberlite and diamond.
- iii. Combine oxygen isotope compositions – $^{18}\text{O}/^{16}\text{O}$ and $^{17}\text{O}/^{16}\text{O}$ – with high quality major- and trace–element compositions of garnet and clinopyroxene from eclogites xenoliths from Roberts Victor, to propose a new interpretive model for the crustal protoliths of the Group II eclogites. The result is a new understanding of the multistage history of the Roberts Victor eclogite suite, highlighting the impact of eclogite petrogenesis on mineral chemistry.

Chapter 2 Statistical approaches to the discrimination of crust- and mantle-derived low-Cr garnet – Major-element-based methods and their application in diamond exploration

2.1 Introduction

2.1.1 Overview

Most diamonds are transported to Earth's surface by magmas belonging to the kimberlite – lamproite – ultramafic lamprophyre variants. The presence of diamond is exceptionally rare even in diamondiferous deposits, typically in the sub-ppm by mass range. Instead of seeking diamonds directly, prospecting focuses on minerals or mineral compositions indicative of diamond-bearing assemblages or diamond-facies pressure and temperature conditions in Earth's mantle. These minerals are transported together with diamond in kimberlite: the so-called “diamond indicator minerals” or more commonly but perhaps less aptly, “kimberlite indicator minerals.” In any given kimberlite field, diamond indicator minerals, such as garnet, chromite, and clinopyroxene, are always in greater abundance than diamond itself (Nowicki *et al.* 2007). These “indicator mineral” prospecting techniques reduce the economic cost of exploration.

Of all dominant lithologies that comprise the deep lithospheric roots where diamond is formed and hosted, garnet is commonly a significant component. While many garnet compositions are fairly resistant to weathering, which increases its preservation potential when it is emplaced at surface and improves its chances of recovery, some garnet compositions – including Fe-rich varieties in warm climates – are more susceptible to weathering (Parisot *et al.* 1983; Nowicki *et al.* 2007). Major-elements in garnet can be rapidly analyzed using existing routine techniques

(e.g., electron probe microanalysis, EPMA), and trace-element analysis is becoming increasingly widespread (e.g., via laser-ablation inductively-coupled plasma mass spectrometry, LA-ICP-MS). Therefore, garnet has historically been a highly-accessible and widely used tool in geochemistry-based diamond indicator mineral assessment (Nowicki *et al.* 2007).

Exploration practices for peridotitic xenocrysts in kimberlite are elaborate and robust (e.g., Sobolev *et al.* 1973; Gurney and Switzer 1973; Gurney 1984; Fipke *et al.* 1995; Grütter *et al.* 2004). Despite several decades of study however, exploration practices for eclogitic samples are relatively underdeveloped. Eclogite comprises a subordinate proportion of the subcontinental lithospheric mantle (SCLM) (< 1 % to 5 %; Schulze 1989; Dawson and Stephens 1975) but is associated with between ~ 30 and 40 % of recovered inclusion-bearing diamonds (Gurney 1989; Stachel and Harris 2008; Gurney *et al.* 2010), dominating the diamond inclusion population at some mines. This disproportionate relationship suggests that mantle eclogite, even in minor abundances, may be of substantial economic interest. There is, however, a significant compositional overlap between garnets from mantle eclogites, pyroxenites, low-Cr megacrystic garnets, and garnets derived from crustal rocks. Crust-derived garnets for example commonly have low Cr₂O₃ contents (< 1 wt%) similar to many mantle eclogitic-pyroxenitic garnets (Figure 2.1). Accurately discriminating garnets from crustal rocks – such as those exposed at surface and recovered during exploration – from mantle rocks permits a better understanding of the nature of a potential kimberlite deposit. At a further level of refinement, distinguishing mantle eclogites based on their derivation from diamond- or graphite-facies pressure and temperature conditions – for example, the works of Sobolev and Lavrent'ev (1971), Gurney (1984), and Grütter *et al.* (2004) – allows for the recognition of potentially diamond-bearing kimberlites as opposed to barren kimberlites.

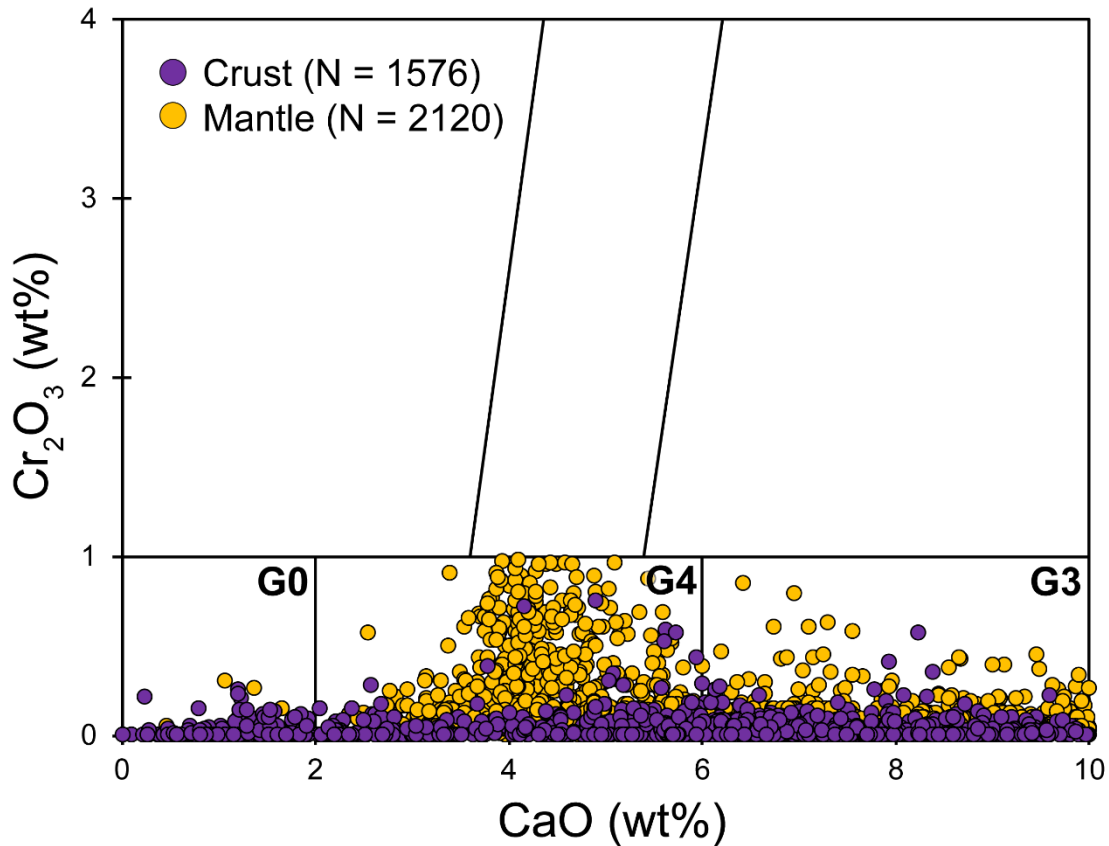


Figure 2.1 Modified Cr_2O_3 (wt%) versus CaO (wt%) plot for garnet after Grütter *et al.* (2004) with the full dataset assessed in this study. The expected overlap of low-Cr crust and mantle garnets ($\text{Cr}_2\text{O}_3 < 1$ wt%) is apparent in the G0, G4, and G3 fields (Unclassified, low-Ca eclogite/pyroxenite, and high-CaO eclogite garnets, respectively). All garnet classes (G) are described in Grütter *et al.* (2004).

Graphical approaches to garnet classification are widely used in the diamond exploration industry because they are simple and, in the case of peridotitic garnets, highly effective. For the peridotitic paragenesis these approaches are capable of discriminating diamond-facies from non-diamond-facies grains (e.g., Grütter *et al.* 2004). For the eclogitic paragenesis, however, one of the first tasks is discriminating mantle eclogitic garnets from some low-Cr garnets derived from crustal rocks, as they may have similar elemental compositions. The most commonly employed graphical approach for crust-mantle discrimination using eclogitic garnets is the Mg# ($\text{Mg}/[\text{Mg}+\text{Fe}]$) versus Ca# ($\text{Ca}/[\text{Mg}+\text{Ca}]$) plot developed by Schulze (2003). The “crust” and

“mantle” fields in the Schulze (2003) method successfully capture a high proportion of the database that was compiled in that study ($> 93\%$ of $N = 2697$ garnets; Schulze 2003). However, many garnets derived from granulites compiled in this study classify as “mantle-derived” using the Schulze (2003) method (Figure 2.2).

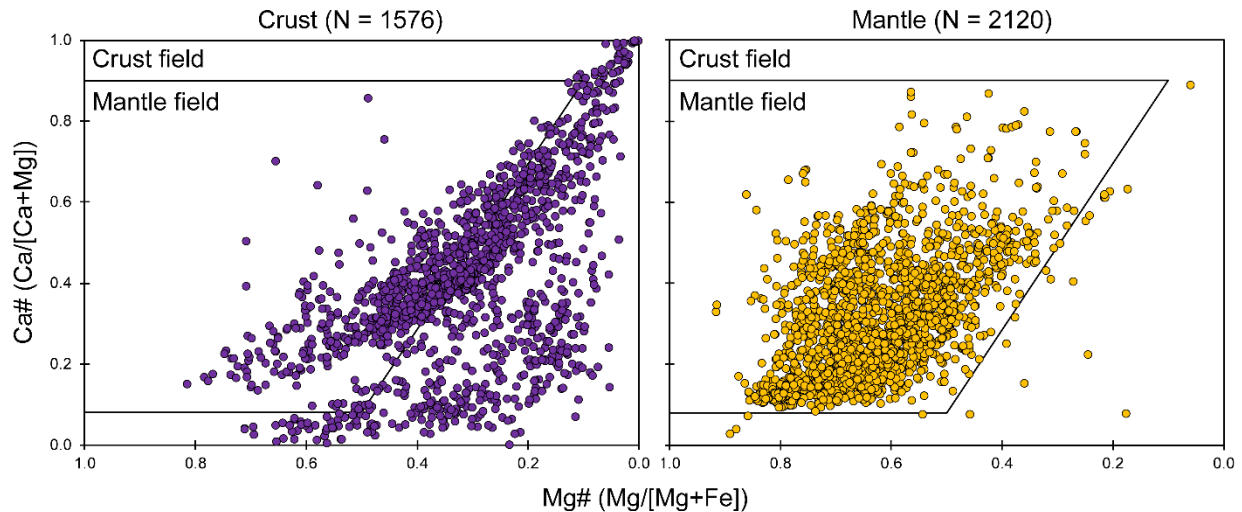


Figure 2.2 Ca# versus Mg# plots (after Schulze 2003) with the full crust (left) and mantle (right) dataset compiled for this study. This expanded dataset improves the lithological variety of the crustal population by including abundant lower-crustal lithologies, which includes garnet granulites.

Krippner *et al.* (2014) reviewed several graphical and quantitative-statistical garnet-based discrimination techniques, focusing on unsupervised statistical methods for the latter (e.g., principal component analysis). These methods do not fully resolve the garnet compositional overlap, even with the original crustal garnet databases containing relatively few lower-crustal garnets. Existing discriminants for kimberlite-derived megacrystic versus mantle garnets (e.g., Schulze 1997; Grütter *et al.* 2004; Rogers and Grütter 2009) are already proficient, but with non-zero error rates: testing my much larger compiled dataset, the distinction between megacrystic and mantle-derived garnets using Na_2O and TiO_2 (Schulze 1997) fails to fully resolve the two populations (Figure 2.3).

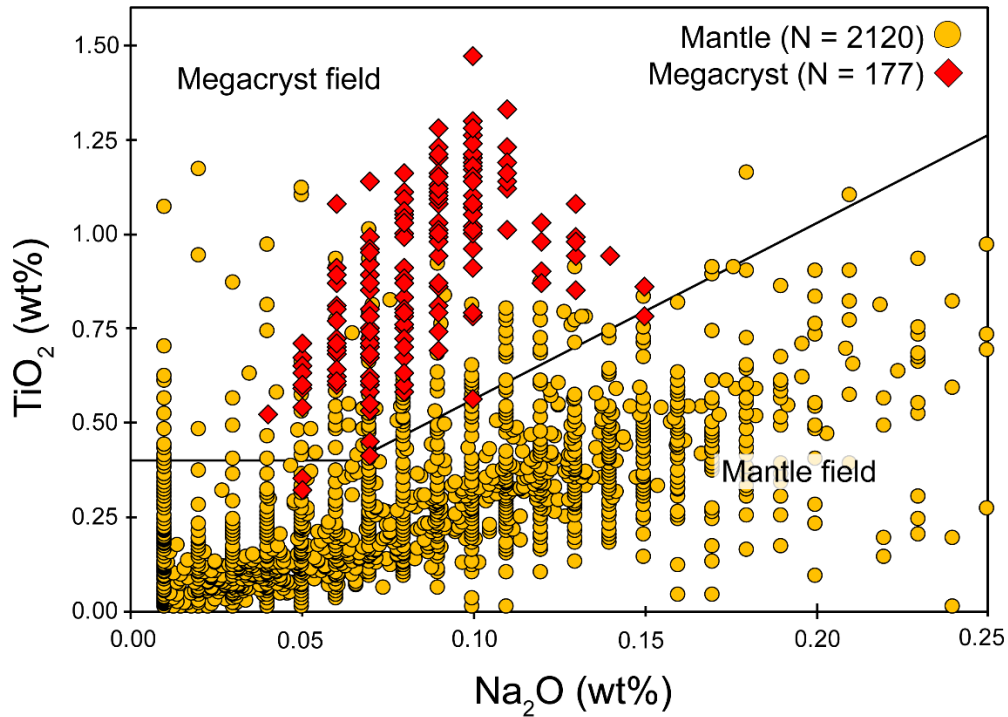


Figure 2.3 Mantle and megacryst garnets from the dataset compiled for this study tested against a Na₂O versus TiO₂ (wt%) plot from Schulze (1997) for the discrimination of mantle and megacryst garnets. This version has been modified from the original by truncating the maximum Na₂O value at 0.25 wt%.

2.1.2 Goals and definitions

A basic goal of this study is to provide a probabilistic approach to the discrimination of mantle-derived garnets from a broad spectrum of crustal garnets sampled during diamond exploration. Beyond that, an additional challenge is to provide discrimination between two sets of mantle-derived garnets with similar compositional characteristics: low-Cr garnet megacrysts (G1), inferred to have a cognate origin with kimberlites (e.g., Garrison and Taylor 1980), and garnets from disaggregated eclogite xenoliths. Although the Grütter *et al.* (2004) G1 classification for “low-Cr megacrysts” extends to < 4 wt% Cr₂O₃, crustal garnets commonly have Cr₂O₃ < 1 wt% and so low-Cr megacryst garnets with Cr₂O₃ < 1 wt% are preferentially discussed in this study.

The term “mantle eclogite” is used here to encompass mantle samples containing low-Cr (< 1 wt% Cr₂O₃) garnets, excluding megacrysts but including pyroxenite and eclogite *sensu stricto* (Desmons and Smulikowski 2007). New graphical methods and multivariate statistical techniques such as logistic regression and linear discriminant analyses are investigated in this text for their potential to discriminate crust-mantle origins of low-Cr garnets. Where complete discrimination is not possible, a probabilistic assessment of the uncertainty of any given sample classification is discussed.

2.2 Background

2.2.1 Garnet compositional variation

Garnet is a mineral whose crystal structure can accommodate the substitution of a wide variety of cations in highly-variable abundances (Table A.1). The garnet crystal structure has three cation sites: a distorted dodecahedral X site for divalent cations, an octahedral Y site for trivalent cations, and a tetrahedral Z site for tetravalent cations. Essentially most (major) discriminatory variability occurs on the X cation site, and the broad range of possible garnet compositions can therefore be simplified via ternary diagrams which cast the high variance Fe₃Al₂Si₃O₁₂ (almandine), Mg₃Al₂Si₃O₁₂ (pyrope), and Ca₃Al₂Si₃O₁₂ (grossular) components as apices (e.g., Coleman *et al.* 1965).

2.2.2 Historical graphical discrimination techniques

Crust-mantle-megacryst discrimination between garnets is possible using the scheme of Schulze (2003), which recasts the major substitutional relationship of the X cation site involving Fe, Mg, and Ca as a bivariate plot (e.g., Figure 2.2). Relative to mantle garnets, metamorphic garnets formed in and derived-from the upper- to mid-continental crust are commonly enriched in

almandine and grossular over the pyrope component (Schulze 2003). However, the training set used by Schulze (2003) was dominated by upper-crustal and low-Cr mantle garnets, leaving garnet granulites and orogenic eclogites underrepresented in the dataset. While the scheme is highly effective using the dataset compiled by Schulze (2003), an expanded dataset containing abundant lower-crustal garnets, particularly those derived from metabasites typical of the lower crust in cratonic settings, results in large degrees of crust-mantle overlap at intermediate Mg# and Ca# values. Specifically, when pyrope-rich crustal garnets comprise a significant proportion of an “unknown” dataset, such compositions overlap strongly into the “mantle” field and greatly reduce the overall success rate of the scheme (Figure 2.2).

The Grütter *et al.* (2004) method discriminates low-Cr megacrysts and other low-Cr mantle samples from more Cr-rich megacrysts, pyroxenite, and peridotites based on Cr₂O₃ content, but is not calibrated to discriminate low-Cr (Cr₂O₃ < 1 wt%) crustal garnets from mantle-derived garnets (Figure 2.1). Mg# and elevated TiO₂ are used to discriminate low-Cr megacrysts as a distinct category (G1 garnets after Grütter *et al.* 2004) and has also been addressed successfully using the methods of Schulze (1997), Schulze (2003), and Rogers and Grütter (2009): Rogers and Grütter (2009) proposed a reclassified G1R category for megacryst garnets with lower TiO₂ contents than G1 garnets, based on a study of the Luxinga kimberlite cluster, Angola. TiO₂ is complemented by Na₂O in the Schulze (1997) discrimination plot of mantle eclogites versus low-Cr megacrysts (Figure 2.3). From the above discussion, it should be clear that a variety of geochemical variables are required to discriminate low-Cr (Cr₂O₃ < 1 wt%) garnets derived from crustal, mantle, and megacrystic sources, with no single currently-used graphical method being fully suitable.

2.2.3 Statistical discrimination methods

Multivariate statistical methods that employ more than two variables can be broadly classified as unsupervised and supervised. Statistical methods classified as “unsupervised” do not consider *a priori* outcome variables or classes (e.g., “crust” or “mantle”) of the training or “calibration” data, instead treating data as “unknowns” and acting based only on variables or features in the data (Hastie *et al.* 2009). This approach posits that a sufficient discriminant is built into the data structure, without requiring known classification information. However, the results may require “ground-truthing” to assign geological meaning. Conversely, in “supervised” learning problems, *a priori* outcome variables or classes of training data are used to guide the learning process, and a discriminant is chosen which adheres to the distribution or separation of populations, as much as a technique dictates (Hastie *et al.* 2009).

Unsupervised methods include principal component analysis (PCA), which recasts geochemical parameters as principal components based on the variance of the explanatory variables used in discrimination. PCA will be a suitable means of discrimination for problems (e.g., lithologies) where the main discriminants are tied to high variance elements (e.g., Fe, Mg, and Ca in garnet). For example, discrimination of garnets from granites and metapelites can be improved using PCA over simple ternary diagrams (Krippner *et al.* 2014). For discrimination problems where centroids and variances become increasingly similar (“geochemical overlap”), PCA becomes less powerful and simple boundaries in principal component-space become increasingly difficult to define (e.g., Krippner *et al.* 2014, and figures therein).

Cluster analysis (CA) is an additional group of unsupervised techniques. CA subdivides data into “clusters” based on similarity (Hastie *et al.* 2009). A CA-based approach was employed by

Dawson and Stephens (1975) to develop a first classification scheme for kimberlite-hosted mantle garnets. However, the clustering process may not be geologically meaningful and therefore it becomes important to assess the nature of returned clusters. Further, without prior calibration using known classification information, unsupervised techniques may fail to subdivide samples which are highly similar (e.g., many low-Cr crust and mantle garnets). In addition, continuing to subdivide or categorize training data until it is completely classified may result in an unmanageably large number of potentially meaningless classification groups, as outlier data or “noise” is classified instead of actual data (“over-fitting;” Schulze 2003, and references therein).

Supervised methods are generally more powerful than the above unsupervised approaches. Cluster Analysis by Regressive Partitioning (CARP) based on the Classification and Regression Trees (CART) methodology is a supervised method employed by Griffin *et al.* (2002) to subdivide populations of subcontinental lithospheric mantle (SCLM) derived Cr-pyrope garnets. CART-based schemes result in trees of successive binary decisions that progressively “purify” the populations by sub-dividing data into mutually exclusive classes. These trees are easy to conceptualize and can easily be used to classify new data. In ideal cases as in the SCLM garnet classification problems addressed by Griffin *et al.* (2002), classes can be assessed as having geologic significance, though this should not be assumed in all instances. Nonetheless, overfitting is also a concern with CART methods, because subdivision is a function of the level of classification quality chosen by the researcher and if this is not carefully monitored the procedure may ultimately subdivide all data, including outlier or spurious information. Training data will therefore be classified very well while test data may be prone to variable degrees of error, particularly if certain compositions are not represented in the training dataset. Therefore,

data should be carefully screened, and irrelevant trees, branches, or nodes must be removed. The training dataset should be sufficiently robust and representative.

Additional supervised methods include linear discriminant analysis (LDA) and logistic regression (LR). LDA is based on least squares estimation (LSE) and uses a linear combination of variables to separate groups of data or objects (Abledu *et al.* 2016). It assumes that independent (or explanatory) variables conform to a Gaussian distribution and have equal covariance matrices or covariance structures (Hastie *et al.* 2009). Conversely, LR is fitted using maximum likelihood estimators (MLE), allowing it to predict the probability that a data point or observation can be classified into one of a mutually exclusive set of classes (Press and Wilson 1978; Hastie *et al.* 2009), essentially a measure of classification confidence. LR makes no assumptions about data distribution for variables or equivalence of covariance matrices (Abledu *et al.* 2016).

As with any statistical method, there are potential drawbacks to LDA and LR. Inter-correlation of variables (multicollinearity) is a strong consideration for both techniques and if prevalent will negatively affect the classification and predictive capabilities of the derived schemes (Næs and Mevik 2001). Multicollinearity may result in regression or classification instability as well as increasing the potential for classification errors when applied to new “first-seen” data (Næs and Mevik 2001). Therefore, explanatory variables should be sufficiently independent from one another. In addition, LR as an MLE-based technique theoretically requires a larger number of observations to ensure quality results when compared to the LSE-based LDA method, though in practice the importance of this stipulation is debated (Abledu *et al.* 2016, and references therein). Although the outputs of LDA and LR may appear similar, they are derived in significantly different ways.

A useful output of LR techniques is that they can be used to assign a “discriminant value” (d) to data, which may be converted to a probability p (Equation 2.1) to assess the confidence of a data point’s calculated classification (e.g., crust versus mantle eclogite). The quality of a scheme can be assessed by considering the difference between the actual probability of a data point and the calculated probability assigned to it by these methods.

$$p = 1/(1 + e^{-d}) \quad (2.1)$$

Experimental studies under highly controlled conditions (e.g., population size, controlled degree of normality, controlled covariance value) indicate that for cases with normal data distributions LDA provides slightly better results than LR (Pohar *et al.* 2004). However, if data depart from a regular distribution – as may be common (or unknown) in smaller datasets – LR continues to provide adequate results while LDA may become less reliable (Pohar *et al.* 2004). In the statistical community debate continues into the practical advantages of each method (Abledu *et al.* 2016, and references therein). Under circumstances where the assumptions are met (e.g., normality), LDA and LR perform equally well and even under circumstances where data departs from a regular distribution (e.g., Gaussian, Normal) assumed by LDA, the resolving power of LR over LDA might not be substantial (Press and Wilson 1978; Hastie *et al.* 2009; Abledu *et al.* 2016). To conclude, similar results may be anticipated for LDA and LR in many instances (Hastie *et al.* 2009).

2.3 Dataset

2.3.1 Overview

A new reference garnet dataset for the training and testing of discrimination schemes has been compiled in this study. This dataset comprises garnet major-element data drawn from a

combination of literature resources as well as 719 new analyses. This study focuses on the geochemical discrimination of kimberlite-hosted lower-crust and low-Cr mantle garnets recovered during diamond exploration programs. Garnets not derived from kimberlites may also be collected during sampling of streams or tills and may geochemically overlap with kimberlite-hosted garnets. Therefore, a variety of additional types of crustal samples are included in this new dataset. All selected garnets have low Cr (< 1 wt% Cr_2O_3). This cut-off distinguishes mantle eclogite from peridotite-derived garnets (Schulze 2003). Crustal garnets rarely approach 1 wt% Cr_2O_3 . All verified mantle-derived garnets with $\text{Cr}_2\text{O}_3 < 1$ wt% (apart from low-Cr megacrysts) are included in the “mantle” dataset. As discussed in Grütter *et al.* (2004), a further subdivision of garnets in their “G4” category (mixed category of garnets with $\text{Cr}_2\text{O}_3 < 1$ wt%, derived from eclogite-websterite-pyroxenite) into eclogitic or pyroxenitic parageneses (traditionally carried-out using coexisting clinopyroxene compositions; Desmons and Smulikowski 2007) cannot be achieved based on garnet chemistry alone. The simplifying nomenclature of “mantle” or “mantle eclogite” is used here to describe all such samples. As for low-Cr megacrysts, megacrystic garnets with $\text{Cr}_2\text{O}_3 < 1$ wt% are compiled here into a separate dataset and referred to as “megacryst” or “low-Cr megacryst.” All new data from this study are included in Tables S1 and S2 in the Supplementary Online Dataset. Data from the literature are included in Table S3 in the Supplementary Online Dataset.

2.3.2 Data quality control and analytical methods for new and literature data

New data in this study were obtained from garnet granulite and eclogite xenoliths from several global localities. Xenoliths were washed thoroughly, crushed, and a single unaltered garnet grain from each was mounted for analysis. Samples were classified as crust- or mantle-derived based on their whole-rock mineralogy: samples containing primary plagioclase and/or amphibole were

classified as crust-derived, and those lacking these minerals classified as mantle-derived. Classification of samples using mineral assemblage differs from that of some previous studies (e.g., Dawson and Stephens 1975). Major-element data was obtained for all garnets using a JEOL JXA-8900R electron probe microanalyser (EPMA) at the University of Alberta. Samples were analyzed with a 20 kV accelerating voltage, 20 nA probe current, and a 2 μm diameter beam. An overview of analyzed elements and count times is included (Table A.2).

For new and literature analyses, only samples with oxide totals between 98.5 and 101.0 wt% are used. The lower limit of detection (LLD) for employed geochemical variables represent the smallest signals that can be observed, typically 3σ over background. However, data that fall very close to the LLD are non-quantitative and may be subject to extreme uncertainties ($\pm 100\%$). Each literature study may, based on analytical conditions, result in slightly different LLD values for analyzed elements. Therefore, to maintain consistency, blanket detection limits were applied to elements which are typically of low abundance in garnet. For the purposes of this study, data are assigned blanket detection limits of 0.01 wt%. These detection limits are applied post hoc to the selection of data based on oxide totals. Values below the detection limit are indicated with *bdl* in Tables S1, S2, and S3 in the Supplementary Online Dataset, and substituted with a value of 0.01 wt% for use in this study. Samples for which data was not analyzed or determined (e.g., “nd” in literature) were avoided where possible. In addition, for literature studies reporting Fe_2O_3 , all Fe is recalculated as FeO mathematically ($\text{FeO} = \text{Fe}_2\text{O}_3 \times 0.8998$). The reference lists for the supplementary datasets of Krippner *et al.* (2014) and Suggate and Hall (2013) were substantial sources of garnet data.

Crust and mantle low-Cr garnets from a wide variety of lithologies were chosen from literature, with a focus on garnet granulites.. For scheme training purposes, crustal versus mantle eclogite

schemes are derived using only the “crust” and “mantle” data within a “calibration” dataset (N = 3696). Megacryst samples are kept separate from the calibration dataset and are tested subsequently using the mantle-megacryst discriminants of Schulze (2003), Grütter *et al.* (2004), and Rogers and Grütter (2009).

2.4 Classification methodology

2.4.1 Geochemical variables and dealing with compositional data

Suitable variables for discrimination should be related geochemically to a crust, mantle, or megacrystic origin but lack strong correlation to other employed variables. At best, correlated variables would provide little additional information and at worst act as serious impediments to statistical methods as high degrees of multicollinearity have direct negative repercussions on their functionality (Section 2.2.3). Hence, the high-variance elements Fe, Mg, and Ca are the primary discriminators in many schemes (e.g., Coleman *et al.* 1965; Schulze 2003). However, usage of minor substituting elements is still prolific. The usage of TiO₂ and Na₂O (Schulze 1997) and Cr₂O₃ (Grütter *et al.* 2004) has already been discussed.

An additional and significant issue for any statistical approach is that compositional data, such as garnet EPMA major-element analyses, are subject to the unit-sum constraint or “closure” (Aitchison 1994; Equation 2.2).

$$x_1 + x_2 + x_3 + x_4 + x_5 = 1 \text{ or } = 100 \% \quad (2.2)$$

As a function of compositional data representing proportions of that sum (e.g., 100 wt% for oxides), increases in one component may be accommodated by apparent decreases in another. Therefore, a correlation between these two components may reflect the unit-sum constraint and

have no further geologic meaning. Autocorrelation between MgO and SiO₂ is particularly strong: a decrease in Fe on the X cation site may be compensated by an increase in Mg and adjustments in the proportions of all other constituents by the unit-sum constraint, particularly SiO₂ (as Fe and Mg vary strongly with respect to molecular weight). To reduce the effects of closure, variables are selected which do not strongly display this relationship. For example, only using either MgO or SiO₂. In addition, Si is used as the denominator: Si is an extensive property of the garnet chemical structure with a value closely approximating 3.00 atoms per formula unit (based on [O] = 12) in most cases. Employing a denominator whose value is conserved while the system is changing serves to define a “Pearce element ratio” which can be used to alleviate closure concerns (Russell *et al.* 1990). The use of the natural logarithm (ln) allows the values of these variables to expand beyond the limited range they are bounded by as a function of the unit-sum constraint. In addition, converting to logarithmic units shifts non-normal or skewed distributions increasingly toward normality, particularly useful for the proper usage of LDA, which assumes normally-distributed variables.

Not all geochemical variables in garnet behave in the same manner. Elevated Mn contents are notable at low Mg# in some crustal samples and elevated Cr contents at high Mg# in some mantle samples. Conversely, Na and Ti are elevated in mantle-derived garnets relative to crustal garnets at moderate Mg# (> ~30 mol% pyrope), where samples overlap most thoroughly in Mg# versus Ca# space (e.g., Schulze 2003). Approximately 39.2 % of crustal garnets and ~ 1.1 % of mantle garnets in the full dataset compiled here misclassify using the method outlined in Figure 8 of Schulze (2003), and the most severe population overlap between crust and mantle garnets occurs at intermediate Mg# and Ca# (e.g., > ~ 30 mol% pyrope; Figure 2.2). Thus, ideal variables would be most distinctly different at such values.

Na₂O and TiO₂ have also been employed as discriminatory variables for crustal, low-Cr mantle, and megacryst garnets (Schulze 1997). In regard to sodium, the dominant control on Na content in eclogitic garnet is whole-rock composition (Grütter and Quadling 1999). Sodium will increasingly partition into eclogitic garnet with increasing pressure (Sobolev and Lavrent'ev 1971), which has been used empirically as a tool in diamond-exploration: Na₂O concentrations ≥ 0.07 wt% (Gurney 1984; Grütter and Quadling 1999; Schulze 2003) or ≥ 0.09 wt% (McCandless and Gurney 1989) have been taken to suggest derivation from diamond-facies pressures. Based on this, sodium may possibly be a first-order discriminant for crust and mantle garnets (in this case, including potentially graphite-facies mantle samples), as higher pressures prevail in the latter. However, while the majority of garnets from crustal rocks in the dataset compiled in this study have Na₂O_{grt} < 0.07 wt% or < 0.09 wt%, many low-Cr garnets from mantle eclogites also have Na₂O < 0.07 or < 0.09 wt% (Figure 2.4). In addition, bulk-rock chemical control on Na may mask the minor changes in garnet composition associated with pressure: bulk-rock corrections may need to be applied before changes associated with pressure can be assessed, as some diamond-facies eclogitic garnets have Na₂O_{grt} < 0.07 wt% (Cookenboo *et al.* 1998; Grütter and Quadling 1999).

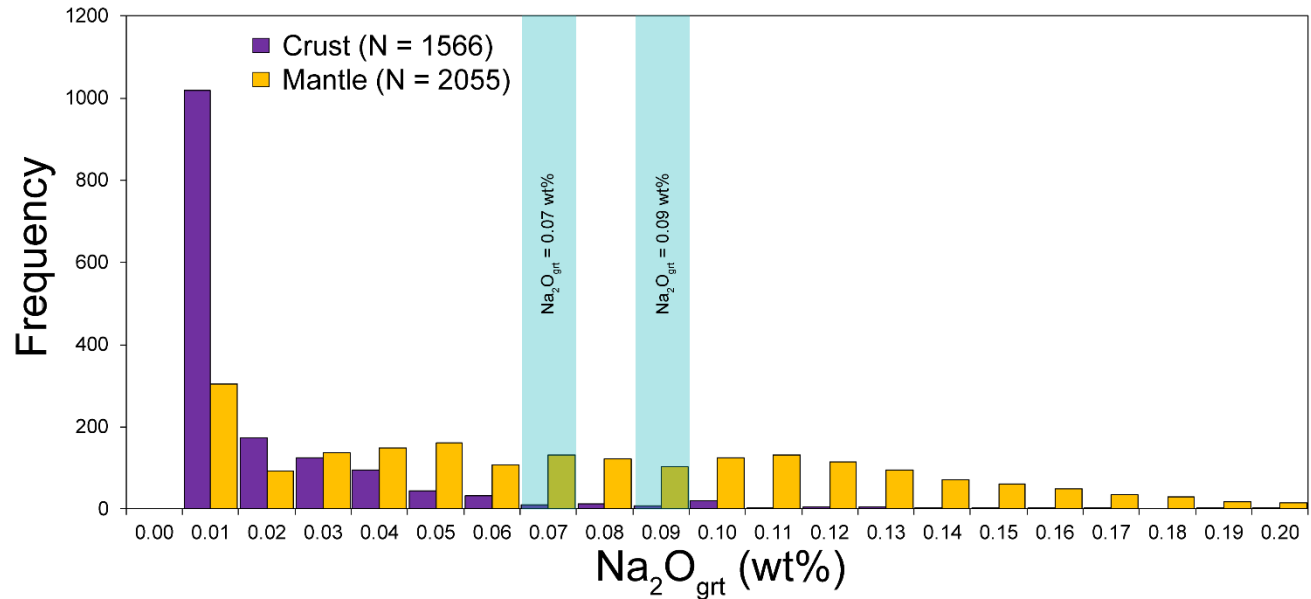


Figure 2.4 Distribution of Na₂O compositions for crustal and mantle garnets compiled in this study. The blanket detection limit is Na₂O = 0.01 wt%. Na₂O compositions extend to higher than 0.20 wt% but are not shown. Blue fields indicate garnet Na₂O = 0.07 wt% and 0.09 wt% cut-offs, which have been inferred as minimum garnet sodium contents for diamond-associated eclogitic garnets, discussed and/or used in practice by Sobolev and Lavrent'ev (1971), Gurney (1984), McCandless and Gurney (1989), Grütter and Quadling (1999), and Grütter *et al.* (2004).

There is in general a positive correlation between Na and Ti for the eclogitic paragenesis (e.g., Bishop *et al.* 1978; Jaques *et al.* 1998). For mantle-megacryst discrimination, both Na₂O and TiO₂ are recommended by some methods (e.g., Schulze 1997): low-Cr megacryst garnets deviate from the Na-Ti correlation observed for mantle eclogites (e.g., Schulze 1997). In addition, low-Cr megacrysts occur predominantly at Mg# > ~0.65 (Schulze 2003; Grütter *et al.* 2004; Rogers and Grütter 2009). Low-Cr megacrysts may be classified as G1 (Grütter *et al.* 2004) and those with lower TiO₂ contents than G1 garnets may be classified as G1R (Rogers and Grütter 2009).

From the above considerations, employing extremely low abundance elements toward crust-mantle discrimination should be done with care. Of the 3696 crustal and mantle garnets in the new compiled dataset, 1142 analyses (~ 30.9 % of the full calibration dataset) have reported Na

contents below the blanket LLD of 0.01 wt% (often reported as either “below detection” or 0.00 wt%), potentially elevating the degree of uncertainty. The same problem applies to Cr₂O₃ (23.3 % of garnets), and TiO₂ (10.1 % of garnets). Extremely low abundance values below or near detection limit will be subject to extreme uncertainties (± 100 %), and their usage may render resultant discriminants less certain as well.

In the following sections, new graphical and statistical methods are developed using garnet major-element compositions. The elemental variables employed in these different methods are discussed below, and are all based on cation values or atomic proportions (based on atomic mass). Equations for calculation using atomic proportions are provided (See Section 2.4.2).

2.4.2 Derivation of a classification scheme: Graphical discrimination

The new crust-mantle garnet dataset employed in this study affords significant advantages in testing the efficacy of new graphical and statistical garnet classification schemes because it offers more coverage of the types of crustal garnets commonly encountered during diamond exploration in cratonic regions. Two goals in generating new graphical schemes for garnet discrimination were to reduce the error rates of both crustal and mantle garnet classification simultaneously, and to choose parameters that are relatively robust against closure effects. Compositional overlap in Mg# versus Ca# space in previous schemes (Schulze 2003; Figure 2.2) between crust and mantle garnets is greatly reduced in a bivariate graphical plot employing axes of $\ln(\text{Ti/Si})$ and $\ln(\text{Mg/Fe})$ (Figure 2.5A).

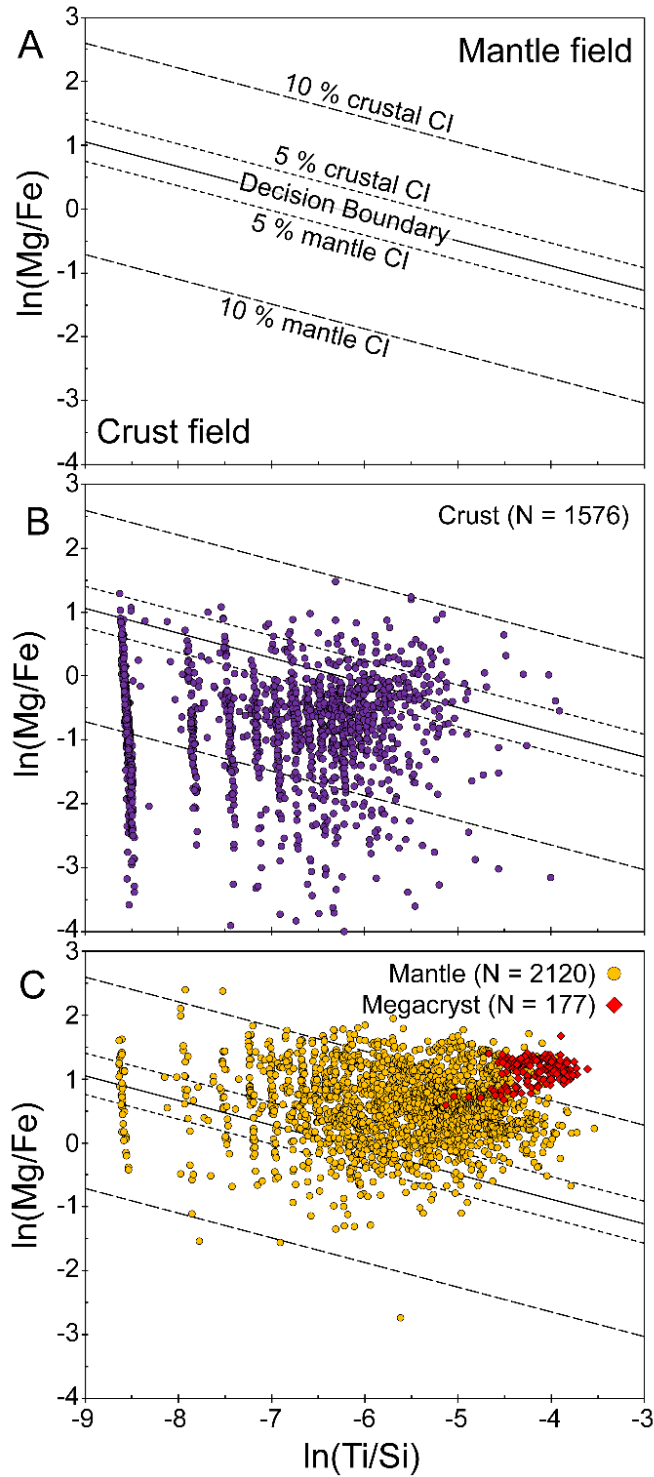


Figure 2.5 A) Blank $\ln(\text{Ti}/\text{Si})$ versus $\ln(\text{Mg}/\text{Fe})$ bivariate plot for the discrimination of low-Cr crust, mantle, and megacryst garnets. Confidence intervals (CI) are indicated which enclose 5 and 10 % of the full 10.1 % error rate of the calibration dataset. B) Crustal garnets are plotted. C) Mantle-derived (yellow) and megacrystic (red) garnets are plotted.

Testing data are plotted (crustal garnets in Figure 2.5B, mantle and megacryst garnets in Figure 2.5C). As discussed above Si is employed as denominator and the natural logarithm of the ratios is taken to alleviate issues associated with the unit-sum constraint (Aitchison 1982). For the $\ln(\text{Mg}/\text{Fe})$ term, however, the Si terms in Mg/Si and Fe/Si cancel through division, leaving a simplified expression with Fe as the denominator.

All schemes derived in this paper are based on garnet elemental concentrations in atomic% (as all employed variables are ratios, using cation values leads to the same results). Atomic% values are calculated from oxide wt% data by division through the oxide molecular weight. Constants for a simplified conversion of oxide wt%-based ratios into atomic%-based ratios are provided in Table A.3.

The decision boundary for crust-mantle classification in Figure 2.5A was initially selected visually using the full calibration dataset of crust and mantle garnets. The quality of the decision boundary was then assessed through trigonometric calculation of perpendicular distances of all data points to the decision boundary, which shifted until the proportion of crust failures and mantle failures were equalized and minimized (equivalent to the intersection of population density curves for misclassifications as a function of perpendicular distance). The final decision boundary for crust-mantle discrimination is a straight line given by Equation 2.3. Equation 2.3 in its presented form minimizes the overall error rate of the dataset, but can be adjusted to minimize the mantle error rate preferentially while increasing the crustal error rate: this can be completed by replacing the y-intercept value of -2.433 with a value of -3.151 instead (Equation 2.4).

$$\ln\left(\frac{\text{Mg}}{\text{Fe}}\right) = -\frac{2.325}{6} \times \ln\left(\frac{\text{Ti}}{\text{Si}}\right) - 2.433 \quad (\text{Minimize overall error rate}) \quad (2.3)$$

$$\ln\left(\frac{Mg}{Fe}\right) = -\frac{2.325}{6} \times \ln\left(\frac{Ti}{Si}\right) - 3.151 \quad (\text{Minimize mantle error rate}) \quad (2.4)$$

Data falling onto this decision boundary are ambiguous and cannot be assessed as crust- or mantle-derived. Data plotting below the decision boundary line in Figure 2.5A (given by Equation 2.3), classify as “crust-derived” and data plotting above the decision boundary are classified as “mantle-composition” (mantle eclogite-pyroxenite plus low-Cr megacryst; see Figure 2.5B and 2.5C). Low-Cr megacrysts must subsequently be separated from mantle eclogite-pyroxenite through usage of existing methods (e.g., methods of Schulze 2003, Grütter *et al.* 2004, and/or Rogers and Grütter 2009).

To provide some measure of uncertainty of the classification of single garnets, “confidence intervals” (CI) are derived. A high proportion of failures in Figures 2.5B and 2.5C occur in close proximity to the decision boundary. Within the 5 % CI field, 5 % of all garnets in the calibration dataset misclassify; within the 10 % CI field, 10 % of all garnets in the calibration dataset misclassify. If the entire misclassified garnet data in the calibration dataset were to be taken into account, the Total CI would be equivalent to 10.1 %. Between the decision boundary and a single CI line, 5 or 10 % of garnets misclassify with respect to their sample group (crust or mantle). The CI boundaries for crust-mantle discrimination are offset and parallel to the main decision boundary. They are shown in Figure 2.5A and can be derived using values provided in Table A.4. It should be noted that those workers interested in maximizing the inclusion of mantle grains using the expression given in Equation 2.4 will risk the inclusion of a very substantial proportion of crustal garnets (~ 33.6 %; Section 2.5.1), which may complicate exploration efforts.

2.4.3 Derivation of a classification scheme: Statistical discrimination

Multivariate statistical methods permit the use of multiple compositional variables. For the classification of garnet, I test the viability of using the eight elements Ti, Al, Cr, Mn, Fe, Mg, Ca, and Na in a single method. Multicollinearity between all variables is calculated to assess their amenability to the statistical methods LDA and LR. Multicollinearity can be quantified using the variance inflation factor (VIF; Equation 2.5), which requires the coefficient of determination (R^2) for variable pairs.

$$VIF = 1/(1 - R^2) \quad (2.5)$$

R^2 can be determined by the degree of correlation between two variables in a bivariate plot (Table A.5). VIF values > 10 are taken to indicate high degrees of multicollinearity (O'Brien 2007). The VIF values for all combinations of variables used in crust-mantle discrimination are given in Table A.5. All values are well below 10 indicating that they are sufficiently uncorrelated to permit their proper application to LDA and LR techniques.

The LDA and LR solutions were derived using the Freeware “R” and RStudio. Runstreams are provided in Table A.6. Crust-mantle discrimination schemes are derived using the calibration dataset comprising all available crust ($N= 1576$) and mantle garnet ($N = 2120$) data. Low-Cr megacrysts are not included in the calibration dataset. The expressions for LDA and LR discrimination of crust-mantle garnets are given by Equations 2.6 and 2.7, respectively, where d is the “decision boundary” value and values of $d_{\text{CM-LDA}} < -0.264$ or $d_{\text{CM-LR}} < 0.000$ are classified as “crust,” and values of $d_{\text{CM-LDA}} > -0.264$ or $d_{\text{CM-LR}} > 0.000$ are classified as “mantle-composition.”

$$d_{CM-LDA} = 4.717 + 0.236 \times \ln\left(\frac{Ti}{Si}\right) - 0.117 \times \ln\left(\frac{Al}{Si}\right) + 0.212 \times \ln\left(\frac{Cr}{Si}\right) - 0.052 \times \ln\left(\frac{Mn}{Si}\right) - 1.874 \times \ln\left(\frac{Fe}{Si}\right) + 0.472 \times \ln\left(\frac{Mg}{Si}\right) + 0.094 \times \ln\left(\frac{Ca}{Si}\right) + 0.515 \times \ln\left(\frac{Na}{Si}\right) \quad (2.6)$$

$$d_{CM-LR} = 14.954 + 0.661 \times \ln\left(\frac{Ti}{Si}\right) + 2.996 \times \ln\left(\frac{Al}{Si}\right) + 0.538 \times \ln\left(\frac{Cr}{Si}\right) - 0.040 \times \ln\left(\frac{Mn}{Si}\right) - 4.330 \times \ln\left(\frac{Fe}{Si}\right) + 1.724 \times \ln\left(\frac{Mg}{Si}\right) + 1.070 \times \ln\left(\frac{Ca}{Si}\right) + 0.985 \times \ln\left(\frac{Na}{Si}\right) \quad (2.7)$$

If present in a sample set, megacrysts will initially be assigned to the “mantle-composition” field and separated through subsequent filtering using Schulze (2003), Grütter *et al.* (2004), and/or Rogers and Grütter (2009) (see above). As all megacrysts classify as “mantle-composition,” their exclusion from the calibration dataset should have no effect on the crust-mantle decision boundaries derived here.

An alternative to a cut-off of $d_{CM-LR} = 0.000$, which minimizes the overall error rate of the full dataset, is to adopt a cut-off of $d_{CM-LR} = -1.650$ which minimizes the mantle error rate regardless of an increased crustal error rate and any attendant problems that arise from that decision.

2.4.4 Probabilities, error quantification, and quality of success

Classification error (CE) is the proportion of misclassified samples relative to the total number of samples (Equation 2.8).

$$CE = \frac{\text{Number of misclassified samples}}{\text{Total number of samples}} \quad (2.8)$$

CE measures the quality of a scheme when tested against the classifying data or calibration dataset, with a lower CE value ideally indicating a higher-quality scheme. To assess the schemes derived in this study, a k-fold cross-validation approach is employed. After deriving the schemes

(Sections 2.4.2 and 2.4.3), the CE is determined using the full calibration set of crust and mantle garnets ($N = 3696$; Table A.7). A more rigorous error rate is then determined via k-fold cross validation with 10 folds (Table A.8). From the full calibration dataset, 10 random training-testing sets of equivalent size (K1 to K10) were chosen with 20 % of garnets allocated to testing/validation and 80 % allocated to training/calibration. A 10-fold approach was chosen to reduce bias in the final averaged error rate (Kohavi 1995). Each training set from K1 to K10 is used to derive a graphical, LR, and LDA scheme in the same manner as outlined in Sections 2.4.2 and 2.4.3, and subsequently tested with its respective testing or validation dataset. The CE values for each scheme and dataset are calculated and then the error rates for sets K1 to K10 are averaged to give a single error rate with two-sigma standard error (Table A.8). The reported two standard deviation (σ) values are on the ten test datasets only. The resulting mean error rate and 2σ are taken as the error rate for each scheme.

CE cannot be used to attach an uncertainty to individual data values. Rather, a larger proportion of misclassified data occurs in close proximity to the decision boundary (e.g., Figures 2.5B and 2.5C). To assess different degrees of uncertainty depending on the location of a data point relative to the decision boundary in the graphical method (e.g., data in Figures 2.5B and 2.5C), “confidence intervals” may be adopted (Section 2.4.2). Relative certainty can be assessed for the statistical technique LR by converting the discriminant value ($d_{\text{CM-LR}}$) for a data point to a probability (p) using Equation 2.1 (Pohar *et al.* 2004; Abledu *et al.* 2016), when a discriminant cut-off of $d_{\text{CM-LR}} = 0.000$ is adopted. Values of p approaching zero based on $d_{\text{CM-LR}}$ from Equation 2.7 indicate a high probability of crustal-derivation and closer to one a high probability of mantle-derivation. Samples assigned $p = 0.5$ ($d_{\text{CM-LR}} = 0.000$) are ambiguous and cannot be assigned to either population. This measure of probability quantitatively improves economic

decision-making for small populations and single grains by helping to quantify the quality (likelihood of correctness) of any single classification.

2.5 Results – Comparison of new graphical and statistical schemes

2.5.1 Graphical methods

All crust and low-Cr mantle garnets in the calibration dataset, as well as the full megacryst dataset, are plotted on a $\ln(\text{Ti/Si})$ versus $\ln(\text{Mg/Fe})$ diagram (Figures 2.5B and 2.5C). All low-Cr megacrysts classify as “mantle-composition” in Figure 2.5C. Crust and mantle populations overlap across the decision boundary and the confidence intervals. The proportion of failed classifications decreases away from the discriminant value as a function of perpendicular distance from the discriminant. Error rates for discrimination of crust and mantle garnets using this plot only are compared with those obtained using the Mg# versus Ca# scheme (Schulze 2003) for the calibration dataset (Table A.7) and via k-fold cross validation (Table A.8).

When testing all crust and mantle garnets, crust discrimination improves from ~ 39.2 to ~ 10.1 % error (mean error rates based on ten test datasets) and mantle discrimination error rates increase from ~ 1.1 % to ~ 10.1 % for the new graphical method relative to the Schulze (2003) scheme. Combined, the new graphical method reduces the error rate on 10 test datasets from ~ 17.1 to ~ 10.1 % relative to the Schulze (2003) method for discrimination of crust and mantle garnets (Table A.8). Applying Equation 2.4 to all garnets (replacing the y-intercept value of -2.433 in Equation 2.3 with -3.151) results in a much lower mantle error rate (~ 2.0 %) but increased crustal error rate (~ 33.6 %; Table A.7).

All data are also tested using sodium contents in garnet ($\text{Na}_2\text{O}_{\text{grt}} = 0.07$ wt%), which has been discussed and applied by Sobolev and Lavrent'ev (1971), Gurney (1984), and Grütter *et al.*

(2004) as a tool for identification of diamond-associated eclogitic garnets. To assess if this compositional cut-off can also be used to discriminate mantle-derived and crust-derived garnets, the data are tested using this cut-off, with $\text{Na}_2\text{O}_{\text{grt}} \geq 0.07$ wt% possibly indicating mantle-derived garnets, and $\text{Na}_2\text{O}_{\text{grt}} < 0.07$ wt% possibly indicating crust-derived garnets. For the data compiled in this study, crust-derived garnets rarely have more than 0.07 wt% Na_2O (~ 5 %), whereas a large number of the mantle garnets (~ 46 %) have less than 0.07 wt% Na_2O which leads to an overall error rate of ~ 29 % (Table A.7).

2.5.2 Statistical methods

Failure rates for crust-mantle discrimination using the LDA and LR methods are assessed by k-fold cross validation and provided as mean error values (Table A.8). The mean error for a ten-fold assessment of the LDA solution (Equation 2.6) is calculated at 8.2 ± 2.3 % for the ten random test sets employed in this study (Table A.8). Similarly, the mean error for LR of a ten-fold assessment is calculated at 7.5 ± 1.9 %. For each test portion of datasets K1 to K10, the error rates on Equation 2.7 (LR) are marginally lower than those of Equation 2.6 (LDA); both are significantly lower than the Schulze (2003) method and my new graphical method (Table A.8).

Changing the $d_{\text{CM-LR}}$ discriminant value for the LR solution has significant impacts on the error rates using the calibration dataset. The default $d_{\text{CM-LR}} = 0.000$ discriminant results in \sim equal crust and mantle error rates (~ 7.6 and 7.2 %, respectively; Table A.7). Adjusting the $d_{\text{CM-LR}}$ discriminant value to -1.650 results in a much lower mantle error rate (~ 2.0 %) and increased crustal error rate (~ 21.0 %), with an overall error rate of 10.1 % (Table A.7).

In addition, for the crust-mantle logistic regression solution (Equation 2.7), $d_{\text{CM-LR}}$ values (when using a discriminant cut-off value of $d_{\text{CM-LR}} = 0.000$) are converted to probability values (p) via

Equation 2.1 and plotted as a histogram of probabilities (Figure 2.6) to better illustrate the relative certainty of classification of a single garnet as a function of d value.

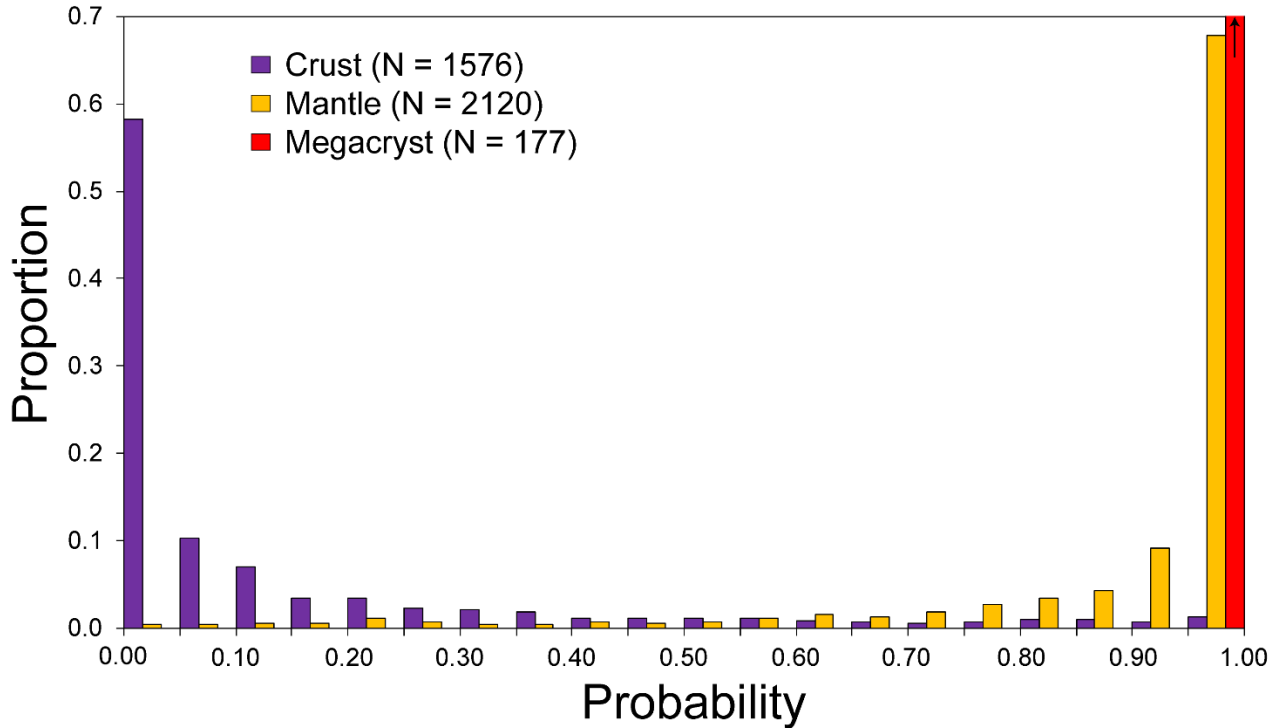


Figure 2.6 Probability density plot for crust, mantle, and megacryst garnets, Y-axis (proportion) truncated at 0.7. The value plotted is probability p , converted from d_{CM-LR} (from Equation 2.7 with a discriminant cut-off value of $d_{CM-LR} = 0.000$) via Equation 2.1. The megacryst population extends to a proportion of 1.00 for the interval $p \geq 0.95$. Bin width is 0.05.

2.5.3 Low-Cr megacryst discrimination

To assess the potential for discrimination of low-Cr megacryst garnets from mantle eclogite-pyroxenite garnets and vice versa, all crust, mantle, and low-Cr megacryst garnets compiled in this study are classified using Figure 9 of Schulze (2003), Section 4.4 of Grütter *et al.* (2004), and Section 3.4 of Rogers and Grütter (2009). No crustal garnets misclassify as megacryst using any of these methods. The Schulze (2003) method has a slightly higher mantle error rate but slightly lower megacryst error rate than does the Grütter *et al.* (2004) method (Table A.9). When

the garnet compositions are classified using the Grütter *et al.* (2004) method followed by the Rogers and Grütter (2009) method, the error rate of megacryst garnets (combined G1 and G1R) decreases to < 1 % while the error rate of mantle garnets increases to ~ 8 % (Table A.9). This result was predicted by Rogers and Grütter (2009) who cautioned that the G1R category may disadvantage the identification of eclogitic garnet compositions.

2.6 Final discussion and conclusions

2.6.1 Graphical methods

Graphical methods are easily-conceptualized and implemented, offering a convenient “first-screening” of test data. However, they may be limited in the number of variables that they may easily express. A $\ln(\text{Ti}/\text{Si})$ versus $\ln(\text{Mg}/\text{Fe})$ plot (Figure 2.5A) is more successful than the existing Mg# versus Ca# plot (Schulze 2003) with respect to the correct classification of kimberlite-hosted, lower-crustal garnets. All test megacryst garnets classify initially as “mantle-composition” rather than “crust” using Figure 2.5A (Equation 2.3) due to their extreme compositions with respect to Ti and Mg/Fe content. It may be feasible that as the megacryst training dataset grows, Figure 2.5A may be modified to include a graphical mantle-megacryst decision boundary. In its current state, some crust and mantle garnets overlap beyond the decision boundary and extend into their opposite field in Figures 2.5B and 2.5C. Specifically, some garnet granulite compositions remain problematic and are geochemically similar to some low-Cr mantle samples with the consequence that both sample types overlap and hence misclassify. The same samples misclassify using existing graphical methods. Discriminant parameters are expressed as Pearce element ratios such that they are robust to the effects of data “closure,” and CI have been derived to indicate areas where a higher proportion of calibration

data misclassify. These are done to attempt to minimize uncertainty in the final solution, which otherwise lacks a statistically-rigorous foundation. Therefore, the confidence in classifications is higher than using existing methods, despite similar misclassifications occurring in each.

While several low abundance elements in garnet vary between crust and mantle garnet populations (e.g., Na₂O, TiO₂, Cr₂O₃), the reliance on data of sufficient quality (above a detection limit of 0.01 wt%) puts an increasing demand on data quality, increasing analytical expenditure. Future analytical studies of garnets should strive to acquire high-quality data to ensure that the certainty of these schemes can be improved, even if the recovered values are very low as a function of geologic processes. Under such future circumstances, it may be reasonable to lower or remove the blanket detection limit applied to low abundance elements, thereby placing greater confidence in crustal garnet data (e.g., specifically Na₂O and Cr₂O₃ contents). The Mg# versus Ca# graphical scheme of Schulze (2003) is more-widely applicable as it requires only the easily obtained Ca, Fe, and Mg concentrations in garnet, but the success rates of the full test dataset (both crust and mantle garnets) using the Schulze (2003) scheme are much lower than in my new graphical scheme, indicating that Ti, at the very least, is needed to increase discriminatory power.

To conclude, non-statistical/graphical discrimination techniques for garnet are powerful and retain an ease of conceptualisation and application. These techniques are highly-suitable for broadly assessing the character of a dataset, although a rigorous probabilistic assessment of data is not possible.

2.6.2 Statistical methods

Supervised statistical methods are preferred over unsupervised statistical approaches and graphical techniques because their training or calibration will be guided by a priori classification information. This feature is necessary for garnet discrimination problems given the broad but overlapping compositional variance of garnet geochemistry, making it unlikely that unsupervised techniques will be sufficient. Many garnet granulite compositions that misclassify using the new graphical method also misclassify using these supervised statistical methods. Complete discrimination cannot be expected for such samples but they can be assessed for their classification certainty via their probability using LR.

Assessment of the LR and LDA methods for their ability to discriminate low-Cr crust and mantle garnets reveals that LR provides slightly higher success rates compared to LDA for crust-mantle discrimination when tested against the test datasets (e.g., sets K1 to K10; Table A.8). In addition, LR is the preferred approach as no assumptions need to be made about data distribution, which is inherently more satisfying as the effects of non-compliant data on a derived scheme are potentially unpredictable. In addition, a probability value is returned for each data point which will aid the diamond explorer in assigning weight to such data.

Despite small differences in success rates between the two approaches, the new LR- and LDA-based statistical solutions presented here are both more effective than the graphical schemes tested in this study for crust-mantle discrimination (Table A.8). The key benefit of the LR approach is the assignment of relative classification certainties to single garnets. This probabilistic assessment of each data point is statistically more rigorous and objective than observations made from graphical techniques. Such functionality affords an end-user the

opportunity to quantitatively address the likelihood of whether a garnet grain has a low-Cr crust or mantle origin.

At present, the Grütter *et al.* (2004), Rogers and Grütter (2009), and Schulze (2003) discriminants for low-Cr megacrysts are recommended for identification of megacryst garnets which classify as “mantle” using the new methods derived in this study. Future studies are recommended for mantle-megacryst discrimination..

As a recommended approach, I suggest:

- 1) Oxide data be applied a correction for low abundance data (< 0.01 wt%), then converted to the required atomic proportion Pearce element ratios (e.g., using the conversion factors given in Table A.3);
- 2) Data be screened using Equation 2.6 (LDA) or Equation 2.7 (LR) for a crust or “mantle-composition” origin. Assuming a cut-off of $d_{CM-LR} = 0.000$ will provide the lowest overall error rates by minimizing and equalizing crust and mantle error rates, while a cut-off of $d_{CM-LR} = -1.650$ will minimize the mantle error rate preferentially while elevating the crustal error rate;
- 3) Garnets which are classified as “mantle-composition” based on choice of d_{CM} cut-off with $d_{CM-LDA} > -0.264$, $d_{CM-LR} > 0.000$, or $d_{CM-LR} > -1.650$ should further be assessed for a potentially megacrystic origin using the Schulze (2003), Grütter *et al.* (2004), and/or Rogers and Grütter (2009) low-Cr megacryst discriminants;
- 4) The remaining “mantle-composition” garnets have compositions that may correspond to the G0, G3, and G4 classes of Grütter *et al.* (2004);

5) Numerical probabilities for crust and “mantle-composition” designations may be derived for $d_{\text{CM-LR}}$ values (Equation 2.7) using Equation 2.1.

The most extreme crustal failures in the logistic regression solution (Equation 2.7 – LR) are assigned incorrect $d_{\text{CM-LR}}$ values ($d_{\text{CM-LR}} > 0.000$) due to combinations of elevated $\ln(\text{Cr/Si})$, $\ln(\text{Ti/Si})$, $\ln(\text{Mg/Si})$ and/or $\ln(\text{Na/Si})$ and lower $\ln(\text{Fe/Si})$ and/or $\ln(\text{Mn/Si})$ which approximate those of mantle garnets. This results in elevated $d_{\text{CM-LR}}$. The same occurs for extreme mantle failures which often have some combination of lower $\ln(\text{Mg/Si})$, $\ln(\text{Cr/Si})$, $\ln(\text{Ti/Si})$, and/or $\ln(\text{Na/Si})$ and higher $\ln(\text{Fe/Si})$ and/or $\ln(\text{Mn/Si})$ that together result in $d_{\text{CM-LR}}$ values consistent with successful crustal garnets. In many failing samples, Mg# values in particular are often highly consistent with correctly assigned samples from the opposing population, but extreme incorrect $d_{\text{CM-LR}}$ values are also possible when combinations of other elements match closely with the opposing population (most notably Cr_2O_3 and TiO_2). This makes it very difficult to reconcile these failing garnets.

Incorrect $d_{\text{CM-LR}}$ values approaching the discriminant ($d_{\text{CM-LR}} = 0.000$) commonly result from the combination of subtle deviations in garnet geochemistry. This renders it difficult to improve the subdivision at $d_{\text{CM-LR}} \sim 0.000$ as it is not possible to identify erroneous samples using broad geochemical cut offs. Adjusting these schemes to capture garnet “failures” results in otherwise correctly-classified garnets being misclassified, which is problematic given the subordinate abundance of failures relative to successes in the same geochemical space. These garnet failures result from the complexity of garnet geochemistry, itself a reflection of host-rock character and history (e.g., melting, metasomatism, accessory mineral assemblage, etc.). It is therefore very difficult to completely predict low-Cr garnet class (crust versus mantle) using major-elements alone.

2.6.3 Quality assessment/valuation

CE can be used to assess a scheme's discrimination quality but weighs all points equally. For the statistical method LR, for example, a sample assigned a probability value (p) of 0.75 would be assigned to the same class and be afforded the same weight via CE as one assigned a probability value of 0.55, despite the former being more probable. This may lead to an over- or under-estimation of scheme quality (Section 2.4.4). This described measure of data classification certainty cannot be assessed for some graphical methods, such as the Schulze (2003) method or Equations 2.3 and 2.4 in this study, as they lack a rigorous statistical foundation. Instead, a subjective assessment of probability is a possible tool as data located at a closer perpendicular distance to the discriminant coincide with areas of lower compositional purity (areas where higher proportions of training data misclassify). By extension, the CI based on the proportion of population failures permits the assignment of a crude form of quantitative-assessment for a data point by indicating areas which contain garnets accounting for 5 % or 10 % of the overall 10.1 % failure rate of the calibration dataset. Sample designations within these intervals should be considered with increased skepticism approaching the decision boundary.

Experimental studies (e.g., Pohar *et al.* 2004) have found a highly comparable success rate of LR and LDA, with LR becoming increasingly stronger than LDA as normality assumptions become progressively violated. My results, which indicate a slightly lower error rate for LR than LDA, are consistent with these observations. In addition, probability may be assigned to individual data points for the statistical method LR using Equation 2.1. This can be used as an internal relative measure of classification quality that quantitatively assesses the assignment of a sample. This probability measure is a more suitable means of assessing classification certainty.

2.6.4 Summary

The accurate assignment of a mantle origin to eclogitic (–pyroxenitic) low-Cr garnets is an important consideration for many diamond exploration programs. However, the widely-used Mg# versus Ca# discrimination scheme (Schulze 2003) fails to correctly discriminate crustal garnets with pyrope contents exceeding ~ 30 mol% from low-Cr mantle garnets. Schulze (2003) is very successful in identification of all mantle garnets. However, such methods may lead explorationists to pursue crustal garnets due to their misclassification as being mantle-derived. To account for this, my new methods can be adjusted to minimize either the overall error rate or mantle error rate preferentially. Furthermore, the method is easily tuned in the light of new data becoming available. My new graphical and multivariate statistical methods for crust-mantle garnet discrimination employ variables that better reconcile effects arising from the unit-sum constraint associated with geochemical data. The new methods in this study are each more successful at lowering the error rate for both crustal and mantle garnets simultaneously than existing methods, with the logistic regression solution being the most effective quantitative crust-mantle garnet discriminator to date.

Chapter 3 Statistical approaches to the discrimination of mantle- and crust-derived low-Cr garnets using major and trace element data

3.1 Introduction

Garnet as an indicator mineral is a useful tool for exploration of diamondiferous kimberlites because it is more abundant than diamond and is relatively robust to alteration/destruction in fluvial and glacial settings (Nowicki *et al.* 2007). There is, however, the potential for misclassification of an indicator garnet as being either crust- or mantle-derived. A misclassification of garnet can lead to misdirection of exploration efforts. Therefore, correct identification of indicator mineral lithological provenance in the early stages of exploration is critical. While classification methods for Cr-rich pyrope garnets are robust (e.g., Grütter *et al.* 2004; Griffin *et al.* 2002), discrimination of low-Cr ($\text{Cr}_2\text{O}_3 < 1 \text{ wt}\%$) garnets has been more error-prone (Chapter 2). A prominent source of low-Cr garnets are eclogites which can be highly diamondiferous, and hence the discrimination of these lithologies is of significant economic importance. In Chapter 2, I proposed a revised classification scheme that is successful in the discrimination of low-Cr crustal and mantle garnets using major-element parameters, but the error rate is non-negligible ($\sim 7.5 \pm 1.9 \%$). This error rate principally relates to a significant compositional overlap of garnets derived from lower crustal mafic rocks and from mantle eclogites.

Low-Cr garnets occur in a variety of host lithologies that form in both the crust and mantle, compounding their classification problems. Crustal rocks form at pressure-temperature conditions outside the diamond-stability field and include garnet granulites, amphibolites, and other plagioclase-bearing metamorphic assemblages formed at high pressures and temperatures

in the lower crust. Garnets derived from the mantle are inherently more desirable in diamond exploration as they may derive from the diamond stability field and include garnets from eclogite, a plagioclase-free assemblage primarily comprising low-Cr garnet ($\text{Cr}_2\text{O}_3 < 1 \text{ wt}\%$) and omphacitic clinopyroxene (combined $\geq 75 \%$ modal abundance of the rock; Desmons and Smulikowski 2007). Garnet and clinopyroxene comprise $> 75 \%$ of an eclogite, with neither garnet nor clinopyroxene being $> 75 \%$. Garnet-clinopyroxene-bearing assemblages with low-Cr garnet may be defined as either pyroxenitic (diopside-augite bearing) or eclogitic *sensu stricto* (omphacite-bearing; Desmons and Smulikowski 2007). However, exploration practice only recovers single garnet grains from surficial deposits, resulting in an inability to apply the above lithological classification schemes because of the absence of co-existing pyroxene. For instance, some eclogites and pyroxenites cannot be discriminated based on garnet alone, i.e., G4 garnets, after Grütter *et al.* (2004), which may be either eclogitic or pyroxenitic. The most frequent misclassification/misidentification of eclogitic garnets is, however, with garnets from granulite-facies crustal metamorphic rocks, which may show strong compositional overlap in all major elements (e.g., Chapter 2; Schulze 2003; Krippner *et al.* 2014).

Currently, low-Cr crustal and mantle garnets are discriminated by major-elements using graphical methods, such as Schulze (2003; Ca# versus Mg#; molar Ca# = $\text{Ca}/[\text{Ca}+\text{Mg}]$, molar Mg# = $\text{Mg}/[\text{Mg} + \text{Fe}]$), and the $\ln(\text{Mg}/\text{Fe})$ versus $\ln(\text{Ti}/\text{Si})$ method described in Chapter 2. Both methods rely on Mg and Fe because metamorphic garnets forming at low pressure-temperature conditions in the upper- to mid-continental crust will incorporate Fe relative to Mg. However, many garnets from metabasites within the lower continental crust have Mg/Fe compositions that overlap the pyrope contents of mantle eclogites and pyroxenites (Chapter 2). The Schulze (2003) scheme, by design, captures mantle garnets at the expense of misclassifying a significant

proportion of lower-crustal (granulitic) garnets with $> \sim 30$ mol% pyrope that were under-represented in the original training dataset. Other garnet classification schemes, such as the method of Grütter *et al.* (2004), are not calibrated for crustal garnets.

Using multivariate statistics, in Chapter 2 I also demonstrated that the crustal-mantle discrimination error rate may be minimised with reference to the compiled calibration dataset, and this enabled the definition of a classifying equation (Equation 2.7). The most successful method is based on logistic regression, a non-parametric statistical technique, and defines a discriminant value d_{CM-LR} (Equation 2.7). The major-element variables used in Equation 2.7 are cast as log-normalised cation ratios. For simplification, this equation is referred to as Equation 3.1 in Chapter 3.

$$d_{CM-LR} = 14.954 + 0.661 \times \ln\left(\frac{Ti}{Si}\right) + 2.996 \times \ln\left(\frac{Al}{Si}\right) + 0.538 \times \ln\left(\frac{Cr}{Si}\right) - 0.040 \times \ln\left(\frac{Mn}{Si}\right) - 4.330 \times \ln\left(\frac{Fe}{Si}\right) + 1.724 \times \ln\left(\frac{Mg}{Si}\right) + 1.070 \times \ln\left(\frac{Ca}{Si}\right) + 0.985 \times \ln\left(\frac{Na}{Si}\right) \quad (3.1)$$

I investigate the viability of an additional non-parametric statistical method, the Classification and Regression Trees (CART) technique (e.g., Hastie *et al.* 2009). The CART technique is a method which casts results as an easily-interpreted decision tree of conditional statements to which new data can then be readily applied (Hastie *et al.* 2009).

The motivation for considering trace-element data in this context is to test whether any of the compositional overlap in major-elements (the error of $\sim 7.5 \pm 1.9$ %) can be reduced. Here I present a new database of trace-elements (Rare earth elements, Zr, Nb, Y, Hf, and Sr) in low-Cr garnets acquired via laser ablation inductively-coupled plasma mass spectrometry (LA-ICP-MS)

to evaluate this. I propose a combined major-trace element method for classification of low-Cr garnets, for use in diamond exploration.

3.2 Dataset and analytical method

Existing trace-element data for crustal garnets, especially in metamorphic rocks from cratons, is sparse, making comparison to the more voluminous mantle low-Cr garnet trace-element data difficult. To address this issue and to generate a more representative database from which to make trace-element statistical analysis, I have produced an extensive new trace-element geochemical data set for garnets from 166 crust- and 405 mantle-derived samples from cratons worldwide (Tables S1 and S2 in the Supplementary Online Dataset; major-elements from the same dataset in Chapter 2). The sample set consists of garnets in xenoliths from kimberlites, recovered during diamond exploration, mining, and resource evaluation. Some samples are derived from lower-crustal granulites exposed at surface. Sample origin (crustal or mantle) was determined based on xenolith petrography, with crustal samples being plagioclase-bearing (primarily garnet granulites; N = 166) and mantle samples being a mixture of eclogite and pyroxenite (N = 405). All garnets contain $\text{Cr}_2\text{O}_3 < 1 \text{ wt}\%$.

Trace-elements were analysed using sector-field LA-ICPMS (Element IIXR) and a Resonetics M-50 LR 193 nm excimer laser. NIST SRM 612 glass was used as the primary calibration standard (^{43}Ca as internal standard) and in-house reference material PHN3511 garnet was used as a secondary standard to assess repeatability and accuracy. Garnets were analysed in grain mounts with a single 130 μm spot, at a repetition rate of 10 Hz and fluence of 3.5 to 4.0 J/cm^2 . Helium was used as carrier gas, with 40 s backgrounds, 60 s ablation/measurement time, and 40 s on washout. Data were processed offline using Iolite version 3.32. Analytes included Sr, Zr, Y, Nb,

Hf, and rare earth elements. Ba formed part of the analyte list and was typically at or below the lower limit of detection (LLD). It was useful to monitor as an aid in the identification of mineral inclusions that cause problems with other elements that are routinely above detection limit, such as Sr. For my analytical runs, the mean values of all analytes in secondary standard (PHN3511) were within $\pm 2\sigma$ of the mean reference values for the Arctic Resources Laboratory (also obtained via LA-ICP-MS; Table S4 in the Supplementary Online Dataset). An assessment of the quality of PHN3511 analyses, as well as of the long-term analytical accuracy of the Arctic Resources Laboratory, is also included in Table S4 in the Supplementary Online Dataset.

These new data are complemented by carefully screened literature trace-element analyses acquired predominantly by LA-ICP-MS (N = 169; Table S5 in the Supplementary Online Dataset). These data are required to have Sr values, as well as Sm, Eu, and Gd values above detection limit to permit calculation of europium anomalies and to be sure that the data were of sufficient quality for use. In addition, all samples have SiO₂, TiO₂, Al₂O₃, Cr₂O₃, MnO, FeO, MgO, CaO, and Na₂O major-element data. I applied a blanket detection limit of 0.01 wt% to all major-element oxide data as sometimes this parameter was not reported. All Fe is reported as FeO_{Total}. Major-elements are cast as log-normalised elemental ratios to attenuate issues arising from the unit sum constraint (Aitchison 1994). All trace-element data are in ppm, reported as *bdl* if below LLD (Tables S1, S2, and S5 in Supplementary Online Dataset). Detection limits are 0.001 ppm for rare earth elements (REE), Y, and Nb, 0.005 ppm for Hf and Zr, and 0.012 ppm for Sr.

3.3 Results: Trace elements in garnet

3.3.1 Rare earth elements and europium anomalies

REE systematics (including yttrium) indicate broad similarities in the shapes of the median chondrite-normalised (N) REE patterns (\pm one quartile) for the full “crustal” and “mantle” garnet groups (e.g., the $MREE_N$ - $HREE_N$ patterns from Sm to Lu are parallel; Figure 3.1). However, the crustal garnet population has up to two times higher median $MREE_N$ and $HREE_N$ concentrations than the mantle garnet population. Additionally, the median REE_N pattern for crustal garnets is steeper in the $LREE_N$ (La to Nd) with lower median La and higher Nd compared to mantle garnets.

Eu anomalies (Eu/Eu^* , calculated arithmetically as $2 \times Eu_N/[Sm_N+Gd_N]$) in garnet broadly correlate with REE_N abundances, in particular, median $HREE_N$ decrease as Eu/Eu^* increases (Figures 3.2A and 3.2B). Although the crustal garnet population tends to have a higher preponderance of garnets with $Eu/Eu^* < 1.00$ (mean = 0.97, median = 0.86; Figure 3.3A) and the mantle population of garnets with $Eu/Eu^* \geq 1.00$ (mean = 1.19, median = 1.11; Figure 3.3A), the median $HREE_N$ for subpopulations of crustal and mantle garnets are in fact quite similar when considered with respect to Eu/Eu^* (Figures 3.2A and 3.2B).

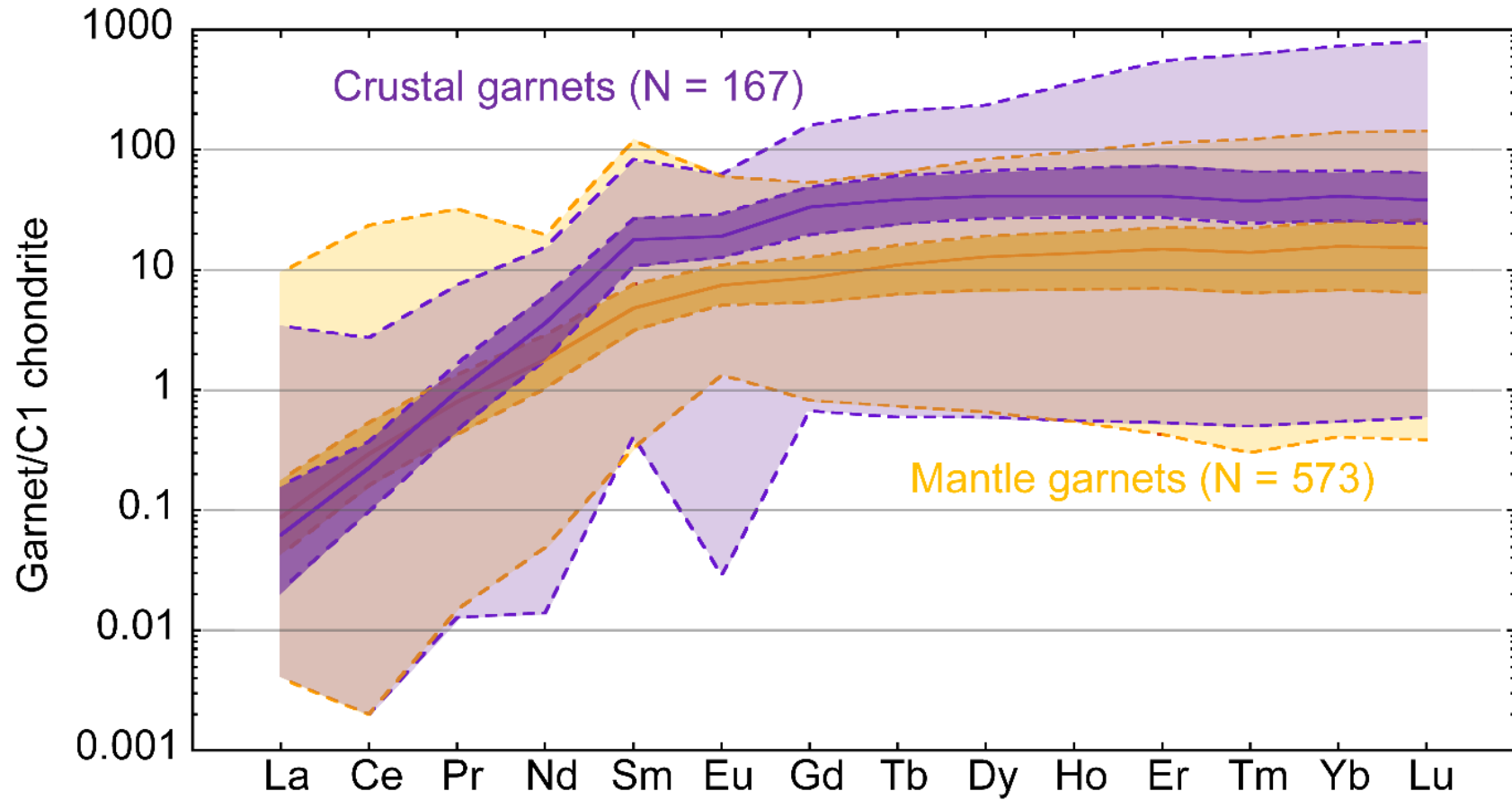


Figure 3.1 Fields showing the interquartile range for REE_N for full crustal (purple) and mantle (yellow) garnet populations compiled in this study. Median values (solid line) \pm one quartile (dashed lines) shown as dark shaded fields. Full compositional ranges are shown as pale shaded fields for both populations. REE ppm values normalised to C1 chondrite (McDonough and Sun 1995).

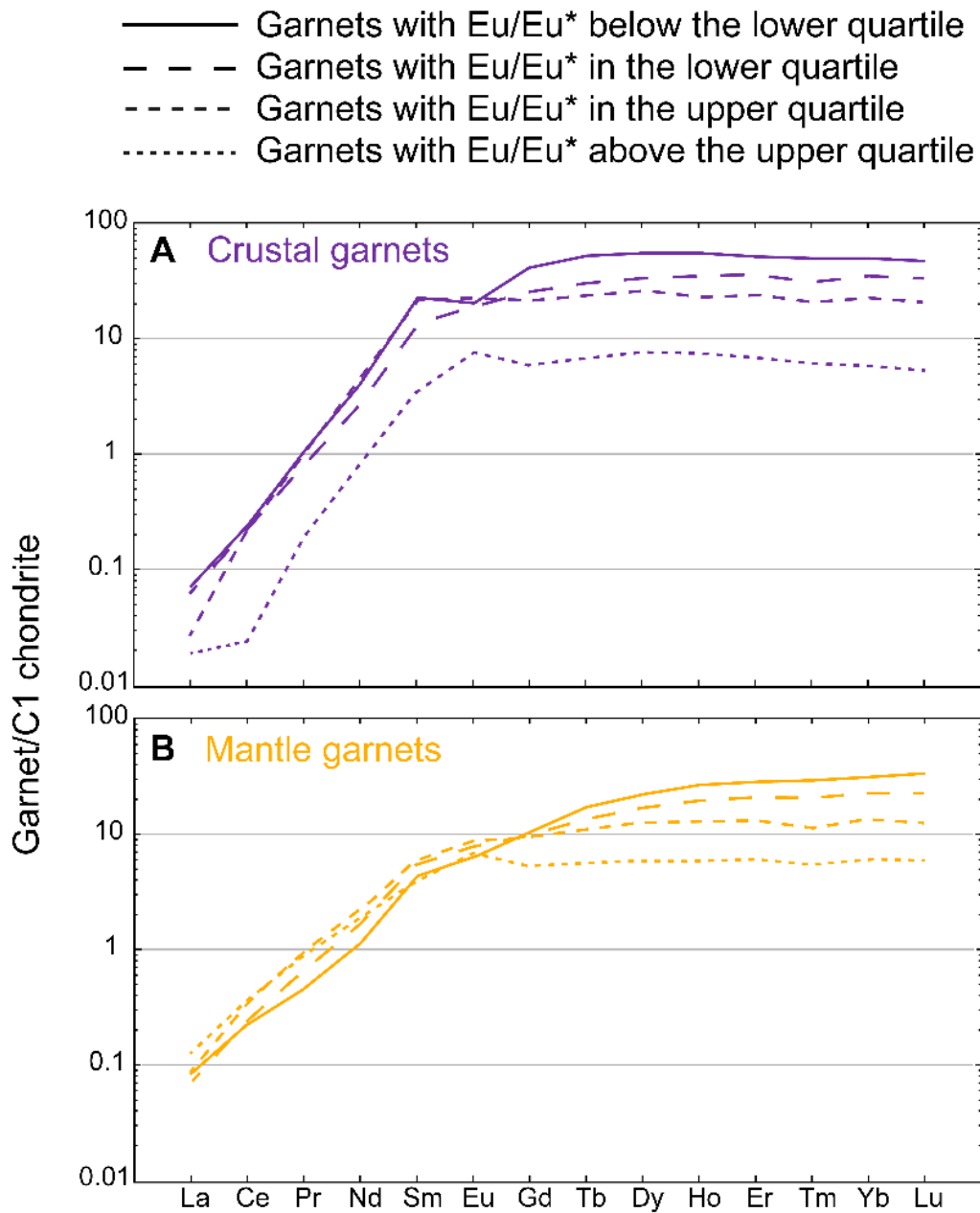


Figure 3.2 Median REE_N curves for (A) crustal garnets and (B) mantle garnets, as a function of Eu/Eu^* . Lines are median REE_N curves for each Eu/Eu^* quartile in the full dataset: less than the lower quartile, between the lower quartile and median, between the median and upper quartile, and greater than or equal to the upper quartile. REE ppm values are normalised to C1 chondrite (McDonough and Sun 1995).

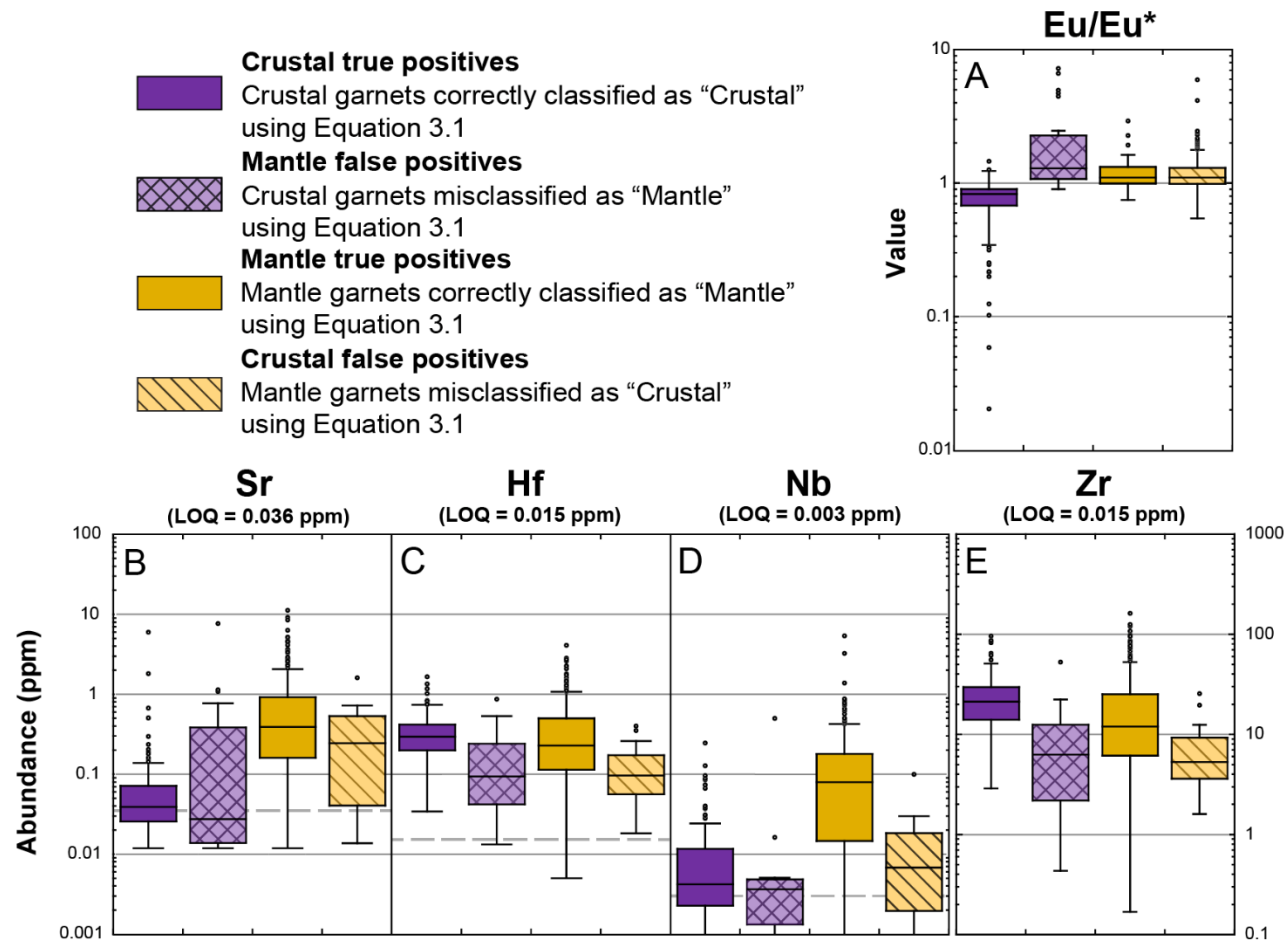


Figure 3.3 Box and whisker plots for trace-elements in garnet, subdivided into crustal true positive garnets, mantle false positive garnets, mantle true positive garnets, and crustal false positive garnets. Dashed grey lines are limits of quantitation (LOQ) for each variable, where applicable. Whiskers extend beyond the interquartile range (IQR) by 1.5 x IQR, but do not extend lower than the lower limit of detection for each variable. Variables plotted are (A) Eu/Eu*, (B) Sr, (C) Hf, (D) Nb, and (E) Zr.

Figures 3.4A, 3.4B, and 3.4C show the REE_N patterns for data classified by the logistic regression major-element method (Equation 3.1). Figure 3.4A demonstrates that the major-element classification using Equation 3.1 is reflected well by the different degree of HREE_N enrichment between crustal and mantle garnets correctly classified by Equation 3.1, hereafter “crustal true positives” and “mantle true positives,” respectively. However, the overlap in data demonstrated by crustal false positive (mantle garnets misclassified using Equation 3.1) and mantle false positive garnets (crustal garnets misclassified using Equation 3.1) suggest that REE_N will not be unequivocal discriminators (Figures 3.4B and 3.4C, respectively).

3.3.2 Strontium

During the course of this study I found that it was critical to monitor the time-resolved LA-ICP-MS signal traces closely during garnet analysis for the occurrence of spikes in Sr, often coincident with spikes in Ba. This coincidence is explained by the ablation of unidentified Sr-rich micro-inclusions within the host garnet and these parts of the spectra were screened-out prior to processing, or the analyses were discarded entirely. When Sr spikes are avoided, garnet Sr, when above detection limit, appears reasonably homogenous. I have also adopted a three times the LLD (LLD already 3σ over background) to limit analytical uncertainty for Sr data close to the limit of detection. A limit of quantitation (LOQ) of 0.036 ppm is assigned to Sr data on this basis.

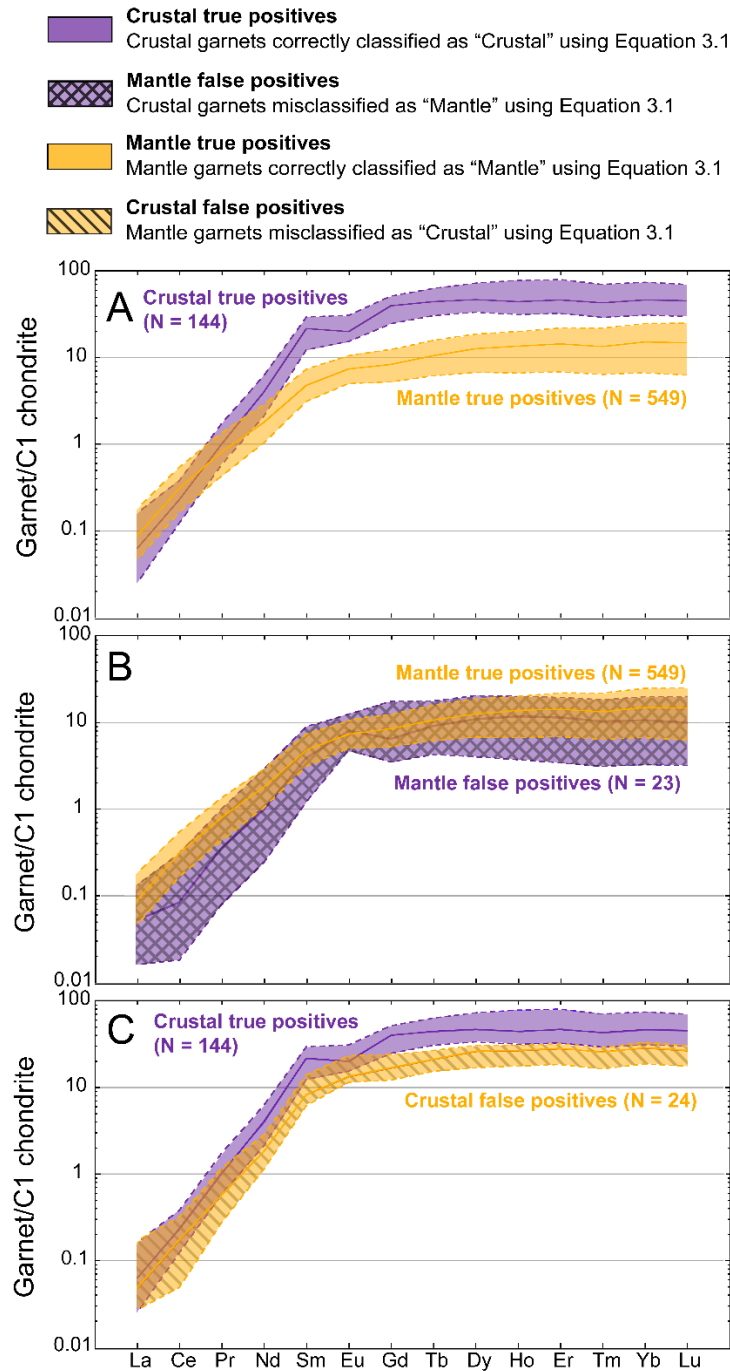


Figure 3.4 Median values and interquartile ranges for populations of garnets, REE ppm values normalised to C1 chondrite (McDonough and Sun 1995). A) Crustal and mantle garnets correctly classified using Equation 3.1 (crustal true positive and mantle true positive). B) Crustal garnets that misclassify as "mantle" (mantle false positive), and mantle garnets that correctly classify as "mantle" (mantle true positive). C) Mantle garnets that misclassify as "crustal" (crustal false positive), and crustal garnets correctly classified as "crustal" (crustal true positive).

Crustal and mantle garnets in the compiled dataset have very different population distributions with respect to Sr content (median values and distribution spreads are summarized in Figure 3.3B). Mantle true positive garnets have high median Sr (~ 0.400 ppm) while the crustal true positive garnets have a much lower median Sr concentration (~ 0.040 ppm). The mantle false positive garnet population overlaps strongly with mantle true positive garnets (within the range of mantle true positive garnets indicated in Figure 3.3B) though median values are disparate. The crustal false positive garnet population overlaps the crustal true positive garnet population but with a median above the crustal true positive upper range boundary indicated in Figure 3.3B, indicating that elevated Sr contents in crustal false positive garnets may be a potential discriminant from crustal true positive garnets. At low Sr the discrimination is equivocal. Hence, garnet Sr contents discriminate crustal-mantle garnets to some degree and are additive to major-element approaches.

3.3.3 Zirconium, Hf, and Nb

The high field strength elements Hf, Nb, and Zr are generally present at levels above the detection limit for the analytical methods in this study (Figures 3.3C, 3.3D, and 3.3E). The difference between the mantle and crustal populations are best exemplified by considering the true positive crustal and mantle data, and their compositional overlap with false positive data (Figures 3.3C, 3.3D, and 3.3E). Clear differences exist for Nb, with many mantle true positive grains having an order of magnitude higher concentration than other garnets (Figure 3.3D), including mantle false positive garnets. Based on these distribution differences, it may be anticipated that elevated Nb concentrations ($> \sim 0.016$ ppm) may be strongly indicative of mantle derivation, while Nb concentrations lower than this are equivocal, as there are still substantial mantle true positive garnets with $\text{Nb} \leq 0.016$ ppm ($N = 176$). Distributions between

crustal true positive garnets and crustal false positive garnets for Nb are very similar in median and compositional range, making it an ineffective discriminator for those compositions.

Hf and Zr concentrations are, however, more equivocal, with medians within approximately one order of magnitude, and full compositional ranges overlapping (Figures 3.3C and 3.3E). In addition, the crustal true positive garnets with highest Hf and Zr contents also have among the lowest Eu/Eu*. This means that the use of elevated Hf and/or Zr as a discriminator for crustal false positives is broadly attenuated with the consideration of Eu/Eu*. Therefore, Hf and Zr as discussed here are anticipated to be additive to a discriminant but not unambiguous.

3.4 Discussion

3.4.1 General remarks

It is clear that trace-element systematics for crustal and mantle garnets are complex, with one factor being the mineral assemblage in the garnet host rock, which can act as a strong control on garnet geochemistry (Grauch 1989). Plagioclase, for example, which partitions Eu^{2+} and Sr relative to garnet (Drake and Weill 1975; McKenzie and O'Nions 1991), is abundant in granulitic assemblages whereas eclogites are plagioclase-free yet may have formed metamorphically from plagioclase-bearing protoliths (e.g., oceanic crust; Green and Ringwood 1972). Pyroxenites form from different processes, for example in hybrid models from melts derived from sources that may have been previously associated with plagioclase (e.g., subducted eclogite; Pearson *et al.* 1993) which react with and refertilise mantle peridotite (Yaxley and Green 1998), or through mantle-only processes (e.g., Haggerty 1995). Equilibrium with certain minerals may drive elemental abundances down in garnet, for instance Sr when in equilibrium with plagioclase, whereas the formation of metamorphic garnet from a reaction involving

plagioclase will lead to inheritance of Sr into eclogitic garnet (e.g., Shu *et al.* 2016). In this context, I consider simplified mineralogical relationships to select geochemical variables that will discriminate garnets where major-elements are otherwise insensitive, i.e., samples that misclassify using major-element approaches such as those developed in Chapter 2.

3.4.2 Trace element systematics in garnet related to petrogenesis

3.4.2.1 Rare earth elements and europium anomalies

Variations in trace-element abundances are considered in the context of protoliths, process (crystal accumulation, metamorphism), and current mineral assemblage. These variations shed light on reasons why some elements are more successful discriminants of garnet class than others. For mantle eclogites formed through prograde metamorphism of oceanic crust protoliths, variations in major- and trace-element chemistry may be imparted based on variations in the oceanic protolith. High-temperature cumulates (e.g., lower oceanic gabbros) will be depleted in LREE (La to Nd) due to the accumulation of abundant cumulus minerals with low $D_{\text{LREE/melt}}$ (e.g., olivine, pyroxene, plagioclase; Perk *et al.* 2007). LREE should therefore be relatively enriched in lower temperature systems such as shallow oceanic basalts. This characteristic will be inherited by the new assemblage during prograde metamorphism, barring secondary processes (e.g., partial melt extraction). In addition, mantle samples may be subject to mantle metasomatism that may preferentially enrich LREE. In crustal rocks LREE-enriched mineral phases such as monazite (though very uncommon in mafic protoliths) will depress the LREE concentrations of any garnets in equilibrium. For the HREE (Dy to Lu), partition coefficients are extremely high in garnet (Johnson 1998) relative to other common minerals in mantle eclogite and garnet granulite (Rollinson 1993) and therefore should dominate the whole-rock HREE.

Europium anomalies occur because Eu readily substitutes for Ca^{2+} in plagioclase when it is in its lower natural oxidation state (Eu^{2+} ; Drake and Weill 1975). Consequently, garnet in equilibrium with plagioclase will have negative europium anomalies ($\text{Eu}/\text{Eu}^* < 1.00$) due to strong partitioning of Eu^{2+} into plagioclase. If plagioclase enrichment occurred during igneous fractionation, the plagioclase signature will be preserved during prograde metamorphism to eclogite in both garnet and clinopyroxene as positive Eu anomalies ($\text{Eu}/\text{Eu}^* \geq 1.00$; e.g., Jacob 2004). Some authors (e.g., Huang *et al.* 2012b) have suggested the formation of Eu anomalies in mantle eclogites during mantle metasomatism. However, this viewpoint was not substantiated by the recent in-situ study of a metasomatically zoned eclogite xenolith from Roberts Victor (Riches *et al.* 2016). Whatever the ultimate origin of Eu anomalies in mantle-derived pyroxenites, their elevated Mg# means that such mantle garnets will almost unfailingly classify correctly as “mantle” anyway using Equation 3.1.

Differences between REE_N for the crustal and mantle garnet populations are somewhat attenuated in the context of Eu/Eu^* (median curves in Figures 3.2A and 3.2B), making REE_N patterns poor discriminants. The Eu/Eu^* parameter, however, is unique for a significant fraction of crustal garnets and, as discussed above, also controlled by petrological processes (equilibrium with or formation from plagioclase). The overlap between crustal true positive garnets and crustal false positive garnets evident in major-elements can be partially resolved by Eu/Eu^* in these two populations (Figures 3.3A).

3.4.2.2 Strontium

Strontium is a highly incompatible large ion lithophile element (LILE) with a low partition coefficient in garnet ($D_{\text{grt/melt}} = 1.1 \times 10^{-3}$; McKenzie and O’Nions 1991) but a much higher

value in plagioclase ($D_{\text{plag/melt}} = 2.0$; McKenzie and O’Nions 1991). This difference in compatibility suggests that garnets in plagioclase-bearing metabasites will have low Sr concentrations due to Sr partitioning into co-existing plagioclase. Sr is also incompatible in clinopyroxene ($D_{\text{cpx/melt}} = 0.067$; McKenzie and O’Nions 1991). The almost two orders of magnitude greater D value of Sr in clinopyroxene compared to garnet means that clinopyroxene will hold the bulk of Sr in an eclogite, given its high modal abundance ($> \sim 30\%$; Jacob 2004). Ultimately, a key controlling factor determining garnet Sr abundance will be the bulk Sr content of the parent rock, since a mantle eclogite may form from protolith assemblages of variable but often high Sr content due to the plagioclase-rich nature of the protolith (e.g., Shu *et al.* 2016).

Sr concentrations are a potentially promising route to successfully discriminating some mantle false positives from mantle true positive garnets due to differences in their median values (Figure 3.3B). The considerable overlap of the populations, however, makes Sr an equivocal discriminant for those compositions. More usefully, the Sr median for crustal false positives occurs above the upper range of crustal true positive garnets indicated in Figure 3.3B indicating a strong propensity for elevated Sr contents in the crustal false positives in the compiled dataset. This indicates that some crustal false positives may be discriminated by their elevated Sr (while relatively lower Sr contents will be equivocal).

3.4.2.3 Zirconium, Hf, and Nb

The elements Zr and Hf have very low partition coefficients in many minerals found within granulites and eclogites (Johnson 1998; McKenzie and O’Nions 1991), including plagioclase, garnet, and clinopyroxene. These elements have higher partition coefficients in rutile ($D_{\text{rut/melt}} = 3.07$ and 4.98 , respectively; Foley *et al.* 2000) and zircon (Zr is a major-element, and Hf has

$D_{\text{zircon/melt}} > 4000$; Fujimaki 1986). In addition, Nb is highly compatible in rutile ($D_{\text{rut/melt}} = 136$; Foley *et al.* 2000). I predict that Hf, Zr, and Nb concentration variability in garnet will be controlled primarily by equilibration with trace phases (e.g., rutile, zircon), as well as variations in these elements within the parental lithology.

Differences in Zr, Hf, and Nb values for mantle and crustal populations described here suggest that only Nb values provide a meaningful discrimination, with elevated values $> \sim 0.016$ ppm indicating mantle true positive garnets, outside the range of compositions for mantle false positive garnets (Figure 3.3D). Close examination of mantle false positive garnets reveals that Nb is uniformly low (22 out of 23 garnets have $\text{Nb} \leq 0.016$ ppm). Of all mantle false positive garnets, 18 have $\text{Eu}/\text{Eu}^* \geq 1.06$ (median value of the full dataset). For this range of Nb (≤ 0.016 ppm) and $\text{Eu}/\text{Eu}^* (\geq 1.06)$, mantle true positive garnet median values for REE_N , Hf, Zr, Sr, and major-elements (e.g., Na_2O , TiO_2 , and Mg#) are comparable and distributions overlap with those of mantle false positive garnets, rendering them all equivocal as discriminants.

The Hf and Zr distributions indicate too much overlap to be unequivocal discriminators. Hf and Zr distributions for mantle false positive garnets fully overlap the compositional range of mantle true positive garnets (Figures 3.3C and 3.3E). Crustal false positive garnets have lower median values for Hf and Zr than do crustal true positive garnets. The crustal true positive garnets with elevated Hf and Zr have lower Eu/Eu^* than the crustal false positives (Figures 3.3C and 3.3E).

3.4.2.4 Synthesis of trace element behaviour systematics

Crustal false positive garnets are characterised by uniformly low Mg# (≤ 0.67), Na_2O (≤ 0.06 wt%), and TiO_2 (≤ 0.14 wt%) all below or approximately equal to the median values for the mantle true positive population of garnets (0.66, 0.07 wt%, and 0.20 wt%, respectively). This

suggests that a subset of mantle garnets (which have relatively low Mg#, Na₂O, and TiO₂) is more susceptible to misclassification as “crustal” using Equation 3.1. The processes affecting major-element chemistry in these garnets apparently lead to systematic variations in their trace-element concentrations as well, as discussed above. In addition to bulk compositional differences, the distribution of trace-elements will be controlled during fractional-melting – crystallisation of a protolith by minerals such as zircon (Zr, Hf), rutile (Ti, Nb), and plagioclase (Sr, Na). Increased crystal fractionation during protolith formation, or variations in mantle source of igneous protoliths, may account for relatively low abundances of Na₂O and TiO₂, leading to the misclassification of these mantle-derived low-Cr garnets as crustal.

Mantle false positive garnets have comparable median and compositional ranges to mantle true positive garnets for Hf and Zr, and a substantial proportion have higher Eu/Eu* values (Figures 3.3A, 3.3C, and 3.3E). Sr median curves for mantle true and false positive garnet populations differ by about one order of magnitude but full compositional ranges overlap and are therefore equivocal as discriminants. The most promising discriminant is Nb for which the median value of mantle false positive garnets is about one order of magnitude lower than mantle true positive garnets. However, given that mantle true positive garnets share similar median REE_N, Hf, Zr, Sr, and major-element abundances for the same range of Nb and Eu/Eu* that the mantle false positive garnets span, it is inferred that one cannot discriminate this suite of false positive garnets from legitimate mantle garnet compositions. A small subset of garnets that are in equilibrium with plagioclase and with Eu/Eu* \geq 1.00 indicate bulk rock positive Eu/Eu*, which I do not discuss further in this study.

3.4.3 New trace element classification method for crustal and mantle garnets

I apply new trace-element variables to classify garnets as “crustal” and “mantle” to supplement the major-element method of Chapter 2 (Equation 3.1). I opt for a decision-tree approach based on Classification and Regression Trees (CART; Hastie *et al.* 2009), using Sr and Eu/Eu* which can be appended to major-element approaches. I favour separate consideration of major- and trace-elements rather than a single, unified discriminator. In this way, the trace-element discrimination is additive to the major-element logistic regression method, the latter derived using a large, robust garnet dataset (Chapter 2).

I choose the logistic regression method from Chapter 2 as the baseline for the new CART trace-element method, because it is a robust statistical technique based on a substantial garnet database with the lowest error rates of a variety of other methods, including graphical methods and the linear discriminant analysis technique. I derive a new decision tree constructed via the CART method using the statistical package “R” with the variables Eu/Eu* and Sr (code provided in Table B.1). The scheme only uses Sr above an effective limit (LOQ; ≥ 0.036 ppm), giving greater confidence in the final derived discriminant values. This decision tree is derived using all garnets that classify as “crustal” via Equation 3.1 when $d_{\text{CM-LR}} < 0.000$, $d_{\text{CM-LR}} = 0.000$ being the discriminant value where crustal and mantle errors are both minimized (Section 2.5.2). This “crustal” population includes many garnets that correctly classify as crustal (crustal true positive garnets, $N = 144$), as well as a subset of mantle garnets ($N = 24$) that misclassify as crustal (crustal false positive garnets). This new method explores ways based on trace-element data to identify these crustal false positive garnets with greater certainty.

Error rates for the full dataset are given as classification error values in Table B.2. The new combined method (Figure 3.5) gives the lowest overall error rate for the discrimination of mantle versus crustal low-Cr garnets, for the full compiled dataset of $\sim 4.7\%$, a decrease from 6.4% due to the slightly better identification of mantle garnets previously identified incorrectly as crustal. This is a reduction of crustal false positives from $N = 24$ to $N = 7$, while the mantle false positives, not discriminated further using this new method, increase from $N = 23$ to $N = 28$. I assess the quality of the new decision tree portion of Figure 3.5 by k-fold cross-validation (Table B.3).

3.4.4 Outcomes

The large trace-element database assembled in this study shows that low abundances of Sr occur in garnets that formed in the presence of plagioclase (e.g., garnet granulites) due to partitioning of Sr to plagioclase. Low Sr abundances are also a feature of garnets from eclogites formed from igneous protoliths depleted in Sr. Garnets in crustal metabasic rocks also generally have $\text{Eu}/\text{Eu}^* < 1.00$ due to partitioning of Eu^{2+} to plagioclase whereas mantle eclogites derived from crustal protoliths have $\text{Eu}/\text{Eu}^* \geq 1.00$ due to common plagioclase accumulation in the protolith, especially in aluminous eclogites (e.g., Shu *et al.* 2016). I do not discern any significant effect of metasomatism in generating Eu anomalies.

Beyond these broad observations, from a garnet classification perspective, I note that the crustal true positive population has a tendency toward $\text{Eu}/\text{Eu}^* < 1.00$ and low Sr, and this is used to refine discrimination of crustal false positive garnets which have a tendency toward relatively higher Eu/Eu^* and Sr.

$$d_{\text{CM-LR}} = 14.954 + 0.661 \times \ln(\text{T}/\text{Si}) + 2.996 \times \ln(\text{Al}/\text{Si}) + 0.538 \times \ln(\text{Ca}/\text{Si}) - 0.040 \times \ln(\text{Mn}/\text{Si}) - 4.330 \times \ln(\text{Fe}/\text{Si}) + 1.724 \times \ln(\text{Mg}/\text{Si}) + 1.070 \times \ln(\text{Co}/\text{Si}) + 0.985 \times \ln(\text{Ni}/\text{Si})$$

Equation 3.1

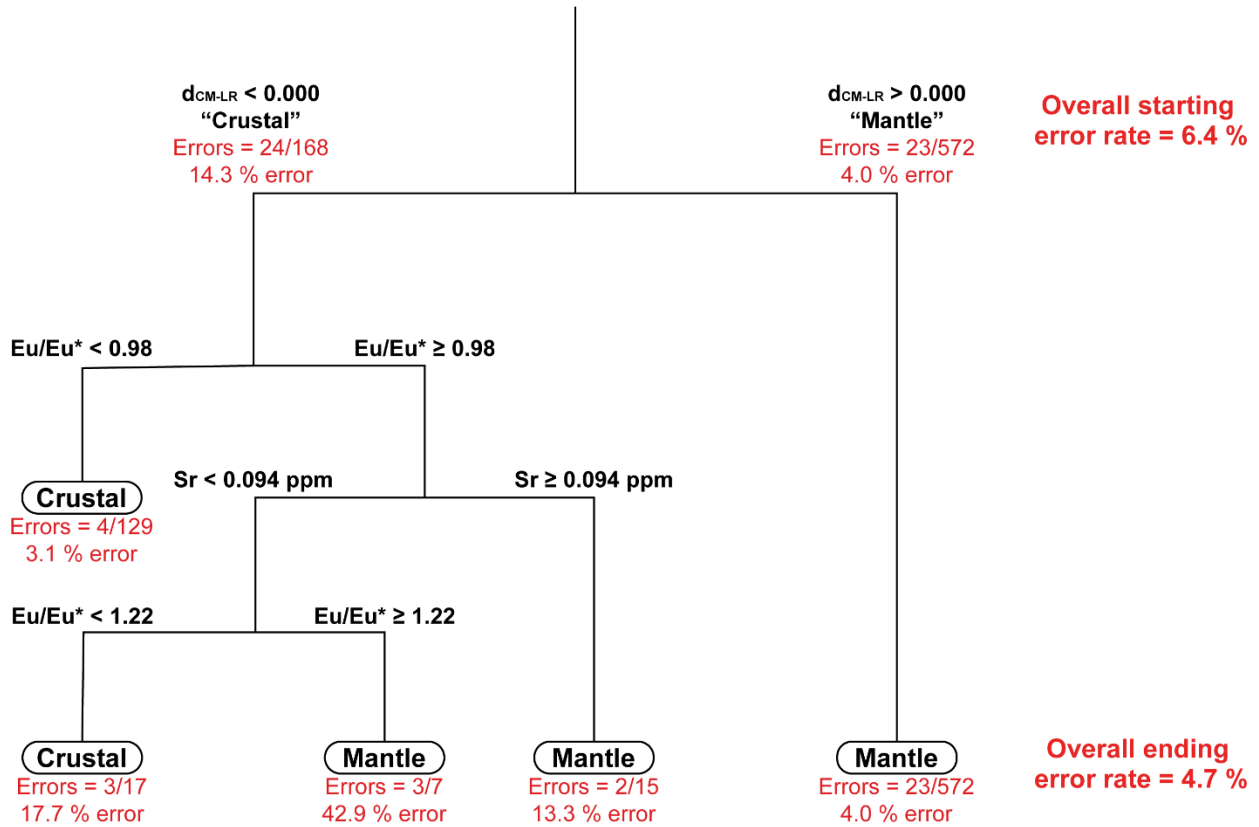


Figure 3.5 New decision tree method using Classification and Regression Trees (CART) for classification of unknown low-Cr garnets using initial major-element characteristics combined with trace-elements. Garnets are initially classified as “crustal” or “mantle” using the logistic regression method defined in Equation 3.1 (logistic regression method from Chapter 2) that is based on major-element data. Garnets with $d_{\text{CM-LR}} = 0.000$ cannot be classified as either “crustal” or “mantle.” Garnets classified as “crustal” by Equation 3.1 are further subdivided using trace-elements. Error rates using the database compiled in this study are indicated next to each node, as well as starting (using Equation 3.1 only) and ending error rates (for the combined major-trace element method).

A discrimination function based on Sr – Eu/Eu* systematics is therefore suitable for discriminating some garnet compositions. The crustal false positive garnets are derived from plagioclase-free eclogite xenoliths in kimberlites that have been assumed to have equilibrated in the mantle. The reason for their misclassification as “crustal” is due, in large part, to their lower Mg#, Na₂O, and/or TiO₂ than typical mantle mean values, likely a result of some combination of

secondary partial melting, protolith geochemical variation, or derivation from the pressure interval within the lower crust (~ 12 to 16 kbar).

Trace-elements may assist in the correct classification of these crustal false positive garnets. Crustal false positive garnets have moderate Eu/Eu* (median = 1.10) and moderate Sr (median = 0.251 ppm). Elevated Sr is expected for eclogitic garnets formed from Sr-rich oceanic crust (e.g., upper basaltic crust). In some cases, where partial melting of slabs occurred during subduction into the hotter Archean and Paleoproterozoic mantle, removal of some minor and accessory mineral phases is possible, such as coesite and rutile (e.g., Jacob 2004). One explanation for these mantle garnets classifying as crustal may be that they are basaltic eclogites which have experienced partial melting. This would result in lower incompatible budgets such as Sr, Hf, Nb, and Zr (Figures 3.3B, 3.3C, 3.3D, and 3.3E), as well as lower TiO₂ and Na₂O, relative to the rest of the mantle set. Garnet Mg# is expected to increase in response to melting, but this is not quantified. Alternatively, accessory rutile in the eclogitic assemblage will lower high field strength element concentrations (Hf, Nb, Zr, and Ti) in garnet (Jacob 2004). If eclogitic garnet contains ≥ 0.094 ppm Sr despite these processes, then the garnet will still correctly classify as “mantle” using the method in Figure 3.5. I infer that in cases of more extreme melting, and where Eu/Eu* is less than 0.98, this signature results in an incorrect “crustal” false positive in the CART scheme (Figure 3.5). Alternatively, if Sr is depleted to less than 0.094 ppm but Eu/Eu* remains above 0.98, the garnet may also misclassify as “crustal” (Figure 3.5).

I propose that the branch of the CART scheme (Figure 3.5) following the sequence of conditional statements $d_{\text{CM-LR}} < 0.000$, $\text{Eu/Eu}^* \geq 0.98$, $\text{Sr} < 0.094$ ppm, and $\text{Eu/Eu}^* < 1.22$ (“Crustal”) may include crustal garnets with non-fractionated Eu (e.g., due to low modal plagioclase), or mantle garnets from rocks which experienced strong melting.

Mantle false positive garnets, some with $\text{Eu}/\text{Eu}^* \geq 1.00$, are troublesome to discriminate from mantle true positive garnets using REE and Eu/Eu^* . These garnets, extracted from plagioclase-bearing xenoliths, indicate a bulk rock positive Eu/Eu^* that is certainly inherited by the garnet.

One advantage of the new trace-element-based CART scheme is that in the event that a mantle-derived eclogitic garnet (e.g., derived from a “gabbroic” lower oceanic crustal protolith) is misclassified as “crustal” using Equation 3.1, for instance as a result of a relatively low $\text{Mg}\#$, it is likely to have elevated Eu/Eu^* and then will be correctly classified as mantle based on the CART scheme.

3.5 Conclusions and implications for garnet-based exploration

Major-element-based discrimination approaches such as described in Chapter 2 discriminate many low-Cr garnets to a high level of accuracy without the need to analyse trace-elements. The proportion of low-Cr garnets that are incorrectly classified by major-element criteria can be further discriminated, yielding an overall error rate of $\sim 4.7\%$ for the combined major-trace element method. Using the combined major- and trace-element approach, the low proportion of mantle-derived eclogites with relatively high $\text{Mg}\#$, inherited from gabbroic protoliths, that misclassify as crustal on a major-element basis will be identified correctly when processed through the trace-element based CART scheme because of their elevated Eu/Eu^* and Sr.

Mantle-derived eclogitic garnets derived from more basaltic protoliths (low $\text{Mg}\#$, elevated Na_2O , elevated TiO_2) are typically classified correctly as “mantle” using the logistic regression method (Equation 3.1) due to their elevated Na_2O and TiO_2 . In a small subset of this garnet group, Na_2O and TiO_2 abundances can be lowered to the extent that they begin to classify as “crustal.” In extreme cases, I infer that Eu/Eu^* and Sr may be reduced as well, perhaps due to the increased

plagioclase fractionation from their magmatic protoliths, and some of these garnets will misclassify as “crustal” using the proposed CART scheme. If such garnets misclassify (crustal false positives), I infer that they will misclassify either at the first branch in the CART scheme ($d_{\text{CM-LR}} < 0.000$ and $\text{Eu}/\text{Eu}^* < 0.98$), or at the terminal node following the sequence of conditional statements $d_{\text{CM-LR}} < 0.000$, $\text{Eu}/\text{Eu}^* \geq 0.98$, $\text{Sr} < 0.094$ ppm, and $\text{Eu}/\text{Eu}^* < 1.22$. For this reason, I suggest that garnets classifying in the latter “crustal” bin should be regarded as of particularly uncertain origin. Conversely, for the mantle false positive garnets, the trace-element data do not help in reclassifying these grains. I point out that these classification error rates are indicative only, as precise measurements of method quality would require larger calibration and validation datasets.

Finally, I note that the new trace-element CART discrimination, added to the initial major-element discrimination method, will improve as more trace-element data is acquired on garnets with known origin. In particular, the compiled dataset is lacking in crustal garnet analyses not derived from granulites (e.g., from garnet amphibolites). Regardless, I conclude that a combination of major- and trace-elemental statistical techniques (Figure 3.5) is the recommended approach for the most robust crustal-mantle discrimination of low-Cr garnets, if the diamond explorer wishes to ensure the best chance of discriminating those garnets that are most difficult to accurately classify using major-elements alone.

Chapter 4 Tracing the crustal and mantle sources of Roberts Victor

eclogites

4.1 Introduction

Eclogite is a plagioclase-free metamorphic rock of basaltic composition, formed at high pressures and temperatures in the deep crust or mantle (Desmons and Smulikowski 2007). Crustal eclogites occur in a variety of continental settings primarily where there is evidence for ultrahigh pressure (UHP) metamorphism, associated with continental collision, orogenesis, or shallow subduction (e.g., Zheng *et al.* 1996; Dongre *et al.* 2015). The origin of mantle eclogites erupted as xenoliths by kimberlites is less clear and has been the focus of an enduring controversy. The two prevalent hypotheses are that they represent either products of crystallisation deep in the mantle from primary mantle-derived melts (e.g., O'Hara and Yoder 1967; Hatton 1978; Smyth *et al.* 1989; Caporuscio and Smyth 1990), or originate from deeply-subducted and metamorphosed oceanic crust (Green and Ringwood 1972; Helmstaedt and Doig 1975; Helmstaedt and Schulze 1989). The broadly basaltic bulk major-element and trace-element compositions of many kimberlite-hosted eclogites is broadly similar to that of mid ocean ridge basalt (MORB), melts formed by extensive adiabatic decompression melting to relatively low pressures (McDonough 1991; Jacob 2004). There is a strong case against a model of eclogite crystallisation in the mantle given that the clinopyroxenes crystallising from melts at high pressures have low jadeite component inconsistent with omphacite in eclogites (Pearson and Nixon 1996, and references therein).

Oxygen isotopes have been decisive in constraining the origin of eclogite xenoliths in kimberlites. Almost all eclogite suites have oxygen isotope compositions ($\delta^{18}\text{O}$) outside the

range for mantle peridotite ($\delta^{18}\text{O} = 5.5 \pm 0.4 \text{ ‰}$; Matthey *et al.* 1994) and beyond the range that is predicted for mantle-derived eclogite in equilibrium with peridotitic mantle ($\delta^{18}\text{O} = 5.4$ to 5.7 ‰ ; Gregory and Taylor 1981; Jacob 2004; Ickert *et al.* 2013). Instead, cratonic eclogites broadly match the $\delta^{18}\text{O}$ distribution reported for ophiolite crustal sequences (Jacob 2004; Ickert *et al.* 2013; Korolev *et al.* 2018). Oxygen isotope compositions outside the canonical mantle range in some mantle rocks, such as eclogites, are difficult to explain through mantle processes: high mantle temperatures permit only relatively minor fractionation of oxygen isotopes (Clayton *et al.* 1975; Eiler 2001) and fluids with initial $\delta^{18}\text{O}$ values outside of the canonical mantle range are easily buffered by the comparatively unlimited peridotitic mantle reservoir (Riches *et al.* 2016; Czas *et al.* 2018). Conversely, in low-temperature crustal settings, oxygen isotope compositions record temperature-dependent fractionations during open-system fluid alteration (Muehlenbachs and Clayton 1972a, 1972b; Gregory and Taylor 1981). “Low” temperature ($< 350 \text{ }^\circ\text{C}$) alteration of upper oceanic strata by fluids enriches oxygen isotope compositions relative to mantle values, while hydrothermal alteration at relatively higher temperatures (equivalent to $\sim 2 \text{ km}$ depth) lowers the $\delta^{18}\text{O}$ of rocks to below mantle values based on temperature and fluid/rock ratios (Gregory and Taylor 1981).

Eclogites from the former Roberts Victor diamond mine on the Kaapvaal craton, South Africa, have played a central role in the cratonic eclogite controversy, perhaps because this location has provided some of the most abundant, large, and spectacular samples ever found on Archean cratons. The history of the subcontinental lithospheric mantle (SCLM) underlying Roberts Victor is marked by numerous events including oceanic subduction, imbrication, and thermal perturbation (Shirey *et al.* 2004; Schmitz *et al.* 2004). To explain the presence of eclogites in the kimberlite xenolith assemblage, Helmstaedt and Schulze (1989) proposed the imbrication of

metamorphosed oceanic crust beneath the Kaapvaal Craton. Roberts Victor eclogite xenoliths were initially classified by texture into two groups, and it has been estimated that only 6 to 8 % of Roberts Victor eclogites in published literature classify as Group II texturally (Gréau *et al.* 2011). Group I eclogites are coarse-grained, have sub-rounded/irregular garnets within an interstitial matrix of omphacitic clinopyroxene; Group II eclogites are characterised by subhedral/subangular garnets and clinopyroxenes, straight grain boundaries, common inter-grain 120° triple junctions, and rutile inclusions in silicate minerals (MacGregor and Carter 1970). This textural classification was subsequently reinforced by oxygen isotope characteristics: Group I eclogites have higher average $\delta^{18}\text{O}$ than Group II eclogites (MacGregor and Manton 1986), and minor element characteristics: Group I eclogites have higher average $\text{Na}_2\text{O}_{\text{grt}}$ and $\text{K}_2\text{O}_{\text{cpx}}$ contents (McCandless and Gurney 1989). Group I eclogites may also host a variety of accessory minerals including kyanite, rutile, and diamond, whereas Group II eclogites are diamond-free and typically lack other accessory minerals. Improved and varied analytical methodologies have expanded the distinguishing criteria to include, among others, radiogenic isotope and trace-element compositions (Table C.1; see summaries in Gréau *et al.* 2011 and Huang *et al.* 2016).

Several models have been proposed to explain the formation of cratonic eclogite xenoliths hosted by kimberlite in general, as well as the differences between Group I and II eclogites at Roberts Victor in particular. Based on elemental chemistry and oxygen isotope systematics, it was proposed that low $\delta^{18}\text{O}$ values in some eclogites could result from fractional crystallisation and accumulation of basaltic melts at high pressure (Garlick *et al.* 1971). Jerde *et al.* (1993) proposed an exsolution origin for a suite of Roberts Victor eclogites from a monomineralic aluminium-rich pyroxene. Jagoutz *et al.* (1984) suggested that Group II eclogites represent recrystallised oceanic Fe-Ti gabbros. Recently, eclogites were subdivided into five distinct subclasses based on texture

and chemistry (Types IA, IB, IK, IIA, and IIB; Huang *et al.* 2012a). Type IK are kyanite-bearing eclogites with Group I textures. Type IA and IB eclogites are biminerally eclogites with Group I textures, Type IA eclogites containing garnet with FeO > 17 wt% and Type IB eclogites containing garnets with FeO ≤ 17 wt%. Eclogites with Group II textures are classified as Type IIA if they contain garnet with MgO > 12 % and Type IIB if they contain garnet with MgO ≤ 12 %. Gréau *et al.* (2011) and Huang *et al.* (2012a) proposed that the alteration of Group II eclogites by kimberlite-carbonatite metasomatism created the Group I eclogites. Riches *et al.* (2016) provided quantitative modeling showing that the diverse oxygen isotope compositions of cratonic eclogites outside of the canonical mantle range cannot originate via mantle processes. Most recently, Radu *et al.* (2019) ascribed the origin of the five subclasses IA, IB, IK, IIA, and IIB to assemblage variations within protolithic oceanic crust, followed by subduction. This multiplicity of interpretations highlights the complexity of Roberts Victor eclogites. In this study, I consolidate available data and present a new model for the formation of Group II eclogites at Roberts Victor.

4.2 Geologic setting

The Roberts Victor pipe is a Group II kimberlite (carbonate-rich lamproite in the terminology of Pearson *et al.* 2019) that erupted through the Kaapvaal cratonic lithosphere approximately 128 ± 15 Ma (Smith *et al.* 1985). The pipe is located directly on the Colesberg Lineament, which marks the collision of the Kimberley and Witwatersrand blocks (Figure 4.1) terminating ~ 2.88 to 2.94 Ga following oceanic subduction (Schmitz *et al.* 2004; Shirey *et al.* 2004, and references therein). Subsequent modification of the Kaapvaal Craton was associated with processes occurring in the SCLM (e.g., magmatism, metasomatism) and continued oceanic subduction at the craton edges (Shirey *et al.* 2004; Schmitz *et al.* 2004). The Kaapvaal craton is bounded to the

south by the Namaqua-Natal orogenic belt (~ 0.9 to 1.3 Ga) and the Limpopo belt to the north (Schmitz *et al.* 2004; Begg *et al.* 2009; Huang *et al.* 2012a; Brey and Shu 2018).

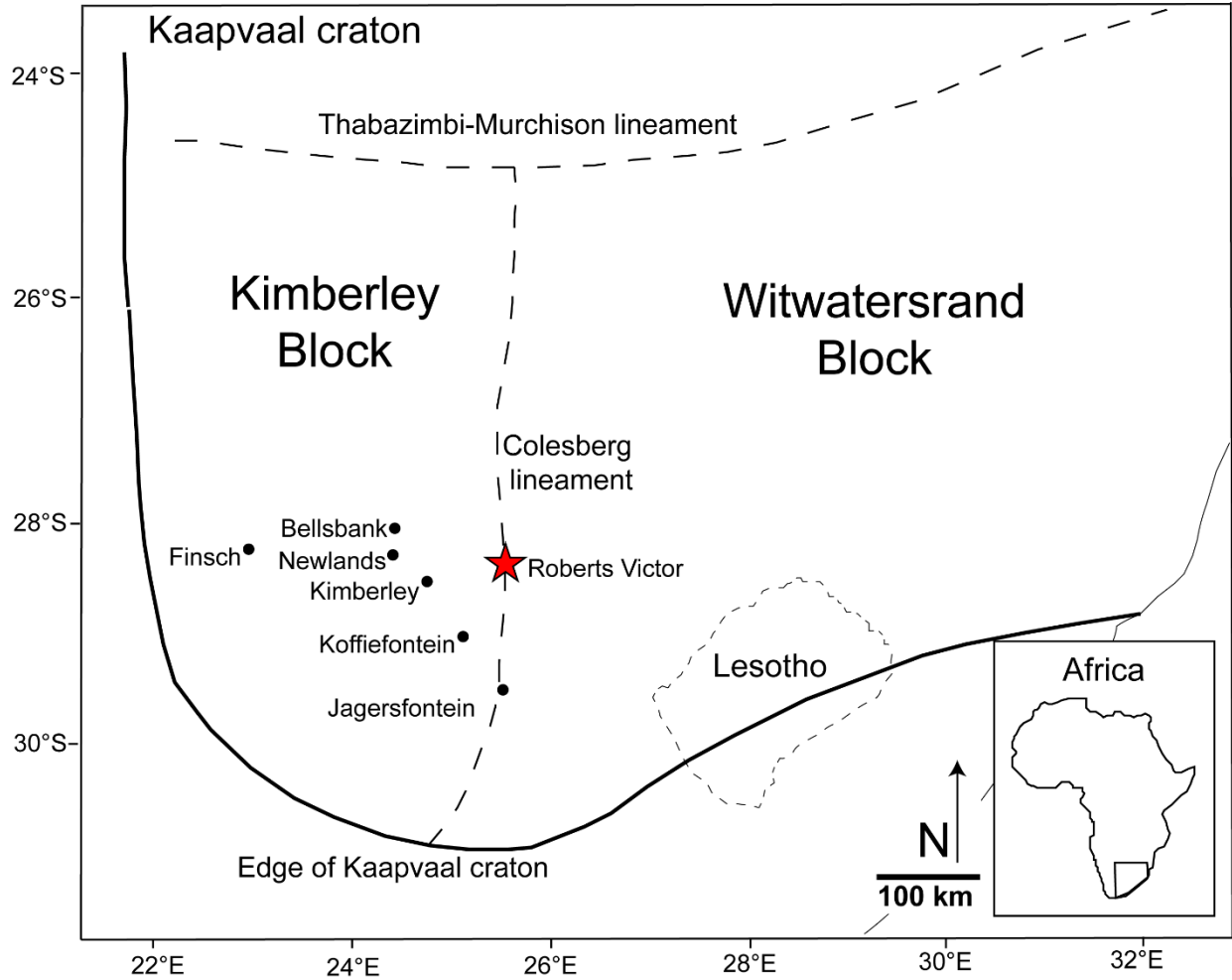


Figure 4.1 Geological map of the Kaapvaal craton, simplified after Schmitz *et al.* (2004). The locations of Roberts Victor and several other mined kimberlites are indicated.

Eclogite dominates the xenolith suite at Roberts Victor, while peridotitic and other ultramafic xenoliths are comparatively rare and highly-altered (e.g., Hatton 1978; Viljoen *et al.* 1994). The overwhelming abundance of eclogite at Roberts Victor (> 90 %; Gréau *et al.* 2011) runs counter to estimates of eclogite abundance in the subcratonic mantle (< 5 % to < 1 %; Dawson and Stephens 1975; Schulze 1989). Helmstaedt and Schulze (1989) proposed imbrication of oceanic

packages which metamorphose to eclogite in the Kaapvaal lithosphere. Griffin and O'Reilly (2007) proposed – on the basis of a kinked geotherm – that all eclogites at Roberts Victor formed in a 10 to 20 km thick layer directly below the lithosphere-asthenosphere boundary (LAB; e.g., depths of ~ 190 km), though this has been shown to be unlikely (Shu *et al.* 2016). Gréau *et al.* (2011) and Huang *et al.* (2012a) reiterated the model of Roberts Victor eclogites having crystallised at the LAB during ponding and cooling of mantle-derived magmas to ambient temperature on the basis of a kinked geotherm model. Contrary to the model of Gréau *et al.* (2011) and Huang *et al.* (2012a), eclogite equilibration temperatures calculated by Fe-Mg thermometry extrapolated to appropriate non-kinked, thermally-realistic model-geotherms (e.g., Rudnick and Nyblade 1999; Hasterok and Chapman 2011) indicate that eclogite occurs through almost the entire SCLM beneath Roberts Victor (e.g., Shu *et al.* 2016, Radu *et al.* 2019). The original Helmstaedt and Schulze (1989) model of Kaapvaal lithosphere development – by way of oceanic slab subduction – posits that eclogite should occur throughout the lithospheric mantle.

4.3 Sample set and Petrography

I analysed 65 new eclogite xenoliths from the former Roberts Victor mine, South Africa, ranging up to 3 cm in maximum dimension. All samples were studied petrographically by binocular microscope. I mounted single garnet and clinopyroxene grains from all 65 xenoliths and prepared nine of the samples as thin sections which were studied via transmitted light microscopy. I classify all new eclogites in this study as Group I or II based on hand sample and thin section texture, after MacGregor and Carter (1970). The characteristic textural features of Group I eclogites include garnets with irregular anhedral shapes within a matrix of interstitial clinopyroxene, while Group II eclogites are characterised by straight garnet-clinopyroxene grain boundaries, inter-mineral triple junctions, and rutile inclusions in silicate minerals (MacGregor

and Carter 1970). Based on the MacGregor and Carter (1970) classification, 54 new samples in this study are classified texturally as Group I, 10 are classified as Group II, and one sample is too small to make a confident determination.

Of the new samples in this study, 53 are biminerally assemblages of garnet and clinopyroxene. Additional samples contain trace accessory rutile (N = 4), kyanite (N = 3), quartz/coesite (N = 4), and sanidine (n = 2; Table C.2). All Group II eclogites in this study are biminerally except for RV-27, which contains trace quartz/coesite. Mica occurs as an accessory phase in 14 samples – all of which are classified texturally as Group I – but a primary or secondary origin for the mica cannot be determined. Garnet and clinopyroxene modes each typically range between 35 to 65 % for all samples. Some samples do not strictly adhere to the mineralogical definition for eclogite (e.g., they have > 75 % garnet or > 75 % clinopyroxene; Desmons and Smulikowski 2007), but these samples may be small portions of larger mineralogically heterogeneous samples. Eclogite *sensu stricto* contains omphacite, which is clinopyroxene that has a composition between 20 and 80 mol% jadeite ($\text{NaAlSi}_2\text{O}_6$; Clark and Papike 1968; Desmons and Smulikowski 2007). Therefore, I consider the samples that contain clinopyroxene with omphacitic compositions as eclogitic, even if they have > 75 % garnet or > 75 % clinopyroxene. Whole-rock eclogite compositions reconstructed using mineral chemistry will vary based on the chosen mineral modes, which may be variable if the studied xenoliths are derived from larger samples with non-uniform mineral distribution. However, reconstructed trace-element budgets – particularly chemical trends – are relatively insensitive to variations in mineral modes (Aulbach *et al.* 2007). Further, while reconstructed major-element compositions are more dependent than trace-elements on chosen mineral modes, Aulbach *et al.* (2020) demonstrated that changes in mineral

mode (~ 10 %) will generally preserve chemical trends involving reconstructed major-element data.

I chose to focus on Group II eclogites because they are texturally and geochemically distinct from the far more abundant Group I type. Hand sample textures for all eclogites in this study are summarised in Table C.2, thin section textures for nine eclogites with Group II textures are summarised in Table C.3, and representative textures under backscattered electron (BSE) imaging are indicated in Figure 4.2. The nine eclogites in thin section have textures that include straight grain boundaries with 120° intersections (triple junctions; Figure 4.2A; MacGregor and Carter 1970). Small ($\leq 150 \mu\text{m}$) secondary minerals are common along grain boundaries, and include rutile, amphibole, plagioclase, analcime, Fe-sulphides, and sulphates (e.g., celestine). Garnets are typically large (up to 1 cm) with straight, polygonal grain boundaries and constitute $> 99 \text{ vol\%}$ of all garnet in thin section (Figures 4.2A, 4.2B). Rarely garnet occurs within clinopyroxene as small ($< 500 \mu\text{m}$) sub-rounded, irregular, or elongate inclusions ($< 1 \text{ vol\%}$; Figure 4.2C), and in sample RV-62 as needles $< 5 \mu\text{m}$ wide and $\leq 80 \mu\text{m}$ long, within clinopyroxene (Figure 4.2D). Irregularly-shaped, intergranular garnet occurs in sample RV-20 with visible zonation in BSE images, adjacent to large texturally-equilibrated garnets that are fractured (Figure 4.2E). Clinopyroxene occurs occasionally as large interstitial “poikilitic” grains but clinopyroxene grains in thin section dominantly have similar habit and size to the large texturally-equilibrated garnets (Figure 4.2A), though typically are much more altered: in almost all cases, “pristine” clinopyroxene is altered to a “spongy/turbid” texture that often follows fractures and grain boundaries (e.g., Figures 4.2A,, 4.2B, 4.2C, and 4.2D). Exsolution lamellae of orthopyroxene in clinopyroxene are very rare, with one grain each containing exsolutions in samples RV-27 and RV-62.

Rutile does not occur as a discrete accessory phase in the Group II eclogite thin sections, but does occur in two other forms. It primarily occurs as small needles ($< 100 \mu\text{m}$ in length), small blocky inclusions, or elongated “rods” up to 1 mm in length within garnet and clinopyroxene (Figures 4.2B, 4.2C, and 4.2D). These rutile inclusions typically show parallel orientation relative to one another within a single host mineral (Figures 4.2C and 4.2D). In sample RV-62, parallel garnet needles are at an angle relative to rutile needles in the same host clinopyroxene (Figure 4.2D).

These rutile grains lack rims or exsolution lamellae and rarely are seen to be touching garnet inclusions within clinopyroxene (Figure 4.2C), but do not occur within garnets that are themselves included within clinopyroxene. Rutile also occurs as rounded to sub-rounded inclusions ($\leq 150 \mu\text{m}$ diameter) that are restricted to grain boundaries of garnet and clinopyroxene in intergranular space (Figures 4.2B, 4.2F), occasionally with a flat edge against garnet or clinopyroxene grains (Figure 4.2F). These rutile grains commonly have thin ilmenite rims ($< 20 \mu\text{m}$ thick) and occasional ilmenite exsolution lamellae, and is commonly intergrown with amphibole and spinel (Figures 4.2B, 4.2F).

To supplement the new samples in this study I have compiled data from the literature. The literature data include elemental and isotopic data for garnet and clinopyroxene from Group I and II eclogites, as well as textural information, where available. I restrict eclogites from the literature to those containing omphacitic clinopyroxene. References for the literature data are summarised in Table C.4, and the data from the literature are included in Table S6 in the Supplementary Online Dataset. Comparison of new data in this study with data from the literature is discussed in Section 4.5.

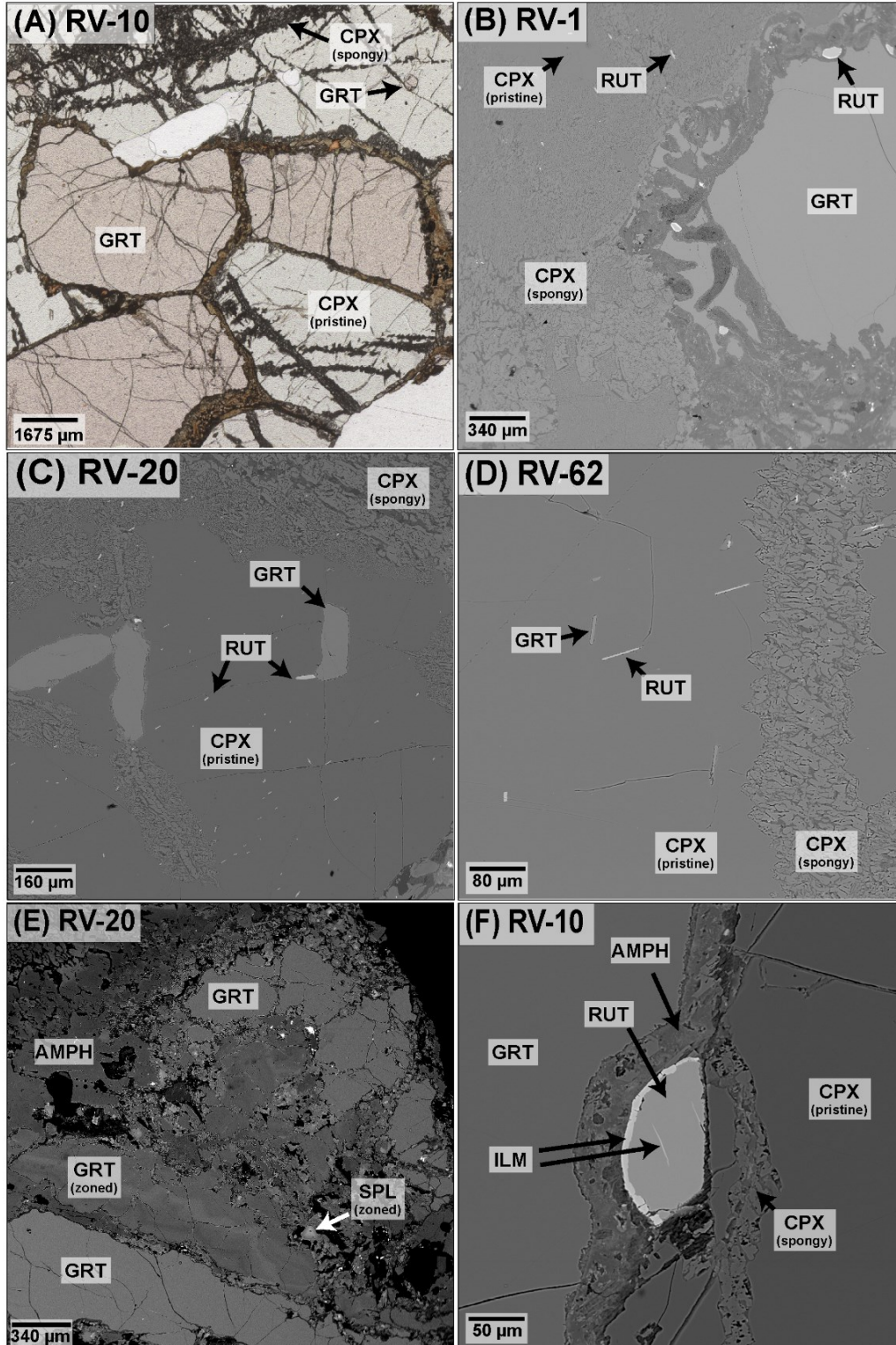


Figure 4.2 Plane polarised transmitted light (A) and backscattered electron images (B through F) of thin sections of select Group II eclogites from this study. Abbreviations: AMPH = amphibole, CPX = clinopyroxene, GRT = garnet, ILM = ilmenite, RUT = rutile, SPL = spinel.

4.4 Analytical Methods

4.4.1 Major-elements

Individual garnet and clinopyroxene grains were analysed for major-element compositions using a JEOL 8900R Electron Probe Microanalyser at the University of Alberta. Grains were analysed in grain mounts, as well as thin section for a subset of nine samples with Group II textures. Samples were analysed with a 2 μm focussed beam with 20 kV accelerating voltage and 20 nA current. Peak count times were 30 s for Mg, Ca, Ti, Cr, Mn, and Fe, 40 s for Al and Si, and 60 s for Na, with equal time spent analysing total background. Lower limits of detection (LLD) as oxide wt% are 0.05 wt% for Nb_2O_5 and between 0.01 and 0.03 wt% for all other elements. To lower the LLD for Na, P, and Ti, I performed replicate analyses at operating conditions of 20 kV and 50 nA with a 10 μm beam diameter and count times of 120, 80, and 60 s, respectively. This reduced the LLD on Na_2O , P_2O_5 , and TiO_2 to 0.007, 0.011, and 0.010 wt%, respectively (Table A.2).

4.4.2 Trace-elements

Trace-element analyses were conducted on the same mounted garnet and clinopyroxene grains as were analysed for major-elements, as well as several grains in thin section, using a sector-field laser ablation inductively-coupled plasma mass spectrometer (LA-ICP-MS; Element IIXR) coupled with a Resonetics RESolution M-50 LR 193 nm excimer laser system. Grains were analysed using a 130 μm diameter spot in low mass resolution mode, with a repetition rate of 10 Hz and fluence of between 3.5 to 4.0 J/cm^2 . Analyses were conducted with 40 s spent on background, 60 s on ablation, and 40 s on post-ablation washout, with helium as the carrier gas. Standard reference material NIST612 glass was used as primary calibration standard with ^{43}Ca as

internal standard. ThO/Th was monitored ($< \sim 0.5\%$) to minimise interference from oxide production during analysis. Data were reduced offline using Iolite version 3.32. The REE, Sr, Zr, Y, Nb, Ba, and Hf, were analysed in all garnets and clinopyroxenes. Garnet PHN3511 was used as a secondary standard to assess long-term repeatability and accuracy for these analyses. An assessment is provided in Table S4 in the Supplementary Online Dataset.

4.4.3 Oxygen isotopes

Oxygen isotope ratios ($^{18}\text{O}/^{16}\text{O}$) were determined for garnets from 34 new eclogite xenoliths in this study, via secondary ion mass spectrometry (SIMS) at the Canadian Centre for Isotopic Microanalysis (CCIM), University of Alberta. Two new garnets from each xenolith were mounted. The mount was coated with high purity Au and imaged by scanning electron microscopy using a Zeiss EVO MA15 (operating conditions of 20 kV, 3 to 4 nA). The oxygen isotope ratio ($^{18}\text{O}/^{16}\text{O}$) in each garnet grain was analysed using a Cameca IMS 1280 multi-collector ion microprobe. Garnet analytical methods and reference materials – S0068 (Gore Mountain Ca-Mg-Fe garnet) and S0088B (grossular garnet) – are detailed by Ickert and Stern (2013). A $^{133}\text{Cs}^+$ primary beam $\sim 12\ \mu\text{m}$ in diameter was operated with impact energy of 20 keV and beam current of $\sim 2.0 - 2.5\ \text{nA}$.

All $^{18}\text{O}/^{16}\text{O}$ ratios are reported in per mil (‰) and expressed in delta notation relative to Vienna Standard Mean Ocean Water (VSMOW; Baertschi 1976; Equation 4.1). Instrumental mass fractionation (IMF) was monitored by repeated analysis of S0068 and S0088B with $\delta^{18}\text{O} = +5.72$ and $+4.13\ \text{‰}$, respectively. Standard deviations are 0.06 to 0.10 ‰ (1σ) after correction for systematic within-session drift ($\leq 0.3\ \text{‰}$). Data for S0088B and unknowns were first IMF-corrected to S0068 garnet, and then further corrected according to their Ca# ($\text{Ca}/[\text{Ca}+\text{Mg}+\text{Fe}]$)

determined by EPMA, using the methods outlined by Ickert and Stern (2013). The 95 % confidence uncertainty estimates for $\delta^{18}\text{O}$ for garnet unknowns average ± 0.30 ‰, and include errors relating to within-spot counting statistics, between-spot (geometric) effects, correction for instrumental mass fractionation, and matrix effects relating to Ca# determined by EPMA.

Garnet and clinopyroxene from a subset of eight samples that span the entire $\delta^{18}\text{O}$ range of Roberts Victor eclogites in this study were selected for analysis of their triple oxygen isotope compositions ($^{17}\text{O}/^{16}\text{O}$, $^{18}\text{O}/^{16}\text{O}$). Ultra-pure mineral separates were picked by binocular microscope and ultrasonically washed successively in 10 MQ water, 6N HCL, and 10 MQ water. Oxygen triple-isotope compositions were determined via laser fluorination (LF) at the Center for Stable Isotopes at the University of New Mexico after the standard LF technique of Sharp (1990). Approximately 1 to 2 mg of dissolved mineral separate were loaded into a 44-well nickel sample plate along with homogeneous San Carlos olivine grains as a mineral standard. Prior to analysis, samples were loaded into the fluorination chamber under high vacuum for 24 to 48 h and heated by a halogen lamp to drive off surficial water from sample preparation. Samples were pre-fluorinated by 120 mbar of BrF_5 gas for 1 h to remove surface contaminants and remaining water.

Extraction of the O_2 gas from the samples was performed by introducing 100 mbar of BrF_5 to the sample chamber and completely reacting the sample using a 50 W CO_2 laser. Any gaseous by-products of fluorination and excess BrF_5 were removed through several steps of cryogenic distillation and a heated NaCl trap. The purified O_2 was passed through a gas chromatograph column using a high purity He stream before being collected in a molecular sieve trap immersed in liquid nitrogen. After excess He was pumped away, the purified sample O_2 gas was expanded into a Thermo Fisher MAT 254 Isotope Ratio Mass Spectrometer specifically configured to run

O₂ gas. Each sample run consisted of 40 iterations, each of which included a 26 s collection time for both the reference and sample gases. All ¹⁷O/¹⁶O ratios are reported in per mil (‰) and relative to VSMOW (Equation 4.2). The δ¹⁷O and δ¹⁸O values are recast as δ'¹⁸O and δ'¹⁷O using Equations 4.3 and 4.4 (Miller 2002) and as Δ¹⁷O using Equation 4.5, where 0.528 corresponds to the reference slope, and the y-intercept in this study is set to 0 ‰ (Sharp *et al.* 2016). Inter-mineral isotopic variations for δ'¹⁷O and δ'¹⁸O determined for garnet and clinopyroxene are reported using θ_{Grt-Cpx} calculated via Equation 4.6 (Sharp *et al.* 2016). Repeat laser fluorination (LF) δ¹⁸O analyses of garnets from eight eclogites in this study are within ± 0.35 ‰ of SIMS analyses of the same samples (Table C.5).

$$\delta^{18}O = \left(\frac{\frac{^{18}O}{^{16}O}_{sample}}{\frac{^{18}O}{^{16}O}_{V-SMOW}} - 1 \right) * 1000 \text{ ‰} \quad (4.1)$$

$$\delta^{17}O = \left(\frac{\frac{^{17}O}{^{16}O}_{sample}}{\frac{^{17}O}{^{16}O}_{V-SMOW}} - 1 \right) * 1000 \text{ ‰} \quad (4.2)$$

$$\delta'^{18}O = 1000 \times \ln\left(1 + \frac{\delta^{18}O}{1000}\right) \quad (4.3)$$

$$\delta'^{17}O = 1000 \times \ln\left(1 + \frac{\delta^{17}O}{1000}\right) \quad (4.4)$$

$$\Delta^{17}O = \delta'^{17}O - 0.528 \times \delta'^{18}O \quad (4.5)$$

$$\theta_{grt-cpx} = \frac{\delta'^{17}O_{grt} - \delta'^{17}O_{cpx}}{\delta'^{18}O_{grt} - \delta'^{18}O_{cpx}} \quad (4.6)$$

4.4.4 Strontium isotopes

Visibly inclusion-free ultrapure garnet separates from nine Group II eclogites were chosen for Sr isotopic study. Inclusion-free clinopyroxene separates from four of the same samples were also chosen. Based on their Sr concentrations, previously determined by LA-ICP-MS, total Sr content of the selected grains were expected to be ~ 2 ng for garnet and ~ 200 ng for clinopyroxene. All the samples were dissolved by a mixture of concentrated HF (48 %) and concentrated HNO₃ (16N) in a 3:1 ratio on a hot plate at 120 °C for 48 to 72 h. Two fractions of BHVO-2 powder were also dissolved at the same time and used as secondary standard. The dissolved samples were passed through a cation column (AG 50W X8 100-200 mesh) where the major elements were separated from the Rb-Ba-Sr fraction. Sr was further purified from this fraction by elution with 0.05M HNO₃ through Sr spec resin (Eichrom 50 to 100 µm, 0.05 ml) columns following the procedure described by Pin *et al.* (1994).

Sr Isotope ratios were measured using a Triton plus instrument, a Thermal Ionisation Mass Spectrometer (TIMS), at the Arctic Resources Lab, University of Alberta. The purified Sr fractions were dried down with 1 µL of 0.1M H₃PO₄ and loaded with 1 µL TaF₅ onto previously outgassed zone-refined rhenium single filaments following Creaser *et al.* (2004). NIST SRM 987 standard solution containing 50 to 100 ng Sr was used as primary standard. Accuracy and instrument stability for Sr isotope analyses were monitored by repeat measurement of the NIST SRM 987 standard, which gave an average value of $^{87}\text{Sr}/^{86}\text{Sr} = 0.71026 \pm 4$ (2σ , N = 4) during the study period. The secondary standard BHVO-2 had an average Sr isotopic composition of 0.70347 ± 3 (2σ , N = 5).

4.5 Results

4.5.1 Overview

I combine new elemental and isotopic data for eclogites in this study with a significant literature dataset for Roberts Victor eclogites. References for literature data are given in Table C.4, and literature data are compiled in Table S6 in the Supplementary Online Dataset. I consider eclogites in the context of their Group I and Group II textural classification (MacGregor and Carter 1970) as well as by subdivision into subgroups based on their chondrite-normalised whole-rock rare earth element patterns (REE_N ; normalised to C1 chondrite values of McDonough and Sun 1995), described below. I restrict samples to those which contain omphacitic clinopyroxene, even if garnet:clinopyroxene modes are not always eclogitic *sensu stricto* (Section 4.3; Desmons and Smulikowski 2007). Reconstructed whole-rock chemistry – major- and trace-elements – is calculated using chemical data and mineral modes, where available. When modes are not given in the literature, I assume garnet to clinopyroxene modes of 50:50.

4.5.2 Sample texture and mineral chemistry

Garnets in Roberts Victor eclogites in this study ($N = 65$) and the literature ($N = 137$) span a wide variety of compositions including pyrope-, almandine-, and grossular-rich varieties (Figure 4.3, Table C.6). In thin section, garnets are fractured, while clinopyroxene has either a pristine (omphacitic in composition) or “spongy” (diopsidic in composition) texture (Figures 4.2A, 4.2B, and 4.2E). All reported clinopyroxene major-element compositions in this study were determined using spots on clinopyroxene grains with a pristine rather than a spongy texture (Table C.7). The new eclogite xenoliths in this study with Group II textures all contain garnet with

Na₂O < 0.09 wt% and clinopyroxene with K₂O < 0.08 wt%, and the eclogites with Group I textures dominantly contain garnets with Na₂O ≥ 0.09 wt% and clinopyroxenes with K₂O ≥ 0.08 wt%. This is similar to the findings of McCandless and Gurney (1989).

4.5.3 REE-based groups and extended trace-element patterns

The most recent classification of Roberts Victor eclogites in the literature is the Type IA, IB, IK, IIA, IIB scheme of Huang *et al.* (2012a) and Gréau *et al.* (2011). In those studies, eclogites were first subdivided into Type I and II by eclogite texture based on the Group I and II method described by MacGregor and Carter (1970), then further subdivided by accessory mineral assemblage and garnet major-element chemistry (Section 4.1). In this study, I propose a new classification scheme for the Roberts Victor eclogites based on chondrite-normalised whole-rock REE_N pattern as a subdivision criteria. The classification method in this study is drafted as a schematic flowchart for visualisation (Figure 4.4). Trace-element compositions for garnet and clinopyroxene from new eclogite xenoliths in this study are reported in Tables 4.8 and 4.9, and the average elemental and isotopic compositions for each new classification in this study are given in Table C.10. In this study I consider all eclogites with Group I textures as “Group I,” without subdivision into the IA, IB, and IK classes defined by Huang *et al.* (2012a). In general, Group I eclogites with whole-rock REE_N data in this study (N = 54) and the literature (N = 45) are characterised by reconstructed whole-rock REE_N patterns with superchondritic Pr through Lu, with occasional subchondritic La and/or Ce (> 0.3x chondrite). The median whole-rock REE_N composition for Group I eclogites is shown together with the interquartile range (1st to 3rd quartile) and full range of compositions in Figure 4.5.

I subdivide eclogites with Group II textures and whole-rock REE data ($N = 38$), shown schematically in Figure 4.4. A set of four samples with Group II textures constitute the Group II_{No} eclogites which lack appreciable whole-rock LREE_N depletion (i.e., they have whole-rock $La_N/Sm_N \geq 1$). The four Group II_{No} eclogites are shown as individual whole-rock REE_N patterns in Figure 4.5. These samples are typically characterised by flat MREE_N-HREE_N slopes, variable LREE_N enrichment, and occasional positive Eu-anomalies ($[Eu/Eu^*]_N$, $Eu^* = 0.5 \times [Sm_N + Gd_N]$, normalised to chondrite; McDonough and Sun 1995). For the Group II_{No} eclogites, the subscript “No” corresponds to the “non-depleted” whole-rock REE_N patterns.

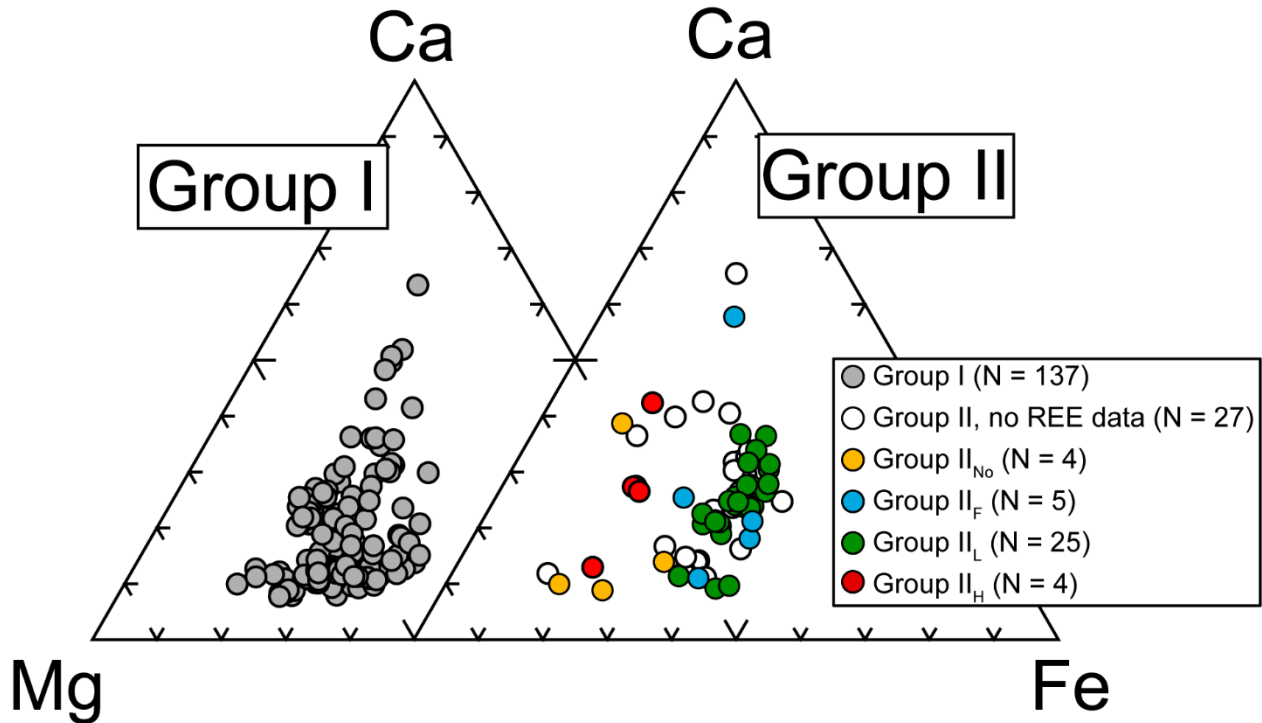


Figure 4.3 Garnet compositions from Roberts Victor eclogites in Mg-Ca-Fe space. Data are from this study ($N = 65$) and the literature ($N = 137$). Literature data sources are included in Table C.4. Eclogites are subdivided into Group I and II eclogites (textural classification of MacGregor and Carter 1970). Group II eclogites are subdivided into Groups II_L , II_H , II_F , and II_{No} based on the classification method in this study (Section 4.5.3).

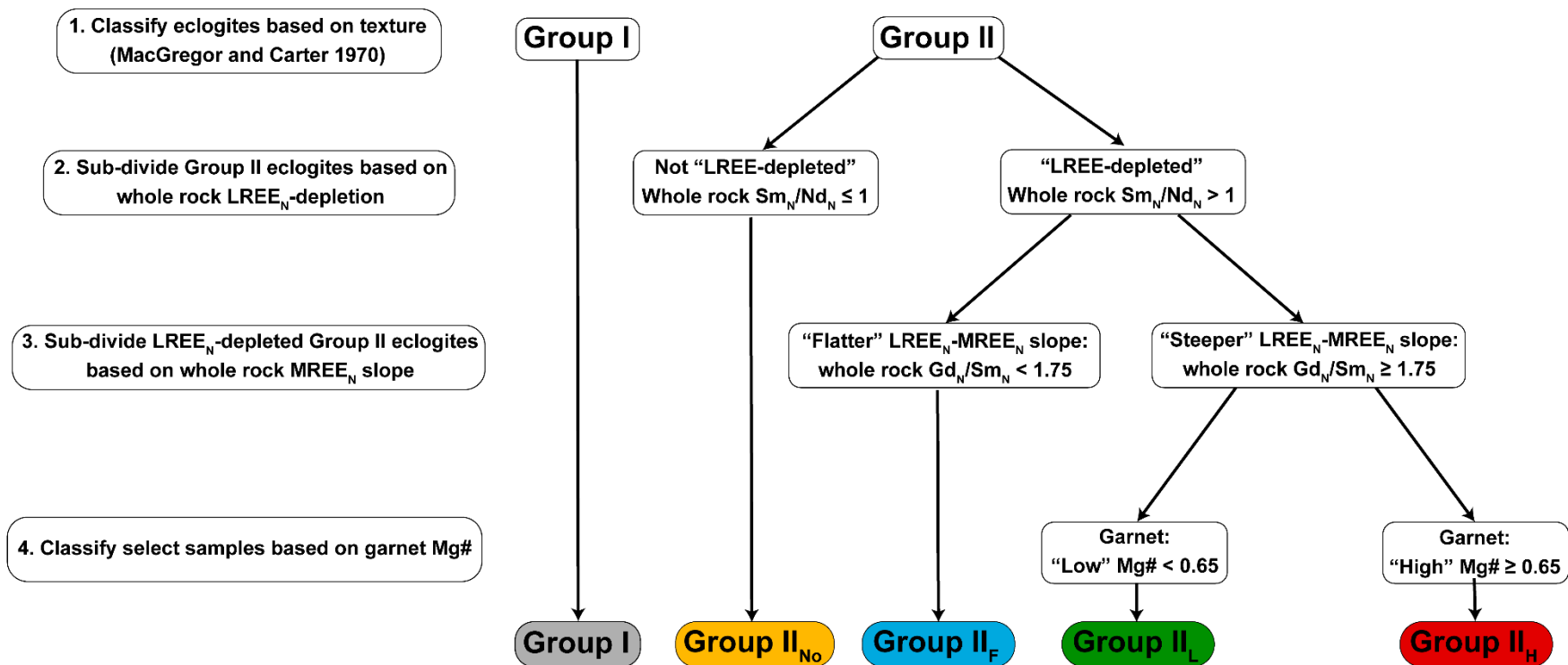


Figure 4.4 Schematic flowchart summarising the classification of Roberts Victor eclogites in this study. See Section 4.5.3 for more details. (1) Eclogites are subdivided into Group I or II based on texture after MacGregor and Carter (1970). (2) Group II eclogites are subdivided based on whether they have whole-rock LREE_N-depletion. (3) Group II eclogites with LREE_N-depletion are subdivided based on their whole-rock MREE_N slope. (4) Applicable samples are classified based on garnet molar Mg# (Mg/[Mg+Fe]). Colours are used for the same eclogite groups in other figures in this study.

The remaining eclogites with Group II textures and whole-rock REE data ($N = 34$) are “LREE-depleted” ($\text{La}_N/\text{Sm}_N < 1$) with subchondritic LREE (La, Ce, and occasionally Pr, Nd, and Sm) and superchondritic, flat to positively-sloped MREE_N-HREE_N ($\text{Lu}_N/\text{Gd}_N \geq 1$). These eclogites are subdivided into Groups II_F, II_L, and II_H as follows. Five eclogites classify as “Group II_F” with positive whole-rock REE_N slopes from La_N to Nd_N, superchondritic Nd concentrations, “shallow” MREE_N slopes ($\text{Gd}_N/\text{Sm}_N < 1.75$), and a relatively flat MREE_N-HREE_N slope from Sm_N to Lu_N than the remaining 29 samples (Figure 4.5). The subscript “F” corresponds to the relatively flat whole-rock MREE_N-HREE_N slopes.

The remaining 29 eclogites with Group II textures are subdivided into Group II_L and II_H eclogites. Both Group II_L and II_H eclogites have LREE_N-depleted whole-rock REE_N patterns, with steeper MREE_N slopes than the Group II_F eclogites ($\text{Gd}_N/\text{Sm}_N \geq 1.75$), which results in steeper MREE_N-HREE_N slopes (Figure 4.5). The difference between the Group II_L and II_H eclogites is based on their garnet Mg# ($\text{Mg}/[\text{Mg}+\text{Fe}]$): Group II_L eclogites ($N = 25$) contain garnet with low Mg# ($\text{Mg}\# < 0.65$) and Group II_H eclogites ($N = 4$) contain garnet with high Mg# ($\text{Mg}\# \geq 0.65$). The subscripts “L” and “H” correspond to the low and high Mg# of the garnet relative to the $\text{Mg}\# = 0.65$ cut-off. Using garnet Mg# as a discriminant, the distributions of Group II_L and II_H eclogitic garnets in Figure 4.3 do not overlap, and the Group II_H eclogites are characterised by slightly lower whole-rock Na₂O, TiO₂, and ΣREE than Group II_L eclogites (Table C.10). An additional 27 eclogites in the literature have Group II textures but lack whole-rock REE data. These samples are not classified into Groups II_{No}, II_F, II_L, or II_H as they lack the required REE data. These samples are included in figures in this study when major-element compositions are plotted, and referred to as “Group II eclogites, no REE data.”

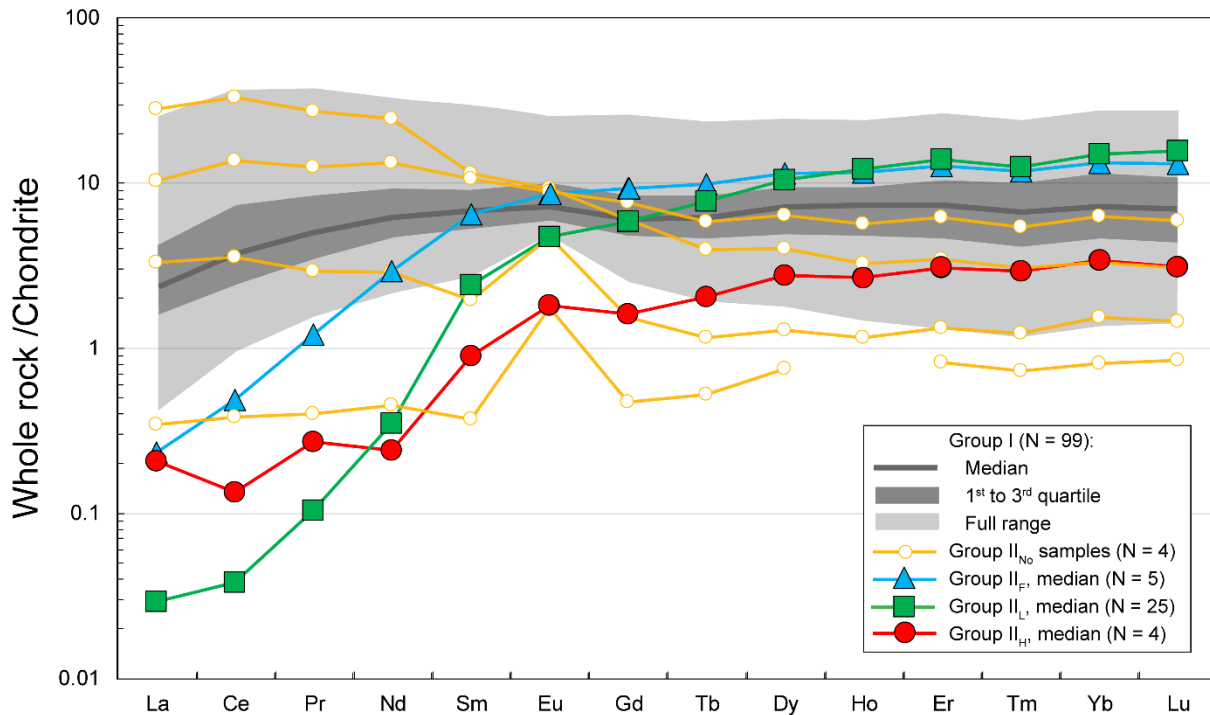


Figure 4.5 Reconstructed whole-rock REE_N compositions of eclogites in this study, normalised to C1 chondrite (McDonough and Sun 1995). Whole-rock compositions are reconstructed based on garnet and clinopyroxene only, using mineral chemistry and known mineral modes. I assume 50:50 garnet to clinopyroxene when modes are not available. Data are from this study (N = 64) and the literature (N = 73). The heavy grey line corresponds to the median REE_N pattern of all reconstructed whole-rock eclogites with Group I textures. The dark grey field corresponds to the interquartile range (1st to 3rd quartile) of REE_N patterns for eclogites with Group I textures. The light grey field corresponds to the full range of REE_N compositions for eclogites with Group I textures. The blue, green, and red curves corresponds to the median REE_N patterns for the Group II_F, II_L, and II_H eclogites, respectively. The reconstructed whole-rock REE_N patterns for four Group II_{No} eclogites (yellow lines) are shown as individual patterns.

Extended trace-element patterns of Group I and II eclogites, when normalised to primitive upper mantle (McDonough and Sun 1995), have negative Ti anomalies ($[\text{Ti}/\text{Ti}^*]_{\text{N}}$, $\text{Ti}^* = 0.5 \times [\text{Eu}_{\text{N}} + \text{Dy}_{\text{N}}]$) and positive Sr anomalies ($[\text{Sr}/\text{Sr}^*]_{\text{N}}$, $\text{Sr}^* = 0.5 \times [\text{Pr}_{\text{N}} + \text{Nd}_{\text{N}}]$; Figure 4.6). The Group II_{No} eclogites are generally more similar compositionally to Group I eclogites than to the remaining

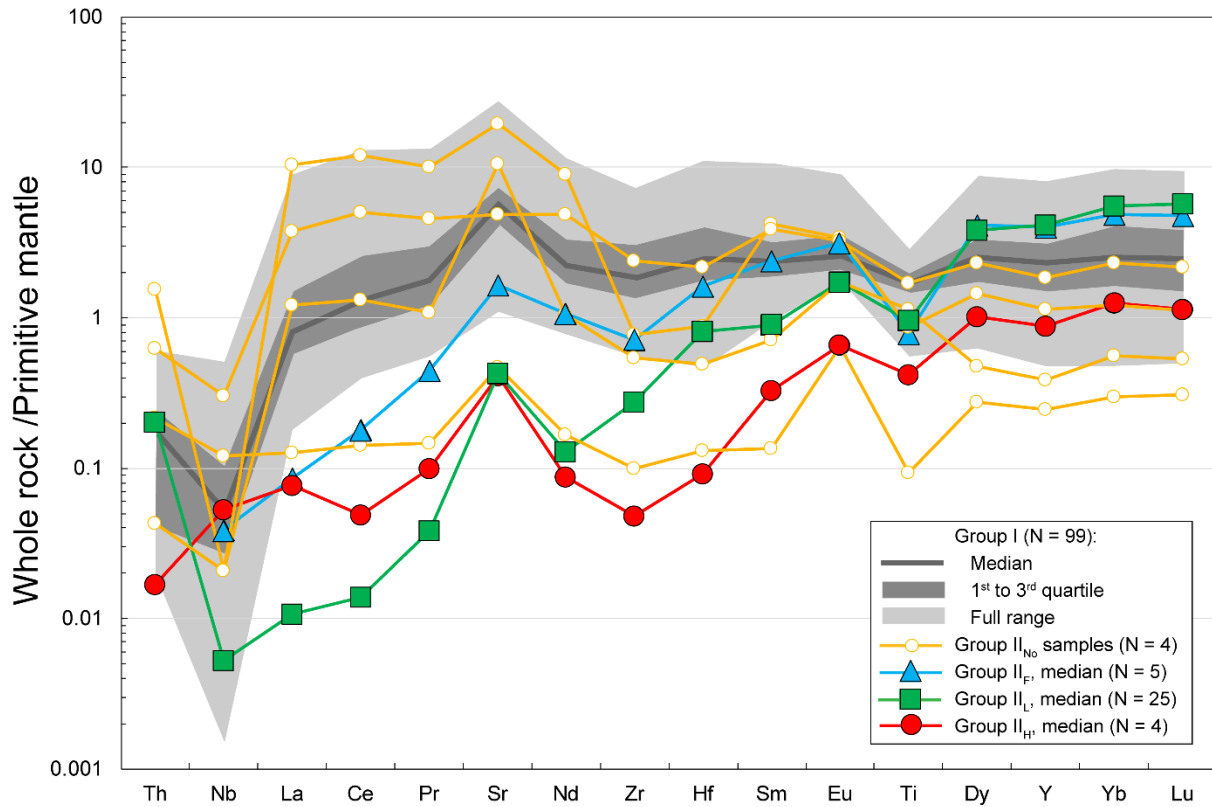


Figure 4.6 Reconstructed whole-rock extended trace-element patterns of Roberts Victor eclogites, normalised to primitive upper mantle (McDonough and Sun 1995). Whole-rock compositions are reconstructed based on garnet and clinopyroxene only, using mineral chemistry and known mineral modes. I assume 50:50 garnet to clinopyroxene when modes are not available. Data are from this study ($N = 64$) and the literature ($N = 73$). The heavy grey line corresponds to the median trace-element composition of all reconstructed whole-rock eclogites with Group I textures. The dark grey field corresponds to the interquartile range (1st to 3rd quartile) of trace-element compositions for eclogites with Group I textures. The light grey field corresponds to the full range of trace-element compositions for eclogites with Group I textures. The blue, green, and red curves corresponds to the median trace-element compositions for the Group II_F, II_L, and II_H eclogites, respectively. The reconstructed whole-rock trace-element patterns for four Group II_{No} eclogites (yellow lines) are shown as individual patterns.

Group II eclogite patterns. Group II_F, II_L, and II_H eclogites have lower high field strength element abundances (HFSE; i.e., Zr, Hf, Nb) and Sr concentrations than Group I and II_{No} eclogites (Figure 4.6; Table C.10). Group II_{No} eclogites have comparable Zr/Hf and Zr/Y ratios to Group I eclogites while Group II_L eclogites have much lower Zr abundances, Zr/Hf ratios, and Zr/Y ratios than other eclogites at Roberts Victor (Figures 4.6 and 4.7).

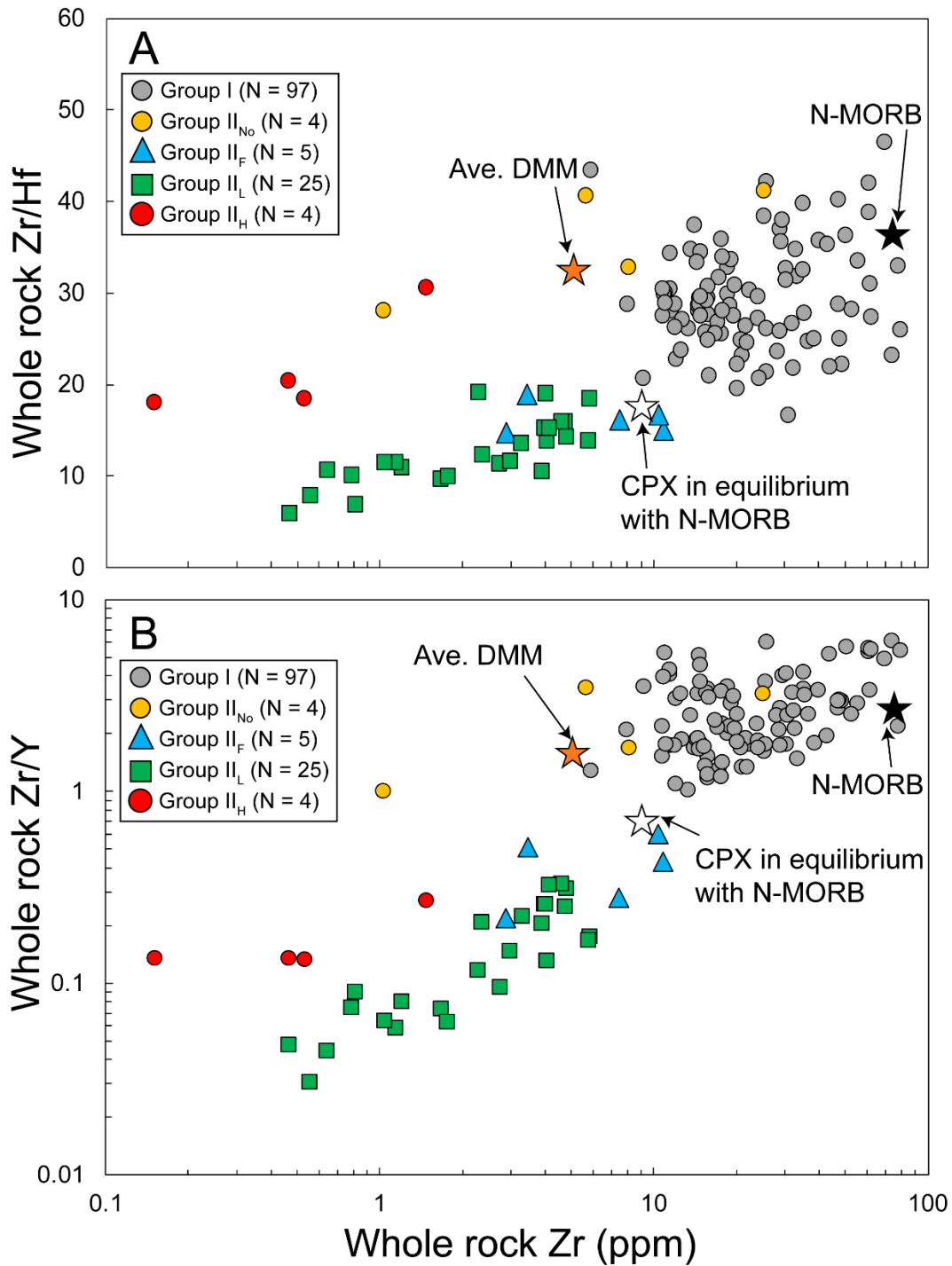


Figure 4.7 Reconstructed whole-rock compositions of Roberts Victor eclogites. (A) Zr abundance and Zr/Hf ratio, and (B) Zr abundance and Zr/Y ratio. Data are from this study (N = 64) and the literature (N = 71). Representative compositions for average depleted MORB mantle (DMM; Workman and Hart 2005) and N-MORB (Sun and McDonough 1989) are indicated. The composition of clinopyroxene (CPX) in equilibrium with N-MORB is calculated using $D_{\text{cpx/melt}}$ of Hart and Dunn (1993).

4.5.4 Oxygen isotope compositions ($\delta^{18}\text{O}$, $\delta^{17}\text{O}$)

Oxygen isotope compositions ($\delta^{18}\text{O}$) determined by SIMS for garnet from the new Roberts Victor eclogites in this study range from 1.8 to 7.6 ‰ (N = 34; Table C.5). These values are within the range for Roberts Victor and worldwide eclogites from the literature (Jacob 2004; Korolev *et al.* 2018; Radu *et al.* 2019). The $\delta^{18}\text{O}$ values determined in this study are dominantly outside of the canonical mantle range ($\delta^{18}\text{O} = 5.5 \pm 0.4$ ‰; Matthey *et al.* 1994) and have an approximately bimodal distribution when combined with literature data (Figure 4.8A; Table C.5). Group II_F, II_L, and II_H eclogites have the lowest garnet $\delta^{18}\text{O}$ values at Roberts Victor (Figures 4.8C and 4.8D). Garnets from Group II_L eclogites have a distribution of lower $\delta^{18}\text{O}$ values ($\delta^{18}\text{O} = 1.8$ to 3.6 ‰, N = 19) than the Group II_H eclogites ($\delta^{18}\text{O} = 4.7$ and 4.8 ‰, N = 2; Figure 4.9D; Table C.10). Garnets from Group II_{No} eclogites have relatively higher $\delta^{18}\text{O}$ ($\delta^{18}\text{O} = 4.7$ to 6.6 ‰, N = 4) than Group II_L, II_H, and II_F eclogites and overlap more closely with Group I eclogite $\delta^{18}\text{O}$ values ($\delta^{18}\text{O} = 5.0$ to 9.1 ‰, N = 70) closer to the canonical mantle range (Figure 4.8B). Group II_F eclogites have variable garnet $\delta^{18}\text{O}$ values that include the lowest reported $\delta^{18}\text{O}$ value for garnet from a kimberlite-hosted eclogite ($\delta^{18}\text{O} = 1.1$ ‰; Radu *et al.* 2019) and a sample with $\delta^{18}\text{O} = 4.6$ ‰ (Figure 4.8C; Table C.5).

Triple oxygen isotope data are available for garnet and/or clinopyroxene from eight eclogites in this study, including four Group II_L eclogites (RV-1, -10, -20, -22), one Group II_F eclogite (RV-27), and three Group I eclogites (RV-16, -19, -24; Table C.5). The new oxygen isotope data determined by LF in this study ($\delta^{18}\text{O}$, $\delta^{17}\text{O}$) are recast as $\delta'^{18}\text{O}$ and $\delta'^{17}\text{O}$ by Equations 4.3 and 4.4, respectively. Equations 4.5 and 4.6 are used to calculate $\Delta'^{17}\text{O}$ and $\theta_{\text{Grt-Cpx}}$ values (Table C.5). The triple oxygen isotope data from this study are shown together with inferred representative values for mid ocean ridge basalt (MORB) and seawater in Figure 4.9.

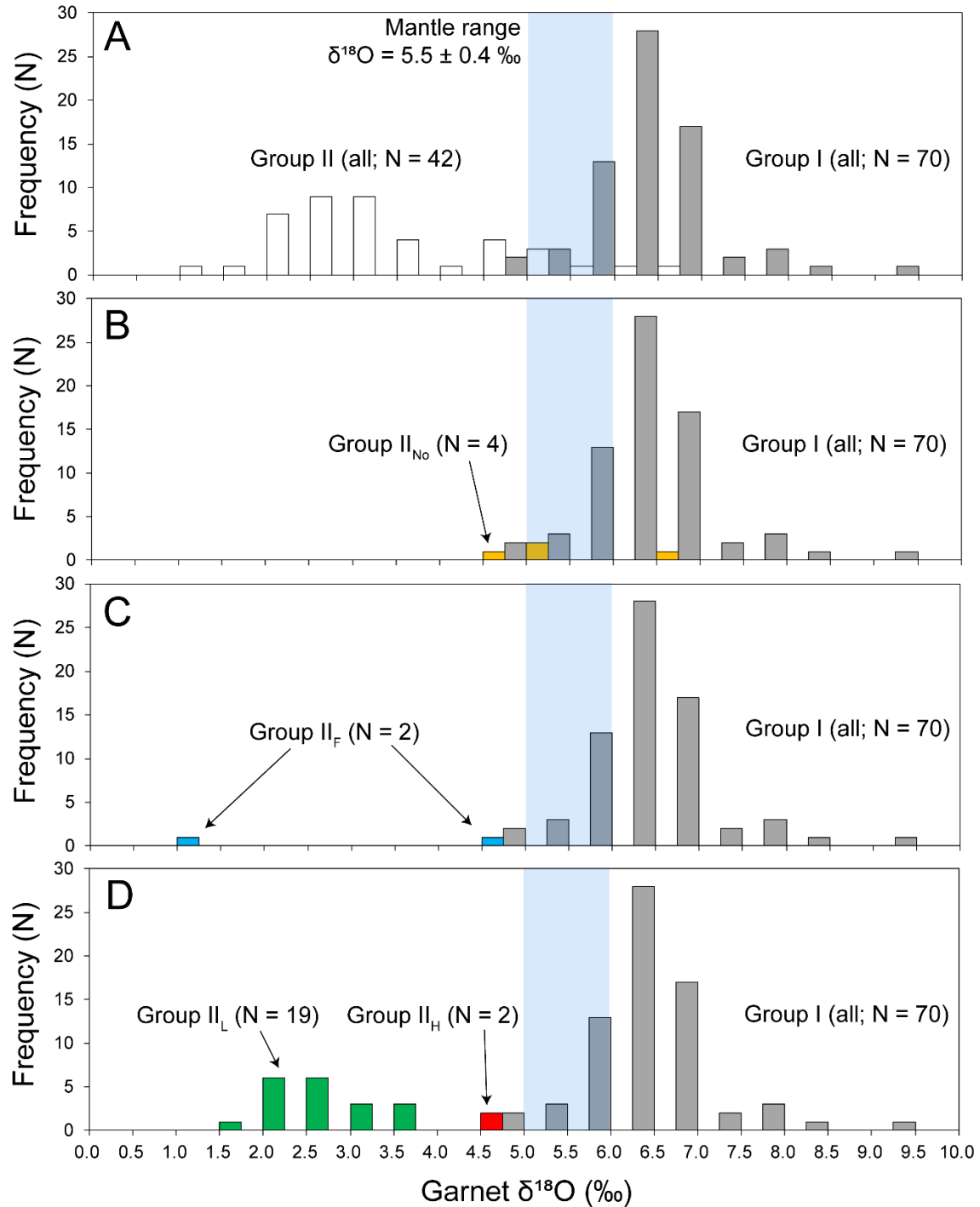


Figure 4.8 Frequency distribution of $\delta^{18}\text{O}$ in garnets from eclogites at Roberts Victor, from this study (N = 34) and the literature (N = 78). The canonical mantle range for $\delta^{18}\text{O}$ (5.5 ± 0.4 ‰; Matthey *et al.* 1994) is shown as a blue field. A) All Group I and Group II eclogites for which textural information and $\delta^{18}\text{O}$ data are available. Group II eclogites lacking whole-rock REE data are included in the Group II distribution. B, C, D) Group II eclogites with whole-rock REE data, subdivided into Groups II_{No}, II_F, II_L, and II_H. The distribution of all Group I eclogitic garnets is shown for comparison.

The eclogites with Group II textures have lower $\delta^{18}\text{O}$ values but comparable $\Delta^{17}\text{O}$ values to MORB, whereas most eclogites with Group I textures have higher $\delta^{18}\text{O}$ and lower $\Delta^{17}\text{O}$ than MORB.

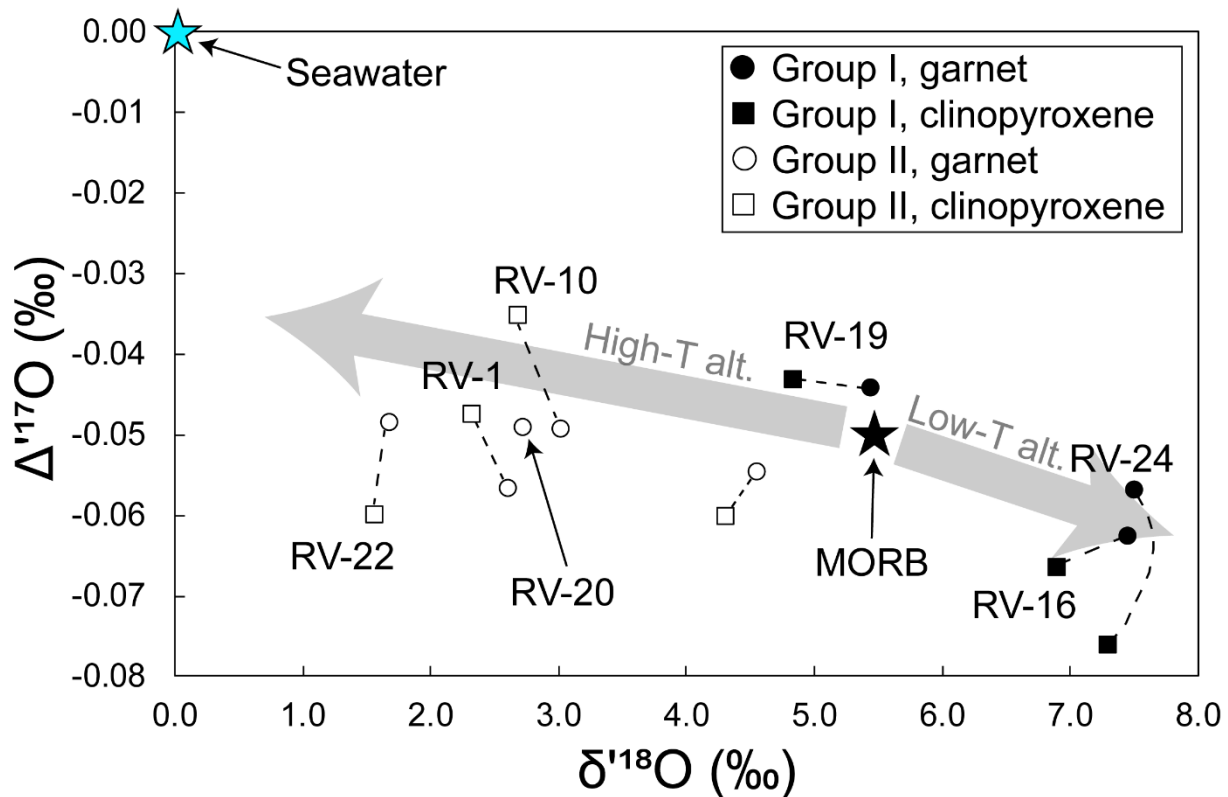


Figure 4.9 $\Delta^{17}\text{O}$ versus $\delta^{18}\text{O}$ (calculated from $\delta^{17}\text{O}$ and $\delta^{18}\text{O}$ by Equations 4.5 and 4.3, respectively) for garnet-clinopyroxene pairs analysed by laser fluorination in this study. Dashed lines connect garnet and clinopyroxene from the same sample. Inferred MORB values ($\Delta^{17}\text{O} = -0.050$ ‰, $\delta^{18}\text{O} = 5.5$ ‰, Matthey *et al.* 1994; Sharp *et al.* 2018) and seawater composition ($\Delta^{17}\text{O} = 0.00$ ‰, $\delta^{18}\text{O} = 0.0$ ‰) are plotted. Large vectors indicate the expected evolution of oxygen isotopes during alteration of MORB by seawater at high temperatures ($> \sim 350$ °C) and low temperatures ($< \sim 350$ °C), from Pack and Herwartz (2014).

Garnet and clinopyroxene $\delta^{18}\text{O}$ values from the same xenolith in this study ($N = 7$, determined by LF) and the literature ($N = 51$) are compared in Figure 4.10. In general garnet and clinopyroxene for the full dataset are strongly correlated ($R^2 = 0.97$) and define a line with a slope of 1.024, slightly steeper than unity. Garnet-clinopyroxene mineral pairs do not all appear

to be in isotopic equilibrium, as clinopyroxene is predicted to be slightly ^{18}O -enriched relative to garnet at equilibrium, for a variety of eclogite bulk compositions (Beard *et al.* 1996).

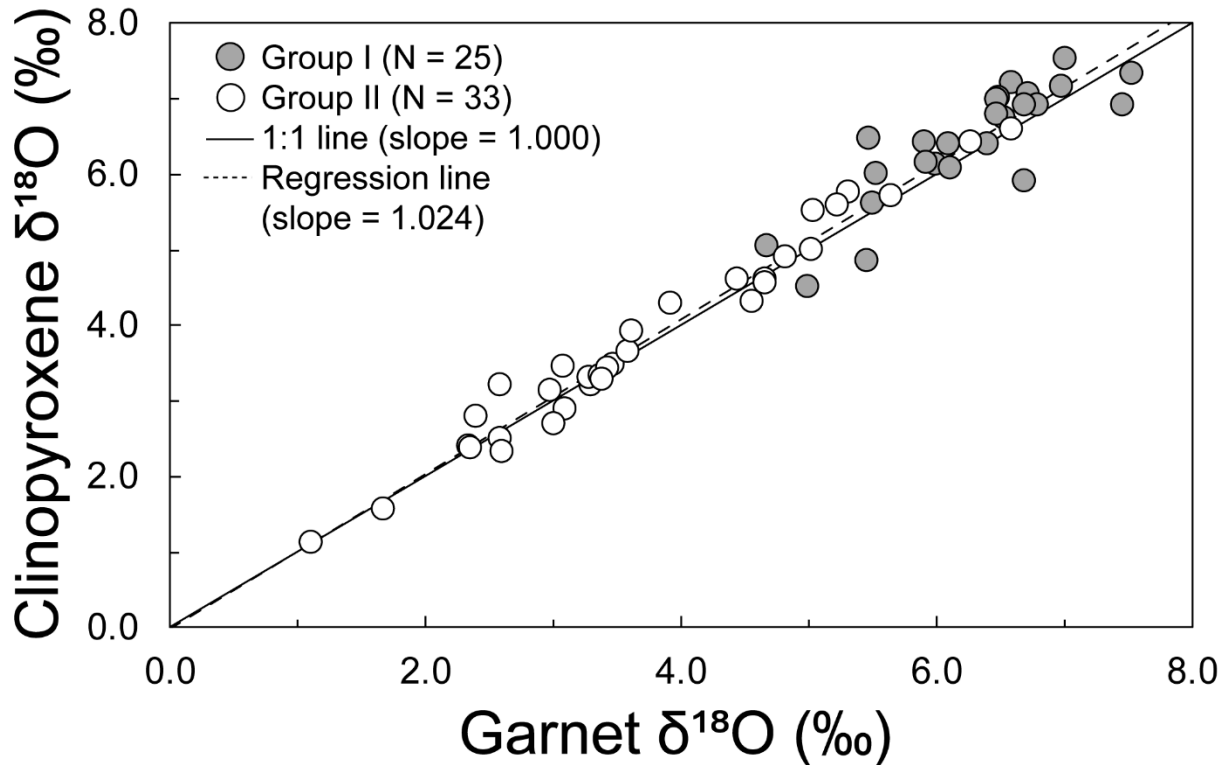


Figure 4.10 Oxygen isotope compositions ($\delta^{18}\text{O}$, ‰) for coexisting garnet and clinopyroxene from eclogite xenoliths from Roberts Victor. Data for garnet-clinopyroxene pairs are from this study (by laser fluorination; $N = 7$) and published literature (various methods; $N = 51$). The regression line for the full dataset has the equation $\delta^{18}\text{O}_{\text{cpx}} = 1.024 \times \delta^{18}\text{O}_{\text{grt}} - 0.014$. The full Roberts Victor dataset has a coefficient of determination (R^2) value of 0.97.

4.5.5 Strontium isotopes

Strontium isotope data are reported as $^{87}\text{Sr}/^{86}\text{Sr}$ for garnet from nine Group II eclogites and coexisting clinopyroxene from four of the same samples (Table C.11), and are compared with data for Roberts Victor eclogites from the literature (Jacob *et al.* 2005; Huang *et al.* 2012). Garnets from eclogites in this study have $^{87}\text{Sr}/^{86}\text{Sr}$ ratios ranging from 0.7085 to 0.7097, similar to garnets from Group II eclogites in the literature (Jacob *et al.* 2005; Huang *et al.* 2012a). The co-

existing clinopyroxenes have more unradiogenic $^{87}\text{Sr}/^{86}\text{Sr}$ compositions (0.7011 to 0.7056) which are also comparable to values in the literature (Jacob *et al.* 2005; Huang *et al.* 2012a).

4.5.6 Equilibration pressures and temperatures

In this study I calculate equilibration temperatures and pressures for all eclogites in the dataset by projection of T_{Krogh88} (Fe-Mg exchange thermometer between garnet and clinopyroxene; Krogh 1988) onto the 38 mW/m² model geotherm of Hasterok and Chapman (2011; Figure 4.11; Table C.2). The 38 mw/m² model geotherm best fits available pressure-temperature data for Roberts Victor (Grütter 2009, and references therein). Beyer *et al.* (2015) proposed a new Ca-Tschermak's-in-clinopyroxene barometer for eclogitic assemblages. However, this barometer is applicable only when clinopyroxene Si < 2.000 apfu, and uncertainties on calculated pressure are elevated when clinopyroxene Si \geq 1.985 apfu. For the eclogites compiled in this study 49 % (N = 97 out of 198) contain clinopyroxene with Si \geq 1.985 apfu, so I do not apply this barometer to pressure determination in this study.

The new eclogites analysed in this study have calculated equilibration pressure-temperatures that overlap with existing data from the literature (Figure 4.11; Table C.2). The distribution of geotherm-projected pressures for all Group I eclogites at Roberts Victor compiled in this study has a prominent broad mode centered close to 53 kbar (\sim 1110 °C; Figure 4.11). Group II eclogites have a wider apparent-depth distribution than Group I with two poorly-defined modes at \sim 41 kbar (\sim 920 °C) and \sim 55 kbar (\sim 1140 °C; Figure 4.11). Three Group II eclogites have calculated temperatures > 1350 °C, which significantly exceed the mantle adiabat at lithospheric depths.

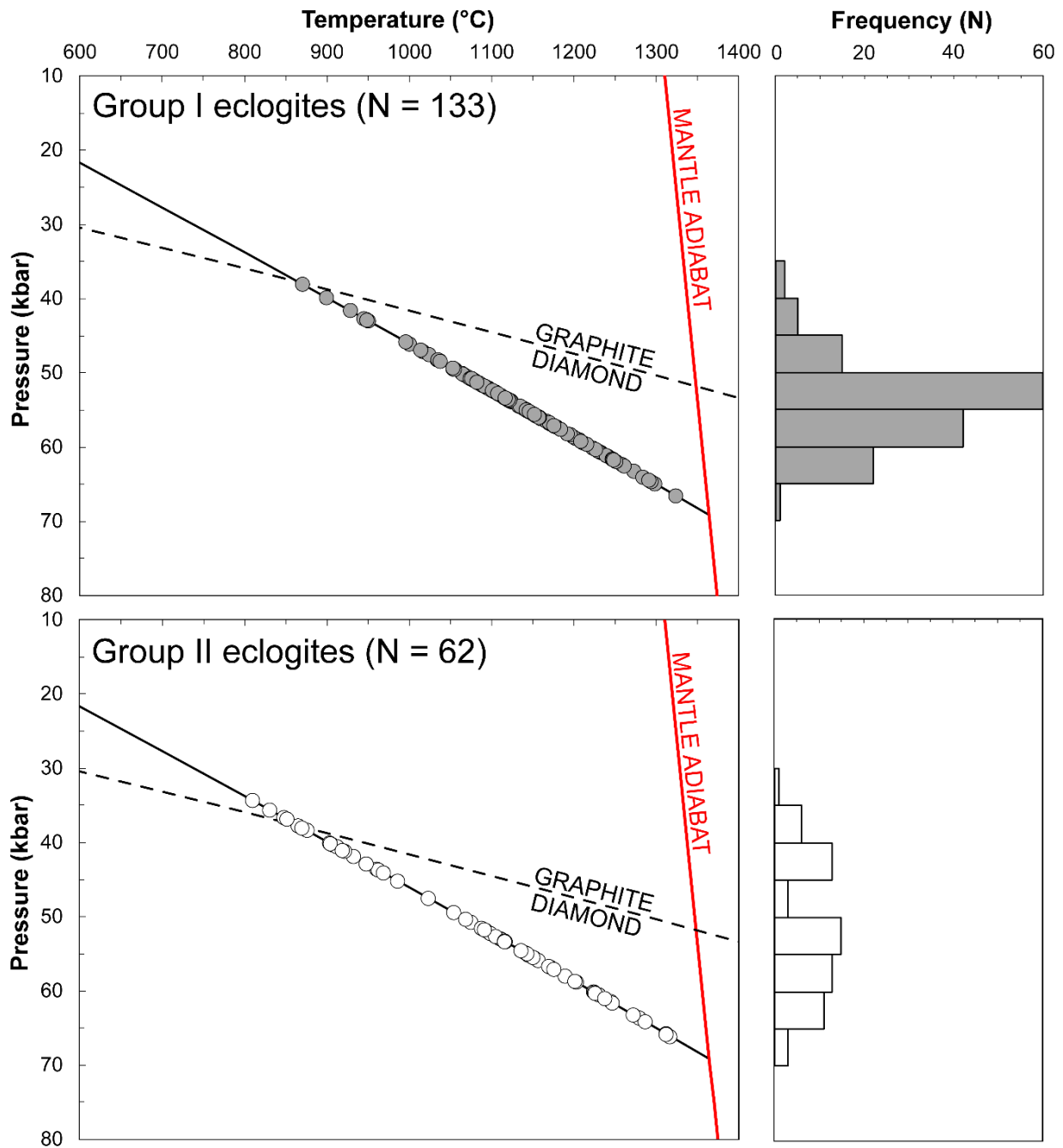


Figure 4.11 Calculated temperature and extrapolated pressure conditions of last equilibration for Group I (top) and Group II (bottom) eclogites from Roberts Victor, from this study (N = 65) and the literature (N = 130). Temperatures are calculated via the Fe-Mg exchange thermometer of Krogh (1988) and pressures are derived by projection of these temperatures onto the 38 mw/m² geotherm of Hasterok and Chapman (2011; solid black line). The graphite-diamond transition from Day (2012) is shown as a dashed black line. Three Group II eclogites with calculated temperatures greater than ~ 1350 °C (hotter than the mantle adiabat, red line) are not shown. Histograms for calculated equilibration pressures for Group I and II eclogites are shown to the right.

4.6 Discussion

4.6.1 Oxygen isotope systematics

4.6.1.1 Background

The Group I and Group II eclogites at Roberts Victor have classically been divided based on sample texture, as well as elemental and isotopic chemistry (Section 4.1; Table C.1; MacGregor and Carter 1970; MacGregor and Manton 1986; McCandless and Gurney 1989). In this chapter, I discuss possible protoliths for the Groups I and Group II eclogites at Roberts Victor, in light of previous interpretations and new data. To better constrain the environment in which Group I and Group II eclogite protoliths formed, I employ oxygen isotope compositions, which can be used as tracers of the character and environment of fluid alteration (Sharp *et al.* 2018). Most mantle eclogite suites, including Roberts Victor, have oxygen isotope compositions outside the canonical mantle range (Jacob 2004; Figure 4.8). Oxygen isotopes ($^{18}\text{O}/^{16}\text{O}$) do not fractionate significantly at high pressures or temperatures (Eiler 2001), and alteration by fluids in the mantle should cause the $\delta^{18}\text{O}$ value of a rock to adjust toward the mantle range, rather than away from it (Czas *et al.* 2018). Instead, variations in $\delta^{18}\text{O}$ values outside of the canonical mantle range are possibly imposed by hydrothermal alteration of oceanic crust by seawater at various temperatures: for hydrothermal alteration at “low” temperatures ($< \sim 350$ °C), $\delta^{18}\text{O}$ values in the altered oceanic crust will increase, and for hydrothermal alteration at “high” temperature ($> \sim 350$ °C), $\delta^{18}\text{O}$ in the altered oceanic crust will decrease (Muehlenbachs and Clayton 1972a, 1972b; Clayton *et al.* 1975; Gregory and Taylor 1981).

Several studies have noted the similarity between the distributions of $\delta^{18}\text{O}$ values from mantle eclogite suites globally and ophiolites, both of which range beyond the canonical mantle range of

5.5 ± 0.4 ‰ (Mattey *et al.* 1994; Jacob 2004; Korolev *et al.* 2018; Ickert *et al.* 2013). This has been taken as partial support for eclogites having protoliths that were oceanic crust. The occurrence of some eclogites with $\delta^{18}\text{O}$ values within the canonical mantle range has alternatively been interpreted to indicate crystallisation of some eclogites from melts at high pressures in the mantle (e.g., Snyder *et al.* 1997). However, $\delta^{18}\text{O}$ values within the canonical mantle range may still occur in oceanic crust. Firstly, the water-rock ratio gradually decreases with depth in oceanic crust and consequently, the deepest ($> \sim 5$ km depth; Gregory and Taylor 1981) oceanic crust will retain its original “mantle-like” $\delta^{18}\text{O}$ value through lack of hydrothermal alteration. Secondly, as temperature increases with depth, the $\delta^{18}\text{O}$ of seawater altered oceanic crust will cross-over the mantle value at intermediate temperatures/depths (~ 2 km; Gregory and Taylor 1981). Therefore, $\delta^{18}\text{O}$ values within the canonical mantle range for some eclogites are not unequivocal indicators of a purely “mantle origin.”

While the Roberts Victor Group I eclogites have a $^{18}\text{O}/^{16}\text{O}$ distribution that overlaps with and generally extends to higher $\delta^{18}\text{O}$ values than the mantle range, the Group II eclogites have a $^{18}\text{O}/^{16}\text{O}$ distribution that is much lower than the mantle range (Figure 4.8). Eclogite xenoliths hosted by kimberlite only rarely have oxygen isotope values < 4 ‰ (Jacob 2004; Korolev *et al.* 2018), and very low values are also uncommon in ophiolites (Ickert *et al.* 2013). However, low $\delta^{18}\text{O}$ values (< 4 ‰) have been reported at several ophiolite localities, including the Rajmi section of the Samail Ophiolite and the Taitao Ophiolite, Chile. The Rajmi section has reported $\delta^{18}\text{O}$ values less than 2 ‰ at depths of ~ 5 km, possibly imposed by fluid penetrating along transform faults (Stakes and Taylor 1992). In the Taitao Ophiolite, peridotites and gabbros have reported $\delta^{18}\text{O}$ values as low as 0.68 ‰ (Schulte *et al.* 2009). Orogenic eclogite suites also often have low $\delta^{18}\text{O}$ ($\delta^{18}\text{O} < 0$ ‰), due to preservation of primary $\delta^{18}\text{O}$ values inherited from protoliths

that interacted with meteoric fluids with $\delta^{18}\text{O} < 0 \text{ ‰}$ at low temperatures ($< 350 \text{ °C}$; e.g., Sulu terrane, China; Yui *et al.* 1995; Zheng *et al.* 1996).

Mechanisms other than surface-water alteration are unlikely to impart significant oxygen isotope variations in mantle-derived rocks. For example, dehydration during subduction, partial melting, or fractional crystallisation – unless driven to very high degrees – are not expected to have significant effects on isotope compositions ($< \sim 1 \text{ ‰}$; Valley 1986; Eiler 2001; Bucholz *et al.* 2017; Korolev *et al.* 2018). Based on this discussion, the oxygen isotope characteristics for both Group I and Group II eclogites are likely inherited from protoliths altered by fluids, prior to subduction. However, the possibility that the Group II eclogite protoliths may have been altered by a fluid other than seawater can be tested using multiple oxygen isotopes.

4.6.1.2 Triple oxygen isotopes

Small, mass-dependent relative fractionations between ^{18}O - ^{16}O and ^{17}O - ^{16}O can be used to assess alteration history (e.g., Sharp *et al.* 2018) via the $\Delta^{17}\text{O}$ value for individual samples (Equations 4.5; Sharp *et al.* 2016, 2018). The $\Delta^{17}\text{O}$ value is a simplified means of indicating the small isotopic deviations between a sample and a reference line. In this case, the reference line is a fractionation line defined by the isotope compositions of terrestrial materials (Sharp *et al.* 2016). Different fluids each have their own value, which can be shown graphically (Figure 4.9). For oceanic crust generated from depleted mantle I assume a starting isotopic composition for MORB of $\Delta^{17}\text{O} = -0.05 \pm 0.01 \text{ ‰}$ and $\delta^{18}\text{O} = 5.5 \pm 0.4 \text{ ‰}$, respectively (Mattey *et al.* 1994; Sharp *et al.* 2018; Figure 4.9). During hydrothermal alteration it is expected that $\delta^{18}\text{O}$ and $\Delta^{17}\text{O}$ of the altered rock will evolve based on the isotopic composition of the altering fluid as well as the temperature of alteration, which will be documented by a different $\Delta^{17}\text{O}$ - $\delta^{18}\text{O}$ slope (Pack

and Herwartz 2014; Figure 4.9). Oceanic basalt altered by seawater at high temperatures ($> \sim 350$ °C) is expected to decrease in $\delta^{18}\text{O}$ and increase in $\Delta^{17}\text{O}$ with a relatively shallow slope (Figure 4.9). For alteration of MORB by seawater at low temperatures an increase in $\delta^{18}\text{O}$ and decrease in $\Delta^{17}\text{O}$ is expected with a slightly steeper slope (Figure 4.9; Pack and Herwartz 2014). In this context, the isotopic compositions of Group I and Group II eclogites correspond broadly to MORB altered by seawater at different temperatures: garnet and clinopyroxenes from Group II eclogites have lower $\delta^{18}\text{O}$ and similar, slightly elevated $\Delta^{17}\text{O}$ compared to MORB, and Group I eclogites have slightly higher $\delta^{18}\text{O}$ and lower $\Delta^{17}\text{O}$ (Figure 4.9). Meteoric fluids are often reported to have significantly lower $\delta^{18}\text{O}$ and higher $\Delta^{17}\text{O}$ than seawater, which should theoretically have a more substantial effect on the triple oxygen isotope evolution (Herwartz *et al.* 2015; Sharp *et al.* 2016, 2018). Thus the overall tendency of the oxygen isotope compositions of the Group I and II eclogites appears to be in-line with expected evolution trends for MORB altered by seawater, and do not require a fluid other than seawater (Pack and Herwartz 2014).

The Roberts Victor eclogites in this study and the literature also define an approximately linear garnet-clinopyroxene $\delta^{18}\text{O}$ array that is broadly consistent with high temperature isotopic equilibrium (Figure 4.10). Evidence for high temperature equilibrium between minerals is expected for rocks that have experienced eclogitisation as any oxygen isotopic disequilibrium between minerals in the oceanic protoliths (i.e., between clinopyroxene and plagioclase) should be “reset” to high temperature equilibrium. High temperature equilibrium can also be assessed using triple oxygen isotopes with the variable $\theta_{\text{Grt-Cpx}}$ (Equation 4.6). The variable $\theta_{\text{Grt-Cpx}}$ is a measure of garnet-clinopyroxene isotopic variation with respect to $\delta^{17}\text{O}$ and $\delta^{18}\text{O}$. The $\theta_{\text{Grt-Cpx}}$ value generally decreases with decreasing temperature, and values between 0.5000 and 0.5305 are inferred to define a range of high temperature isotopic equilibrium (Cao and Liu 2011; Sharp

et al. 2018; Wostbrock *et al.* 2018). Group I eclogite RV-19 has $\theta_{\text{Grt-Cpx}} = 0.5262$ and therefore appears to be consistent with high temperature equilibrium, whereas the Group II eclogites and other Group I eclogites fall outside of the range, to both higher and lower values, possibly indicating some degree of inter-mineral isotopic disequilibrium (Table C.5). Garnets in eclogites analysed in this study typically have a relatively small range in $\Delta^{17}\text{O}$ (average = -0.053 ± 0.013 [2σ]) compared with the clinopyroxenes (average = -0.055 ± 0.029 [2σ]). This may suggest that clinopyroxene is relatively more susceptible to isotope modification in the mantle, if this is the cause of the $\Delta^{17}\text{O}$ variations. However, the approximately linear array for $\delta^{18}\text{O}$ between garnet and clinopyroxene is largely preserved, suggesting that the effect of post-eclogitisation alteration, if any, may have been minor.

4.6.1.3 Summary

The interpretation of oxygen isotope systematics of the Roberts Victor eclogites is complex due to their multi-stage evolution, as well as a lack of precise knowledge of the protoliths and the altering fluids involved. Nonetheless, I find no clear signal of the involvement of low-temperature meteoric waters with elevated $\Delta^{17}\text{O}$ and low $\delta^{18}\text{O}$ values in the alteration of the protoliths to the Group II Roberts Victor eclogites. This is consistent with the lack of reported $\delta^{18}\text{O} < 0$ ‰ in the more than 100 eclogites analysed from Roberts Victor. Such $\delta^{18}\text{O} < 0$ ‰ values sometimes occur in continental magmatic and metamorphic rock suites that interacted with meteoric water at low temperatures (< 350 °C; Zheng *et al.* 1996, and references therein). Instead, low $\delta^{18}\text{O}$ values (< 4 ‰) can be generated by seawater alteration of oceanic crust at depth if water/rock ratios are sufficient to change the $\delta^{18}\text{O}$ of the oceanic crust (Stakes and Taylor 1992). Therefore, the $\delta^{18}\text{O}$ values of the Group II eclogites below the mantle range do not require an additional fluid species, rather they likely arise from high-temperature (> 350 to

400 °C) fluid-rock interaction between oceanic crustal protoliths and seawater, as concluded by previous studies (Jagoutz *et al.* 1984; MacGregor and Manton 1986; Jacob 2004; Radu *et al.* 2019). Based on the lower $\delta^{18}\text{O}$ values of Group II eclogites (Figure 4.8), I infer that some Group II eclogite protoliths may have experienced hydrothermal alteration at higher-temperature (and possibly deeper) in oceanic crust than the Group I eclogite protoliths. The low $\delta^{18}\text{O}$ values could also possibly arise from interaction between the Group II eclogite protoliths and seawater at higher water/rock ratios than some of the deep Group I eclogite protoliths.

4.6.2 Radiogenic isotope systematics

Radiogenic isotope compositions determined in this study and available in the literature indicate a substantial difference between Groups I and Group II eclogites at Roberts Victor (Jacob *et al.* 2005; Gonzaga *et al.* 2010; Huang *et al.* 2012a; Table C.11). Group II eclogites typically have unradiogenic present-day whole-rock $^{87}\text{Sr}/^{86}\text{Sr}$ (< 0.704) and extremely radiogenic $^{143}\text{Nd}/^{144}\text{Nd}$ (≥ 0.518 , up to 0.539), $^{147}\text{Sm}/^{144}\text{Nd}$ (≥ 0.29 , up to 1.57), $^{176}\text{Hf}/^{177}\text{Hf}$ (≥ 0.285), and $^{176}\text{Lu}/^{177}\text{Hf}$ (≥ 0.11 , up to 0.51; Jacob *et al.* 2005; Huang *et al.* 2012a). Group I eclogites have relatively more radiogenic $^{87}\text{Sr}/^{86}\text{Sr}$ (≥ 0.706) and less radiogenic $^{143}\text{Nd}/^{144}\text{Nd}$ (< 0.515), $^{147}\text{Sm}/^{144}\text{Nd}$ (≤ 0.31), $^{176}\text{Hf}/^{177}\text{Hf}$ (≤ 0.282), and $^{176}\text{Lu}/^{177}\text{Hf}$ (< 0.283 ; Jacob *et al.* 2005; Huang *et al.* 2012a). The highly radiogenic isotope compositions of some Group II eclogites, for example radiogenic $^{143}\text{Nd}/^{144}\text{Nd} > 0.525$, are uncommon in the literature but have been reported in eclogites from the Sulu orogenic terrane, China (Jahn *et al.* 1996), and several mantle eclogites from Bellsbank (Shu *et al.* 2014). Jahn *et al.* (1996) ascribed the strongly radiogenic compositions in the Sulu eclogites to long-term radiogenic in-growth following an ancient Sm-Nd fractionation event.

The Roberts Victor eclogites also have variable mineral isochron ages in the literature. Sm-Nd and Lu-Hf isochron age for Group I eclogites approximate the age of the host kimberlite (128 ± 15 Ma; Smith *et al.* 1985), likely reflecting isotopic closure at or shortly after the time of eruption (Jacob *et al.* 2005; Huang *et al.* 2012a). Sm-Nd isochron ages for Group II eclogites are generally ~ 743 to ~ 1143 Ma, and Lu-Hf isochron ages are typically ~ 764 to 1544 (Huang *et al.* 2012a). These data indicate an age of last equilibration that is older than the host kimberlite. Based on calculated temperatures in this study, Group II eclogites equilibrated throughout the lithospheric mantle, including at temperatures higher than assumed for isotopic exchange closure. These temperature are ~ 850 °C for the Sm-Nd system and ~ 920 °C for the Lu-Hf system (Shu *et al.* 2014; Brey and Shu 2018; Figure 4.11; Table C.2). To account for the fact that Group II eclogites have isochron ages that are older than kimberlite – with the Sm-Nd system overlapping with and closing after the Lu-Hf system – it has been suggested that the Group II eclogites had higher isotopic closure temperatures due to being dry, medium-grained rocks (see discussions in Jagoutz 1988, Huang *et al.* 2012a, and Shu *et al.* 2014). The range in isochron ages for Group II eclogites may represent partial resetting of isotope systematics (Jacob *et al.* 2005; Gonzaga *et al.* 2010; Brey and Shu 2018). The Rb-Sr system may be modified in oceanic crust during alteration by seawater (MacGregor and Manton 1986). Based on the Lu-Hf system which is the relatively more robust system to secondary metasomatic effects (Jacob *et al.* 2005), Group II eclogites in the literature have Paleoproterozoic model ages (T_{DM} ; 1.37 to 2.32 Ga), and Group I eclogites range from future ages to ages older than the earth (Huang *et al.* 2012a). Therefore, it is apparent that the Roberts Victor eclogite age systematics are not straightforward. Based on their isotopic study, Gonzaga *et al.* (2010) inferred that the full suite of Roberts Victor eclogites likely was not cogenetic or comagmatic.

4.6.3 Existing models for the origin of Group II eclogites

4.6.3.1 Are Group II eclogites partial melt residues?

4.6.3.1.1 Overview

One of the primary compositional differences between the Group I and Group II eclogites at Roberts Victor is that Group II eclogites have extremely low incompatible element contents relative to Group I eclogites, including LREE, Sr, TiO₂, K₂O, and HFSE (Zr, Hf, Nb; Figures 4.5, 4.6, and 4.7; Table C.10). The incompatible element depletions as well as elevated HREE abundances of some eclogites, such as the Group II eclogites, have been inferred as evidence that eclogites or their protoliths experienced significant partial melt extraction following their formation as oceanic crust (e.g., Viljoen *et al.* 2005; Shu *et al.* 2018; Radu *et al.* 2019). Eclogites have variably been interpreted as subduction-melting residues of hydrated Archean basalt, picrite, or komatiite (Pearson *et al.* 2003; Jacob *et al.* 2005; Smit *et al.* 2014; Aulbach and Arndt 2019), so it may be that Group II eclogites – or their protoliths – underwent more extreme melt extraction than Group I eclogites.

The origin for some Group II eclogites as melt-residues is a possibility based on the low Zr abundances and Zr/Hf ratios of many of the Group II eclogites (Figure 4.7), which cannot readily be explained by crystallisation of oceanic crust from MORB-like magmas. Clinopyroxene has among the highest D_{Zr} and D_{Hf} but lowest D_{Zr}/D_{Hf} ratio (~ 0.50) of typical cumulate minerals (Blundy *et al.* 1998; Ionov *et al.* 2002; Kelemen *et al.* 2003, and references therein; Aigner-Torres *et al.* 2007). Variation in Zr/Hf ratios is possible during accumulation of minerals like clinopyroxene with low D_{Zr}/D_{Hf} ratios, but the range in Zr/Hf ratios possible by accumulation alone is considered to be relatively restricted (David *et al.* 2000; Pfänder *et al.* 2007). For

example, the clinopyroxene calculated to be in equilibrium with N-type MORB (N-MORB; $D_{\text{cpx/melt}}$ of Hart and Dunn 1993; Sun and McDonough 1989) has a higher Zr abundance and Zr/Hf ratio than many of the Group II_L eclogites (Figure 4.7). Therefore, precipitation of the Group II eclogite protoliths from N-MORB-like magmas does not appear to be able to account for the Zr and Hf contents of many Group II_L eclogites. The Group I eclogites, however, have a more-restricted range of Zr abundances and Zr/Hf ratios, both of which are higher than that of the clinopyroxene calculated to be in equilibrium with N-MORB (Figure 4.7). Therefore, clinopyroxene accumulation from N-MORB-like magmas may be a controlling factor for bulk Zr and Hf for the Group I eclogite protoliths. For the Group II_L eclogites, in this section I test whether melt extraction can explain some of the low Zr/Hf ratios, as melt extraction from clinopyroxene-rich residues is considered one of the principal processes to fractionate Zr and Hf (Lundstrom *et al.* 1998; Klemme *et al.* 2002). The inference that Group II eclogites underwent more extreme melt extraction than Group I eclogites, however, makes the *a priori* assumption that Group I and Group II eclogites, or their protoliths, had similar pre-melting compositions (that is, after formation in oceanic crust but prior to melting during subduction).

4.6.3.1.2 Melt modeling

Shu *et al.* (2018) modeled LREE depletion during anhydrous partial melting at eclogite-facies with a starting composition of N-MORB (Sun and McDonough 1989) and mineralogy of 60 % garnet, 40 % clinopyroxene. Assuming melting proportions of 50:50 garnet to clinopyroxene, Shu *et al.* (2018) demonstrated that LREE fractionation develops in the eclogite residues at low melt degrees (~ 10 %) and progressive MREE fractionation and HREE enrichment ensues at higher melting degrees (up to 40 %). To assess how the REE_N compositions of residues vary due to melt extraction in the eclogite facies, I have reproduced these partial melting conditions. I

have also added the elements Zr, Hf, and Y as additional process monitors as Group I and Group II eclogites have significantly different Zr abundance versus Zr/Hf ratio and Zr abundance versus Zr/Y ratio distributions (Figure 4.7). Zr and Hf have almost identical ionic radii and the same valence, and terrestrial rocks, including basalts, were assumed to have approximately chondritic Zr/Hf ratios (~ 36.3 to 37.1; Sun and McDonough 1989; McDonough and Sun 1995; David *et al.* 2000; Huang *et al.* 2011). However, Zr is fractionated from Hf during mantle melting with clinopyroxene ± garnet ± spinel in the residue ($D_{Zr[grt]} > D_{Zr[cpX]} > D_{Zr[sp]}, D_{Zr/D_{Hf[grt]} > D_{Zr/D_{Hf[sp]} > D_{Zr/D_{Hf[cpX]}}$; Lundstrom *et al.* 1998; Klemme *et al.* 2002; Kelemen *et al.* 2003), and during mineral accumulation processes (David *et al.* 2000; Pfänder *et al.* 2007; Aulbach *et al.* 2011). Therefore, the addition of Zr and Hf as monitors during melting may indicate whether partial melting in the eclogite facies is responsible for both the REE_N patterns as well as the Zr/Hf and Zr/Y ratios of the Group II eclogites (Figures 4.5 and 4.7).

For this modeling I use conditions as described by Shu *et al.* (2018), starting with an N-MORB trace-element composition (Sun and McDonough 1989) and eclogite mineralogy (50 % garnet, 50 % clinopyroxene), with equal mineralogical contribution to the melt. I use the mineral-melt partition coefficients from Green *et al.* (2000) determined for the assemblage garnet-clinopyroxene-melt. Consistent with the findings of Shu *et al.* (2018), LREE are fractionated from HREE in the modeled residues during non-modal fractional melting under these conditions (Figure 4.12A) but due to abundant garnet which retains Zr in the residue, Zr/Hf ratios in the modeled residues increase rather than decrease, and therefore the residue compositions do not overlap most whole-rock Group II eclogite compositions (Figure 4.12C). Therefore, the extraction of melt from N-MORB causes the residue REE_N patterns to approach the shape of the median Group II eclogite REE_N patterns, principally the LREE depletion and HREE enrichment.

However, it cannot also account for the whole-rock Zr/Hf ratios, based on the trajectory of residue Zr/Hf ratios during melting.

Given that garnet has a higher D_{Zr}/D_{Hf} ratio than clinopyroxene and therefore exerts a strong control on residue Zr/Hf ratios during melting, I also consider a hypothetical extreme endmember scenario to assess the trajectory of Zr/Hf ratios in residues during melting. For this, I consider a rock with a starting composition of N-MORB for simplicity, but with a mineralogy of 20 % garnet and 80 % clinopyroxene, much lower than the $\sim 1:1$ present day ratios in the Group II eclogites. This is conducted only to assess the broad effect of a diminished garnet mode on the change in residue REE_N pattern shape and Zr and Hf composition during melt extraction. Under these modified conditions, LREE are still fractionated from HREE (Figure 4.12B). The modeled residue compositions evolve from the N-MORB composition toward lower Zr abundances and Zr/Hf ratios, and begin to approximate the compositions of whole-rock Group II_L eclogites (Figure 4.12C). However, this requires garnet:clinopyroxene ratios ($\sim 1:3$ to $1:4$) far below the observed $\sim 1:1$ ratio, and therefore does not appear to be a suitable mechanism to explain the whole-rock compositions of the Group II_L eclogites.

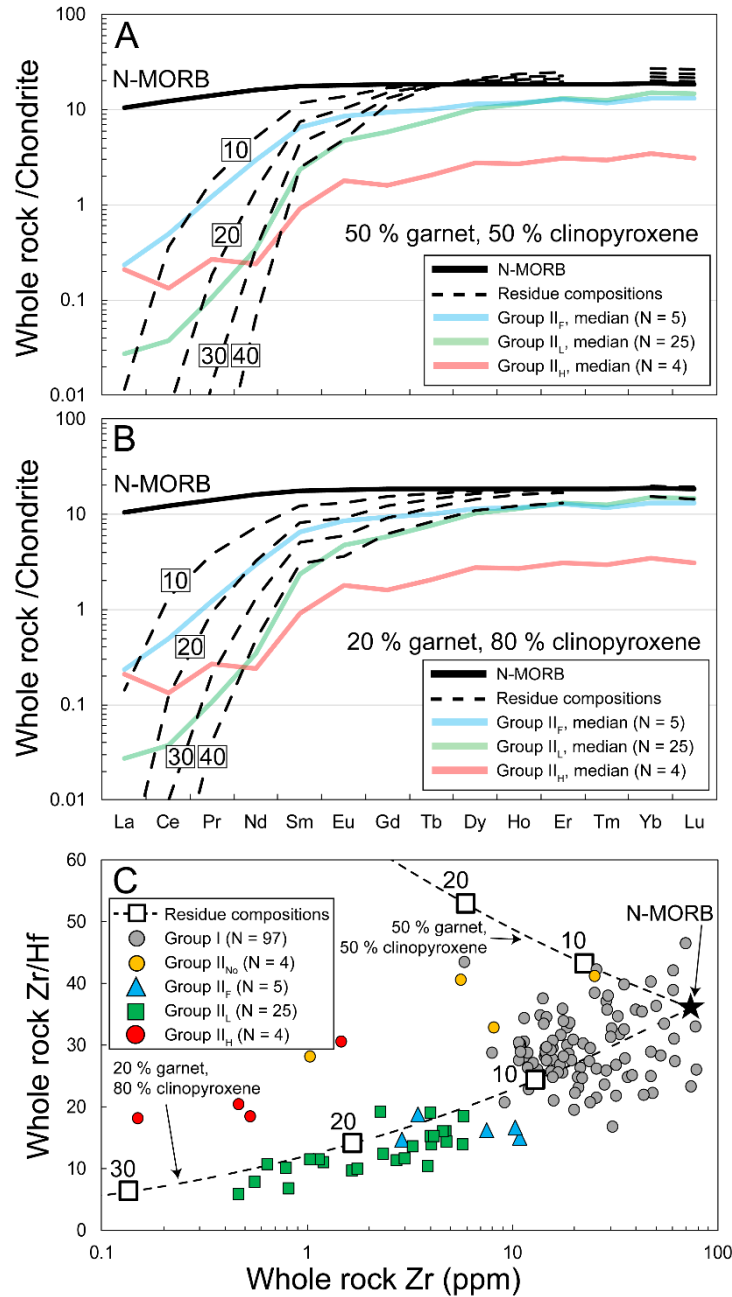


Figure 4.12 Bulk REE_N patterns (dashed lines) for melting residues with an N-MORB starting composition (Sun and McDonough 1989) after eclogite-facies non-modal fractional melting. To explore the effect of residue mineralogy, calculations are conducted for residues with A) 50 % garnet, 50 % clinopyroxene (preferred case), and B) 20 % garnet, 80 % clinopyroxene (as an extreme endmember scenario). $D_{cpx/melt}$ and $D_{grt/melt}$ are from Green *et al.* (2000). Median REE_N patterns for Groups II_L, II_H, and II_F eclogites are shown for comparison. Extent of partial melting is indicated with a number (%) adjacent to residue compositions. C) The Zr abundance and Zr/Hf ratio of the modeled residues during melt extraction under the same conditions as A and B. Data are compared with eclogite compositions in this study (N = 64) and the literature (N = 71).

The combination of LREE depletion and low Zr/Hf ratios in some of the Group II eclogites (e.g., Group II_L eclogites) is also not achieved by modeling the melting of eclogite protoliths, such as rocks with starting bulk compositions and mineralogy corresponding to deeper levels of oceanic crust (e.g., layered and non-layered gabbros). Partial melting of model oceanic gabbro (e.g., Smart *et al.* 2017) results in a systematic decrease in all REE, including HREE, and does not reproduce the median Group II_L, II_H, or II_F eclogite REE_N patterns at Roberts Victor. Barth *et al.* (2002) and Smart *et al.* (2017) modeled partial melting of basalt, and their results demonstrate that partial melting of model oceanic basalt does not reproduce the combination of LREE-depleted REE_N patterns and low Zr/Hf ratios seen in Group II eclogites at Roberts Victor. Specifically, fractionation of Zr from Hf is not significant during melting of basalt, and modeling by Barth *et al.* (2002) indicates development of significant negative Sr/Sr* in residues whereas strong positive Sr/Sr* are present in Roberts Victor Group II eclogites (Figure 4.6; Section 4.6.3.1.3). During melting of garnet amphibolite to generate TTG (i.e., Foley *et al.* 2002), amphibole tends to have D_{Zr}/D_{Hf} ratios less than unity (Tiepolo *et al.* 2001) so its extraction, particularly at high melting extents, should tend to increase the Zr/Hf ratio in residues, particularly if garnet is also residual. Loss of garnet during melt extraction should develop negative Sr/Sr* in the residues (Barth *et al.* 2002).

The use of N-MORB as the starting bulk composition in the modeling of eclogite melting is a generalisation considering the wide range of whole-rock REE_N compositions for eclogites from Roberts Victor, and possibly the variation in the MORB composition through time. However, one of the primary controls on Zr/Hf ratios in residues during melt extraction is the garnet:clinopyroxene ratio. Substitution of a different starting bulk trace-element composition with the eclogite mineral modes in Group II eclogites does not change the overall trajectory of

the Zr/Hf ratios in the residues, which increase during eclogite-facies melting, rather than decrease. Therefore, based on these findings I find it difficult to account for the combined HFSE and REE composition of Group II eclogites by partial melting either of eclogite, or its possible oceanic protoliths.

4.6.3.1.3 Additional considerations

Several elemental characteristics of Group II eclogites further contradict that the incompatible element depletions of Group II eclogites are due solely to partial melt extraction during subduction or in the mantle, either from the eclogites or their protoliths. Within the Group II_L eclogites, whole-rock Sr-anomalies ($[\text{Sr}/\text{Sr}^*]_{\text{N}}$) are correlated negatively with Nd_{N} in a similar direction to Group I eclogites, as well as to troctolite compositions from Pito Deep, southeast Pacific Ocean (Figure 4.13A; Perk *et al.* 2007). The enrichment of Sr relative to LREE is a plagioclase signature (Schiavi *et al.* 2015, and references therein), and positive $(\text{Sr}/\text{Sr}^*)_{\text{N}}$ are present in Group II_L, II_H, and II_F eclogites despite having more than an order of magnitude lower average Sr and LREE than Group I eclogites (Table C.10). Instead, the variation in $(\text{Sr}/\text{Sr}^*)_{\text{N}}$ and Nd_{N} could have developed during magmatic evolution by precipitation of plagioclase-rich cumulates from an incompatible-element-poor parental magma, hence possibly represents a protolith signature that was not obliterated in the course of secondary melt extraction (Barth *et al.* 2002). Whole-rock Mg# and Ni are also correlated in a direction suggestive of magmatic evolution that is similar to Mg# and Ni variation in troctolites from Pito Deep (Figure 4.13B; Perk *et al.* 2007).

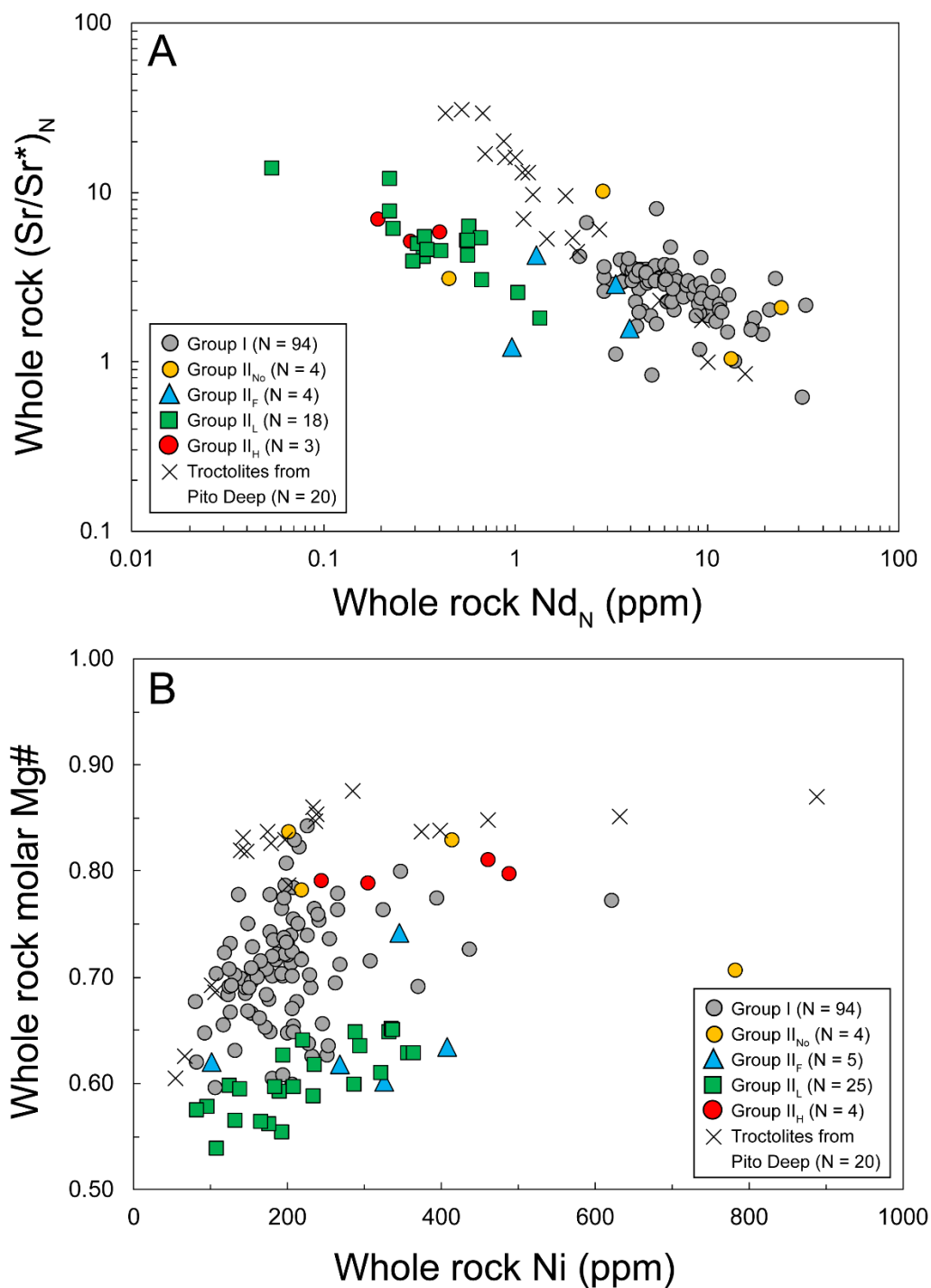


Figure 4.13 Reconstructed whole-rock Roberts Victor eclogite compositions. (A) Sr-anomalies ($[\text{Sr}/\text{Sr}^*]_N$, $\text{Sr}^* = 0.5 \times [\text{Pr}_N + \text{Nd}_N]$) and Nd_N , normalised to chondrite (McDonough and Sun 1995), as well as (B) molar Mg# ($\text{Mg}/[\text{Mg} + \text{Fe}]$) and Ni (ppm). Eclogite data are from this study ($N = 64$) and the literature ($N = 123$ for A, $N = 132$ for B). Data are compared with whole-rock compositions of oceanic crust troctolites from Pito Deep, southeast Pacific Ocean ($N = 20$; Perk *et al.* 2007).

Σ HREE versus Eu/Eu^* variation for Group II eclogites is also similar to that of Group I eclogites and Pito Deep troctolites (Figure 4.14); low-pressure oceanic rocks are expected to have an anti-correlated Σ HREE and Eu/Eu^* relationship (Aulbach and Jacob 2016). Group II eclogites also have higher Eu/Eu^* for a given Σ HREE than Group I eclogites (Figure 4.14): if Group II eclogites are melt residues from eclogites that had similar pre-melt REE_N compositions to Group I eclogites prior to subduction, then Group II eclogites should have lower Eu/Eu^* than Group I eclogites, as Eu/Eu^* decreases in residues during melting (Aulbach and Jacob 2016).

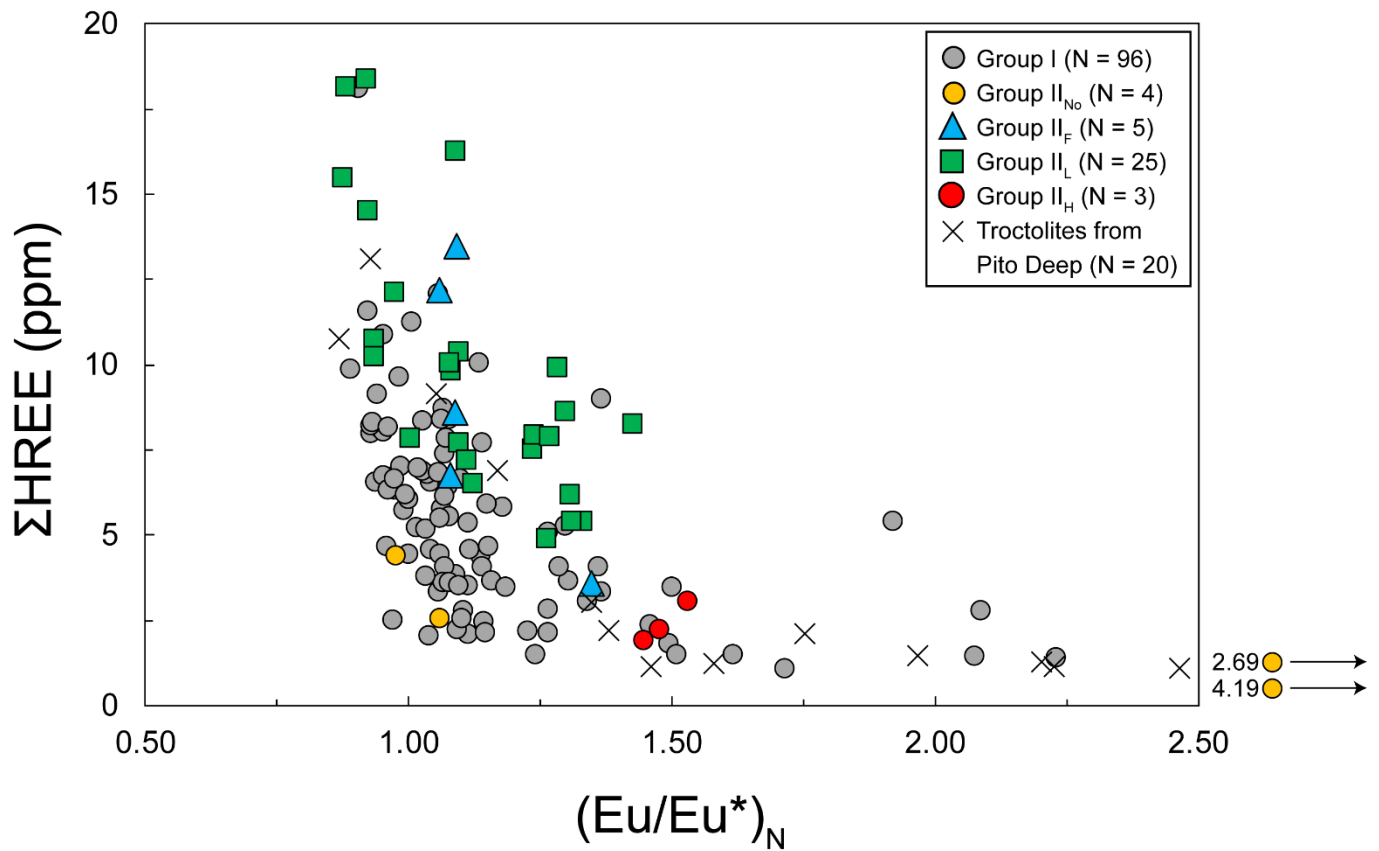


Figure 4.14 Reconstructed whole-rock Σ HREE (Tb to Lu, ppm) and $(\text{Eu}/\text{Eu}^*)_N$ ($\text{Eu}^* = 0.5 \times [\text{Sm}_N + \text{Gd}_N]$) normalised to C1 chondrite (McDonough and Sun 1995) for Roberts Victor eclogites. Eclogite data are from this study ($N = 64$) and the literature ($N = 69$). Two Group II_{No} eclogites have $(\text{Eu}/\text{Eu}^*)_N > 2.50$, shown outside the plot and indicated by arrows parallel to their Σ HREE values. Data are compared with whole-rock compositions of oceanic crust troctolites from Pito Deep, southeast Pacific Ocean ($N = 20$; Perk *et al.* 2007).

Based on this, I infer that Group I and II eclogites are not related to one another by partial melting. Further, I infer that the significant incompatible element depletion of the Group II eclogites is not solely due to melt extraction during subduction, assuming that their protoliths had initial REE_N patterns similar to Group I eclogites at the time of subduction (that is, following protolith formation as oceanic crust).

4.6.3.1.4 Summary

Group II eclogites have several chemical characteristics indicative of partial melt extraction, including extreme depletion of incompatible elements (LREE, TiO₂, Sr, HFSE) and positive MREE_N-HREE_N slopes, which have been shown to develop during partial melting of eclogite (Shu *et al.* 2018). However, the modeling in this study has demonstrated that both the LREE-depleted whole-rock REE_N patterns and low Zr/Hf ratios of the Group II eclogites cannot be achieved by partial melting under a variety of circumstances. During melting of model eclogite using present-day mineral modes (~ 1:1 garnet to clinopyroxene), Zr/Hf ratios in residues increase, so cannot explain some of the very low Zr/Hf ratios (~ 5) of some Group II_L eclogites. Several systematic chemical variation trends for the Group II_L eclogites – between Eu/Eu* and Σ HREE, (Sr/Sr*)_N and Nd_N, and Ni and Mg# (Figures 4.13 and 4.14) – are more consistent with characteristics developed during mineral accumulation in a low pressure oceanic crust protolith, which were not attenuated by later partial melting.

4.6.3.2 Can Group I eclogites derive through metasomatism of Group II eclogites?

The interpretation that cratonic eclogites have in-situ igneous origins (e.g., O'Hara and Yoder 1967; Hatton 1978; Smyth *et al.* 1989; Caporuscio and Smyth 1990) has recently been augmented by a proposal that Roberts Victor Group I eclogites represent fluid/melt-

metasomatised Group II eclogites (Gréau *et al.* 2011; Huang *et al.* 2012a). In that model, the Group II eclogite suite crystallised as high-Al clinopyroxene-rich assemblages at the lithosphere-asthenosphere boundary from upwelling magma (Gréau *et al.* 2011; Huang *et al.* 2012a). The Group II eclogites were then metasomatised by carbonatitic-kimberlitic spectrum melts shortly before they were entrained by the Roberts Victor kimberlite, which materially overprinted sample textures, $\delta^{18}\text{O}$ values, incompatible element contents, and Ca-Fe-Mg chemistry to form the Group I eclogites. However, Gréau *et al.* (2011) and Huang *et al.* (2012a) argue that Group II to Group I metasomatism increased $\delta^{18}\text{O}$ values from values below the mantle range to above the mantle range, which is not supported by studies that demonstrate that $\delta^{18}\text{O}$ values outside of the canonical mantle range cannot be imposed upon eclogites in the mantle: significant fractionation of oxygen isotopes does not occur at mantle temperatures (Eiler 2001) and $\delta^{18}\text{O}$ in fluids is buffered by peridotitic mantle (i.e., Riches *et al.* 2016; Czas *et al.* 2018). Gréau *et al.* (2011) and Huang *et al.* (2012a) also fail to explain why the Group II eclogites, of mantle origin in their model, have $\delta^{18}\text{O}$ values below the canonical mantle range whereas values within the canonical mantle range are expected for a mantle origin.

Instead, the oxygen isotope characteristics of the Roberts Victor eclogites, which are dominantly outside of the canonical mantle range, can also be explained by the hydrothermal alteration of oceanic crust by seawater at temperatures $< 350\text{ }^{\circ}\text{C}$ (for $\delta^{18}\text{O}$ above the canonical mantle range) and $< 350\text{ }^{\circ}\text{C}$ (for $\delta^{18}\text{O}$ values above the canonical mantle range). These $\delta^{18}\text{O}$ values were preserved upon metamorphism of the oceanic crust to eclogite during subduction. The distribution of $\delta^{18}\text{O}$ values in the Roberts Victor eclogite suite outside of the canonical mantle range (Figure 4.8) is similar to $^{18}\text{O}/^{16}\text{O}$ distributions in Cretaceous ophiolites (Gregory and

Taylor 1981; Jacob 2004; Ickert *et al.* 2013). The oxygen isotope systematics of the Roberts Victor eclogites are addressed in more detail in Section 4.6.1.

Gréau *et al.* (2011) and Huang *et al.* (2012a) further argue that the carbonatite-kimberlite metasomatic overprint changed the elemental chemistry of the Group II eclogites, principally increasing incompatible element contents and modifying whole-rock Fe-Ca-Mg compositions, and introduced a range of accessory minerals including kyanite, rutile, and occasionally diamond. In contrast, Radu *et al.* (2019) ascribed the chemical variation of the Group II eclogites to magmatic differentiation processes in oceanic crust, indicating that they can be associated with lavas and cumulates formed at oceanic spreading ridges. Based on this, I find no clear evidence that Group I eclogites formed by metasomatic overprinting of Group II eclogites.

4.6.4 Chemical characteristics of the Roberts Victor eclogite protoliths

4.6.4.1 Chemical relationship between the Group I and Group II eclogites

I propose that the protoliths of the Roberts Victor Group II eclogites precipitated as oceanic crust from a parental magma that was chemically less-enriched than the magma that precipitated the Group I eclogite protoliths. In this model, the oceanic cumulates inherited their incompatible element depletion from their parental magma. A cumulate origin of the Group II eclogite protoliths is documented by variable whole-rock Sr- and Eu-anomalies (Figures 4.13A and 4.14) and elevated Na₂O contents (Figures 4.15A and 4.16A) indicating plagioclase-rich cumulates precipitating from a magma. This is supported by Group II garnet $\delta^{18}\text{O}$ values below the canonical mantle range (Figure 4.8) that indicate protolith precipitation at depths ≥ 2 km in oceanic crust (Gregory and Taylor 1981; Schiavi *et al.* 2015).

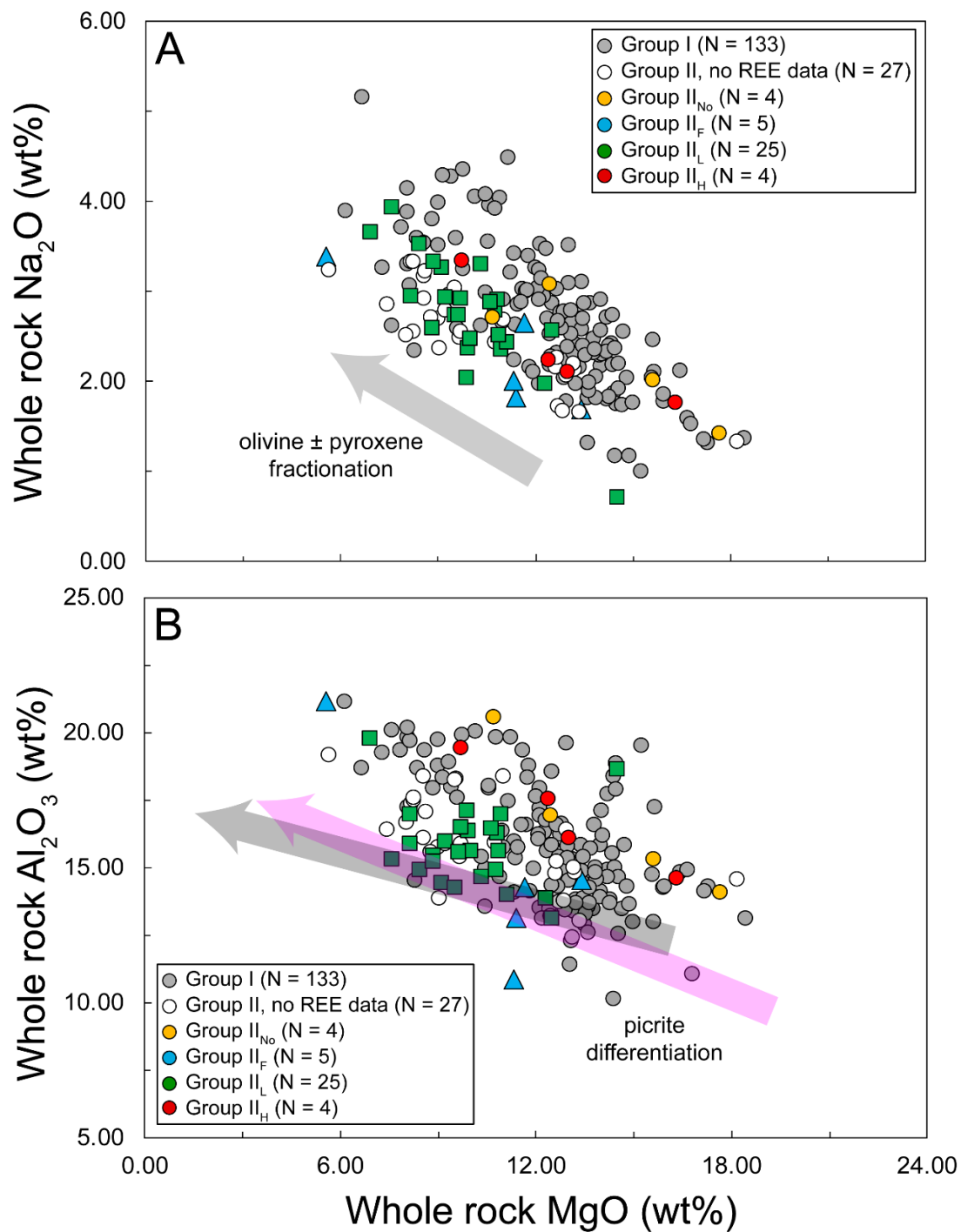


Figure 4.15 Reconstructed whole-rock Roberts Victor eclogites from this study (N = 65) and the literature (N = 133). A) Reconstructed whole-rock Na_2O (wt%) versus MgO (wt%). Vector is from Radu *et al.* (2019) and indicates expected magma evolution in response to mineral fractionation. B) Reconstructed whole-rock Al_2O_3 (wt%) versus MgO (wt%). Vectors are after Smart *et al.* (2014), based on data from Eggins (1993) and Alonso-Perez (2006), and correspond to the expected evolution of a differentiating picritic magma.

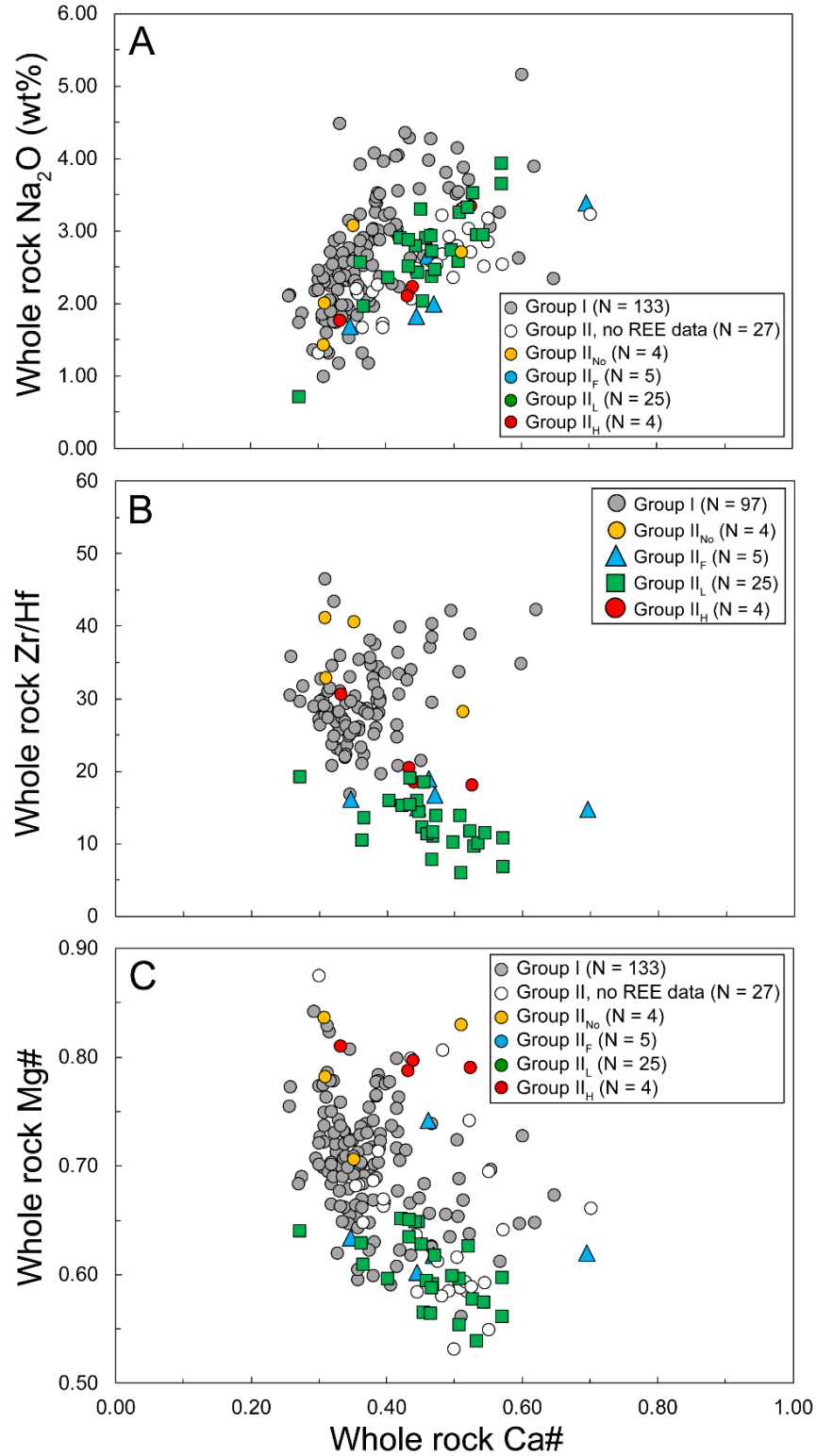


Figure 4.16 Reconstructed whole-rock molar Ca# ($\text{Ca}/[\text{Ca}+\text{Mg}]$) for Roberts Victor eclogites relative to (A) Na_2O (wt%), (B) Zr/Hf ratios, and (C) molar Mg# ($\text{Mg}/[\text{Mg}+\text{Fe}]$). Data are from this study (N = 65 for A and C; N = 64 for B) and the literature (N = 133 for A and C; N = 71 for B).

However, when compared with the Group I eclogites both the Group II_L and II_H eclogites have much lower whole-rock incompatible element contents including LREE, Sr, TiO₂, and HFSE (Figures 4.5, 4.6, and 4.7; Table C.10), including for samples with the same whole-rock FeO/MgO ratio (oxide wt%; Figure 4.17). The Group II_L and II_H eclogites define scattered arrays in plots of TiO₂ against FeO/MgO and V against Ti/1000 that document lower TiO₂ contents in Group II than in Group I eclogites (Figures 4.17 and 4.18; Shervais 1982). However, all reconstructed Roberts Victor eclogites based on garnet- and clinopyroxene-only have negative Ti anomalies when normalized to primitive upper mantle (McDonough and Sun 1995; Figure 4.6). This includes large Group I eclogite samples that are clearly rutile-free, suggesting that the negative Ti-anomalies might be a feature of the mantle source region for the protoliths of many Roberts Victor eclogites, Group I eclogites included (i.e., Aulbach and Jacob 2016).

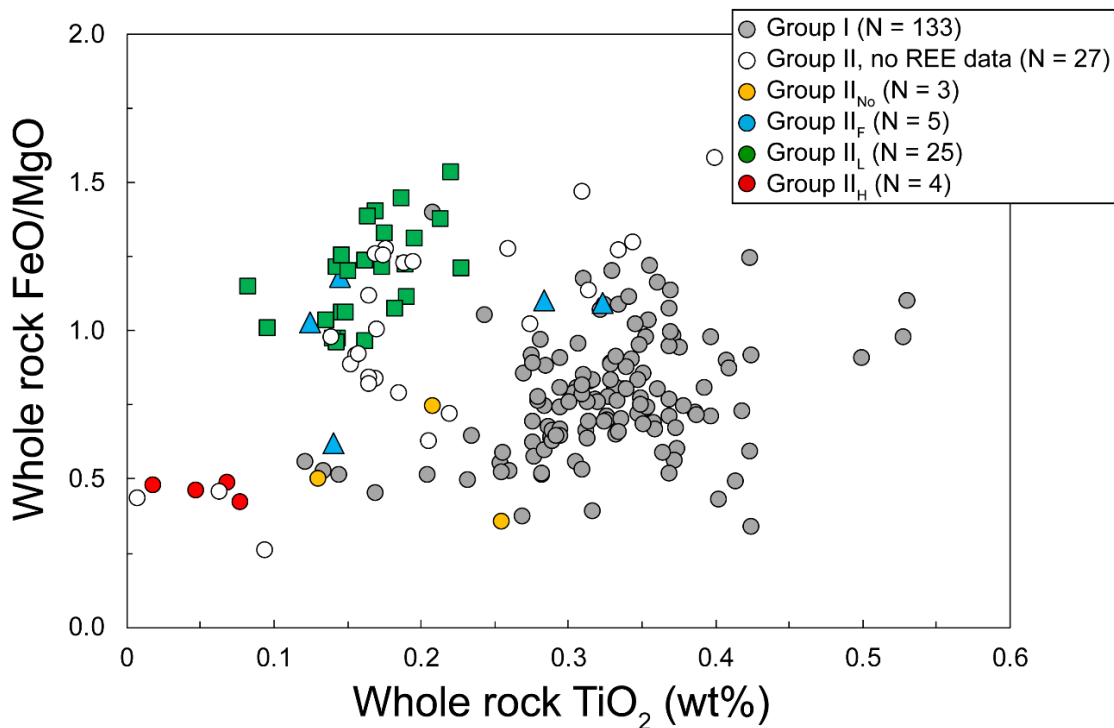


Figure 4.17 Reconstructed whole-rock TiO₂ (wt%) and FeO/MgO (oxide wt%) ratios for Roberts Victor eclogites. Data are from this study (N = 65) and the literature (N = 132).

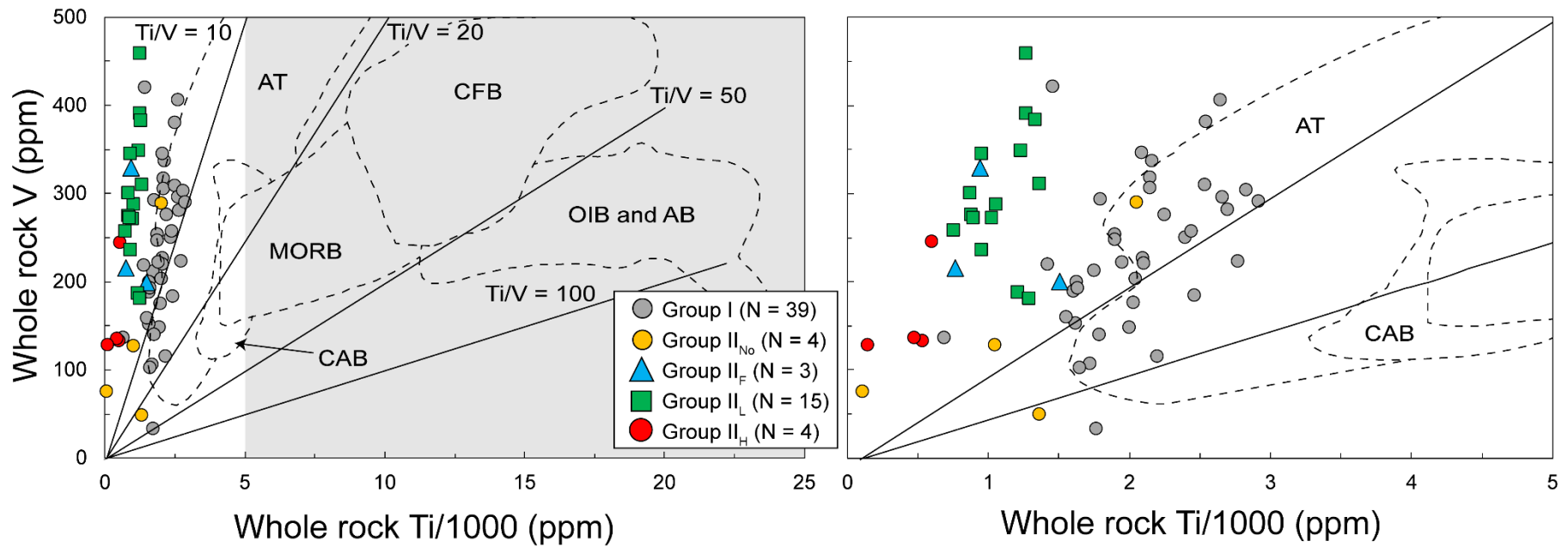


Figure 4.18 Reconstructed whole-rock V (ppm) and Ti/1000 (ppm) contents for Roberts Victor eclogites. Data are from the literature (N = 65). The white box in the left figure is shown in the right figure with a reduced Ti/1000 axis. Fields in the V vs Ti/1000 plot are from Shervais (1982). Abbreviations: AB = alkaline basalt, AT = arc tholeiite, CAB = calc-alkaline basalt, CFB = continental flood basalt; MORB = mid ocean ridge basalt; OIB = ocean island basalt.

Thin section study of Group II eclogites in this study does not reveal discrete rutile that might have been excluded from the whole-rock reconstructions, but does indicate low volume (< 1 vol%) rutile needles within silicates (Figures 4.2B, 4.2C, and 4.2D) that are reported to have low Zr/Hf ratios and Σ HFSE similar to their host silicates (Jacob *et al.* 2005). Therefore, even if the low volume of needles are added into whole-rock reconstructions, the whole-rock will still have negative Ti-anomalies and lower HFSE, TiO₂, and Zr/Hf ratios than Group I eclogites (see also Schmickler *et al.* 2004). Intergranular rutile and Ti-rich amphibole are inferred to be secondary due to lack of textural equilibrium with garnet and clinopyroxene (Figure 4.2F).

An alternative explanation for the low TiO₂ contents in Group II eclogites is melt extraction. TiO₂ is a moderately incompatible element, so FeO/MgO ratios and TiO₂ contents will both decrease in residues during melting (Figure 4.17; Prytulak and Elliott 2007). The low TiO₂ and HFSE contents of Group II eclogites at Roberts Victor have previously been ascribed to partial melt extraction (Jacob *et al.* 2005). Therefore, to assess the possibility that the low TiO₂ contents of Group II eclogites compared with Group I eclogites (Figures 4.17 and 4.18) reflect primary protolith chemistry rather than melt depletion during subduction, I note that Group II_L eclogites define a scattered negative correlation between FeO/MgO and Zr/Hf ratios (Figure 4.19). Residues are expected to have decreasing FeO/MgO ratios during melt extraction. Since Group II_L eclogites define a negative correlation between FeO/MgO and Zr/Hf ratios, this implies that Zr/Hf ratios are increasing in residues during melting. However, the Group II_L eclogites with the highest Zr/Hf ratios have the highest relative Zr abundances of the Group II_L eclogites (Figure 4.7), which is inconsistent with a melting scenario.

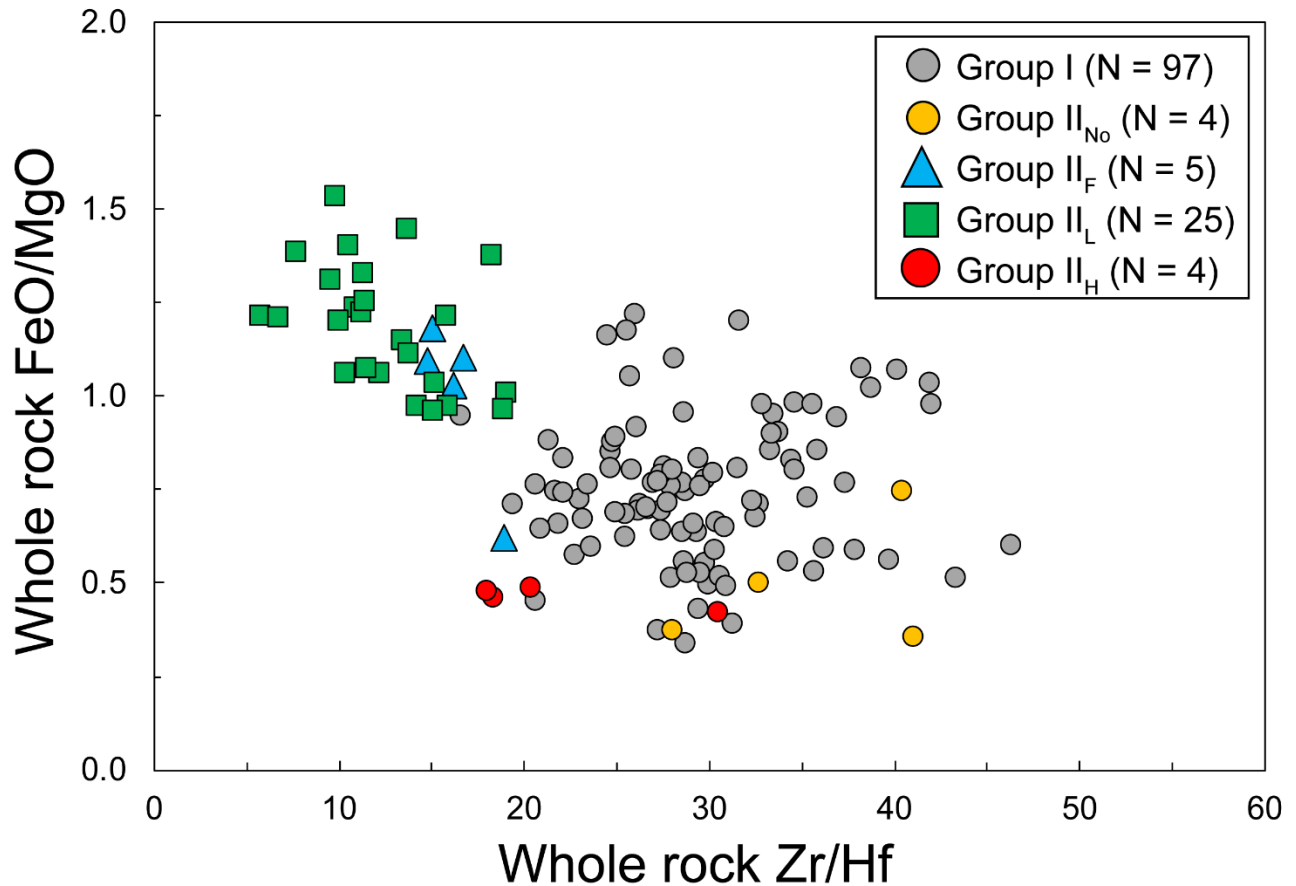


Figure 4.19 Reconstructed whole-rock Zr/Hf and FeO/MgO ratios of Roberts Victor eclogites. Data are from this study (N = 64) and the literature (N = 71).

Additional mechanisms to reduce the TiO₂ and HFSE budget of the Group II eclogites are the loss of rutile or zircon by melting. However, rutile has only marginally lower D_{Zr} than D_{Hf} (Foley *et al.* 2000) which would make rutile removal during melting unlikely to account for the very low Zr/Hf ratios of some Group II_L eclogites (Figure 4.7). The Group II eclogites may have instead lost zircon by melting. However, zircon-bearing mantle eclogites are comparatively rare in the literature (e.g., V. Grib and Jericho; Heaman *et al.* 2002, 2006; Shchukina *et al.* 2018) and the zircon has been inferred to be mostly metasomatic in origin (Shchukina *et al.* 2018). If Zr/Hf ratios decrease in the residue due to zircon extraction, then FeO/MgO ratios are expected to decrease, whereas they are increasing (Figure 4.19).

Instead of Group II eclogites having a reduced TiO₂ and HFSE budget due to melt extraction during subduction, I infer that their protoliths were cumulates with lower bulk TiO₂ contents than the protoliths of the Group I eclogites. TiO₂ is moderately incompatible during melting of peridotite (Prytulak and Elliott 2007) so successive melt increments of a peridotitic source (i.e., depleted MORB mantle) will be increasingly depleted in TiO₂. Accordingly, low TiO₂ is a characteristic of second-stage melts that are extracted from residual peridotite (Pearce and Reagan 2019). Back-arc basin (BAB) basalts are reported to have lower TiO₂ contents than MORB, which has been attributed to different degrees of chemical depletion in the source regions for the different basalt types (Gale *et al.* 2013). Decreased TiO₂ and ΣHFSE in Group II eclogite protoliths could, therefore, be inherited from the parental magma. The offset distributions of the Group I and Group II eclogites in V vs Ti/1000 documents independent evolution of the eclogite protoliths. This inference satisfies the preserved trends related to whole-rock Sr/Sr* and Eu/Eu* (Figures 4.13A and 4.14) that reflect mineral accumulation from a fractionating magma, as these trends may be obliterated during high degrees of melt extraction (Section 4.6.3.1.3).

4.6.4.2 The magmatic sources of the Group II_L and Group II_H eclogites

In this section I attempt to decipher the protoliths of – primarily – the Group II_L and II_H eclogites at Roberts Victor, as they are relatively more abundant than the Group II_{N₀} and II_F eclogites. One of the most striking differences between the Group II_L and II_H eclogites is their FeO/MgO (oxide wt%) ratios, documented by a clear separation between the suites in whole-rock FeO/MgO versus SiO₂ (Figure 4.20) and MgO versus FeO (Figure 4.21). However, despite the clear difference in FeO and MgO the whole-rock REE_N pattern shapes of the Group II_L and II_H

eclogites are very similar to each other, with the exception that the Group II_L eclogites have higher whole-rock Σ REE (Figure 4.5).

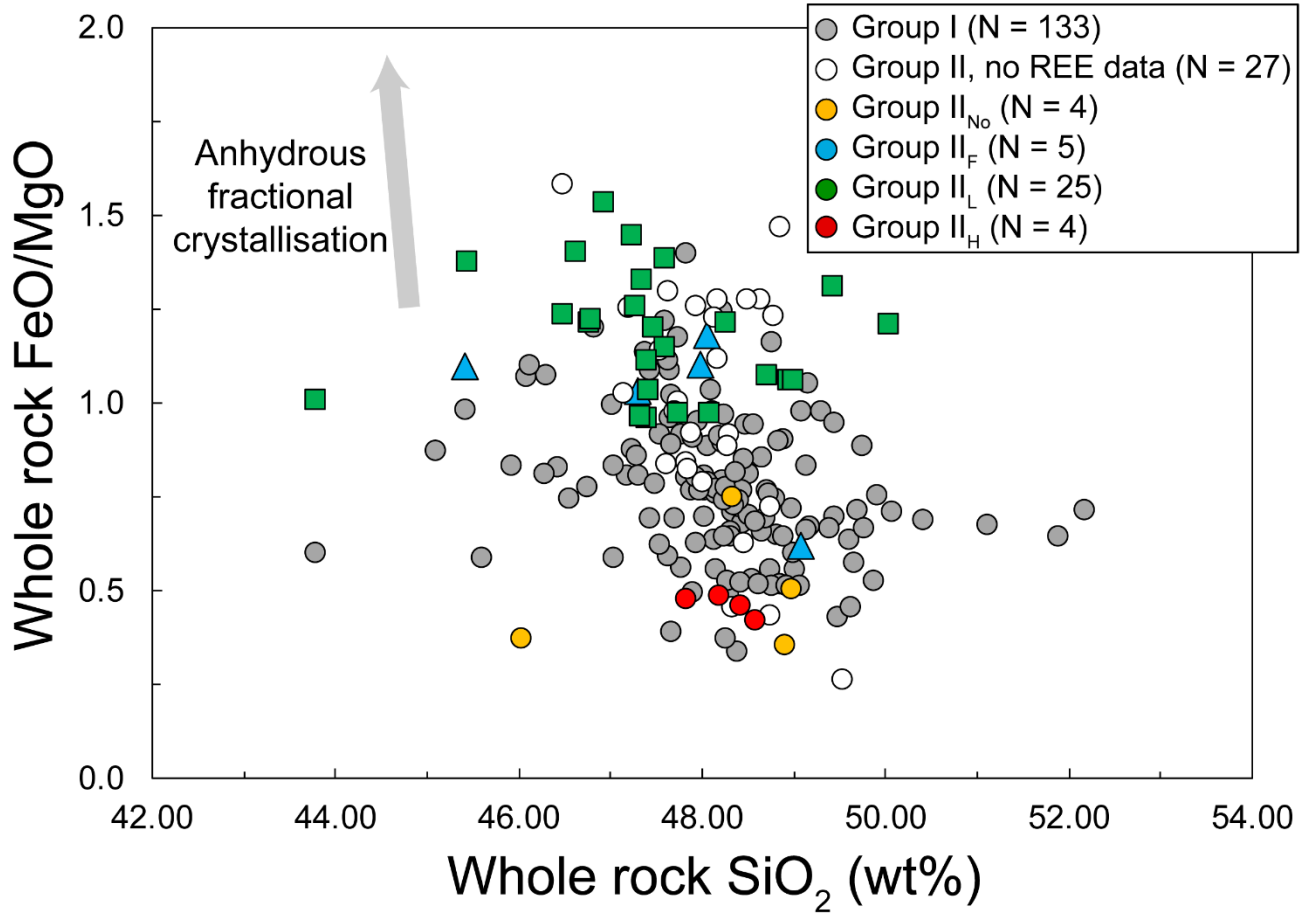


Figure 4.20 Reconstructed whole-rock FeO/MgO ratios and SiO₂ (wt%) of Roberts Victor eclogites. Data are from this study (N = 65) and the literature (N = 133). Vector is from Grove *et al.* (2003) and indicates the expected evolution of a magma via anhydrous fractional crystallisation at low pressures.

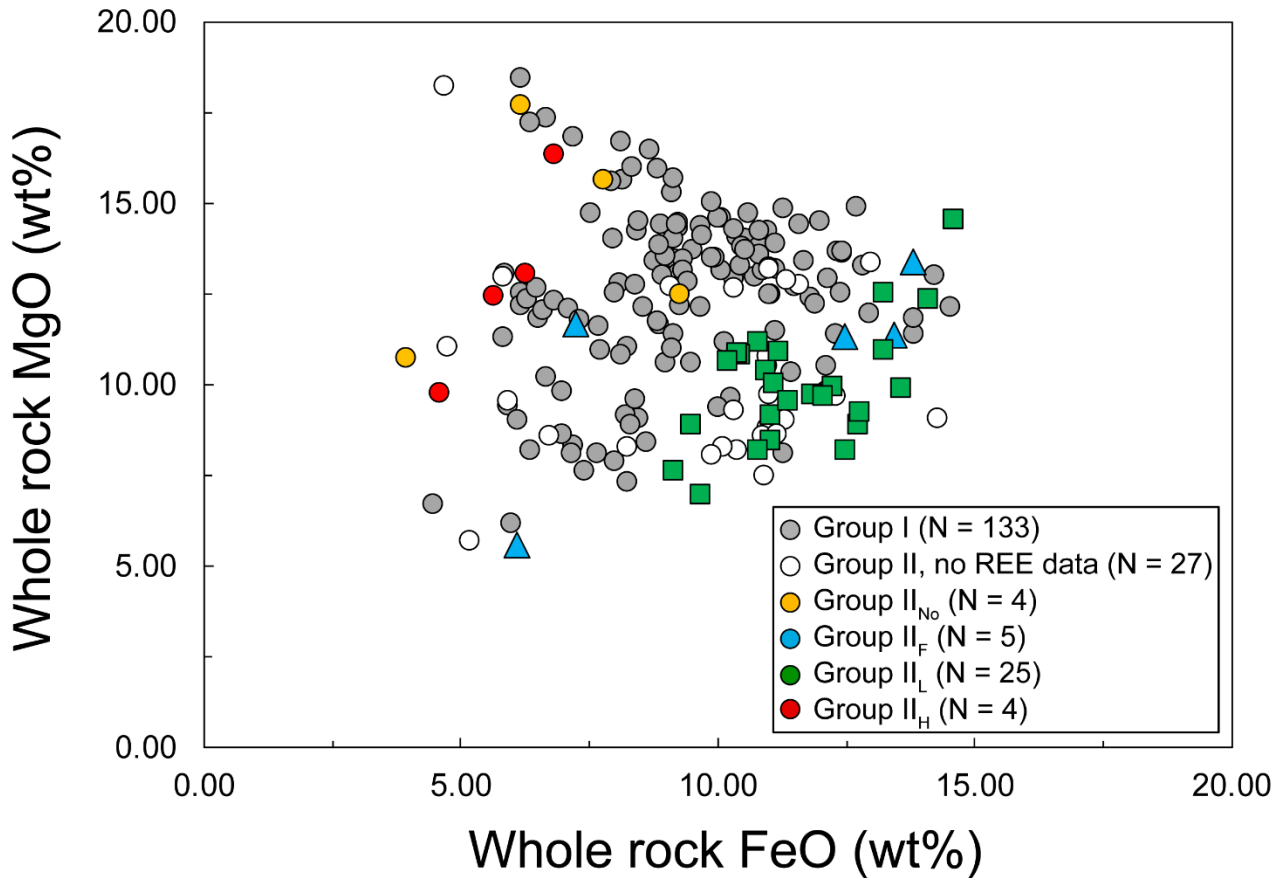


Figure 4.21 Reconstructed whole-rock MgO (wt%) and FeO (wt%) contents of Roberts Victor eclogites. Data are from this study (N = 65) and the literature (N = 133).

The Group II_L eclogites also have marginally higher whole-rock Na₂O, TiO₂, and Sr contents (Figures 4.15A, 4.16A, 4.17, and 4.18; Table C.10). These chemical differences may be explained by the protoliths of the Group II_L eclogites having precipitated as cumulates (containing at least plagioclase) from a magma that had fractionated more olivine than the magma that precipitated the Group II_H eclogite protoliths – resulting in lower Mg# and relatively higher incompatible element contents for the Group II_L eclogite protoliths. This is also apparent based on whole-rock Al₂O₃ and MgO contents, with Group II_L and II_H eclogites offset from one another in a direction corresponding to picrite differentiation (Figure 4.15B). The Group II_H eclogite protoliths may have crystallised when the magma was relatively olivine-saturated

(resulting in low ΣREE , FeO/MgO ratios, and TiO₂) and the Group II_L eclogite protoliths may have precipitated following olivine fractionation from the magma, which retained the whole-rock REE_N pattern shape but with increased ΣREE , FeO/MgO ratios, and TiO₂ contents (Figures 4.5, 4.17, and 4.20; Table C.10). This inference is broadly in-line with the interpreted evolution of MORB magmas by olivine fractionation (Falloon and Green 1988; Hess 1992).

The low incompatible element contents of Group II eclogites compared with Group I eclogites were discussed in Section 4.6.4.1. It was proposed that the low incompatible element contents of the Group II eclogites may be a function of cumulate chemistry inherited from their parental magma, rather than caused by melt extraction during subduction. In this section, I propose that the variation in Zr/Hf ratio for the Group II_L eclogites is better explained by clinopyroxene accumulation in their protoliths than by partial melt extraction of the eclogites during subduction. This is based on the low $D_{\text{Zr}}/D_{\text{Hf}}$ (~ 0.50) of clinopyroxene relative to other cumulate minerals (Hart and Dunn 1993; Kelemen *et al.* 2003; Section 4.6.3.1.1). Precipitation of clinopyroxene from a magma may influence cumulate Zr/Hf ratios if it crystallises in moderate abundance (David *et al.* 2000). To assess the possibility of bulk composition in cumulate assemblages varying due to clinopyroxene precipitation, I address several key chemical variations amongst the Group II_L eclogites.

Firstly, the Group II_L eclogites with the lowest Zr abundances and Zr/Hf ratios have relatively higher TiO₂, Na₂O, Ca# (Ca/[Ca+Mg]), FeO/MgO ratios and Sr/Sr*, but lower ΣREE , FeO, MgO, and Ni than do the Group II_L eclogites with higher Zr abundances and Zr/Hf ratios (e.g., Figures 4.16B and 4.19). I infer from this that the protoliths of Group II_L eclogites with the lowest Zr abundances and Zr/Hf ratios were plagioclase- and clinopyroxene-bearing cumulates (with undetermined modal abundance) that precipitated earliest from the parental magma. The

co-precipitation of plagioclase and clinopyroxene in the cumulate protoliths of the Group II_L eclogites is recorded by lower whole-rock MgO contents for a given Na₂O than Group I eclogites (Figure 4.15A) as well as higher whole-rock Ca# for a given Na₂O content than Group I eclogites (Figure 4.16A). The Group II_L eclogites with the lowest Zr/Hf ratios have the lowest incompatible element contents (low Σ REE, Zr, and Hf), FeO, and MgO contents, but the highest Na₂O, Ca#, Eu/Eu*, and Sr/Sr* compared with the other Group II_L eclogites. This suggests the combined precipitation of plagioclase (based on Eu/Eu*, Sr/Sr*, Na₂O) and clinopyroxene (Zr/Hf ratio variation within the Group II_L eclogites) – though with undetermined relative proportions – resulting in relatively low whole-rock FeO and MgO contents. As crystallisation of the magma proceeded, the relative abundances of plagioclase and clinopyroxene decreased in favour of more ferromagnesian-enriched minerals, likely olivine. This led to a systematic negative correlation between Ca# and Mg# (Figure 4.16C) and an increase in whole-rock FeO and MgO contents. Due to the crystallisation of olivine, a positive correlation between whole-rock Mg# and Ni and Mg# developed (Figure 4.13B), and whole-rock TiO₂ contents decreased due to the relative increase in olivine abundance (documented by a negative correlation between the whole-rock FeO/MgO ratio and TiO₂ content; Figure 4.17). As precipitation from the magma proceeded, the cumulate Zr abundance and Zr/Hf ratio increased and the cumulate Eu/Eu* and Sr/Sr* decreased, reflecting the reduced elemental input of clinopyroxene and plagioclase on the cumulate composition.

With respect to the Group II_H eclogites, they are characterised by low whole-rock Σ REE (Figure 4.7), moderately high positive Eu/Eu* and Sr/Sr* (Figures 4.13A and 4.14), low FeO/MgO ratios (Figures 4.17 and 4.20), and moderate Ca# (Figures 4.16). These chemical characteristics may be explained by the precipitation of Ca-rich plagioclase + olivine \pm clinopyroxene. The elevated

Zr/Hf ratios of the Group II_H eclogites relative to the Group II_L eclogites suggest that the parental magma for their protoliths had a different Zr/Hf ratio during cumulate precipitation.

4.6.4.3 Effects of pressure on mineral precipitation from magma

To better constrain the formation environment of the Group II eclogite protoliths, I consider the possibility that the protoliths of these rocks were crystallised at higher pressures in oceanic crust than suggested by ophiolites that are comparatively young (i.e., the Cretaceous-aged Samail Ophiolite). Pressure (corresponding to depth) is a control on crystallising mineral assemblage. Modern oceanic crust is approximately 7 km thick whereas during the Archean, oceanic crust has been estimated to have been ~ 21 km thick (Hynes 2014; Palin and Dyck 2018). Due to the fact that the Lu-Hf T_{DM} model ages for the Group II eclogites indicate at least a Paleoproterozoic age (Huang *et al.* 2012a), the Group II eclogite protoliths may have precipitated in thicker oceanic crust than modern ophiolites. In the An-Di-Fo system at 1 atm, a tholeiitic-picritic magma is expected to crystallise in the sequence olivine, olivine + plagioclase, and olivine + plagioclase + clinopyroxene (Shu *et al.* 2016; Presnall *et al.* 1978; Figure 4.22). This sequence represents a limiting case as oceanic cumulates will not crystallise at 1 atm. At higher pressures (7 kbar, ~ 20 km depth) the stability fields for clinopyroxene and spinel expand, and tholeiitic-picritic magma crystallises in the sequence olivine, olivine + spinel, olivine + spinel + clinopyroxene, and spinel + clinopyroxene + plagioclase (Figure 4.22).

The Group II_H eclogites are relatively uncommon but are characterised by moderate positive whole-rock Eu/Eu*, moderate Ca#, high Mg#, and relatively high Ni contents (Figures 4.13B, 4.14, and 4.16) which I ascribed in Section 4.6.4.2 to co-precipitation of plagioclase and MgO-

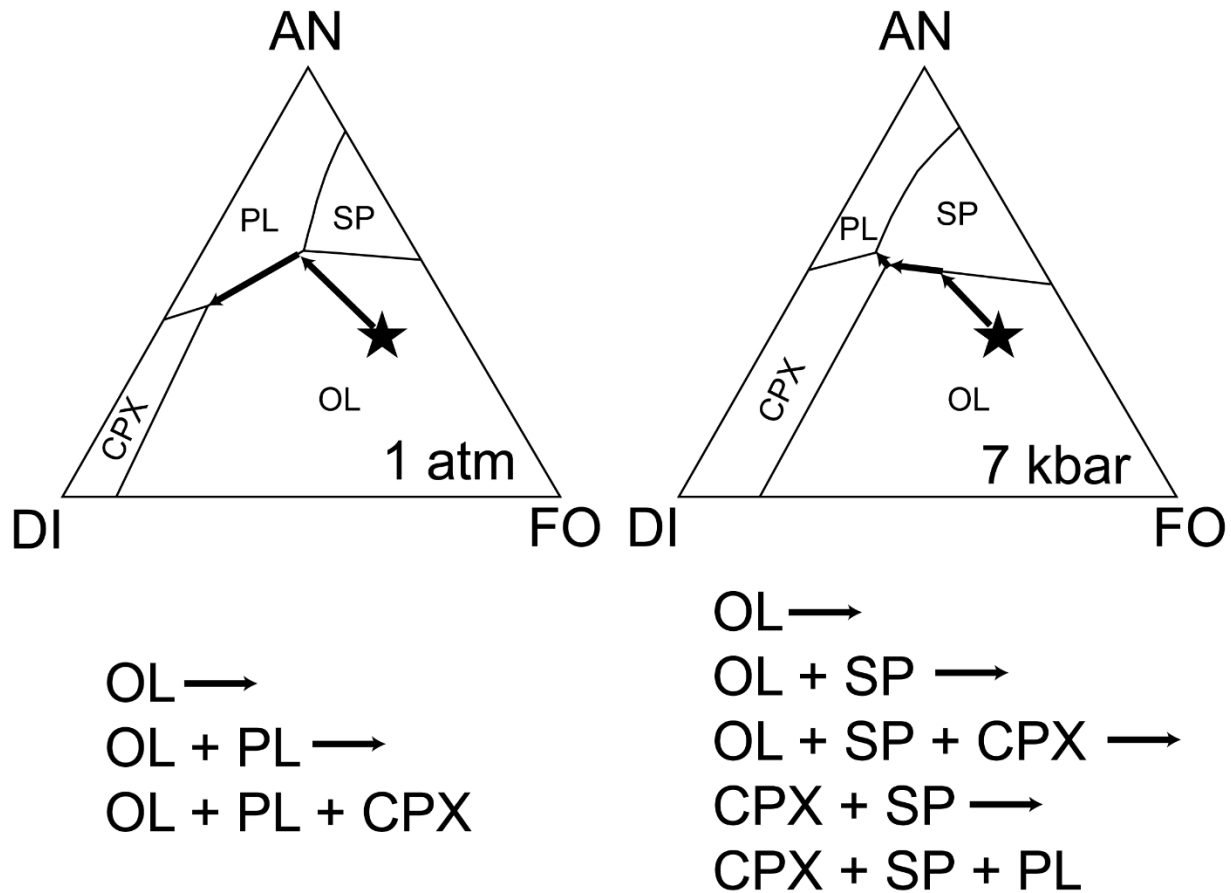


Figure 4.22 Schematic phase diagrams for crystallisation of basaltic-picritic magma (black star) in the Di-An-Fo system at 1 atm and 7 kbar pressure, simplified after Shu *et al.* (2016) and based on figures from Presnall *et al.* (1978) and Hess (1992). The expected crystallisation pathway for each pressure is indicated by thick black arrows, terminating at the eutectic composition at each pressure. The expected crystallisation sequence is indicated below each diagram. Abbreviations: AN = anorthite, CPX = clinopyroxene, DI = diopside, FO = forsterite, OL = olivine, PL = plagioclase, SP = spinel.

rich minerals such as olivine, or possibly clinopyroxene (troctolites to olivine gabbros; Shu *et al.* 2016). This favours their crystallisation at pressures < 7 kbar where olivine and plagioclase share a cotectic (Figure 4.22). The $\delta^{18}\text{O}$ values of the Group II_H eclogites are more equivocal indicators of their protolith precipitation depth. The $\delta^{18}\text{O}$ values are below the mantle range ($\delta^{18}\text{O} = 4.7$ and 4.8 ‰, N = 2), which indicates that their protoliths precipitated in oceanic crust deeper than at least ~ 2 km, though possibly much more deeply (~ 5 km or deeper): water/rock ratios tend to

decrease with stratigraphic depth, which will cause less-substantial decreases in the $\delta^{18}\text{O}$ values of the altered oceanic crust during hydrothermal alteration even at high temperatures ($> 350\text{ }^\circ\text{C}$).

The Group II_L eclogites are characterised by moderate whole-rock Ca#, elevated Na₂O, low Mg#, and variable Sr/Sr* and Eu/Eu* (ranging from positive to negative; Figures 4.13A, 4.14, and 4.16). The Group II_L eclogite whole-rock compositions have similar elemental trends to troctolites from Pito Deep, southeast Pacific Ocean (Figures 4.13A and 4.14; Perk *et al.* 2007). On this basis, in Section 4.6.4.2 I inferred that the cumulate protoliths of Group II_L eclogites comprised varying abundances of at least plagioclase + clinopyroxene + olivine. The inference of plagioclase + olivine co-precipitation implies protolith formation depths shallower than ~ 20 km. Shu *et al.* (2016) reported an eclogite from Bellsbank with an LREE-depleted whole-rock REE_N pattern similar to Group II_L eclogites at Roberts Victor. Those authors inferred that the protolith of the Bellsbank sample precipitated as a clinopyroxene-rich cumulate at ~ 20 km depth in oceanic crust, in part on the basis of negligible whole-rock Eu/Eu*. The low $\delta^{18}\text{O}$ values of the Group II_L eclogites ($\delta^{18}\text{O} = 1.8$ to $3.6\text{ }‰$, $N = 19$) also indicate that their protoliths may have precipitated at ~ 5 km depth or greater in oceanic crust (Rajmi locality, Samail Ophiolite; Stakes and Taylor 1992). This requires that seawater was able to percolate deeply enough and with sufficiently-high water/rock ratios to lower the $\delta^{18}\text{O}$ values of the oceanic crust below the canonical mantle range. Precipitation of the eclogite protoliths as deeply as 20 km in thick Archean crust, similar to the model of Shu *et al.* (2016), would require high seawater water/rock ratios at those depths. However, the penetration of seawater to depth is controlled in part by the brittle-ductile transition in oceanic crust, and lower Archean oceanic crust was likely ductile (Hoffman and Ranalli 1988; Carmody *et al.* 2013).—Further, based on the co-crystallisation of plagioclase and olivine inferred from the chemical trends for Group II_L eclogites and positive

Eu/Eu* (Figure 4.14), there does not appear to be a requirement for the Roberts Victor Group II_L eclogite protoliths to have formed in very deep (~ 20 km) oceanic crust.

4.6.4.4 Summary

The Group I and II eclogites have similar – though often offset – chemical trends (e.g., Figures 4.13, 4.14, 4.15, 4.16, 4.17, and 4.18). I infer the chemical differences to indicate that the parental magma that precipitated the Group II eclogite protoliths was depleted in incompatible elements compared with the magma that precipitated the Group I eclogite protoliths. However, the Group I and Group II eclogite protoliths may have each formed during magmatic evolution in oceanic crust. The Group II eclogites have significant incompatible element depletion relative to Group I eclogites, as well as, in the case of Group II_L eclogites, low Zr/Hf ratios. The combination of these chemical characteristics is not consistent with partial melt extraction during subduction, but can be explained by precipitation of Group II_L eclogite protoliths as cumulates of plagioclase + clinopyroxene + olivine. However, while in this section the effect of clinopyroxene on cumulate Zr abundance and Zr/Hf ratios is discussed, the Group II_L eclogites have lower Zr and Zr/Hf than Group I eclogites, and lower than the clinopyroxene in equilibrium with N-MORB (Figure 4.7). In the following section, mechanisms to crystallise clinopyroxene with lower Zr/Hf ratios than predicted for precipitation from N-MORB are discussed.

4.6.5 HFSE and REE systematics during melting of depleted MORB mantle

4.6.5.1 Overview

Mineral precipitation from magma to generate oceanic crust can explain major- and trace-element trends of the Group II_L eclogites (Section 4.6.4.2). While it is thought that oceanic crust is generated from MORB-like magmas (Johnson *et al.* 1990; Nonnotte *et al.* 2005), several

aspects of Group II eclogite compositions are inconsistent with a MORB-like magma origin. As discussed in Section 4.6.3.1.1, the clinopyroxene in equilibrium with N-MORB using $D_{\text{cpx/melt}}$ of Hart and Dunn (1993) has a higher Zr abundance and Zr/Hf ratio than most whole-rock Group II_L eclogites (Figure 4.7). Therefore, the parental magma of the Group II_L eclogite protoliths may have had a lower starting Zr abundance and Zr/Hf ratio than N-MORB, to accommodate the chemical variation in the Group II_L eclogite suite during cumulate precipitation.

To assess the origin of a magma that is chemically less-enriched than N-MORB (i.e., with a lower Zr abundance and Zr/Hf ratio), in this section I model the compositions of single-increment melts from “residual” mantle sources within the framework of MORB generation. In the context of Figure 4.23, residual mantle sources refer to upwelling DMM that has lost some melt during decompression. Upwelling DMM melts within the “mantle melt zone” and becomes increasingly depleted with progressive melt extraction (akin to abyssal peridotites, which underlie oceanic crust and are residual after MORB generation; Johnson *et al.* 1990; Warren 2016). Melts of the residual mantle source (i.e., residual DMM) will have lower incompatible element contents relative to earlier extracted melts, as the source is increasingly depleted (Aulbach *et al.* 2011, Basch *et al.* 2019). However, it has been shown that MORB magma generation is by near-fractional polybaric melting of DMM and that the melts may mix en route to the surface, generally approximating the composition of batch melting (Johnson *et al.* 1990). Therefore during decompression melting, melts of residual DMM may be mixed with other DMM melts, to produce approximately the MORB composition. To assess the composition of melts of residual mantle sources prior to possible homogenisation as MORB, I conduct non-modal fractional melt modeling of DMM to simulate melting of DMM in a natural system. I assess the composition of single-increment melts of residual DMM and compare them with the

composition of the aggregated MORB composition. Using the calculated melt compositions, I assess if mineral precipitation from the melts of residual mantle sources can better satisfy the HFSE and REE distribution of Group II eclogites than can mineral precipitation from N-MORB.

4.6.5.2 Modeling conditions

For this modeling I follow previous workers (e.g., Johnson *et al.* 1990; Hellebrand *et al.* 2002; Weyer *et al.* 2003; Marchesi *et al.* 2016; Warren 2016; Basch *et al.* 2019; Shervais *et al.* 2019) and model melt extraction from model spinel- and garnet-lherzolite. For the model spinel-lherzolite I use a starting mineralogy of 53 % olivine, 27 % orthopyroxene, 17 % clinopyroxene, and 3 % spinel (Johnson 1998). For the model garnet-lherzolite I use a starting mineralogy of 57 % olivine, 21 % orthopyroxene, 13 % clinopyroxene, and 9 % garnet (calculated by Hellebrand *et al.* 2002, after Johnson 1990 and Johnson *et al.* 1998). Bulk partition coefficients for spinel-facies melting are calculated using mineral-melt partition coefficients for clinopyroxene, orthopyroxene, olivine, and spinel compiled by Kelemen *et al.* (2003, and references therein). For clinopyroxene, Kelemen *et al.* (2003) compiled the partition coefficient values from Hart and Dunn (1993), and interpolated the $D_{\text{cpx/melt}}$ values for the elements Pr, Eu, Gd, Tb, Ho, and Tm using $D_{\text{cpx/melt}}$ values for the adjacent REE from Hart and Dunn (1993). For garnet-facies melting I use the mineral-melt partition coefficients for garnet, clinopyroxene, orthopyroxene, and olivine compiled by Donnelly *et al.* (2004, and references therein). For spinel-facies, the melting proportions are based on the reaction $0.56\text{opx} + 0.72\text{cpx} + 0.04\text{spl} = 0.34\text{ol} + 1.0\text{liq}$ (1.0 GPa; Wasylenki *et al.* 2003). For garnet-facies the melting proportions are based on the reaction $0.027\text{ol} + 0.492\text{grt} + 1.67\text{cpx} = 1.0\text{liq} + 1.18\text{opx}$ (2.8 GPa; Salters and Longhi 1999).

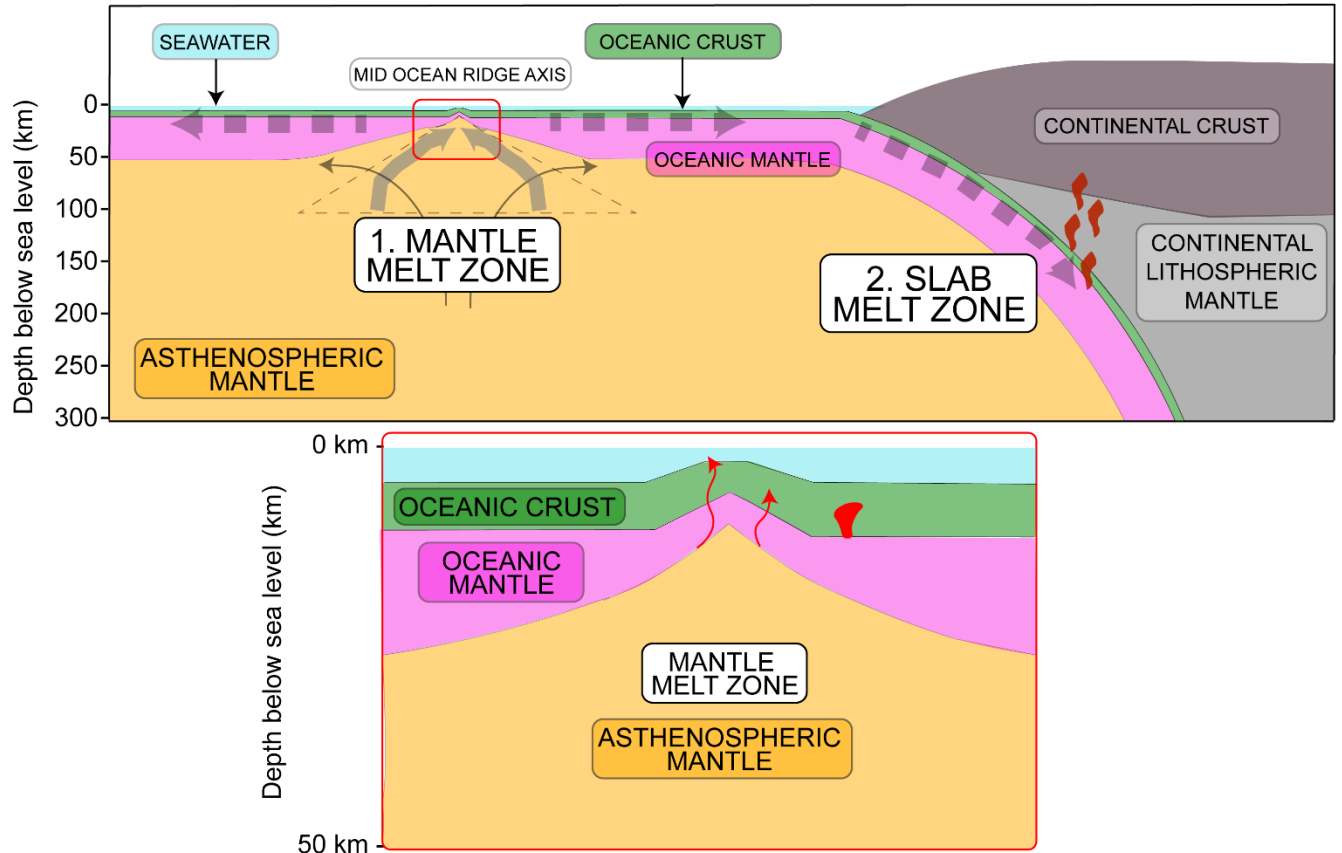


Figure 4.23 Top: Simplified schematic diagram overviewing the process of oceanic crust formation and oceanic slab subduction. (1) Upwelling asthenospheric mantle (depleted MORB mantle; DMM) melts during adiabatic decompression within a melt extraction zone (thin dashed line) – broadly defined as the “mantle melt zone.” Oceanic crust is generated at the mid ocean ridge axis under seawater, from magmas generated from DMM. The melts are channeled upward (grey arrows) to a mixing zone and broadly homogenised (~ MORB). The residual upwelling mantle underlying the crust is the suboceanic lithospheric mantle. Together the oceanic crust and underlying residual suboceanic lithospheric mantle comprise the oceanic slab. (2) Following formation of oceanic crust, the oceanic slab spreads from the mid ocean ridge (thick dashed arrows) and may subduct beneath either oceanic or continental (shown) lithosphere. During subduction the oceanic slab will dehydrate and/or melt, generating TTG/adakite-type melts – broadly defined as the “slab melting zone.” Bottom: Simplified schematic of the mid ocean ridge axis area showing possible sources for melts from DMM escaping homogenisation. These include melts that percolate upward through the oceanic mantle into oceanic crust, or diapirs from the suboceanic lithospheric mantle.

4.6.5.3 Fractional melt modeling

I have modeled non-modal fractional melt extraction from both model spinel-lherzolite and garnet-lherzolite, using the HFSE and REE as process monitors. Both starting rocks have a bulk trace-element composition of average DMM (Workman and Hart 2005). Melt modeling was conducted using the partition coefficients and mineral modes defined in Section 4.6.5.2. With respect to the elements Zr and Hf, the calculated residue compositions for melting of garnet-lherzolite and spinel-lherzolite are shown in Figures 4.24A and 4.24B, respectively. For the spinel-lherzolite, the residue compositions evolve toward lower Zr abundances and Zr/Hf ratios during melting. For the garnet-lherzolite, the residues evolve to lower Zr abundance but an increased Zr/Hf ratio. This is due in part to the relatively high garnet mode (9 %) in the model rock, as garnet has a higher D_{Zr}/D_{Hf} ratio than spinel resulting in retention of Zr relative to Hf in the residue (Klemme *et al.* 2002; Kelemen *et al.* 2003; Weyer *et al.* 2003). Next, I calculate the Zr abundance and Zr/Hf ratio of the fractional melts that are extracted from each residue during melting. The first fractional melts extracted from the garnet- and spinel-lherzolites are enriched in Zr and have elevated Zr/Hf ratios relative to the starting DMM composition (Figures 4.24A and 4.24B). The fractional melts extracted from the residues following progressive melt extraction show gradually decreasing Zr abundances; Zr/Hf ratios in the melts decrease for spinel-facies melting, and increase for the garnet-melting case, broadly in-line with modeling in other studies (e.g., Aulbach *et al.* 2011). I also calculate the Zr and Hf compositions composition of the clinopyroxene in equilibrium with each of the fractional melts, using $D_{cpx/melt}$ of Hart and Dunn (1993; Figure 4.24). The calculated clinopyroxene compositions for the spinel-lherzolite melt scenario have Zr abundances and Zr/Hf ratios comparable to or lower than the clinopyroxene calculated to be in equilibrium with N-MORB (Figures 4.7 and 4.24).

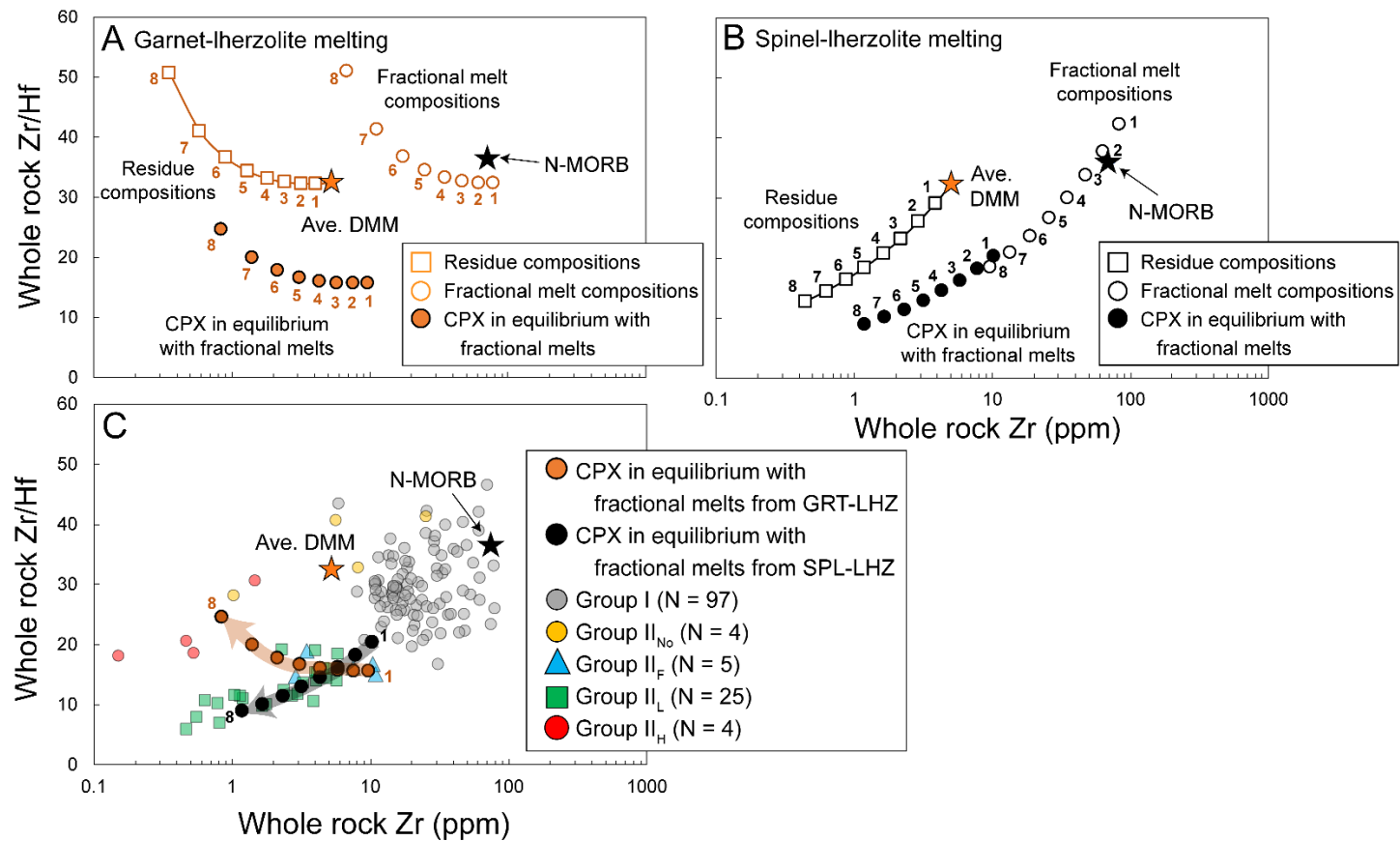


Figure 4.24 Modeled residues, melt compositions, and equilibrium clinopyroxene compositions for melting of DMM. Average DMM (Workman and Hart 2005) and N-MORB (Sun and McDonough 1989) compositions are shown. Residues of non-modal fractional melt extraction (boxes) of A) model garnet-lherzolite and B) model spinel-lherzolite shown, with melting degree (%) indicated by numbers. Fractional melt compositions (empty circles) extracted from each residue have the same number as their respective residue. The clinopyroxene compositions (filled circles) in equilibrium with each fractional melt ($D_{\text{cpx/melt}}$ from Hart and Dunn 1993) are shown. C) The compositions of clinopyroxenes in equilibrium with fractional melts from garnet- and spinel-lherzolite (from A and B) are compared with whole-rock Roberts Victor eclogites. Numbers indicate the percent melt extracted from the model garnet- or spinel-lherzolite. See Section 4.6.5.2 and 4.6.5.3 for modeling conditions.

In Figure 4.24C the modeling results are compared with the distribution of whole-rock Roberts Victor eclogite compositions. In general, the fractional melts that are extracted from spinel-lherzolite after it has lost some melt previously have lower Zr abundances and Zr/Hf ratios than N-MORB. Therefore, the clinopyroxene in equilibrium with these melts have lower Zr abundances and Zr/Hf ratios than clinopyroxene in equilibrium with N-MORB. As a result, these clinopyroxene compositions overlap closely with the whole-rock Group II_L eclogite compositions (Figure 4.26C).

This modeling indicates that a melt of a residual mantle source (i.e., residual DMM within the “mantle melt zone,” Figure 4.23) has suitable Zr/Hf ratios to permit precipitation of clinopyroxene with lower Zr/Hf ratios than predicted for cumulates from N-MORB-like magmas. For the REE, during the modeled melt extraction the LREE in the residues are fractionated from MREE and HREE. Fractionation of MREE from HREE is stronger in the garnet-facies residues than the spinel-facies residues (Figure 4.25; Weyer *et al.* 2003; Marchesi *et al.* 2016; Warren 2016; Basch *et al.* 2019).

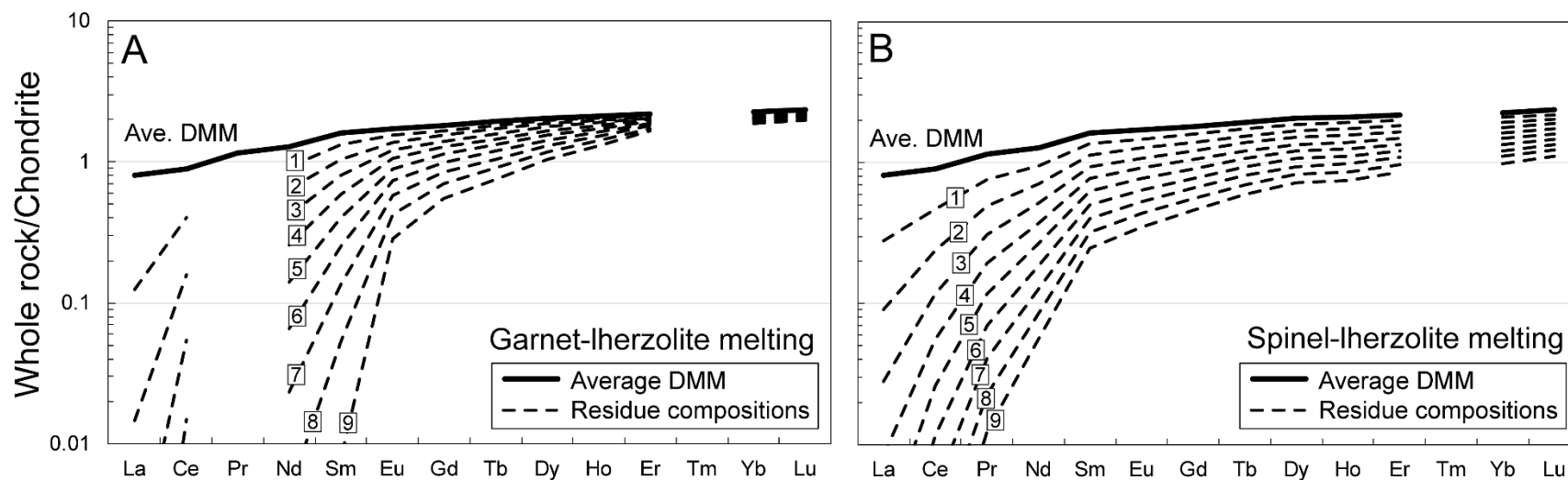


Figure 4.25 A) REE_N patterns of residues during non-modal fractional melting of model garnet-lherzolite with a starting bulk composition of average depleted MORB mantle (DMM; Workman and Hart 2005). Data are normalised to C1 chondrite (McDonough and Sun 1995). Numbers adjacent to each residue indicate the percent melt extracted from the residue. Modeling conditions, including partition coefficients used, are described in Section 4.6.5.2. B) REE_N patterns of residues during non-modal fractional melting of model spinel-lherzolite with a starting bulk composition of average depleted MORB mantle (DMM; Workman and Hart 2005). Data are normalised to C1 chondrite (McDonough and Sun 1995). Numbers adjacent to each residue indicate the percent melt extracted from the residue. Modeling conditions, including partition coefficients used, are described in Section 4.6.5.2.

To simulate decompression melting of DMM in a natural (polybaric) system, I have modeled the behaviour of Zr, Hf, and the REE during melting of average DMM. For the melting conditions, I infer an arbitrary 2 % fractional melting in the garnet-facies, as several studies suggest that the amount of melting in the garnet-facies may be low during upwelling (Warren 2016, Shervais *et al.* 2019). I then model an additional 6 % fractional melting in the spinel-facies. I refer to this residue as an “8 %-melted residue.” The REE patterns of average DMM and the 8 %-melted residue are shown in Figure 4.26A. The REE_N pattern of the fractional melt extracted in the spinel-facies from the 8 %-melted residue is shown in Figure 4.26A, and its Zr abundance and Zr/Hf ratio are shown in Figure 4.26B. The clinopyroxene in equilibrium with the fractional melt of the 8 %-melted residue, calculated using $D_{\text{cpx/melt}}$ from Hart and Dunn (1993), is shown as well in terms of its REE_N pattern, Zr abundance, and Zr/Hf ratio (Figures 4.26A and 4.26B). The data are compared with the distribution of whole-rock Roberts Victor eclogites. The clinopyroxene calculated to be in equilibrium with the fractional melt composition has a lower Zr abundance and Zr/Hf ratio than the clinopyroxene in equilibrium with N-MORB. Moreover, the clinopyroxene has a similar Zr abundance and Zr/Hf ratio to many of the whole-rock Group II_L eclogites, particularly, those with among the lowest Zr/Hf ratios (Figure 4.26B). The calculated clinopyroxene also has a similar REE_N pattern shape to the median Group II_L REE_N pattern (Figure 4.26A).

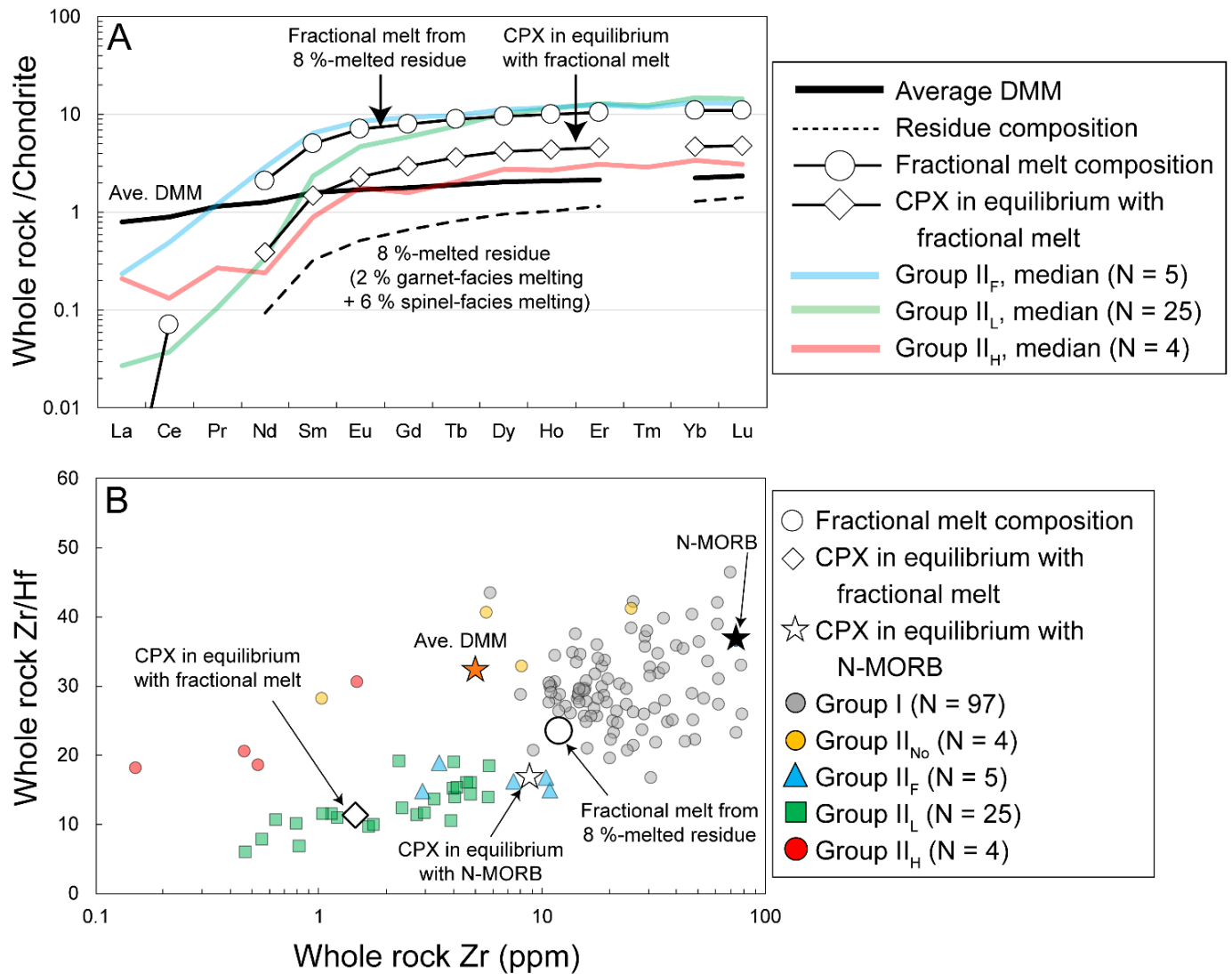


Figure 4.26 Non-modal fractional melt modeling of a rock with a bulk composition of average DMM (Workman and Hart 2005) that experienced 2 % melting in the garnet facies and 6 % melting in the spinel-facies. A) Model garnet-lherzolite with average DMM composition (heavy black line) is melted 2 % at garnet-facies and 6 % at spinel-facies resulting in a residue composition (“8 %-melted residue,” dashed line). A fractional melt is extracted from this residue (open circles). The clinopyroxene in equilibrium with this melt ($D_{\text{cpx/melt}}$ of Hart and Dunn 1993) has the composition indicated by open diamonds. These REE_N patterns are compared with the median REE_N compositions of Group II_F, II_L, and II_H eclogites. All data are normalised to C1 chondrite (McDonough and Sun 1995). B) The same scenario described in (A) is shown in Zr/Hf versus Zr space. The composition of the fractional melt (empty circle) from the 8 %-melted residue as well as the clinopyroxene in equilibrium with this melt (empty diamond) are compared with the distribution of Roberts Victor eclogites from this study (N = 64) and the literature (N = 71). The clinopyroxene in equilibrium with N-MORB is shown for comparison.

In Section 4.6.4.2 it was discussed that the chemical characteristics of the Group II_L eclogites may be attributed to cumulate precipitation from a magma, specifically, that the low D_{Zr}/D_{Hf} ratio of clinopyroxene is one possible mechanism to exert a control on the cumulate Zr/Hf ratio. The modeling in this section demonstrates that the starting Zr abundance and Zr/Hf ratio of a magma can be reduced if it is generated from a residual source. Clinopyroxene that precipitates from this calculated melt (with a composition that is not MORB-like) has a similar REE_N pattern, Zr abundance, and Zr/Hf ratio as some whole-rock Group II_L eclogites. This is not to say that the Group II_L eclogite protoliths were purely clinopyroxene that crystallised from such melts, but that the chemical variation in the Group II_L eclogite suite might be a function of such clinopyroxenes having accumulated in their protoliths. Melting of DMM to produce a residual mantle source (8 %-melted residue) can, upon further melting, produce a melt from which the Group II_L eclogite protoliths may have precipitated as cumulates.

4.6.5.4 The oceanic protoliths of the Group II_L, II_H, II_F, and II_{No} eclogites

So far I have primarily discussed the Group II_L eclogites because they are relatively more abundant than the Group II_H, Group II_F, and II_{No} eclogites. For the Group II_L eclogites I have proposed that their protoliths may have precipitated as oceanic crust from melts that were extracted from, or in equilibrium with, residual DMM. This melt may be equivalent to a “single-increment melt” of residual DMM, which is chemically less-enriched than the aggregated MORB composition. The Group II_H eclogites share low incompatible element contents with the Group II_L eclogites but in some chemical parameters are offset from them (e.g., Figures 4.13B, 4.16, 4.19, 4.20, and 4.21). However, occasionally the Group II_H eclogites appear to be somewhat “continuous” chemically with the Group II_L eclogites (Figures 4.17 and 4.18). On this basis, I infer that both the Group II_L and II_H eclogites may have precipitated from a magma with

an overall similar chemical composition, characterised by low incompatible element contents. One of the main compositional differences between the Group II_L and II_H eclogites is their disparate whole-rock Mg#, which may be due to varying fractionation of olivine in their parental magmas. The Group II_H eclogites also have relatively elevated Zr/Hf ratios compared with the Group II_L eclogites (Figure 4.7). This may indicate that the bulk Zr and Hf abundances of the magma that precipitated the Group II_H eclogite protoliths may have been different from that which precipitated the Group II_L eclogite protoliths.

The Group II_{No} eclogites have similar REE_N patterns, extended trace-element patterns, and similar Zr/Hf and Zr/Y ratios to some Group I eclogites (Figures 4.5, 4.6, and 4.7). Their $\delta^{18}\text{O}$ values are a closer match to Group I eclogites and overlaps more closely with the canonical mantle range than with the other Group II eclogites (Figure 4.8B). The Group II_{No} eclogites have low whole-rock Na₂O (average whole-rock Na₂O = 2.30 wt%) and FeO/MgO ratios similar to the Group II_H eclogites (FeO/MgO \leq 0.75; Figure 4.20). The Group II_{No} eclogites also appear to follow chemical trends similar to Group I and II_L eclogites, corresponding to picrite differentiation (e.g., Figure 4.15). One possibility is that the Group II_{No} eclogites may have been generated from a parental magma with a MORB-like trace-element composition, which may account for the similarities in REE_N between Group I eclogites and some of the Group II_{No} eclogites (Figure 4.5). The low FeO/MgO ratios and positive Eu/Eu* of some Group II_{No} eclogites indicates that some of their protoliths may have been relatively primitive, olivine + plagioclase-bearing cumulates. The Group II_{No} eclogites have a distribution of garnet $\delta^{18}\text{O}$ values (4.7 to 6.6 ‰) that overlaps the mantle range (Figure 4.8B). The Group II_{No} eclogites with garnet $\delta^{18}\text{O}$ values below the mantle range may have precipitated at stratigraphic depths \sim 2 km in oceanic crust, possibly shallower than the Group II_L eclogite protoliths and more similar to some

of the Group I eclogites. Alternatively, they could have precipitated much more deeply in oceanic crust and avoided significant interaction with seawater (≥ 5 km). The Group II_{No} eclogites likely do not have a straightforward origin as they have Group II textures but lack the significant incompatible element depletion that characterises the other eclogites with Group II textures (Groups II_L, II_H, and II_F).

This study also includes five Group II_F eclogites that are characterised by whole-rock LREE-depletion but less significant MREE_N-HREE_N slopes than the Group II_L and II_H eclogites (Figure 4.5). Similarly to the Group II_L eclogites, the Group II_F eclogites generally have lower Zr abundances and Zr/Hf ratios than many Group I eclogites, as well as the clinopyroxene in equilibrium with N-MORB (Figure 4.7). However, the whole-rock Zr/Hf ratios of the Group II_F eclogites are not as low as the Group II_L eclogites with the lowest Zr/Hf ratios (Figure 4.7). If the Group II_F eclogites have a similar genetic history to the Group II_L eclogites, then their flatter MREE_N-HREE_N slopes and less-significant Zr-Hf fractionation than many Group II_L eclogites might reflect the composition of their parental magma. The Group II_F eclogite protoliths may have precipitated from a parental magma that was derived from a residual mantle source. The mantle source may have undergone less melt-extraction than the mantle source that generated the Group II_L eclogite protolith magma. Hence, the Group II_F eclogite protoliths inherited shallower MREE_N-HREE_N slopes and less significant Zr-Hf fractionation reflecting that their mantle source was not as strongly melt-depleted. Beyond elemental chemistry, with respect to oxygen isotope compositions the Group II_F eclogites are variable. The subgroup includes eclogite RV344 (Radu *et al.* 2019) which has the lowest reported $\delta^{18}\text{O}$ value for kimberlite-hosted eclogitic garnet (1.1 ‰), indicative of high-temperature hydrothermal alteration possibly at ~ 5 km depth or greater (similar to the Rajmi locality, Samail Ophiolite; Stakes and Taylor 1992). Only one

other Group II_F eclogite has a reported garnet $\delta^{18}\text{O}$ value ($\delta^{18}\text{O} = 4.6 \text{ ‰}$, this study), a value that is closer to the canonical mantle range and to Group I eclogites (Figure 4.8). Therefore, the Group II_F eclogites also do not appear to have an easily explainable origin.

4.6.5.5 Summary

The modeling in this study demonstrates that fractional melts of residual peridotites have lower LREE abundances and Zr/Hf ratios than N-MORB. With respect to REE_N patterns and Zr/Hf ratios, the similarity in composition between clinopyroxene in equilibrium with the fractional melts extracted from residual mantle, and the median REE_N patterns for whole-rock Group II_L eclogites, is striking. For the Group II eclogites at Roberts Victor, systematic variation in Sr/Sr* and Eu/Eu* (Figures 4.13A and 4.14) as well as major-element chemistry (Figures 4.15, 4.16, and 4.17) is inferred to indicate that their protoliths were cumulates that precipitated as oceanic crust. Based on the melt modeling in this study I conclude that the source of the melts from which some of the Roberts Victor Group II eclogite protoliths precipitated was not MORB-like. Rather, the parental magma may have been generated from a residual, previously-melted source. Mineral precipitation from this melt may explain the uniquely low incompatible element contents of Zr/Hf ratios of some of the Group II eclogites (the Group II_L eclogites in particular) compared with Group I eclogites.

4.6.6 Possible settings for magmas less-enriched than MORB in oceanic crust

4.6.6.1 Overview

The elemental composition of eclogites or their protoliths can be modified by melt extraction during subduction (in the “slab melt zone;” Figure 4.23), which has been one of the longstanding interpretations for the incompatible element depletions of Group II eclogites from Roberts

Victor. In Sections 4.6.4 and 4.6.5 I instead speculate that the significant incompatible element depletions are at least partially the result of the Group II eclogite protoliths having precipitated as incompatible-element-poor cumulates. The parental cumulates possibly precipitated from magmas that were derived from mantle sources that had undergone previous melt extraction (“residual DMM”), similar to single-increment melts extracted from the “mantle melt zone” (Figure 4.23). Ophiolites provide important context to validate this latter proposal because rocks in ophiolites, having avoided subduction, may have avoided post-crystallisation mantle metasomatism and partial melt extraction during subduction. Hence, their chemical composition may largely be primary from their formation, representative of oceanic crust formed from melts that were extracted from the mantle melt zone.

Most oceanic crust is crystallised from MORB-like magmas. This composition is the result of early incipient melts of the convecting depleted mantle – which will be chemically more-enriched – and later major melting regime melts of the residual source which will be less-enriched. It has been commonly accepted that the early- and late-stage melts of upwelling DMM typically are homogenised by the mixing process, resulting in an aggregated MORB composition (Johnson *et al.* 1990; Blundy *et al.* 1998). There are, however, numerous reports of rocks in ophiolites with incompatible-element depletions that lack a clear relationship to MORB-like magmas.

4.6.6.2 Chemically-depleted rocks in oceanic crust

Benoit *et al.* (1999) described “D-” and “N-type” cumulates in the deep crustal sections of the Oman Ophiolite associated with a fossil mantle diapir. Both cumulate types crystallised as pyroxenites or gabbronorites containing clinopyroxene + plagioclase + orthopyroxene ± olivine.

The D-type cumulates contain relatively anorthite-rich plagioclase, and clinopyroxene with relatively low TiO₂ contents (average TiO_{2cpx} = 0.17 wt%). These cumulates were shown to have been in equilibrium with magmas chemically less-enriched than MORB-like magmas, i.e., their calculated equilibrium liquids are characterised by low (Nd/Yb)_N. The N-type cumulates contain clinopyroxene with relatively higher TiO₂ (average TiO_{2cpx} = 0.60 wt%) and Sr contents, and plagioclase with moderately lower anorthite component. They were calculated to have been in equilibrium with liquids more MORB-like (MORB-like [Nd/Yb]_N). Benoit *et al.* (1999) concluded that the D-type cumulates were crystallised within the crustal section of the Oman Ophiolite from melts of previously-depleted, residual mantle peridotite. However, the D-type cumulates that share very close spatial proximity to the N-type cumulates were formed from more-typical aggregated MORB-like parental magmas. Both cumulate types are rich in clinopyroxene and plagioclase indicating that the less-enriched chemical character of the D-type parental magma did not preclude plagioclase or clinopyroxene precipitation.

Piccardo and Guarnieri (2011) described gabbronorite cumulates within oceanic peridotites of the Monte Maggiore Ophiolite, Corsica. The cumulate rocks precipitated within dykelets (~ 10 cm size) and bodies up to several hundreds of metres in size. The gabbronorites are characterised by unusually low whole-rock Sr (~ 20 ppm) and LREE abundances (strongly subchondritic) that are comparable to whole-rock Sr abundances and REE_N patterns of Group II_L eclogites at Roberts Victor (Table C.10). The clinopyroxenes in those gabbronorites have comparable Zr abundances and Zr/Hf ratios to whole-rock low Mg# eclogites (< 10 ppm and < 20, respectively). The liquids calculated to be in equilibrium with the gabbronorite clinopyroxenes indicate that the cumulates likely precipitated from unaggregated MORB-like single-increment melts, which were extracted from a mantle residue that had previously undergone between 5 to 7 % fractional melt

extraction in the spinel facies (Johnson *et al.* 1990; Piccardo and Guarnieri 2011). Piccardo and Guarnieri (2011) inferred some amount of reactive flow between the rising magma and oceanic peridotite, which precipitated olivine and dissolved some orthopyroxene. The peridotites were also intruded later, separately, by dykes that crystallised gabbros with an order of magnitude higher whole-rock Sr contents as well as higher (generally superchondritic) LREE abundances. The clinopyroxenes in these later (cross-cutting) gabbros have higher Zr abundances and Zr/Hf ratios (> 10 ppm and > 20 , respectively), more similar to Group I eclogites at Roberts Victor. Piccardo and Guarnieri (2011) inferred that the gabbro cumulates crystallised from aggregated MORB magmas.

Deep gabbros on the Mid Atlantic Ridge (MAR; Deep Sea Drilling Project Site 334) have been described as having chemical compositions – characterised by clinopyroxene with anomalous LREE-depletion – that are consistent with their having precipitated from magmas that were less-enriched than MORB-like magmas (Ross and Elthon 1993; Nonnotte *et al.* 2005). The melts calculated to be in equilibrium with these gabbros have subchondritic LREE and approximately flat $MREE_N$ - $HREE_N$ slopes, different from the more MORB-like rocks which occur in close spatial proximity to the gabbros (Ross and Elthon 1993). A similar scenario is described for samples from the Kane Fracture Zone (Mid-Atlantic Ridge) that are cumulates determined to have formed from a magma with a chemical composition less-enriched than aggregated MORB-like magmas (Ross and Elthon 1997).

Fields of whole-rock compositions for ophiolite-hosted tholeiites and lavas overlap with many Group I eclogites but do not typically overlap with the compositions of Group II_L eclogites (Figure 4.27). Reported gabbros in ophiolites have a wider chemical range, overlapping with Group I eclogites and plotting more closely with whole-rock Group II_L eclogite compositions.

The samples in the cumulate gabbro field with $Zr < 10$ ppm are dominantly plagioclase-bearing cumulates from crustal sections of the Samail Ophiolite reported by Peucker-Ehrerbrink *et al.* (2012) and Nicolle *et al.* (2016). The latter authors concluded that the cumulates were precipitated from diapiric melts that were generated from underlying pyroxenite sources and thus, not associated with magmas having an aggregated MORB-like composition. Based on the distribution of reported ophiolite data, it is apparent that oceanic crustal rocks do not exclusively precipitate from MORB-like magmas.

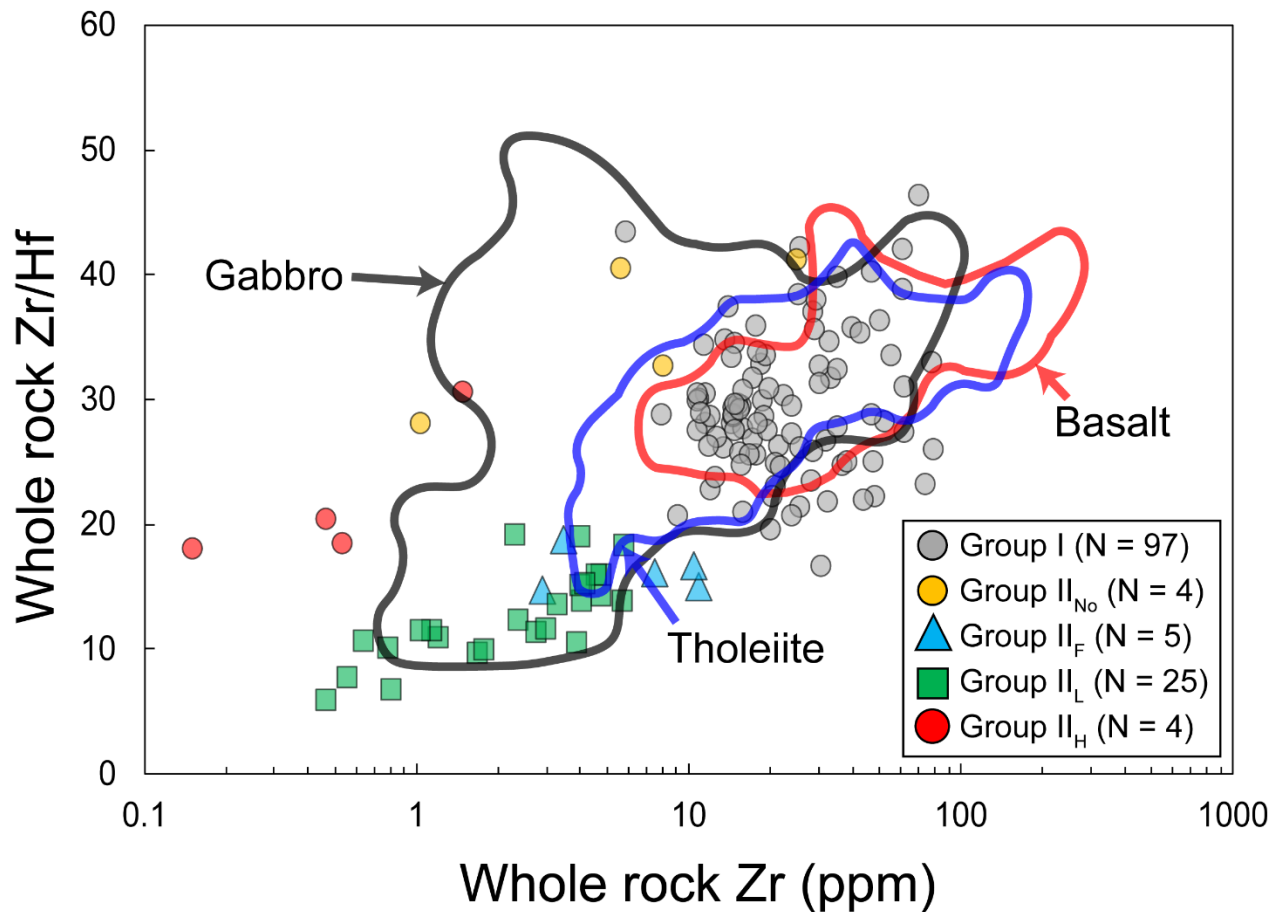


Figure 4.27 Distribution of Roberts Victor eclogites based on whole-rock Zr abundances and Zr/Hf ratios. Eclogite data are from this study ($N = 64$) and the literature ($N = 71$). The data are compared with lithologies hosted by Cretaceous ophiolites, indicated by drawn fields. The fields enclose whole-rock data, and were obtained from the PetDB Database (www.earthchem.org/petdb) on 15 December, 2019, using the parameter tectonic setting: ophiolite.

4.6.6.3 Summary

Eclogites with compositions similar to the Group II eclogites at Roberts Victor, characterised by low (< 15) Zr/Hf ratios, LREE_N-depletion, and/or positive MREE_N-HREE_N slopes, have been previously reported from kimberlite localities on the Slave and Siberian cratons (Jacob and Foley 1999; Aulbach *et al.* 2011; Smart *et al.* 2014, 2017). However, there is no general consensus in the literature for the process that generates each of these chemical features in mantle eclogites. Likewise, the ophiolite literature discusses rocks that may have formed from magmas that are not MORB-like, but has not reached consensus on how such rocks are formed (see discussion by Piccardo and Guarnieri 2011). Jacob and Foley (1999) speculated that several Archean-aged Siberian eclogites might have formed by Archean-only processes which are not acting at present. However, the discussion in this section has highlighted that there are several ways to produce melts that are less-enriched than the aggregated MORB composition in natural systems, and that cumulates with non-MORB affinity do occur in deep oceanic crust. Similarly, Group II eclogites with low TiO₂ contents and positive MREE_N-HREE_N slopes are broadly consistent with protoliths that precipitated from melts of refractory mantle sources (Smithies *et al.* 2004). I hypothesise that Roberts Victor Group II eclogite protoliths precipitated from single-increment melts of residual DMM, melts which escaped mixing with earlier, more-enriched melts, possibly by lateral injection into oceanic crust, diapiric upwelling, or upward percolating melts (Figure 4.23; Basch *et al.* 2019).

4.7 Summary and Conclusions

Eclogites from the former Roberts Victor diamond mine have classically been classified into Groups I and II based on their texture, as well as their elemental and isotopic composition

(MacGregor and Carter 1970; MacGregor and Manton 1986; McCandless and Gurney 1989). New triple oxygen isotope evidence in this study together with published chemical data agree with previous studies indicating that both groups of eclogites at Roberts Victor have oceanic crustal protoliths that were altered by seawater. I concur with previous authors, that Group I eclogites originated as picritic to basaltic MORB melts crystallising as lavas (extrusive) or cumulate enriched gabbros (intrusive). However, my new interpretation suggests that Group II eclogite protoliths precipitated in oceanic crust from a magma with a different composition.

Here I focus on a genetic model specific to the Group II eclogites. Group II eclogites typically have $\delta^{18}\text{O}$ values below the canonical mantle range and $\text{Eu}/\text{Eu}^* > 1$, indicating that their protoliths crystallised as plagioclase-bearing cumulates at deep levels in oceanic crust (≥ 2 km). The Group II_L, II_H, and II_F eclogites have low incompatible element contents compared with Group I eclogites, as well as positive $\text{MREE}_N\text{-HREE}_N$ slopes, that are broadly consistent with melt extraction, such as may occur in hydrated basaltic rocks during subduction. However, modeling in this study demonstrates that it is unlikely that Group II eclogites achieved their LREE_N -depleted REE_N patterns and low Zr/Hf ratios during partial melt extraction, since significant partial melting may obliterate other chemical evidence consistent with mineral accumulation (e.g., Eu/Eu^* vs HREE, Sr/Sr^* vs Nd, $\text{Mg}\#$ vs Ni; Figures 4.13 and 4.14; Aulbach and Jacob 2016). Rather, I have shown that the combination of incompatible element depletion and low Zr/Hf ratios in Group II eclogites is consistent with their oceanic protoliths having precipitated from melts chemically less-enriched than N-MORB. Polybaric decompression melting of DMM in the “mantle melt zone” (Figure 4.23) extracted incompatible elements, leaving a clinopyroxene-bearing residue depleted in incompatible elements with a low Zr/Hf ratio. The elements Sm-Nd, Lu-Hf, and Rb-Sr were also fractionated in the residue. Further

melting of this residue generated melts that were less-enriched than the aggregated N-MORB composition, and these melts then precipitated as cumulates forming oceanic crust. The cumulates inherited the incompatible element depletions and lower Zr/Hf ratios of the parental magma, and developed extremely radiogenic present day $^{143}\text{Nd}/^{144}\text{Nd}$, $^{147}\text{Sm}/^{144}\text{Nd}$, $^{176}\text{Hf}/^{177}\text{Hf}$, and $^{176}\text{Lu}/^{177}\text{Hf}$ compositions during long-term radiogenic decay. The exact mechanism how such melts escaped homogenisation in N-MORB reservoirs is not clear, but I note that gabbros in Cretaceous ophiolites extend towards the composition of Group II_L eclogites (Figure 4.27).

Only 6 to 8 % of Roberts Victor eclogites in the literature are classified as Group II on a textural basis (Gréau *et al.* 2011), and the reason for the textural difference from Group I eclogites is enigmatic. However, it is the Group II eclogites with LREE_N-depletion – the Groups II_L, II_H, and II_F eclogites – that have $\delta^{18}\text{O}$ values much lower than the canonical mantle range. The relatively low abundance of Group II eclogites which appear to have precipitated from less-enriched magmas than N-MORB, combined with $\delta^{18}\text{O}$ values lower than the canonical mantle range, might be explained by the formation of the Group II eclogite protoliths by small-volume magmatic intrusions (i.e., dykes, diapirs) in deep oceanic crust. Thus, this study highlights the complexity in parental magmas that formed the spectrum of cumulate protoliths to the Group I eclogites at Roberts Victor, the same spectrum evident in Phanerozoic ophiolites.

Chapter 5 Conclusions

There were two primary objectives of this thesis. The first objective was to develop new chemical discriminants that can be applied to diamond exploration practices to reduce the uncertainty of classification of unknown single garnets in concentrate. By improving the classification of garnets from the lower crust versus the mantle – using their major- and trace-element compositions – kimberlites containing mantle lithologies may be more accurately located. Secondly, using a combination of new high-quality major- and trace-element data as well as oxygen isotope compositions from a suite of Roberts Victor eclogites, this thesis presents a new genetic model for the formation of the Group II eclogite protoliths. This interpretation highlights the complexities of eclogite chemical composition, even at a single locality, which provides some perspective on the nature of classification methods that employ garnet compositions.

5.1 Major-element discrimination of crust-mantle garnets using statistical methods

Exploration practices for diamond – or, more specifically, kimberlites that may be diamondiferous – often employ the geochemistry of single minerals to identify deposits. Minerals that accompany diamond in the lithosphere – so-called “diamond indicator minerals” – may also be entrained by kimberlite and are in much higher abundances than diamond, thus often sought out instead of diamond itself. The chemistry of these minerals can, in some cases, reflect the mineralogy of their host rock, which might have a particular association with diamond. Of the common diamond indicator minerals, garnet is particularly useful as it occurs in a wide-range of lithologies where diamond may be stable. Garnet composition has been shown to be a robust indicator of its source rock lithology, even when found as a single grain in concentrate (e.g.,

Grütter *et al.* 2004). While practices that employ high-Cr garnet geochemistry are robust in identification of diamondiferous deposits hosted by peridotitic substrates, low-Cr garnets from mantle eclogites – which are potentially diamond-rich substrates – are compositionally similar to garnets from lower crustal lithologies such as granulites. This geochemical overlap may result in the misclassification of garnets from the crust as mantle-derived: a “false positive.” Existing methods for the identification of single low-Cr crustal- and mantle-derived garnets include the Schulze (2003) Ca# vs Mg# classification method. This method was derived using a calibration dataset with little weight on garnet from lower crustal granulites, which are very difficult to differentiate compositionally from garnets from mantle eclogites. Further, the Schulze (2003) method was calibrated to not exclude any mantle garnets, at the expense of a significant number of crustal garnets misclassifying as mantle-derived.

To rectify this situation, in Chapter 2 I analysed a suite of garnets from 719 new xenoliths with known paragenesis. I focused on the rock types from which the garnets are most difficult to distinguish geochemically – lower crustal garnet granulites and mantle eclogites. These data are combined with a substantial literature database for garnets from known lithology. Application of the Schulze (2003) method to this combined database confirms that the method results in a broad misclassification of crustal garnets: ~ 39 % of all garnets from lower crustal granulites in the database misclassify as mantle-derived using the Schulze (2003) method. Using the new representative database in this study, I derived new graphical methods for classification, which can be rapidly applied to garnet major-element data. These methods employ variables recast as “Pearce element ratios” that overcome some of the inherent complexities inherent to geochemical data, namely, the unit sum constraint, and are applied using the multivariate statistical techniques linear discriminant analysis (LDA) and logistic regression (LR).

Multivariate statistical methods have the advantage of identifying underlying patterns in data in high-order chemical space, which is advantageous for garnet as even with three or four variables, garnet compositions overlap (Schulze 2003; Suggate and Hall 2013; Krippner *et al.* 2014). The results of the application of LDA and LR to garnet classification are positive: for the method developed using LR, the overall error rate is 7.5 ± 1.9 %, much lower than the error rate of the Schulze (2003) method for the same dataset (17.1 ± 2.1 %). The error rate of crustal garnets is reduced from 39.2 % with the Schulze (2003) method to 7.6 % with the new LR method. This method also permits a probabilistic assessment of classification certainty for every garnet. These results will have a positive effect on diamond exploration practices by improving the accuracy of the classification of single concentrate garnets.

5.2 Trace-element discrimination of crust-mantle garnets using statistical methods

Despite the improvements to garnet classification success provided by a robust major-element database combined with multivariate statistics, the final error rates of major-element LR and LDA methods are non-negligible: garnet chemical overlap persists, even when eight chemical variables are used. To rectify this situation, in Chapter 3 I analysed garnets from 571 new xenoliths – lower crustal granulites and mantle eclogites - to assess whether trace-elements can provide additional benefit in the geochemical classification of single garnets. These data are combined with 169 garnet compositions from the literature, which are relatively sparse owing to the added cost of trace-element analyses.

Based on the full dataset in this study, trace-element compositions – when added as variables to discriminate garnet compositions - tend only to repeat the discrimination of garnets using major-elements. That is, garnets from lower crustal granulites and mantle eclogites with distinctly

different major-element compositions from one another – hence, already classified correctly by major-element methods – also have different REE compositions. This result indicates that major-element compositions are relatively potent as garnet classifiers and that trace-element data, if applied to garnet classification using a trace-element only method, provide comparable to worse results than the major-element methods. Therefore, I applied trace-elements to the outputs from the major-element method, hence, they are used in an additive way. Specifically, garnets that were classified as “crust-derived” using the major-element logistic regression method are more accurately classified by adding garnet Eu-anomalies and Sr abundances as chemical variables. The trace-element method is applied using the statistical method Classification and Regression Trees (CART), which outputs the discrimination as a flowchart for easy readability and application to new data. The addition of Eu-anomalies and Sr abundances as variables reduces the error rate on the calibration dataset to 4.7 % based on calibration data, an improvement to classification error rates. The value of these variables for garnet discrimination appears to be related to the petrogenesis of the host rock. Eu and Sr in eclogitic garnet is inherited from former plagioclase in the crustal protoliths. Therefore, Eu-anomalies and Sr contents in eclogitic garnets are generally higher than garnets from crustal rocks that are in equilibrium with plagioclase.

These results imply that an explorationist can make an informed choice during exploration: the added cost of trace-element acquisition can be weighed against the improvements to garnet classification rates. The choice can be made depending on the fraction of garnets that are difficult to classify from major-element methods. Combined with the results in Chapter 2, it is apparent that garnet elemental chemistry is robust and its use in paragenetic classification benefits positively from the application of multivariate statistics.

5.3 The protoliths of Group II eclogites at Roberts Victor

Eclogite xenoliths are abundant at Roberts Victor and have been classically divided into two groups based on texture and elemental and isotopic chemistry: Group I eclogites are potentially diamondiferous with disequilibrium-type textures and high sodium-in-garnet ($\text{Na}_2\text{O}_{\text{grt}}$) and potassium-in-clinopyroxene ($\text{K}_2\text{O}_{\text{cpx}}$); Group II eclogites are barren, with equilibrium-type textures, and low $\text{Na}_2\text{O}_{\text{grt}}$ and $\text{K}_2\text{O}_{\text{cpx}}$ contents. Group II eclogites also have significant incompatible element depletions relative to Group I eclogites, and oxygen isotope compositions ($\delta^{18}\text{O}$) below the canonical mantle range. One of the longstanding interpretations of the Group II eclogites is that they underwent significant partial melt extraction during subduction without subsequent metasomatic re-enrichment. However, in this study I re-interpret the major- and trace-element compositions of the Group II eclogites and propose a new model specific to the origin of the Roberts Victor Group II eclogites. In this model, the incompatible element depletion of the Group II eclogites resulted from the crystallisation of their protoliths as cumulates in oceanic crust from a parental magma that had lower incompatible element contents compared to the magma that generated the Group I eclogite protoliths. Based on Zr abundances and Zr/Hf ratios – which are much lower in Group II than Group I eclogites – I propose that the source of this parental magma was not MORB-like but instead a melt of residual depleted mantle that was not subsequently mixed with the volumetrically much more abundant MORB-like melts. Based on the $\delta^{18}\text{O}$ values below the mantle range, I infer that the Group II eclogites may have precipitated as cumulates in oceanic crust as deeply as 5 km, or deeper, where the protoliths were altered by seawater at high temperatures. This result highlights the significant variability in eclogite chemistry even within a single locality, and shows that eclogite is a unique recorder of ocean-floor processes possibly as old as the Paleoproterozoic or even Archean.

References

- Abledu GK, Buckman A, Adade T, Kwofie S (2016) Comparison of logistic regression and linear discriminant analyses of the determinants of financial sustainability of rural banks in Ghana. *American Journal of Theoretical and Applied Statistics* 5:49–57
- Ackermann S, Kunz M, Armbruster T, Schefer J, Hänni H (2005) Cation distribution in a Fe-bearing K-feldspar from Itrongay, Madagascar. A combined neutron- and X-ray single crystal diffraction study. *Schweizerische Mineralogische und Petrographische Mitteilungen* 84:345-354
- Aigner-Torres M, Blundy J, Ulmer P, Pettke T (2007) Laser ablation ICPMS study of trace element partitioning between plagioclase and basaltic melts: an experimental approach. *Contributions to Mineralogy and Petrology* 153:647-667
- Aitchison K (1982) The statistical analysis of compositional data. *Journal of the Royal Statistical Society, Series B (Methodological)* 44:139-177
- Aitchison J (1994) Principles of compositional data analysis. *Multivariate analysis and its applications. IMS Lectures Notes-Monograph Series* 24:73–81
- Alonso-Perez R (2006) The role of garnet in the evolution of hydrous, calc-alkaline magmas: an experimental study at 0.8-1.5 GPa. PhD thesis, Swiss Federal Institute of Technology, Zurich
- Aulbach S, Arndt NT (2019) Eclogites as palaeodynamic archives: evidence for warm (not hot) and depleted (but heterogeneous) Archaean ambient mantle. *Earth and Planetary Science Letters* 505:162-172
- Aulbach S, Jacob DE (2016) Major- and trace-elements in cratonic mantle eclogites and pyroxenites reveal heterogeneous sources and metamorphic processing of low-pressure protoliths. *Lithos* 262:586-605
- Aulbach S, Massuyeau M, Garber J, Gerdes A, Heaman LM, Viljoen KS (2020) Ultramafic carbonated melt- and auto-metasomatism in mantle eclogites: compositional effects and geophysical consequences. *Geochemistry, Geophysics, Geosystems* (in press)
- Aulbach SA, O'Reilly SY, Pearson NJ (2011) Constraints from eclogite and MARID xenoliths on origins of mantle Zr/Hf-Nb/Ta variability. *Contributions to Mineralogy and Petrology* 162:1047-1062

- Aulbach S, Pearson NJ, O'Reilly SY, Doyle BJ (2007) Origins of xenolithic eclogites and pyroxenites from the Central Slave Craton, Canada. *Journal of Petrology* 48:1843-1873
- Baertschi P (1976) Absolute ^{18}O content of standard mean ocean water. *Earth and Planetary Science Letters* 31:341-344
- Barth MG, Foley SF, Horn I (2002) Partial melting in Archean subduction zones: constraints from experimentally determined trace element partition coefficients between eclogitic minerals and tonalitic melts under upper mantle conditions. *Precambrian Research* 113:323-340
- Basch V, Rampone E, Borghini G, Ferrando C, Zanetti A (2019) Origin of pyroxenites in the oceanic mantle and their implications on the reactive percolation of depleted melts. *Contributions to Mineralogy and Petrology* 174:97
- Beard BL, Fraracci KN, Taylor LA, Snyder GA, Clayton RA, Mayeda TK, Sobolev NV (1996) Petrography and geochemistry of eclogites from the Mir kimberlite, Yakutia, Russia. *Contributions to Mineralogy and Petrology* 125:293-310
- Begg GC, Griffin WL, Natapov LM, O'Reilly SY, Grand SP, O'Neill CJ, Hronsky JMA, Poudjom Djomani Y, Swain CJ, Deen T, Bowden P (2009) The lithospheric architecture of Africa: Seismic tomography, mantle petrology, and tectonic evolution. *Geosphere* 5:23-50
- Benoit M, Ceuleneer G, Polvé M (1999) The remelting of hydrothermally altered peridotite at mid-ocean ridges by intruding mantle diapirs. *Nature* 402:514-518
- Beyer C, Frost DJ, Miyajima N (2015) Experimental calibration of a garnet-clinopyroxene geobarometer for mantle eclogites. *Contributions to Mineralogy and Petrology* 169:18
- Bishop FC, Smith JV, Dawson JB (1978) Na, K, P and Ti in garnet, pyroxene and olivine from peridotite and eclogite xenoliths from African kimberlites. *Lithos* 11:155-173
- Blundy JD, Robinson JAC, Wood BJ (1998) Heavy REE are compatible in clinopyroxene on the spinel lherzolite solidus. *Earth and Planetary Science Letters* 160:493-504
- Boyd FR, Gurney JJ (1986) Diamonds and the African Lithosphere. *Science* 232:472-477
- Brey GP, Shu Q (2018) The birth, growth and ageing of the Kaapvaal subcratonic mantle. *Mineralogy and Petrology* 112:S23-S41

- Bucholz CE, Jagoutz O, VanTongeren JA, Setera J, Wang Zhengrong (2017) Oxygen isotope trajectories of crystallising melts: insights from modeling and the plutonic record. *Geochimica et Cosmochimica Acta* 207:154-184
- Cao X, Liu Y (2011) Equilibrium mass-dependent fractionation relationships for triple oxygen isotopes. *Geochimica et Cosmochimica Acta* 75:7435-7445
- Caporuscio FA (1990) Oxygen isotope systematics of eclogite mineral phases from South Africa. In: Okrusch M (ed), Third International Eclogite Conference. *Lithos* 25:203-210
- Caporuscio FA, Smyth JR (1990) Trace element crystal chemistry of mantle eclogites. *Contributions to Mineralogy and Petrology* 105:550-561
- Carmody L, Barry PH, Shervais JW, Kluesner JW, Taylor LA (2013) Oxygen isotopes in subducted oceanic crust: a new perspective from Siberian diamondiferous eclogites. *Geochemistry, Geophysics, Geosystems* 14:3479-3493
- Clark JR, Papike JJ (1968) Crystal-chemical characterization of omphacites. *American Mineralogist* 53:840-868
- Clayton RN, Goldsmith JR, Karel KJ, Mayeda TK, Newton RC (1975) Limits on the effect of pressure on isotopic fractionation. *Geochimica et Cosmochimica Acta* 39:1197-1201
- Coleman RG, Lee DE, Beatty LB, Brannock WW (1965) Eclogites and eclogites: their similarities and differences. *Geological Society of America Bulletin* 76:483-508
- Cookerboon HO, Kopylova MG, Daoud DK (1998) A chemically and texturally distinct layer of diamondiferous eclogite beneath the central Slave craton, northern Canada. 7th International Kimberlite Conference, Extended Abstracts, pp. 164-165
- Creaser RA, Grütter H, Carlson J, Crawford B (2004) Macrocrystal phlogopite Rb-Sr dates for the Ekati property kimberlites, Slave Province, Canada: evidence for multiple intrusive episodes in the Paleocene and Eocene. *Lithos* 76:399-414
- Czas J, Stachel T, Pearson DG, Stern RA, Read GH (2018) Diamond brecciation and annealing accompanying major metasomatism in eclogite xenoliths from the Sask Craton, Canada. *Mineralogy and Petrology* 112 (Suppl 1):S311-S323
- Danchin RV, Wyatt BA (1979) Statistical cluster analysis of garnets from kimberlites and their xenoliths. Extended Abstracts, 2nd Kimberlite Symposium, Cambridge, pp. 22-27

- David K, Schiano P, Allegre CJ (2000) Assessment of the Zr/Hf fractionation in oceanic basalts and continental materials during petrogenetic processes. *Earth and Planetary Science Letters* 178:285-301
- Dawson JB, Stephens WE (1975) Statistical classification of garnets from kimberlite and associated xenoliths. *Journal of Geology* 83:589-607
- Desmons J, Smulikowski W (2007) High P/T Metamorphic Rocks. In: Fettes D, Desmons J (eds), *Metamorphic Rocks: A Classification and Glossary of Terms*. Cambridge University Press, Cambridge, pp. 32-35
- Dongre AN, Jacob DE, Stern RA (2015) Subduction-related origin of eclogite xenoliths from the Wajrakarur kimberlite field, Eastern Dharwar craton, Southern India: Constraints from petrology and geochemistry. *Geochimica et Cosmochimica Acta* 166:165-188
- Donnelly KE, Goldstein SL, Langmuir CH, Spiegelman M (2004) Origin of enriched ocean ridge basalts and implications for mantle dynamics. *Earth and Planetary Science Letters* 226:347-366
- Drake MJ, Weill DF (1975) Partition of Sr, Ba, Ca, Y, Eu^{2+} , Eu^{3+} , and other REE between plagioclase feldspar and magmatic liquid: an experimental study. *Geochimica et Cosmochimica Acta* 39:689–712
- Eggins SM (1993) Origin and differentiation of picritic arc magmas, Ambae (Aoba), Vanuatu. *Contributions to Mineralogy and Petrology* 114:79-100
- Eiler JM (2001) Oxygen isotope variations of basaltic lavas and upper mantle rocks. *Reviews in Mineralogy and Geochemistry* 43:319-364
- Falloon TJ, Green DH (1988) Anhydrous partial melting of peridotite from 8 to 35kb and the petrogenesis of MORB. *Journal of Petrology, Special Lithosphere Issue*:379-414
- Fipke CE, Gurney JJ, Moore RO (1995) Diamond exploration techniques emphasizing indicator mineral geochemistry and Canadian examples. *Geological Survey of Canada Bulletin* 423, 86 pp.
- Foley SF, Barth MG, Jenner GA (2000) Rutile/melt partition coefficients for trace elements and an assessment of the influence of rutile on the trace element characteristics of subduction zone magmas. *Geochimica et Cosmochimica Acta* 64:933-938
- Foley SF, Tiepolo M, Vannucci R (2002) Growth of early continental crust controlled by melting of amphibolite in subduction zones. *Nature* 417:837-840

- Fujimaki H (1986) Partition coefficients of Hf, Zr, and REE between zircon, apatite, and liquid. *Contributions to Mineralogy and Petrology* 94:42–45
- Gale A, Dalton CA, Langmuir CH, Su Y, Schilling J-G (2013) The mean composition of ocean ridge basalt. *Geochemistry, Geophysics, Geosystems* 14:489-518
- Garlick GD, MacGregor ID, Vogel DE (1971) Oxygen isotope ratios in eclogites from kimberlites. *Science* 172:1025-1035
- Garrison Jr. JR, Taylor LA (1980) Megacrysts and xenoliths in Kimberlite, Elliott County, Kentucky: a mantle sample from beneath the Permian Appalachian Plateau. *Contributions to Mineralogy and Petrology* 75:27–42
- Gonzaga RG, Menzies MA, Thirlwall MF, Jacob DE, Le Roex A (2010) Eclogites and garnet pyroxenites: problems resolving provenance using Lu-Hf, Sm-Nd and Rb-Sr isotope systems. *Journal of Petrology* 51:513-535
- Grauch RI (1989) Rare earth elements in metamorphic rocks. *Reviews in Mineralogy and Geochemistry* 21: 147–167
- Gréau Y, Huang J-X, Griffin WL, Renac C, Alard O, O'Reilly SY (2011) Type I eclogites from Roberts Victor kimberlites: Products of extensive mantle metasomatism. *Geochimica et Cosmochimica Acta* 75:6927-6954
- Green DH, Ringwood AE (1972) A comparison of recent experimental data on the gabbro-garnet granulite-eclogite transition. *Journal of Geology* 80:277-288
- Green TH, Blundy JD, Adam J, Yaxley GM (2000) SIMS determination of trace element partition coefficients between garnet, clinopyroxene and hydrous basalt liquids at 2-7.5 GPa and 1080-1200°C. *Lithos* 53:165-187
- Gregory RT, Taylor HP (1981) An oxygen isotope profile in a section of Cretaceous oceanic crust, Samail Ophiolite: evidence for $\delta^{18}\text{O}$ buffering of the oceans by deep (>5 km) seawater-hydrothermal circulation at mid-ocean ridges. *Journal of Geophysical Research* 86:2737-2755
- Griffin WL, Fisher NI, Friedman JH, O'Reilly SY, Ryan CG (2002) Cr-pyrope garnets in the lithospheric mantle 2. Compositional populations and their distribution in time and space. *Geochemistry, Geophysics, Geosystems* 3:1073–1107
- Griffin WL, O'Reilly SY (2007) Cratonic lithospheric mantle: is anything subducted? *Episodes* 30:43-53

- Grove TL, Elkins-Tanton LT, Parman SW, Chatterjee N, Muntener O, Gaetani GA (2003) Fractional crystallization and mantle-melting controls on calc-alkaline differentiation trends. *Contributions to Mineralogy and Petrology* 145:515-533
- Grütter HS (2009) Pyroxene xenocryst geotherms: techniques and application. *Lithos* 112S:1167-1178
- Grütter HS, Gurney JJ, Menzies AH, Winter F (2004) An updated classification scheme for mantle-derived garnet, for use by diamond explorers. *Lithos* 77:841–857
- Grütter HS, Quadling KE (1999) Can sodium in garnet be used to monitor eclogitic diamond potential? In: Gurney JJ, Gurney JL, Pascoe MD, Richardson SH (eds), *Proceedings of the 7th International Kimberlite Conference, Red Roof Design, Cape Town*, pp. 314-319
- Gurney JJ (1984) A correlation between garnets and diamonds in kimberlites. In: Glover JE, Harris PG (eds), *Kimberlite occurrence and origin: a basis for conceptual models in exploration*. Geology Department and University Extension, University of Western Australia, Publication 8, pp. 143-166
- Gurney JJ (1989) Diamonds. In: Ross J (ed), *Kimberlites and Related Rocks, Vol. 1*. Geological Society of Australia, Special Publication, Vol. 14. Blackwell Scientific Publications, Perth, pp. 935–965
- Gurney JJ, Helmstaedt HH, Richardson SH, Shirey SB (2010) Diamonds through time. *Economic Geology* 105:689–712
- Gurney JJ, Switzer GS (1973) The discovery of garnets closely related to diamonds in the Finsch pipe, South Africa. *Contributions to Mineralogy and Petrology* 39:103-116
- Haggerty SE (1995) Upper mantle mineralogy. *Journal of Geodynamics* 20:331–364
- Hart SR, Dunn T (1993) Experimental cpx/melt partitioning of 24 trace elements. *Contributions to Mineralogy and Petrology* 113:1-8
- Harte B, Kirkley MB (1997) Partitioning of trace elements between clinopyroxene and garnet: data from mantle eclogites. *Chemical Geology* 136:1-24
- Hasterok D, Chapman DS (2011) Heat Production and Geotherms for the Continental Lithosphere. *Earth and Planetary Science Letters* 307:59-70
- Hastie T, Tibshirani R, Friedman J (2009) *The elements of statistical learning: data mining, inference, and prediction, Second Edition*. Springer-Verlag, New York, 745 pp.

- Hatton CJ (1978) The geochemistry and origin of xenoliths from the Roberts Victor mine. Unpublished PhD thesis, University of Cape Town, Cape Town
- Heaman LM, Creaser RA, Cookenboo HO (2002) Extreme enrichment of high field strength elements in Jericho eclogite xenoliths: A cryptic record of Paleoproterozoic subduction, partial melting, and metasomatism beneath the Slave craton, Canada. *Geology* 30:507-510
- Heaman LM, Creaser RA, Cookenboo HO, Chacko T (2006) Multi-stage modification of the Northern Slave mantle lithosphere: evidence from zircon- and diamond-bearing eclogite xenoliths entrained in Jericho kimberlite, Canada. *Journal of Petrology* 47:821-858
- Heaman LM, Pearson DG (2010) Nature and evolution of the Slave Province subcontinental lithospheric mantle. *Canadian Journal of Earth Sciences* 47:369-388
- Hellebrand E, Snow JE, Hoppe P, Hofmann AW (2002) Garnet-field melting and late-stage refertilization in 'residual' abyssal peridotites from the Central Indian Ridge. *Journal of Petrology* 43:2305-2338
- Helmstaedt H, Doig R (1975) Eclogite nodules from kimberlite pipes of the Colorado Plateau – samples of subducted Franciscan-type oceanic lithosphere. *Physics and Chemistry of the Earth* 9:95-111
- Helmstaedt H, Schulze DJ (1989) Southern African kimberlites and their mantle sample: implications for Archaean tectonics and lithosphere evolution. In: Ross J (ed), *Kimberlites and Related Rocks*, Vol. 1. Geological Society of Australia, Perth, Special Publication 14, pp. 358-368
- Herwartz D, Pack A, Krylov D, Xiao Y, Muehlenbachs K, Sengupta S, Di Rocco T (2015) Revealing the climate of snowball Earth from $\Delta^{17}\text{O}$ systematics of hydrothermal rocks. *Proceedings of the National Academy of Sciences of the United States of America* 112:5337-5341
- Hess PC (1992) Phase equilibria constraints on the origin of ocean floor basalts. In: Morgan JP, Blackman DK, Sinton JM (eds), *Mantle flow and melt generation at mid-ocean ridges*, pp. 67-102
- Hoffman PF, Ranalli G (1988) Archean oceanic flake tectonics. *Geophysical Research Letters* 15:1077-1080

- Huang H, Niu Y, Zhidan Z, Huixin H, Dicheng Z (2011) On the enigma of Nb-Ta and Zr-Hf fractionation – a critical review. *Journal of Earth Science* 22:52-66
- Huang J-X, Gréau Y, Griffin WL, O'Reilly SY, Pearson NJ (2012a) Multi-stage origin of Roberts Victor eclogites: Progressive metasomatism and its isotopic effects. *Lithos* 142-143:161-181
- Huang J-X, Griffin WL, Gréau Y, O'Reilly SY (2012b) Seeking the primary compositions of mantle xenoliths: isotopic and elemental consequences of sequential leaching treatments on an eclogite suite. *Chemical Geology* 328:137–148
- Huang J-X, Li P, Griffin WL, Xia Q-K, Gréau Y, Pearson NJ, O'Reilly SY (2014) Water contents of Roberts Victor eclogites: primary and metasomatic controls. *Contributions to Mineralogy and Petrology* 168:1092
- Huang J-X, Xiang YX, An Y, Griffin WL, Gréau Y, Xie L, Pearson NJ, Yu H, O'Reilly SY (2016) Magnesium and oxygen isotopes in Roberts Victor eclogites. *Chemical Geology* 438:73-83
- Hynes A (2014) How feasible was subduction in the Archean? *Canadian Journal of Earth Sciences* 51:286-296
- Ickert RB, Stern RA (2013) Matrix corrections and error analysis in high-precision SIMS $^{18}\text{O}/^{16}\text{O}$ measurements of Ca-Mg-Fe garnet. *Geostandards and Geoanalytical Research* 37:429-448
- Ickert RB, Stachel T, Stern RA, Harris JW (2013) Diamond from recycled crustal carbon documented by coupled $\delta^{18}\text{O}$ - $\delta^{13}\text{C}$ measurements of diamonds and their inclusions. *Earth and Planetary Science Letters* 364:85-97
- Ionov DA, Bodinier J-L, Mukasa SB, Zanetti A (2002) Mechanisms and sources of mantle metasomatism: major and trace element compositions of peridotite xenoliths from Spitsbergen in the context of numerical modeling. *Journal of Petrology* 43:2219-2259
- Jacob DE (2004) Nature and origin of eclogite xenoliths from kimberlites. *Lithos* 77:295-316
- Jacob DE, Bizimis M, Salters VJM (2005) Lu-Hf and geochemical systematics of recycled ancient oceanic crust: evidence from Roberts Victor eclogites. *Contributions to Mineralogy and Petrology* 148:707-720
- Jacob DE, Foley SF (1999) Evidence for Archean ocean crust with low high field strength element signatures from diamondiferous eclogite xenoliths. *Lithos* 48:317-336

- Jacob DE, Schmickler B, Schulze DJ (2003) Trace element geochemistry of coesite-bearing eclogites from the Roberts Victor kimberlite, Kaapvaal craton. *Lithos* 71:337-351
- Jagoutz E (1988) Nd and Sr systematics in an eclogite xenolith from Tanzania: Evidence for frozen mineral equilibria in the continental lithosphere. *Geochimica et Cosmochimica Acta* 52:1285-1293
- Jagoutz E, Dawson JB, Hoernes S, Spettel B, Waenke H (1984) Anorthositic oceanic crust in the Archean Earth. Proceedings of the 15th Lunar and Planetary Science Conference, *Journal of Geophysical Research Supplement*, pp. 395-396, abstract
- Jahn B-m, Cornichet J, Cong B, Yui T-F (1996) Ultrahigh- ϵ Nd eclogites from an ultrahigh-pressure metamorphic terrane in China. *Chemical Geology* 127:61-79
- Jaques AL, Hall AE, Sheraton JW, Smith CB, Sun S-s, Drew RM, Foudoulis C, Ellingsen K (1998) Composition of crystalline inclusions and C-isotopic composition of Argyle and Ellendale diamonds. In: Ross J (ed), *Kimberlites and Related Rocks*, Geological Society of Australia Special Publication. vol. 2. Blackwell, Oxford, pp. 966–989
- Jarosewich E, Nelen JA, Norberg JA (1980) Reference samples for electron microprobe analysis. *Geostandards Newsletter* 4:43-47
- Jerde EA, Taylor LA, Crozaz G, Sobolev NV (1993) Exsolution of garnet within clinopyroxene of mantle eclogites: major- and trace-element chemistry. *Contributions to Mineralogy and Petrology* 114:148-159
- Jochum KP, Nohl U, Herwig K, Lammel E, Stoll B, Hofmann AW (2005) GeoReM: A new geochemical database for reference materials and isotopic standards. *Geostandards and Geoanalytical Research* 29:333-338
- Johnson KTM (1998) Experimental determination of partition coefficients for rare earth and high-field-strength elements between clinopyroxene, garnet, and basaltic melt at high pressures. *Contributions to Mineralogy and Petrology* 133:60–68
- Johnson KTM, Dick HJB, Shimizu N (1990) Melting in the oceanic upper mantle: an ion microprobe study of diopsides in abyssal peridotites. *Journal of Geophysical Research* 95:2661-2678
- Kelemen PB, Yogodzinski GM, Scholl DW (2003) Along-strike variation in the Aleutian Island Arc: Genesis of high Mg# andesite and implications for continental crust. In: Eiler J

- (ed), *Inside the Subduction Factory*, American Geophysical Union, vol. 138, pp. 223-276
- Kiseeva ES, Kamenetsky VS, Yaxley GM, Shee SR (2017) Mantle melting versus mantle metasomatism – “The chicken or the egg” dilemma. *Chemical Geology* 455:120-130
- Klemme S, Blundy JD, Wood BJ (2002) Experimental constraints on major and trace element partitioning during partial melting of eclogite. *Geochimica et Cosmochimica Acta* 66:3109-3123
- Kohavi (1995) A study of cross-validation and bootstrap for accuracy estimation and model selection. In: Mellish CS (ed), *Proceedings of the International Joint Conference on Artificial Intelligence*. Morgan Kaufmann, Los Altos, California, pp. 1137–1143
- Korolev NM, Melnik AE, Li X-H, Skublov SG (2018) The oxygen isotope composition of mantle eclogites as a proxy of their origin and evolution: A review. *Earth-Science Reviews* 185:288-300
- Krippner A, Meinhold G, Morton AC, von Eynatten H (2014) Evaluation of garnet discrimination diagrams using geochemical data of garnets derived from various host rocks. *Sedimentary Geology* 306:36–52
- Krogh EJ (1988) The garnet-clinopyroxene Fe-Mg geothermometer – a reinterpretation of existing experimental data. *Contributions to Mineralogy and Petrology* 99:44-48
- Lundstrom CC, Shaw HF, Ryerson FJ, Williams Q, Gill J (1998) Crystal chemical control of clinopyroxene-melt partitioning in the Di-Ab-An system: implications for elemental fractionations in the depleted mantle. *Geochimica et Cosmochimica Acta* 62:2849-2862
- MacGregor ID, Carter JL (1970) The chemistry of clinopyroxenes and garnets of eclogite and peridotite xenoliths from the Roberts Victor mine, South Africa. *Physics of the Earth and Planetary Interiors* 3:391-397
- MacGregor ID, Manton WI (1986) Roberts Victor eclogites: ancient oceanic crust. *Journal of Geophysical Research* 91:14063-14079
- Marchesi C, Garrido CJ, Proenza JA, Hidas K, Varas-Reus MI, Butjosa L, Lewis JF (2016) Geochemical record of subduction initiation in the sub-arc mantle: insights from the Loma Caribe peridotite (Dominican Republic). *Lithos* 252-253:1-15
- Mattey D, Lowry D, Macpherson C (1994) Oxygen isotope composition of mantle peridotite. *Earth and Planetary Science Letters* 128:231-241

- McCandless TE, Gurney JJ (1989) Sodium in garnet and potassium in clinopyroxene: criteria for classifying eclogites. In: Ross J, Jaques AL, Ferguson J, Green DH, O'Reilly SY, Danchin RV, Janse AJA (eds), *Kimberlites and Related Rocks*, Geological Society of Australia Special Publication. Vol. 2, Blackwell, Oxford, pp. 827-832
- McDade P (1999) An experimental and geochemical study of the products of extreme metamorphic processes: ultrahigh-temperature granulites and the Roberts Victor eclogites. University of Edinburgh, Unpublished PhD thesis, 390 pp.
- McDonough WF (1991) Partial melting of subducted oceanic crust and isolation of its residual eclogitic lithology. *Philosophical Transactions of the Royal Society A* 335:407-418
- McDonough WF, Sun S-s (1995) The composition of the Earth. *Chemical Geology* 120:223-253
- McKenzie D, O'Nions RK (1991) Partial melt distributions from inversion of rare earth element concentrations. *Journal of Petrology* 32:1021-1091
- Meyer HOA, Boyd FR (1972) Composition and origin of crystalline inclusions in natural diamonds. *Geochimica et Cosmochimica Acta* 36:1255-1273
- Miller MF (2002) Isotopic fractionation and the quantification of ^{17}O anomalies in the oxygen three-isotope system: an appraisal and geochemical significance. *Geochimica et Cosmochimica Acta* 66:1881-1889
- Morgan VI GB, London D (1999) Crystallization of the Little Three layered pegmatite-aplite dike, Ramona District, California. *Contributions to Mineralogy and Petrology* 136:310-330
- Muehlenbachs K, Clayton RN (1972b) Oxygen isotope studies of fresh and weathered submarine basalts. *Canadian Journal of Earth Sciences* 9:172-184
- Muehlenbachs K, Clayton RN (1972a) Oxygen isotope geochemistry of submarine greenstones. *Canadian Journal of Earth Sciences* 9:471-478
- Næs T, Mevik B-H (2001) Understanding the collinearity problem in regression and discriminant analysis. *Journal of Chemometrics* 15, 413–426
- Nicolle M, Jousset D, Reisberg L, Bosch D, Stephant A (2016) Major and trace element and Sr and Nd isotopic results from mantle diapirs in the Oman ophiolite: Implications for off-axis magmatic processes. *Earth and Planetary Science Letters* 437:138-149

- Nonnotte P, Ceuleneer G, Benoit M (2005) Genesis of andesitic-boninitic magmas at mid-ocean ridges by melting of hydrated peridotites: Geochemical evidence from DSDP Site 334 gabbro-norites. *Earth and Planetary Science Letters* 236:632-653
- Nowicki TE, Moore RO, Gurney JJ, Baumgartner MC (2007) Diamonds and associated heavy minerals in kimberlite: a review of key concepts and applications. *Developments in Sedimentology* 58:1235–1267
- O'Brien R.M (2007) A caution regarding rules of thumb for variance inflation factors. *Quality & Quantity* 41:673–690
- O'Hara MJ, Yoder HS (1967) Formation and fractionation of basic magmas at high pressures. *Scottish Journal of Geology* 3:67-117
- Ongley JS, Basu AR, Kyser TK (1987) Oxygen isotopes in coexisting garnets, clinopyroxenes and phlogopites of Roberts Victor eclogites: implications for petrogenesis and mantle metasomatism. *Earth and Planetary Science Letters* 83:80-84
- Pack A, Herwartz D (2014) The triple oxygen isotope composition of the Earth mantle and understanding $\Delta^{17}\text{O}$ variations in terrestrial rocks and minerals. *Earth and Planetary Science Letters* 390:138-145
- Palin RM, Dyck B (2018) Metamorphic consequences of secular changes in oceanic crust composition and implications for uniformitarianism in the geological record. *Geoscience Frontiers* 9:1009-1019
- Parisot JC, Delvigne J, Grocke MCT (1983) Petrographical aspects of the supergene weathering of garnet in the “Serra Dos Carajas” (Para, Brasil). *Sciences Géologiques, bulletins et mémoires* 72:141-148
- Pearce JA, Reagan MK (2019) Identification, classification, and interpretation of boninites from Anthropocene to Eoarchean using Si-Mg-Ti systematics. *Geosphere* 15:1008-1037
- Pearson DG, Canil D, Shirey SB (2003) Mantle samples included in volcanic rocks: xenoliths and diamonds. In: Carlson RW, Holland HD, Turekian KK (eds), *Treatise on Geochemistry, Vol. 2, The Mantle and Core*. Elsevier, New York, pp. 171-275
- Pearson DG, Davies GR, Nixon PH (1993) Geochemical Constraints on the petrogenesis of diamond facies pyroxenites from the Beni Bousera peridotite massif, North Morocco. *Journal of Petrology* 34:125-172

- Pearson DG, Nixon PH (1996) Diamonds in young orogenic belts: graphitized diamonds from Beni Bousera, N. Morocco, a comparison with kimberlite-derived diamond occurrences and implications for diamond genesis and exploration. *Africa Geoscience Reviews* 3:295-316
- Pearson DG, Woodhead J, Janney PE (2019) Kimberlites as geochemical probes of Earth's mantle. *Elements* 15:387-392
- Perk NW, Coogan LA, Karson JA, Klein EM, Hanna HD (2007) Petrology and geochemistry of primitive lower oceanic crust from Pito Deep: implications for the accretion of the lower crust at the Southern East Pacific Rise. *Contributions to Mineralogy and Petrology* 154:575-590
- Peucker-Ehrenbrink B, Hanghoj K, Atwood T, Kelemen PB (2012) Rhenium-osmium isotope systematics and platinum group element concentrations in oceanic crust. *Geology* 40:199-202
- Pfänder JA, Münker C, Stracke A, Mezger K (2007) Nb/Ta and Zr/Hf in ocean island basalts – Implications for crust-mantle differentiation and the fate of Niobium. *Earth and Planetary Science Letters* 254:158-172
- Piccardo GB, Guarnieri L (2011) Gabbro-norite cumulates from strongly depleted MORB melts in the Alpine-Apennine ophiolites. *Lithos* 124:200-214
- Pin C, Briot D, Bassin C, Poitrasson F (1994) Concomitant separation of strontium and samarium-neodymium for isotopic analysis in silicate samples, based on specific extraction chromatography. *Analytica Chimica Acta* 298:209-217
- Pohar M, Blas M, Turk S (2004) Comparison of logistic regression and linear discriminant analysis: a simulation study. *Metodološki zvezki* 1:143–161
- Presnall DC, Dixon SA, Dixon JR, O'Donnell TH, Brenner NL, Schrock RL, Dycus DW (1978) Liquidus phase relations on the join diopside-forsterite-anorthite from 1 atm to 20 kbar: their bearing on the generation and crystallisation of basaltic magma. *Contributions to Mineralogy and Petrology* 66:203-220
- Press J, Wilson S (1978) Choosing between logistic regression and discriminant analysis. *Journal of the American Statistical Association* 73: 699–705
- Prytulak J, Elliot T (2007) TiO₂ enrichment in ocean island basalts. *Earth and Planetary Science Letters* 263:388-403

- Raczek I, Jochum KP, Hofmann AW (2003) Neodymium and strontium isotope data for USGS Reference Materials BCR-1, BCR-2, BHVO-1, BHVO-2, AGV-1, AGV-2, GSP-1, GSP-2 and eight PMI-DING Reference Glasses. *Geostandards and Geoanalytical Research* 27:173-179
- Radu I-B, Harris C, Moine BN, Costin G, Cottin J-Y (2019) Subduction relics in the subcontinental lithospheric mantle evidence from variation in the $\delta^{18}\text{O}$ value of eclogite xenoliths from the Kaapvaal craton. *Contributions to Mineralogy and Petrology* 174:19
- Riches AJV, Ickert RB, Pearson DG, Stern RA, Jackson SE, Ishikawa A, Kjarsgaard BA, Gurney JJ (2016) In situ oxygen-isotope, major-, and trace-element constraints on the metasomatic modification and crustal origin of a diamondiferous eclogite from Roberts Victor, Kaapvaal Craton. *Geochimica et Cosmochimica Acta* 174:345-359
- Rogers AJ, Grütter HS (2009) Fe-rich and Na-rich megacryst clinopyroxene and garnet from the Luxinga kimberlite cluster, Lunda Sul, Angola. *Lithos* 112S:942-950
- Rollinson HR (1993) *Using geochemical data*. Longman Scientific and Technical, London 352 pp.
- Ross K, Elthon D (1993) Cumulates from strongly depleted mid-ocean-ridge basalt. *Nature* 365:826-829
- Ross K, Elthon D (1997) 17. Cumulus and postcumulus crystallization in the oceanic crust: major- and trace-element geochemistry of Leg 153 gabbroic rocks. In: Karson JA, Cannat M, Miller DJ, Elthon D (eds), *Proceedings of the Ocean Drilling Program, Scientific Results, Vol. 153*, pp. 333-350
- Rudnick RL, Nyblade AA (1999) The thickness and heat production of Archean lithosphere: constraints from xenolith thermobarometry and surface heat flow. In: Fei Y, Bertka CM, Mysen BO (eds), *Mantle Petrology: Field observations and high pressure experimentation: A tribute to Francis R. (Joe) Boyd*. The Geological Society, Special Publication No. 6, pp. 3-12
- Russell JK, Nicholls J, Stanley CR, Pearce TH (1990) Pearce element ratios: a paradigm for testing hypotheses. *EOS* 71:234-246
- Salters VJM, Longhi J (1999) Trace element partitioning during the initial stage of melting beneath mid-oceanic ridges. *Earth and Planetary Science Letters* 166:15-30

- Schiavi F, Rosciglione A, Kitagawa H, Kobayashi K, Nakamura E, Mario Nuccio P, Ottolini L, Paonita A, Vannucci R (2015) Geochemical heterogeneities in magma beneath Mount Etna recorded by 2001-2006 melt inclusions. *Geochemistry, Geophysics, Geosystems* 16:2109-2126
- Schmickler B, Jacob DE, Foley SF (2004) Eclogite xenoliths from the Kuruman kimberlites, South Africa: geochemical fingerprinting of deep subduction and cumulate processes. *Lithos* 75:173-207
- Schmitz MD, Bowring SA, de Wit MJ, Gartz V (2004) Subduction and terrane collision stabilize the western Kaapvaal craton tectosphere 2.9 billion years ago. *Earth and Planetary Science Letters* 222:363-376
- Schulte RF, Schilling M, Anma R, Farquhar J, Horan MF, Komiya T, Piccoli PM, Pitcher L, Walker RJ (2009) Chemical and chronologic complexity in the convecting upper mantle: evidence from the Taitao ophiolite, southern Chile. *Geochimica et Cosmochimica Acta* 73:5793-5819
- Schulze DJ (1989) Constraints on the abundance of eclogite in the upper mantle. *Journal of Geophysical Research* 94:4205-4212
- Schulze DJ (1997) The significance of eclogite and Cr-poor megacryst garnets in diamond exploration. *Exploration and Mining Geology* 6:349-366
- Schulze DJ (2003) A classification scheme for mantle-derived garnets in kimberlite: a tool for investigating the mantle and exploring for diamonds. *Lithos* 71:195-213
- Schulze DJ, Valley JW, Spicuzza MJ (2000) Coesite eclogites from the Roberts Victor kimberlite, South Africa. *Lithos* 54:23-32
- Sharp ZD (1990) A laser-based microanalytical method for the in situ determination of oxygen isotope ratios of silicates and oxides. *Geochimica et Cosmochimica Acta* 54:1353-1357
- Sharp ZD, Gibbons JA, Maltsev O, Atudorei V, Pack A, Sengupta S, Shock EL, Knauth LP (2016) A calibration of the triple oxygen isotope fractionation in the SiO₂-H₂O system and applications to natural samples. *Geochimica et Cosmochimica Acta* 186:105-119
- Sharp ZD, Wostbrock JAG, Pack A (2018) Mass-dependent triple oxygen isotope variations in terrestrial materials. *Geochemical Perspectives Letters* 7:27-31
- Shchukina EV, Agashev AM, Zedgenizov DA (2018) Origin of zircon-bearing mantle eclogites entrained in the V. Grib kimberlite (Arkhangelsk region, NW Russia): evidence from

- mineral geochemistry and the U-Pb and Lu-Hf isotope compositions of zircon. *Mineralogy and Petrology* 112 (Suppl 1):S85-S100
- Shervais JW (1982) Ti-V plots and petrogenesis of modern and ophiolitic lavas. *Earth and Planetary Science Letters* 59:101-118
- Shervais JW, Reagan M, Haugen E, Almeev RR, Pearce JA, Prytulak J, Ryan JG, Whattam SA, Godard M, Chapman T, Li H, Kurz W, Nelson WR, Heaton D, Kirchenbaur M, Shimizu K, Sakuyama T, Li Y, Vetter SK (2019) Magmatic response to subduction initiation: Part 1. Fore-arc basalts of the Izu-Bonin Arc From IODP Expedition 352. *Geochemistry, Geophysics, Geosystems* 20:314-338
- Shervais JW, Taylor LA, Lugmair GW, Clayton RN, Mayeda TK, Korotev RL (1988) Early Proterozoic oceanic crust and the evolution of subcontinental mantle: eclogites and related rocks from southern Africa. *Geological Society of America Bulletin* 100:411-423
- Shirey SB, Richardson SH, Harris JW (2004) Integrated models of diamond formation and craton evolution. *Lithos* 77:923-944
- Shu Q, Brey GP, Gerdes A, Hofer HE (2014) Mantle eclogites and garnet pyroxenites – the meaning of two-point isochrones, Sm-Nd and Lu-Hf closure temperatures and the cooling of the subcratonic mantle. *Earth and Planetary Science Letters* 389:143-154
- Shu Q, Brey GP, Hofer HE, Zhao Z, Pearson DG (2016) Kyanite/corundum eclogites from the Kaapvaal Craton: subducted troctolites and layered gabbros from the Mid- to Early-Archean. *Contributions to Mineralogy and Petrology* 171:11
- Shu Q, Brey GP, Pearson DG (2018) Eclogites and garnet pyroxenites from Kimberley, Kaapvaal craton, South Africa: their diverse origins and complex metasomatic signatures. *Mineralogy and Petrology* 112 (Suppl 1):S43-S56
- Smart KA, Chacko T, Simonetti A, Sharp ZD, Heaman LM (2014) A record of Paleoproterozoic subduction preserved in the northern Slave cratonic mantle: Sr-Pb-O isotope and trace-element investigations of eclogite xenoliths from the Jericho and MuskoX kimberlites. *Journal of Petrology* 55:549-583
- Smart KA, Tappe S, Simonetti A, Simonetti SS, Woodland AB, Harris C (2017) Tectonic significance and redox state of Paleoproterozoic eclogite and pyroxenite components in

- the Slave cratonic mantle lithosphere, Voyageur kimberlite, Arctic Canada. *Chemical Geology* 455:98-119
- Smit KV, Stachel T, Creaser RA, Ickert RB, DuFrane SA, Stern RA, Seller M (2014) Origin of eclogite and pyroxenite xenoliths from the Victor kimberlite, Canada, and implications for Superior craton formation. *Geochimica et Cosmochimica Acta* 125:308-337
- Smith CB, Allsopp HL, Kramers JD, Hutchinson G, Roddick JC (1985) Emplacement ages of Jurassic-Cretaceous South African kimberlites by the Rb-Sr method on phlogopite and whole-rock samples. *Transactions of the Geological Society of South Africa* 88:249-266
- Smithies RH, Champion DC, Sun S-s (2004) The case for Archean boninites. *Contributions to Mineralogy and Petrology* 147:705-721
- Smyth JR, Caporuscio FA, McCormick TC (1989) Mantle eclogites: evidence of igneous fractionation in the mantle. *Earth and Planetary Science Letters* 93:133-141
- Snyder GA, Taylor LA, Crozaz G, Halliday AN, Beard BL, Sobolev VN, Sobolev NV (1997) The origins of Yakutian eclogite xenoliths. *Journal of Petrology* 38:85-113
- Sobolev NV (1977) Deep-seated inclusions in kimberlites and the problem of the composition of the upper mantle (Translated from the Russian edition, 1974). AGU, Washington, 279 pp.
- Sobolev Jr. NV, Lavrent'ev JG (1971) Isomorphous sodium admixture in garnets formed at high pressures. *Contributions to Mineralogy and Petrology* 31:1-12
- Sobolev NV, Lavrent'ev YG, Pokhilenko NP, Usova LV (1973) Chrome-rich garnets from the Kimberlites of Yakutia and their parageneses. *Contributions to Mineralogy and Petrology* 40:39-52
- Stachel T, Harris JW (2008) The origin of cratonic diamonds - constraints from mineral inclusions. *Ore Geology Reviews* 34:5-32
- Stakes DS, Taylor HP (1992) The northern Samail ophiolite: an oxygen isotope, microprobe, and field study. *Journal of Geophysical Research* 97:7043-7080
- Suggate SM, Hall R (2013) Using detrital garnet compositions to determine provenance: a new compositional database and procedure. In: Scott RA, Smyth HR, Morton AC, Richardson N (eds), *Sediment Provenance Studies in Hydrocarbon Exploration and Production*. Geological Society, London, Special Publications 386:373-393

- Sun S-s, McDonough WF (1989) Chemical and isotopic systematics of oceanic basalts: implications for mantle composition and processes. In: Saunders AD, Norry MN (eds), *Magmatism in the Ocean Basins*, Geological Society Special Publication No. 42, pp. 313-345
- Tacker RC (2004) Hydroxyl ordering in igneous apatite. *American Mineralogist* 89:1411-1421
- Tiepolo M, Bottazzi P, Foley SF, Oberti R, Vannucci R, Zanetti A (2001) Fractionation of Nb and Ta from Zr and Hf at mantle depths: the role of titanian pargasite and kaersutite. *Journal of Petrology* 42:221-232
- Valley JW (1986) Stable isotope geochemistry of metamorphic rocks. In: Valley JW, Taylor HP, O'Neil JR (eds), *Stable Isotopes in High Temperature Geological Processes*. Mineralogical Society of America, Washington DC, pp. 445-489
- Viljoen KS, Robinson DN, Swash PM, Griffin WL, Otter ML, Ryan CG, Win TT (1994) Diamond- and graphite-peridotite xenoliths from the Roberts Victor mine. In: Meyer HOA, Leonardos OH (eds), *Proceedings of the 5th International Kimberlite Conference*, Vol 1/A, pp. 285-303
- Viljoen KS, Schulze DUJ, Quadling AG (2005) Contrasting Group I and Group II eclogite xenolith petrogenesis: petrological, trace element and isotopic evidence from eclogite, garnet-websterite and alkremite xenoliths in the Kaalvallei kimberlite, South Africa. *Journal of Petrology* 46:2059-2090
- Walter MJ (1998) Melting of garnet peridotite and the origin of komatiite and depleted lithosphere. *Journal of Petrology* 39:29-60
- Warren JM (2016) Global variations in abyssal peridotite compositions. *Lithos* 248-251:193-219
- Wasylenki LE, Baker MB, Kent AJ, Stolper EM (2003) Near-solidus melting of the shallow upper mantle: partial melting experiments on depleted peridotite. *Journal of Petrology* 44:1163-1191
- Weyer S, Münker C, Mezger K (2003) Nb/Ta, Zr/Hf and REE in the depleted mantle: implications for the differentiation history of the crust-mantle system. *Earth and Planetary Science Letters* 205:309-324
- Workman RK, Hart SR (2005) Major and trace element composition of the depleted MORB mantle (DMM). *Earth and Planetary Science Letters* 231:53-72

- Wostbrock JAG, Sharp ZD, Sanchez-Yanez C, Reich M, van den Heuvel DB, Benning LG (2018) Calibration and application of silica-water triple oxygen isotope thermometry to geothermal systems in Iceland and Chile. *Geochimica et Cosmochimica Acta* 234:84-97
- Yaxley GM, Green DH (1998) Reactions between eclogite and peridotite: mantle refertilisation by subduction of oceanic crust. *Schweizerische Mineralogische und Petrographische Mitteilungen* 78:243–255
- Yui T-F, Rumble III D, Lo C-H (1995) Unusually low $\delta^{18}\text{O}$ ultra-high-pressure metamorphic rocks from the Sulu Terrain, eastern China. *Geochimica et Cosmochimica Acta* 59:2859-2864
- Zheng Y-F, Fu B, Gong B, Li S (1996) Extreme ^{18}O depletion in eclogite from the Su-Lu terrane in East China. *European Journal of Mineralogy* 8:317-323

Appendix A

Tables accompanying Chapter 2. The complete dataset is available through the University of Alberta UAL Dataverse as “Matthew F Hardman PhD thesis Supplementary Online Dataset” (<https://doi.org/10.7939/DVN/XULIRM>).

Table A.1 General garnet chemical formula and commonly substituting cations.

General garnet formula: $X_3Y_2Z_3O_{12}$	
Cation site	Cations
X site	Fe^{2+} , Mg, Ca, Mn, Na
Y site	Al, Cr, Ti, Fe^{3+}
Z site	Si, P

Table A.2 Analytical conditions for analysis of garnet and clinopyroxene by EPMA, including crystal setup and reference materials for garnet and clinopyroxene. Reference materials are described in footnotes to the table. Most samples were analysed by a 2 µm focused electron beam operated at 20 kV accelerating voltage and 20 nA current. For Chapter 4, a small subset of Roberts Victor eclogites were analysed using modified conditions: a 20 µm beam was operated at 20 kV and 50 nA. On-peak count times and average lower limits of detection (LLD) are given for both conditions. Combined off-peak count times are equal to the on-peak count times.

Element	Crystal	On-peak count time (s)	Average LLD (oxide wt%)	On-peak count time (s), modified conditions	Average LLD (oxide wt%), modified conditions	Garnet reference material	Clinopyroxene reference material
Si	TAP	40	0.02	20	0.01	1. Frank Smith pyrope garnet	13. Diopside
Ti	PET	30	0.02	60	0.010	2. Rutile	2. Rutile
Al	TAP	40	0.01	20	0.01	1. Frank Smith pyrope garnet	1. Frank Smith pyrope garnet
V	PET	30	0.02	20	0.02	3. Vanadium	3. Vanadium
Cr	PET	30	0.03	20	0.02	4. Chromium oxide	4. Chromium oxide
Fe	LIFH	30	0.01	20	0.01	5. Fayalite	5. Fayalite
Ni	LIFH	30	0.02	20	0.01	6. Nickel wire	6. Nickel wire
Mn	LIFH	30	0.02	20	0.01	7. Spessartine	7. Spessartine
Mg	TAP	30	0.02	20	0.01	1. Frank Smith pyrope garnet	13. Diopside
Ca	PETH	30	0.01	20	0.01	8. Labradorite	13. Diopside
Na	TAP	60	0.01	120	0.007	9. Albite	9. Albite
K	PETH	30	0.01	20	0.01	10. Sanidine	10. Sanidine
P	PETH	30	0.03	80	0.011	11. Apatite	11. Apatite
Nb	PETH	30	0.05	<i>na</i>	<i>na</i>	12. Niobium	12. Niobium

na not analysed

1. Frank Smith pyrope garnet: Frank Smith kimberlite, South Africa. Royal Ontario Museum collection
2. Rutile: synthetic rutile standard from MTI corporation (<http://www.mtixtl.com/tio2substrates.aspx>)
3. Vanadium: synthetic standard from Alfa Aesar
4. Chromium oxide: synthetic. Alfa Aesar. Sample ID 36258, 99.6 % purity (metals basis)
5. Fayalite: Rockport, Massachusetts, USA. Sample ID USNM 85276. Similar to Jarosewich *et al.* (1980)
6. Nickel wire: synthetic. Alfa Aesar, 43132. Nickel wire, 0.5 mm dia, annealed, 99.98 % (metals basis)
7. Spessartine: Little Three, California. Similar to Morgan and London (1999)
8. Labradorite: Lake County, Oregon, USA. Sample ID USNM 115900. Similar to Jarosewich *et al.* (1980)
9. Albite: Virginia, USA. Sample ID USNM 115900. Similar to Jarosewich *et al.* (1980)
10. Sanidine: Fe-bearing K-feldspar. Itrongay, Madagascar. Similar to Ackermann *et al.* (2005)
11. Apatite: Apatite from alkaline source. Dwyer Mine, Wilberforce, Ontario, Canada. Similar to Tacker (2004)
12. Niobium: synthetic niobium standard.
13. Diopside: Wakefield, Quebec, Canada. Astimex, palest blue (<http://astimex.com/com/catalog/min.html>)

Table A.3 Calculation of chemical variables used in this study. Cation data can be used as-is. Data as oxide wt% must be converted using the listed Factor.

Using Cations	Using Oxides	
	Oxides (wt%)	Factor ^a
Mg/Fe	MgO/FeO	1.782
Ti/Si	TiO ₂ /SiO ₂	0.752
Al/Si	Al ₂ O ₃ /SiO ₂	1.179
Cr/Si	Cr ₂ O ₃ /SiO ₂	0.791
Mn/Si	MnO/SiO ₂	0.847
Fe/Si	FeO/SiO ₂	0.836
Mg/Si	MgO/SiO ₂	1.491
Ca/Si	CaO/SiO ₂	1.071
Na/Si	Na ₂ O/SiO ₂	1.939

^aThe factor is multiplied by the ratio of the relevant oxides. The factor is calculated from the inverted ratio of the atomic weights of the elements that are being recalculated.

Table A.4 Y-intercept (B) values for all curves in Figure 2.5A. The equations have the form $\ln(\text{Mg}/\text{Fe}) = (-2.325/6) \times \ln(\text{Ti}/\text{Si}) + B$, with B listed in this table. CI refers to the Confidence Interval.

Curve	B (Y-intercept)
Decision boundary	-2.433
5 % crustal CI, enclosing crustal misclassifications	-2.080
10 % crustal CI, enclosing crustal misclassifications	-0.890
5 % mantle CI, enclosing mantle misclassifications	-2.735
10 % mantle CI, enclosing mantle misclassifications	-4.200

Table A.5 Coefficient of determination (R^2) and variance inflation factor (VIF) values for combinations of discriminant variables used in statistical methods in this study.

		ln(Ti/Si)	ln(Al/Si)	ln(Cr/Si)	ln(Mn/Si)	ln(Fe/Si)	ln(Mg/Si)	ln(Ca/Si)	ln(Na/Si)
ln(Ti/Si)	R^2	-	1.178E-04	0.154	0.070	0.195	0.095	0.097	0.415
	VIF	-	1.000	1.182	1.075	1.243	1.105	1.108	1.708
ln(Al/Si)	R^2	1.178E-04	-	3.630E-05	1.373E-08	3.349E-05	0.038	0.008	0.001
	VIF	1.000	-	1.000	1.000	1.000	1.040	1.008	1.001
ln(Cr/Si)	R^2	0.154	3.630E-05	-	0.070	0.333	0.243	1.949E-6	0.096
	VIF	1.182	1.000	-	1.075	1.498	1.320	1.000	1.106
ln(Mn/Si)	R^2	0.070	1.373E-08	0.070	-	0.340	0.361	0.030	0.083
	VIF	1.075	1.000	1.075	-	1.516	1.564	1.031	1.090
ln(Fe/Si)	R^2	0.195	3.349E-05	0.333	0.340	-	0.354	0.086	0.149
	VIF	1.243	1.000	1.498	1.516	-	1.548	1.094	1.176
ln(Mg/Si)	R^2	0.095	0.038	0.243	0.361	0.354	-	0.026	0.094
	VIF	1.105	1.040	1.320	1.564	1.548	-	1.027	1.104
ln(Ca/Si)	R^2	0.097	0.008	1.949E-06	0.030	0.086	0.026	-	0.033
	VIF	1.108	1.008	1.000	1.031	1.094	1.027	-	1.034
ln(Na/Si)	R^2	0.415	0.001	0.096	0.083	0.149	0.094	0.033	-
	VIF	1.708	1.001	1.106	1.090	1.176	1.104	1.034	-

- not applicable

Table A.6 “R” runstreams for derivation of statistical methods in Chapter 2

Required information for all garnet data in data sheet	Description
Group	“Crust” or “Mantle”
Probability	Crust = 0 Mantle = 1
Data for chemical variables (see Table A.3)	ln(Ti/Si), ln(Al/Si), ln(Cr/Si), ln(Mn/Si), ln(Fe/Si), ln(Mg/Si), ln(Ca/Si), ln(Na/Si)
<hr/>	
Import R, and import data	Description
Install R (version 3.5.0)	https://www.r-project.org/
Install RStudio	https://www.rstudio.com/
Import calibration dataset as .csv (e.g., data.csv)	Dataset contains garnet data in rows. Columns include “Group” (crust or mantle), “Probability” (0 or 1), and data for the variables ln(Ti/Si), etc.
<hr/>	
R commands to generate linear discriminant analysis solution (Equation 2.6)	Description
> library(MASS)	Load the MASS library so that the necessary functions for LDA are loaded. Install MASS first, if not already installed
> data.lda = lda(data\$Probability ~ data\$lnTiSi + data\$lnAlSi + data\$lnCrSi + data\$lnMnSi + data\$lnFeSi + data\$lnMgSi + data\$lnCaSi + data\$lnNaSi)	Generate the LDA solution using the input variables in data.csv
> data.lda	View details of the LDA solution, including the coefficients of linear discriminants for the input variables
> data.lda.values = predict(data.lda, data[x:y])	Calculate the d_{CM-LDA} value for a garnet by multiplying its compositional variables (ln[Ti/Si], etc.) by the respective coefficient of linear discriminants. This can also be calculated using “R” directly using the following command. The [x:y] portion of the command refers to the column numbers, as a range, that contain the input variables (i.e., ln[Ti/Si], etc.). A binary decision boundary of $d_{CM-LDA} = -0.264$ is chosen by noting the intersection of crust and mantle density curves for data.lda.values. Samples with $d_{CM-LDA} < -0.264$ are classified as “Crustal,” and samples with $d_{CM-LDA} > -0.264$ are classified as “Mantle.”
<hr/>	
R commands to generate logistic regression solution (Equation 2.7)	Description
> data.lr = glm(data\$Probability ~ data\$lnTiSi + data\$lnAlSi + data\$lnCrSi + data\$lnMnSi + data\$lnFeSi + data\$lnMgSi + data\$lnCaSi + data\$lnNaSi, family = binomial(), data = data)	Generate the LR solution using the input variables in data.csv
> data.lr	View details, including coefficients for the input variables
> data.lr.values = predict(data.lr, data[x:y])	Calculate the d_{CM-LR} value for a garnet by multiplying its compositional variables (ln[TiSi], etc.) by the respective coefficient. This can also be calculated using “R” directly using the given command. A binary decision boundary of $d_{CM-LR} = 0.260$ is chosen by noting the intersection of crust and mantle density curves for data.lr.values. Samples with $d_{CM-LR} < 0.260$ are classified as “Crustal” and samples with $d_{CM-LR} > 0.260$ are classified as “Mantle.”

Table A.7 Error rates for numerous methods using the calibration dataset, showing the number (N) of crust and mantle garnets that classify as crust or mantle using each scheme

Method		Crust	Mantle	Error rate (%)
Schulze (2003; Figure 8 therein)	Crust	959	617	39.15
	Mantle	23	2097	1.08
	Overall:			17.32
Sodium in garnet ($\text{Na}_2\text{O}_{\text{grt}} = 0.07$ wt% cut-off); Sobolev and Lavrent'ev (1971), Gurney (1984)	Crust	1491	85	5.39
	Mantle	992	1128	46.79
	Overall:			29.14
Graphical method (Figure 2.5A and Equation 2.3, this study); y-intercept = -2.433	Crust	1418	158	10.03
	Mantle	215	1905	10.14
	Overall:			10.09
Graphical method (Figure 2.5A and Equation 2.4, this study); y-intercept = -3.151	Crust	1046	530	33.63
	Mantle	43	2077	2.03
	Overall:			15.50
Linear discriminant analysis (Equation 2.6, this study)	Crust	1447	128	8.12
	Mantle	167	1954	7.88
	Overall:			7.98
Logistic regression (Equation 2.7, this study); d = 0.000	Crust	1455	120	7.61
	Mantle	152	1968	7.17
	Overall:			7.36
Logistic regression (Equation 2.7, this study); d = -1.650	Crust	1245	331	21.00
	Mantle	43	2077	2.03
	Overall:			10.12

Table A.8 Error rates for numerous methods, assessed by k-fold cross validation (10 folds). The overall error rate of each method (the “Method uncertainty”) is the average ($\pm 2\sigma$; 95 %) of the error rates for the 10 folds (K1 through K10).

Method		K1 test data			K2 test data			K3 test data		
		Crust	Mantle	Error rate (%)	Crust	Mantle	Error rate (%)	Crust	Mantle	Error rate (%)
Schulze (2003; Figure 8 therein)	Crust	189	126	40.00	204	128	38.55	187	123	39.68
	Mantle	2	422	0.47	5	402	1.23	4	425	0.93
	Overall			17.32			18.00			17.19
Graphical method (Figure 2.5A and Equation 2.3, This Study)	Crust	271	44	13.97	291	41	12.35	282	28	9.03
	Mantle	41	383	9.67	45	362	11.06	35	394	8.16
	Overall			11.50			11.64			8.53
Linear discriminant analysis (Equation 2.6, This Study)	Crust	274	41	13.02	307	25	7.53	289	21	6.77
	Mantle	34	390	8.02	45	362	11.06	30	399	6.99
	Overall			10.15			9.47			6.90
Logistic regression (Equation 2.7, This Study); $d = 0.000$	Crust	275	40	12.70	309	23	6.93	287	23	7.42
	Mantle	30	394	7.08	40	367	9.83	27	402	6.29
	Overall			9.47			8.53			6.77

Method		K4 test data			K5 test data			K6 test data		
		Crust	Mantle	Error rate (%)	Crust	Mantle	Error rate (%)	Crust	Mantle	Error rate (%)
Schulze (2003; Figure 8 therein)	Crust	187	112	37.46	188	128	40.51	185	123	39.94
	Mantle	1	439	0.23	4	419	0.95	5	426	1.16
	Overall			15.29			17.86			17.32
Graphical method (Figure 2.5A and Equation 2.3, This Study)	Crust	275	24	8.03	286	30	9.49	275	33	10.71
	Mantle	57	383	12.95	39	384	9.22	32	399	7.42
	Overall			10.96			9.34			8.80
Linear discriminant analysis (Equation 2.6, This Study)	Crust	280	19	6.35	291	25	7.91	277	31	10.06
	Mantle	46	394	10.45	35	388	8.27	23	408	5.34
	Overall			8.80			8.12			7.31
Logistic regression (Equation 2.7, This Study); $d = 0.000$	Crust	283	16	5.35	294	22	6.96	278	29	9.74
	Mantle	41	399	9.32	31	392	7.33	21	410	4.87
	Overall			7.71			7.17			6.77

Table A.8 continued

Method		K7 test data			K8 test data			K9 test data		
		Crust	Mantle	Error rate (%)	Crust	Mantle	Error rate (%)	Crust	Mantle	Error rate (%)
Schulze (2003; Figure 8 therein)	Crust	202	110	35.26	206	109	34.60	188	131	41.07
	Mantle	5	422	1.17	10	414	2.36	4	416	0.95
	Overall			15.56			16.10			18.27
Graphical method (Figure 2.5A and Equation 2.3, This Study)	Crust	288	24	7.69	289	26	8.25	283	36	11.29
	Mantle	49	378	11.48	51	373	12.03	44	376	10.48
	Overall			9.88			10.42			10.83
Linear discriminant analysis (Equation 2.6, This Study)	Crust	290	22	7.05	297	18	5.71	292	27	8.46
	Mantle	43	384	10.07	37	387	8.73	36	384	8.57
	Overall			8.80			7.44			8.53
Logistic regression (Equation 2.7, This Study); $d = 0.000$	Crust	296	16	5.13	299	16	5.08	294	25	7.84
	Mantle	42	385	9.84	31	393	7.31	33	387	7.86
	Overall			7.85			6.36			7.85

Method		K10 test data			Method Uncertainty	
		Crust	Mantle	Error rate (%)	Mean Error (%)	2σ (%)
Schulze (2003; Figure 8 therein)	Crust	172	130	43.05		
	Mantle	5	432	1.14		
	Overall			18.27	17.12	2.08
Graphical method (Figure 2.5A and Equation 2.3, This Study)	Crust	271	31	10.26		
	Mantle	37	400	8.47		
	Overall			9.20	10.11	2.13
Linear discriminant analysis (Equation 2.6, This Study)	Crust	281	21	6.95		
	Mantle	26	411	5.95		
	Overall			6.36	8.19	2.27
Logistic regression (Equation 2.7, This Study); $d = 0.000$	Crust	279	23	7.62		
	Mantle	26	411	5.95		
	Overall			6.63	7.51	1.86

Table A.9 Error rates of crust, mantle, and megacryst garnets when applied to mantle-megacryst discrimination methods in the literature. Error rates are not reported for the Rogers and Grütter (2009) method as the G1R category is additional to the G1 category of Grütter *et al.* (2004). The error rates for the combination of the Grütter *et al.* (2004) and Rogers and Grütter (2009) methods are calculated based on the sequence of classification proposed by Rogers and Grütter (2009), which is G1 followed by G1R.

Method	Schulze (2003; Figure 8 therein)			Grütter <i>et al.</i> (2004; Section 4.4 therein)			Rogers and Grütter (2009; Section 3.4 therein)			Grütter <i>et al.</i> (2004) and Rogers and Grütter (2009)		
	Mantle	Megacryst	Error rate (%)	Mantle	Megacryst (G1)	Error rate (%)	Mantle	Megacryst (G1R)	Error rate (%)	Mantle	Megacryst (G1 + G1R)	Error rate (%)
Crust (N = 1576)	1576	0	-	1576	0	-	1576	0	-	1576	0	-
Mantle (N = 2120)	2042	78	3.68	2062	58	2.74	1995	125	-	1937	183	8.63
Megacryst (N = 177)	4	173	2.26	15	162	8.47	163	14	-	1	176	0.56

- not applicable

Appendix B

Tables accompanying Chapter 3. The complete dataset is available through the University of Alberta UAL Dataverse as “Matthew F Hardman PhD thesis Supplementary Online Dataset” (<https://doi.org/10.7939/DVN/XULIRM>).

Table B.1 Derivation of trace-element decision tree based on the statistical method Classification and Regression Trees (CART), using R (version 3.5.0).

Procedure	Description
Install R (version 3.5.0)	https://www.r-project.org/
Install Rstudio	https://www.rstudio.com/
Import calibration dataset as .csv (e.g., data.csv)	Dataset contains garnet data in rows. Columns include “Group” (crust or mantle), “Sr” (Sr as ppm, rounded to 0.00x figures), and “EuAnomaly” (Eu/Eu* rounded to 0.0x figures. Eu* calculated as $0.5 \times [Sm_N + Gd_N]$)
Text commands into R	Description
> library(rpart)	Load the rpart library to generate a CART tree, if the library rpart is installed
> tree = rpart(data\$Group ~ data\$Sr + data\$EuAnomaly)	Derives the details of the decision tree using the CART method (named “tree”)
> plot(tree)	Draws the decision tree
> text(tree)	Writes conditional statements to the drawn tree

Table B.2 Classification error rates for the full dataset using various crustal-mantle garnet classification methods in this study, and Schulze (2003).

Dataset	Ca# vs Mg#, Schulze (2003)			Equation 3.1, this study			Figure 3.5, this study		
	Correct (N)	Errors (N)	Error rate ^a (%)	Correct (N)	Errors (N)	Error rate (%)	Correct (N)	Errors (N)	Error rate (%)
Crustal garnets	65	102	61.1	144	23	13.8	139	28	16.8
Mantle garnets	573	0	0.0	549	24	4.2	566	7	1.2
All garnets	638	102	13.8	693	47	6.4	705	35	4.7

^aError rates are given as classification error (CE) using the calibration dataset in this study. CE is calculated as the number of misclassified samples/total number of samples x 100 %.

Table B.3 Specifications for the k-fold cross-validation assessment of the new CART-based decision tree. K-fold cross-validation is applied to the new decision tree only. Therefore, the computed error rate corresponds only to the trace-element CART tree for those garnets initially classified as "crustal" using Equation 3.1. Garnets used are those classified as “crustal” using Equation 3.1 (N = 168), which comprises 144 crustal garnets (crustal true positives) and 24 mantle garnets (crustal false positives).

K-fold cross-validation specifications	
Total N = 168 garnets	
Number of folds = 10	
Calibration data = 80 % (N = 134)	
Validation data = 20 % (N = 34)	
Fold	Error rate (%)
K1	17.6
K2	14.7
K3	5.9
K4	5.9
K5	11.8
K6	17.6
K7	2.9
K8	11.8
K9	5.9
K10	5.9
Average error rate	10.6 ± 10.4 % (2σ)

Appendix C

Tables accompanying Chapter 4. The complete dataset is available through the University of Alberta UAL Dataverse as “Matthew F Hardman PhD thesis Supplementary Online Dataset” (<https://doi.org/10.7939/DVN/XULIRM>).

Table C.1 Compilation of petrographic and geochemical characteristics of Group I and II eclogites from Roberts Victor, from published literature

	Group I eclogites	Group II eclogites
Texture		
Grain shape	Subhedral/rounded garnets within a matrix of interstitial clinopyroxene	Garnet and clinopyroxene have equilibrium-type textures: straight interlocking grain boundaries, ~ 120° triple junctions
Fluid inclusions, melt pockets	Fluid inclusions or melt pockets in minerals occasionally reported	Fluid inclusions or melt pockets in minerals not reported
Mineral exsolution	Uncommonly reported	Garnet or kyanite may occur as exsolutions in clinopyroxene. Clinopyroxene may occasionally occur as an exsolution in garnet. Rutile exsolutions in garnet and clinopyroxene are commonly reported
Accessory minerals		
Diamond	Diamond occasionally reported	Diamond not reported
Rutile	Occasionally reported as accessory phase. Rutile exsolutions in garnet or clinopyroxene not reported	Not reported as accessory phase. Reported as exsolutions (typically needles) in garnet and clinopyroxene
Phlogopite	Primary phlogopite occasionally reported	No primary phlogopite reported
Additional accessory phases	Reasonably common Include coesite, rutile, corundum, kyanite, sanidine	Rare Include corundum, kyanite, coesite
Elemental chemistry		
Major- and minor-elements	Na ₂ O-in-grt ≥ 0.07 wt% K ₂ O-in-cpx ≥ 0.08 wt%	Na ₂ O-in-grt < 0.07 wt% K ₂ O-in-cpx < 0.08 wt%
Trace-elements	Higher whole-rock LREE, HFSE, and LILE contents than Group II eclogites	Lower whole-rock LREE, HFSE, and LILE contents than Group I eclogites
Isotopic chemistry		
δ ¹⁸ O (garnet)	5.0 to 9.1 ‰, average 6.4 ± 1.4 ‰	1.1 to 6.6 ‰, average 3.5 ± 2.4 ‰
Whole-rock (⁸⁷ Sr/ ⁸⁶ Sr); (128 Ma)	0.70605 to 0.70749	0.70135 to 0.70324
Whole-rock (¹⁴³ Nd/ ¹⁴⁴ Nd); (128 Ma)	0.51199 to 0.51402	0.51656 to 0.52950
Whole-rock (¹⁷⁶ Hf/ ¹⁷⁷ Hf); (128 Ma)	0.28225 to 0.28296	0.28508 to 0.30318
Garnet-clinopyroxene isochron ages	Sm-Nd ~ 103 Ma Lu-Hf ~ 132 Ma	Sm-Nd ~ 800 Ma Lu-Hf ~ 1300 Ma

Data sources: MacGregor and Carter (1970); Garlick *et al.* (1971); McCandless and Gurney (1989); Jacob *et al.* (2005); Gréau *et al.* (2011); Huang *et al.* (2012a); Huang *et al.* (2016); Radu *et al.* (2019)

Table C.2 Hand sample petrography and calculated pressure-temperature conditions of eclogite xenoliths in this study. Group II eclogite textures are described in more detail in Table C.3.

Sample ID	Group	Lithology	Grt	Cpx	San	Ky	SiO ₂	Rut	Texture	T (°C) ^a	P (kbar) ^a
RV-1	II _L	eclogite	45	55	-	-	-	-	<i>See Table C.3</i>	1226	60.3
RV-3	I	eclogite	50	50	-	-	-	trace	Cpx highly altered, preserved cpx occasionally visible	1142	54.9
RV-4	II _F	eclogite	40	60	-	-	-	-	Subhedral grt, occasional straight grain boundaries with cpx; weak triple junctions visible	1055	49.5
RV-5	I	eclogite	50	50	-	-	-	-	Rounded to irregular grt in cpx matrix	1196	58.4
RV-6	I	eclogite	40	60	-	-	-	-	Rounded to irregular grt in cpx matrix	997	45.9
RV-7	I	eclogite	40	60	-	-	-	-	Rounded to irregular grt in cpx matrix. Cpx highly altered	1292	64.5
RV-8	I	eclogite	45	55	-	-	-	-	Rounded grt in cpx matrix. Rare euhedral grt in cpx matrix	1247	61.6
RV-9	I	eclogite	50	50	-	-	-	-	Rounded to irregular grt in cpx matrix. Mica present	1135	54.5
RV-10	II _L	eclogite	45	55	-	-	-	-	<i>See Table C.3</i>	1069	50.3
RV-11	I	eclogite	48	52	-	-	-	-	Irregular grt in cpx matrix. Cpx altered, cores rarely pristine	1147	55.3
RV-12	I	eclogite	55	45	-	-	-	-	Irregular grt in cpx matrix. Mica present	1082	51.2
RV-13	I	eclogite	55	45	-	-	-	-	Irregular grt in cpx matrix. Cpx altered to grey, rare pristine cpx is pale green	1228	60.4
RV-14	II _L	eclogite	45	55	-	-	-	-	<i>See Table C.3</i>	1105	52.7
RV-15	I	eclogite	80	20	-	-	-	-	Irregular grt and cpx	1117	53.4
RV-16	I	eclogite	40	60	trace	-	-	trace	Rounded to irregular grt in cpx matrix	1038	48.4
RV-17	I	eclogite	50	50	-	-	-	-	Rounded to irregular grt in cpx matrix	1075	50.7
RV-18	I	eclogite	60	40	-	-	-	-	Irregular grt in cpx matrix. Cpx irregular in shape, bright green colour	1193	58.2
RV-19	I	eclogite	40	60	trace	-	-	-	Irregular grt in cpx matrix. Mica present	1161	56.2
RV-20	II _L	eclogite	50	50	-	-	-	-	<i>See Table C.3</i>	1092	51.8
RV-21	I	eclogite	40	60	-	-	-	-	Irregular grt in cpx matrix	1120	53.6
RV-22	II _L	eclogite	40	60	-	-	-	-	<i>See Table C.3</i>	1116	53.3
RV-23	I	eclogite	60	40	-	-	-	-	Irregular grt in cpx matrix. Cpx is moderately altered	1248	61.7
RV-24	I	eclogite	50	50	-	-	-	-	Subhedral grt in cpx matrix. Cpx is moderately altered. Mica present	946	42.7
RV-25	I	eclogite	60	40	-	-	-	-	Irregular grt in cpx matrix. Small black minerals on grt edges	1092	51.8
RV-26	I	eclogite	45	55	-	trace	-	-	Rounded to irregular grt in cpx matrix. Cpx heavily altered, pale green colour	1262	62.6
RV-27	II _F	eclogite	40	60	-	-	trace	-	<i>See Table C.3</i>	913	40.6
RV-28	-	eclogite	50	50	-	-	trace	-	Cpx is moderately altered. Sample is too small for further description	1158	56.0
RV-29	I	eclogite	65	35	-	trace	-	-	Irregular grt in cpx matrix. Cpx is heavily altered	1252	61.9
RV-30	I	eclogite	50	50	-	-	-	-	Rounded to irregular grt in cpx matrix	1171	56.8
RV-31	I	eclogite	40	60	-	-	-	-	Irregular grt in cpx matrix. Mica present	1212	59.4
RV-32	I	eclogite	45	55	-	-	-	-	Subhedral grt in cpx matrix	1113	53.1
RV-33	I	eclogite	45	55	-	-	-	-	Rounded to irregular grt in cpx matrix	1151	55.5
RV-34	I	eclogite	40	60	-	-	-	-	Rounded to irregular grt in cpx matrix	1146	55.2
RV-35	I	eclogite	50	50	-	-	-	-	Irregular grt in cpx matrix. Minor calcite on xenolith exterior	1209	59.2
RV-36	I	eclogite	50	50	-	-	-	-	Rounded grt in cpx matrix	1167	56.5
RV-37	I	eclogite	45	55	-	-	-	-	Subrounded grt in cpx matrix. Cpx is moderately altered. Mica present	1121	53.7
RV-38	I	eclogite	50	50	-	-	-	-	Irregular grt in cpx matrix. Small black minerals on grt edges	1109	52.9
RV-39	I	eclogite	40	60	-	-	-	trace	Irregular grt in cpx matrix. Cpx is moderately altered	1185	57.7
RV-40	I	eclogite	45	55	-	-	-	-	Irregular grt in cpx matrix. Cpx is moderately altered. Mica present	1142	55.0
RV-41	I	eclogite	60	40	-	-	-	-	Rounded to subrounded grt in cpx matrix. Small black minerals on grt edges	1123	53.7
RV-42	I	eclogite	37	63	-	-	-	-	Rounded grt in cpx matrix	1120	53.6
RV-43	I	eclogite	53	47	-	-	-	-	Irregular grt in cpx matrix	1216	59.7
RV-44	I	eclogite	50	50	-	-	-	-	Irregular grt in cpx matrix. Cpx is moderately altered	1152	55.6

Table C.2 continued

Sample ID	Group	Lithology	Grt	Cpx	San	Ky	SiO ₂	Rut	Notes	T (°C) ¹	P (kbar) ¹
RV-45	I	eclogite	45	55	-	-	-	-	Rounded grt in cpx matrix. Cpx is heavily altered. Mica present	1155	55.8
RV-46	I	eclogite	45	55	-	-	-	-	Rounded to irregular grt in cpx matrix	1078	50.9
RV-47	I	eclogite	47	53	-	-	-	-	Rounded to irregular grt in cpx matrix	1102	52.4
RV-48	I	eclogite	50	50	-	-	-	-	Irregular grt in cpx matrix. Cpx is heavily altered. Mica present	1108	52.8
RV-49	I	eclogite	45	55	-	-	-	trace	Irregular grt in cpx matrix. Cpx is heavily altered. Cpx is pale green to grey	1249	61.8
RV-50	I	eclogite	35	65	-	trace	-	-	Subrounded to irregular grt in cpx matrix	1171	56.8
RV-51	I	eclogite	55	45	-	-	-	-	Irregular grt in cpx matrix. Cpx is heavily altered	1159	56.0
RV-52	I	eclogite	45	55	-	-	-	-	Subrounded to subhedral grt in cpx matrix. Small black minerals on grt edges	1176	57.1
RV-53	I	eclogite	45	55	-	-	-	-	Rounded to subrounded grt in cpx matrix. Mica present	1119	53.5
RV-54	II _L	eclogite	50	50	-	-	-	-	See Table C.3	1273	63.3
RV-55	I	eclogite	55	45	-	-	-	-	Irregular grt in cpx matrix. Cpx irregular in shape	1121	53.6
RV-56	I	eclogite	50	50	-	-	trace	-	Rounded to subrounded grt in cpx matrix. Cpx is moderately altered; small black minerals on grt edges	1158	56.0
RV-57	I	eclogite	39	59	-	-	trace	-	Subhedral grt in cpx matrix. Cpx is moderately altered. Mica present	1147	55.3
RV-58	I	eclogite	47	53	-	-	-	-	Rounded to irregular grt in cpx matrix. Mica present	1209	59.2
RV-59	I	eclogite	50	50	-	-	-	-	Rounded to subrounded grt in cpx matrix. Cpx is moderately altered; small black minerals on grt edges	1076	50.8
RV-60	II _L	eclogite	50	50	-	-	-	-	See Table C.3	1176	57.1
RV-61	I	eclogite	50	50	-	-	-	-	Irregular grt in cpx matrix. Cpx is moderately altered. Small black minerals on grt edges	900	39.9
RV-62	II _L	eclogite	50	50	-	-	-	-	See Table C.3	1117	53.4
RV-63	I	eclogite	45	55	-	-	-	-	Subrounded grt in cpx matrix. Cpx is pale green	1054	49.4
RV-64	I	eclogite	45	55	-	-	-	-	Subrounded to irregular grt in cpx matrix. Mica present	1153	55.7
RV-65	I	eclogite	50	50	-	-	-	-	Irregular grt in cpx matrix. Cpx is heavily altered. Small black minerals on grt edges. Mica present	1083	51.2
RVSA71	I	eclogite	50	50	-	-	-	-	Irregular grt in cpx matrix	949	42.9

¹Temperatures (T) are calculated using the Krogh (1988) thermometer, and pressures (P) by extrapolation to the Hasterok and Chapman (2011) 38 mw/m² model geotherm
Abbreviations: Cpx = clinopyroxene, Grt = garnet, Ky = kyanite, Rut = rutile, San = sanidine, SiO₂ = quartz/coesite

Table C.3 Detailed petrography of thin sections for select Roberts Victor eclogites in this study

Sample	Lithology	Group	Grt	Cpx	San	Ky	SiO ₂	Rut
RV-1	eclogite	II _L	45	55	-	-	-	-
Thin section textures								
Garnet occurs primarily as large (up to ~ 3000 μm) anhedral to subhedral grains that interlock with anhedral to subhedral clinopyroxene, sharing straight grain boundaries and inter-grain triple junctions (~ 120 °). Clinopyroxene cores are often pristine with omphacitic chemistry, while grain edges are often highly-altered with a “spongy” texture and diopsidic chemistry. Spongy textures also occur along cross-cutting fractures through clinopyroxene grains. Garnet grains with a “rod-like” shape – ~ 150 μm thick and up to 1100 μm long, with straight edges - occur occasionally within clinopyroxene. Rutile commonly occurs as needle-like inclusions (< 100 μm long) in garnet and clinopyroxene. These needles are often orientated relative to one another. Rutile needles do not occur in garnet grains that are themselves included within clinopyroxene. Rutile also occurs as sub-rounded inclusions (< 120 μm in maximum dimension) along garnet/clinopyroxene grain boundaries (intergranular). The intergranular rutile often have ilmenite rims and occasional ilmenite exsolution lamellae. Additional intergranular minerals include spinel and plagioclase, which are often intergrown with each other, with intergranular rutile, and with spongy clinopyroxene.								
Sample	Lithology	Group	Grt	Cpx	San	Ky	SiO ₂	Rut
RV-10	eclogite	II _L	45	55	-	-	-	-
Thin section textures								
Garnet occurs primarily as large (up to ~ 4000 μm) anhedral to subhedral grains that interlock with anhedral to subhedral clinopyroxene, sharing straight grain boundaries and inter-grain triple junctions (~ 120°). Clinopyroxene cores are often pristine with omphacitic chemistry, while grain edges are often highly-altered with a “spongy” texture and diopsidic chemistry. Spongy textures also occur along cross-cutting fractures through clinopyroxene grains. The RV-10 thin section contains a large poikilitic clinopyroxene grain (up to 1.5 cm in maximum dimension). Small sub-rounded garnets rarely occur within this grain (up to 500 μm in maximum dimension). Rutile commonly occurs as needle-like inclusions (< 100 μm in length) in garnet and clinopyroxene, including one elongate rutile needle within clinopyroxene that is ~ 10 μm thick and ~ 900 μm long. The rutile needles are often orientated relative to one another. Rutile needles do not occur in garnet grains that are themselves included within clinopyroxene. In one instance, a rutile needle is observed to be touching an irregularly-shaped garnet inclusion within a single clinopyroxene grain. Rutile also occurs as intergranular sub-rounded inclusions (< 200 μm) along garnet/clinopyroxene grain boundaries (intergranular). The intergranular rutile often have ilmenite rims and occasional ilmenite exsolution lamellae. Additional intergranular minerals include spinel, amphibole, and plagioclase, which are often intergrown with each other, with intergranular rutile, and with spongy clinopyroxene.								

Table C.3 continued

Sample	Lithology	Group	Grt	Cpx	San	Ky	SiO ₂	Rut
RV-14	eclogite	II _L	45	55	-	-	-	-

Thin section textures

Garnet occurs primarily as large (up to ~ 4000 μm) anhedral to subhedral grains that interlock with anhedral to subhedral clinopyroxene, sharing straight grain boundaries and inter-grain triple junctions (~ 120°). Clinopyroxene cores are often pristine with omphacitic chemistry, while grain edges are often highly-altered with a “spongy” texture and diopsidic chemistry. Spongy textures also occur along cross-cutting fractures through clinopyroxene grains. Garnet occurs occasionally as subrounded inclusions in clinopyroxene (< 100 μm in maximum dimension). Rutile commonly occurs as needle-like inclusions (< 100 μm) in garnet and clinopyroxene. The rutile needles are often orientated relative to one another. Rutile needles do not occur in garnet grains that are themselves included within clinopyroxene. Rutile also occurs as sub-rounded inclusions (< 150 μm) along garnet/clinopyroxene grain boundaries (intergranular). The intergranular rutile often have ilmenite rims and occasional ilmenite exsolution lamellae. Additional intergranular minerals include spinel, amphibole, Fe-sulfide, celestine, and plagioclase, which are often intergrown with each other, with intergranular rutile, and with spongy clinopyroxene.

Sample	Lithology	Group	Grt	Cpx	San	Ky	SiO ₂	Rut
RV-20	eclogite	II _L	50	50	-	-	-	-

Thin section textures

Garnet occurs primarily as large (up to ~ 4000 μm) anhedral to subhedral grains that interlock with anhedral to subhedral clinopyroxene, sharing straight grain boundaries and inter-grain triple junctions (~ 120°). Clinopyroxene cores are often pristine with omphacitic chemistry, while grain edges are often highly-altered with a “spongy” texture and diopsidic chemistry. Spongy textures also occur along cross-cutting fractures through clinopyroxene grains. Garnet occurs occasionally as subrounded inclusions in clinopyroxene (up to 250 μm), and clinopyroxene occurs rarely as sub-rounded inclusions within garnet (< 250 μm). Rutile commonly occurs as needle-like inclusions (< 100 μm) in garnet and clinopyroxene. These needles are often orientated relative to one another. Rutile needles do not occur in garnet grains that are themselves included within clinopyroxene. In one instance a clinopyroxene inclusion and rutile inclusion in garnet are touching. Rutile also occurs as sub-rounded inclusions (< 150 μm) along garnet/clinopyroxene grain boundaries (intergranular). The intergranular rutile often have ilmenite rims and occasional ilmenite exsolution lamellae. Additional intergranular minerals include spinel, amphibole, analcime, garnet, and plagioclase, which are often intergrown with each other, with intergranular rutile, and with spongy clinopyroxene. The intergranular garnet has significant zonation visible in BSE images, and is intergrown rarely with concentrically-zoned spinel. The intergranular garnet occurs next to fragmented texturally-equilibrated garnet grains.

Table C.3 continued

Sample	Lithology	Group	Grt	Cpx	San	Ky	SiO ₂	Rut
RV-22	eclogite	II _L	40	60	-	-	-	-

Thin section textures

Garnet occurs primarily as large (up to ~ 5000 μm) anhedral to subhedral grains that interlock with anhedral to subhedral clinopyroxene, sharing straight grain boundaries and inter-grain triple junctions (~ 120°). Clinopyroxene cores are often pristine with omphacitic chemistry, while grain edges are often highly-altered with a “spongy” texture and diopsidic chemistry. Spongy textures also occur along cross-cutting fractures through clinopyroxene grains. Rutile commonly occurs as needle-like inclusions (< 100 μm) in garnet and clinopyroxene. The rutile needles are often orientated relative to one another. Rutile needles do not occur in garnet grains that are themselves included within clinopyroxene. Rutile also occurs as sub-rounded inclusions (< 150 μm) along garnet/clinopyroxene grain boundaries (intergranular). The intergranular rutile often have ilmenite rims and occasional ilmenite exsolution lamellae. Additional intergranular minerals include spinel, amphibole, plagioclase, and rare sulfides, which are often intergrown with each other, with intergranular rutile, and with spongy clinopyroxene.

Sample	Lithology	Group	Grt	Cpx	San	Ky	SiO ₂	Rut
RV-27	eclogite	II _F	40	60	-	-	trace	-

Thin section textures

Garnet occurs primarily as large (up to ~ 4000 μm) anhedral to subhedral grains that interlock with anhedral to subhedral clinopyroxene, sharing straight grain boundaries and inter-grain triple junctions (~ 120°). Clinopyroxene are often pristine with omphacitic chemistry. Highly-altered clinopyroxene with a “spongy” texture and diopsidic chemistry is comparatively rare. Rutile commonly occurs as needle-like inclusions (< 100 μm long) in garnet and clinopyroxene. Intergranular minerals include plagioclase, alkali feldspar, and SiO₂. Orthopyroxene exsolution lamellae are observed in one clinopyroxene grain.

Table C.3 continued

Sample	Lithology	Group	Grt	Cpx	San	Ky	SiO ₂	Rut
RV-54	eclogite	II _L	50	50	-	-	-	-

Thin section textures

Garnet occurs primarily as large (up to ~ 6500 μm) anhedral to subhedral grains that interlock with anhedral to subhedral clinopyroxene, sharing straight grain boundaries and inter-grain triple junctions (~ 120°). Clinopyroxene cores are often pristine with omphacitic chemistry, while grain edges are often highly-altered with a “spongy” texture and diopsidic chemistry. Spongy textures also occur along cross-cutting fractures through clinopyroxene grains. Small sub-rounded garnets rarely occur within this grain (up to 450 μm). Rutile commonly occurs as needle-like inclusions (< 100 μm) in garnet and clinopyroxene. The rutile needles are often orientated relative to one another. Rutile needles do not occur in garnet grains that are themselves included within clinopyroxene. Rutile also occurs as sub-rounded inclusions (< 150 μm) along garnet/clinopyroxene grain boundaries (intergranular). The intergranular rutile often have ilmenite rims and occasional ilmenite exsolution lamellae. Additional intergranular minerals include spinel, amphibole, Fe-sulfide, and plagioclase, which are often intergrown with each other, with intergranular rutile, and with spongy clinopyroxene.

Sample	Lithology	Group	Grt	Cpx	San	Ky	SiO ₂	Rut
RV-60	eclogite	II _L	50	50	-	-	-	-

Thin section textures

Garnet occurs primarily as large (up to ~ 3500 μm) anhedral to subhedral grains that interlock with anhedral to subhedral clinopyroxene, sharing straight grain boundaries and inter-grain triple junctions (~ 120°). Clinopyroxene cores are often pristine with omphacitic chemistry, while grain edges are often highly-altered with a “spongy” texture and diopsidic chemistry. Spongy textures also occur along cross-cutting fractures through clinopyroxene grains. Rutile commonly occurs as needle-like inclusions (< 100 μm) in garnet and clinopyroxene. The rutile needles are often orientated relative to one another. Intergranular minerals include plagioclase and epidote, which are often intergrown with spongy clinopyroxene.

Table C.3 continued

Sample	Lithology	Group	Grt	Cpx	San	Ky	SiO ₂	Rut
RV-62	eclogite	II _L	50	50	-	-	-	-

Thin section textures

Garnet occurs primarily as large (up to ~ 5500 μm) anhedral to subhedral grains that interlock with anhedral to subhedral clinopyroxene, sharing straight grain boundaries and inter-grain triple junctions (~ 120°). Clinopyroxene cores are often pristine with omphacitic chemistry, while grain edges are often highly-altered with a “spongy” texture and diopsidic chemistry. Spongy textures also occur along cross-cutting fractures through clinopyroxene grains. Garnet grains with a “rod-like” shape – ~ 150 μm thick and up to 2000 μm long, with straight edges - occur occasionally within clinopyroxene. Rutile commonly occurs as needle-like inclusions (< 100 μm) in garnet and clinopyroxene. These needles are often orientated relative to one another. In one instance, garnet occurs as needles in clinopyroxene (< 100 μm in length), and these needles are orientated relative to rutile needles included in the same clinopyroxene grain. Rutile needles do not occur in garnet grains that are themselves included within clinopyroxene. Rutile also occurs as sub-rounded inclusions (< 150 μm) along garnet/clinopyroxene grain boundaries (intergranular). The intergranular rutile often have ilmenite rims and occasional ilmenite exsolution lamellae. Additional intergranular minerals include spinel, amphibole, and plagioclase, which are often intergrown with each other, with intergranular rutile, and with spongy clinopyroxene. Orthopyroxene exsolution lamellae are observed in one clinopyroxene grain.

Abbreviations: Cpx = clinopyroxene, Grt = garnet, Ky = kyanite, Rut = rutile, San = sanidine, SiO₂ = quartz/coesite

Table C.4 Literature sources for elemental and isotopic data for Roberts Victor eclogite data compiled in this study from published literature. Crosses indicate the type of data used in each study.

Citation	Major-elements	Trace-elements	Oxygen isotope compositions ($\delta^{18}\text{O}$)	Radiogenic isotope compositions (Rb-Sr, Sm-Nd, Lu-Hf)
Caporuscio (1990)	-	-	x	-
Caporuscio and Smyth (1990)	x	x	-	-
Garlick <i>et al.</i> (1971)	-	-	x	-
Greau <i>et al.</i> (2011)	x	x	x	-
Harte and Kirkley (1997)	x	-	-	-
Hatton (1978)	x	-	-	-
Huang <i>et al.</i> (2012a)	x	x	x	x
Huang <i>et al.</i> (2014)	x	x	-	-
Huang <i>et al.</i> (2016)	-	-	x	-
Jacob <i>et al.</i> (2005)	x	x	x	x
Jacob <i>et al.</i> (2003)	-	x	-	-
Kiseeva <i>et al.</i> (2017)	x	x	-	-
MacGregor and Manton (1986)	x	x	-	-
McDade (1999)	-	x	-	-
Ongley <i>et al.</i> (1987)	-	-	x	-
Radu <i>et al.</i> (2019)	x	x	x	-
Schulze <i>et al.</i> (2000)	x	-	x	-

Table C.5 Average oxygen isotope compositions for garnet and clinopyroxene from eclogite xenoliths in this study. $^{18}\text{O}/^{16}\text{O}$ were determined for select garnets by SIMS and laser fluorination (LF), and for select clinopyroxenes by LF only. $^{17}\text{O}/^{16}\text{O}$ for select garnet and clinopyroxene were determined by LF only. All SIMS and LF values are averages of two analyses. See Tables S7 and S8 in the Supplementary Online Dataset for the non-averaged data.

Sample	Group	$\delta^{18}\text{O}_{\text{grt}}^{\text{a}}$ (SIMS)	$\delta^{18}\text{O}_{\text{grt}}$ (LF)	$\delta^{18}\text{O}_{\text{cpx}}$ (LF)	$\delta^{17}\text{O}_{\text{grt}}^{\text{b}}$ (LF)	$\delta^{17}\text{O}_{\text{cpx}}$ (LF)	$\Delta^{17}\text{O}_{\text{grt}}^{\text{c}}$	$\Delta^{17}\text{O}_{\text{cpx}}$	$\theta_{\text{Grt-Cpx}}^{\text{d}}$
RV-1	II _L	2.37	2.609	2.324	1.320	1.179	-0.057	-0.047	0.4953
RV-3	I	6.13	-	-	-	-	-	-	-
RV-6	I	6.83	-	-	-	-	-	-	-
RV-7	I	5.68	-	-	-	-	-	-	-
RV-9	I	5.73	-	-	-	-	-	-	-
RV-10	II _L	2.83	3.015	2.682	1.542	1.38	-0.049	-0.035	0.4857
RV-11	I	5.72	-	-	-	-	-	-	-
RV-13	I	6.04	-	-	-	-	-	-	-
RV-16	I	7.13	7.471	6.914	3.875	3.578	-0.063	-0.066	0.5351
RV-19	I	5.37	5.457	4.843	2.833	2.511	-0.044	-0.043	0.5262
RV-20	II _L	2.80	2.725	-	1.389	-	-	-	-
RV-21	I	6.60	-	-	-	-	-	-	-
RV-22	II _L	1.79	1.673	1.564	0.835	0.766	-0.048	-0.060	0.6335
RV-24	I	7.59	7.530	7.320	3.912	3.782	-0.057	-0.076	0.6203
RV-25	I	6.32	-	-	-	-	-	-	-
RV-27	II _F	4.60	4.562	4.311	2.352	2.214	-0.055	-0.060	0.5499
RV-29	I	5.09	-	-	-	-	-	-	-
RV-30	I	6.27	-	-	-	-	-	-	-
RV-31	I	5.75	-	-	-	-	-	-	-
RV-34	I	6.63	-	-	-	-	-	-	-
RV-37	I	6.20	-	-	-	-	-	-	-
RV-38	I	6.53	-	-	-	-	-	-	-
RV-42	I	6.46	-	-	-	-	-	-	-
RV-45	I	6.46	-	-	-	-	-	-	-
RV-46	I	6.68	-	-	-	-	-	-	-
RV-48	I	6.29	-	-	-	-	-	-	-
RV-49	I	6.27	-	-	-	-	-	-	-
RV-51	I	6.63	-	-	-	-	-	-	-
RV-54	II _L	2.27	-	-	-	-	-	-	-
RV-56	I	6.34	-	-	-	-	-	-	-
RV-58	I	6.61	-	-	-	-	-	-	-
RV-59	I	6.77	-	-	-	-	-	-	-
RV-61	I	7.10	-	-	-	-	-	-	-
RV-62	II _L	2.73	-	-	-	-	-	-	-

$$^{\text{a}}\delta^{18}\text{O} = \left[\frac{^{18}\text{O}/^{16}\text{O}_{\text{sample}}}{^{18}\text{O}/^{16}\text{O}_{\text{VSMOW}}} - 1 \right] \times 1000 \text{ ‰}$$

$$^{\text{b}}\delta^{17}\text{O} = \left[\frac{^{17}\text{O}/^{16}\text{O}_{\text{sample}}}{^{17}\text{O}/^{16}\text{O}_{\text{VSMOW}}} - 1 \right] \times 1000 \text{ ‰}$$

$$^{\text{c}}\Delta^{17}\text{O} = \delta^{17}\text{O} - 0.528 \times \delta^{18}\text{O}, \delta^{17}\text{O} = 1000 \times \ln[1 + (\delta^{17}\text{O}/1000)],$$

$$\delta^{18}\text{O} = 1000 \times \ln[1 + (\delta^{18}\text{O}/1000)]$$

$$^{\text{d}}\theta_{\text{Grt-Cpx}} = (\delta^{17}\text{O}_{\text{grt}} - \delta^{17}\text{O}_{\text{cpx}}) / (\delta^{18}\text{O}_{\text{grt}} - \delta^{18}\text{O}_{\text{cpx}})$$

Table C.6 Average major-element compositions of garnets from eclogite xenoliths in this study, reported as oxide wt%. Reported compositions are averages of multiple analyses indicated by N, the number of replicate analyses. All point data are included in Table S2 in the Supplementary Online Dataset. Cations are calculated on the basis of 12 oxygen. All iron is reported as FeO. The oxygen isotope compositions ($\delta^{18}\text{O}$) for different garnet grains from the same sample are reported, as determined by SIMS (see Table C.5).

Sample Group	RV-1 II _L	RV-3 I	RV-4 II _F	RV-5 I	RV-6 I	RV-7 I	RV-8 I	RV-9 I	RV-10 II _L	RV-11 I	RV-12 I	RV-13 I	RV-14 II _L	RV-15 I	RV-16 I	RV-17 I
$\delta^{18}\text{O}$ (‰)	2.37	6.13	na	na	6.83	5.68	na	5.73	2.83	5.72	na	6.04	na	na	7.13	na
N	19	4	4	2	4	5	2	4	21	6	4	4	13	2	6	2
Oxides (wt%)																
SiO ₂	38.93	40.01	39.52	40.77	40.46	40.80	41.10	42.01	39.54	41.16	41.90	41.29	40.07	41.08	39.78	40.93
TiO ₂	0.13	0.34	0.38	0.37	0.34	0.29	0.25	0.47	0.11	0.20	0.31	0.20	0.11	0.35	0.32	0.22
Al ₂ O ₃	21.68	22.48	21.00	22.52	21.94	22.91	23.10	22.67	22.04	23.16	22.75	23.28	22.37	22.64	21.85	22.72
V ₂ O ₃	0.04	0.03	0.04	bdl	bdl	bdl	bdl	0.04	0.03	bdl	bdl	bdl	0.03	bdl	bdl	bdl
Cr ₂ O ₃	0.04	0.06	0.03	0.47	0.19	0.05	0.05	0.59	0.06	0.05	0.74	0.06	0.06	0.60	0.11	0.09
MnO	0.32	0.27	0.41	0.23	0.91	0.26	0.21	0.33	0.30	0.24	0.28	0.19	0.30	0.22	0.53	0.40
FeO	18.27	13.90	20.40	11.56	17.91	11.61	11.00	9.02	17.91	11.46	9.71	9.71	17.52	10.75	20.57	15.99
NiO	0.02	0.02	bdl	0.02	bdl	bdl	bdl	0.02	0.02	0.02	bdl	bdl	0.02	bdl	0.03	0.02
MgO	9.38	9.46	9.97	13.88	13.89	12.36	15.65	20.58	11.49	15.24	19.27	15.27	11.60	15.97	11.04	15.90
CaO	10.28	13.24	7.91	9.64	4.10	11.65	8.01	3.84	7.82	8.29	4.90	9.73	7.96	7.73	5.49	3.48
Na ₂ O	0.04	0.14	0.07	0.13	0.11	0.11	0.11	0.11	0.04	0.09	0.08	0.09	0.05	0.11	0.11	0.10
K ₂ O	bdl	bdl	bdl	bdl	bdl	0.01	bdl	bdl	bdl	bdl	bdl	bdl	bdl	bdl	bdl	bdl
P ₂ O ₅	bdl	0.10	0.02	0.06	0.06	0.05	0.04	0.05	0.02	0.05	0.04	0.03	bdl	0.04	0.05	0.02
Nb ₂ O ₅	bdl	na	na	na	na	na	na	na	bdl	na	na	na	bdl	na	na	na
Sum	99.12	100.05	99.74	99.65	99.89	100.08	99.54	99.72	99.37	99.95	99.99	99.85	100.10	99.49	99.89	99.86
Cations (apfu)																
Si	2.974	2.984	3.008	2.990	3.006	2.992	2.990	2.994	2.982	2.990	2.995	2.990	2.991	2.990	3.002	2.999
Ti	0.007	0.019	0.022	0.020	0.019	0.016	0.014	0.025	0.006	0.011	0.017	0.011	0.006	0.019	0.018	0.012
Al	1.952	1.976	1.884	1.947	1.921	1.980	1.980	1.904	1.959	1.982	1.917	1.987	1.968	1.942	1.943	1.962
V	0.002	0.002	0.002	-	-	-	-	0.002	0.002	-	-	-	0.002	-	-	-
Cr	0.003	0.004	0.002	0.027	0.011	0.003	0.003	0.033	0.004	0.003	0.042	0.004	0.003	0.034	0.007	0.005
Mn	0.020	0.017	0.027	0.015	0.057	0.016	0.013	0.020	0.019	0.015	0.017	0.012	0.019	0.014	0.034	0.025
Fe	1.167	0.867	1.299	0.709	1.113	0.712	0.669	0.537	1.129	0.696	0.581	0.588	1.093	0.654	1.298	0.980
Ni	0.001	0.001	-	0.001	-	-	-	0.001	0.001	0.001	-	-	0.001	-	0.002	0.001
Mg	1.068	1.052	1.131	1.518	1.539	1.351	1.697	2.186	1.292	1.651	2.053	1.648	1.291	1.732	1.242	1.737
Ca	0.841	1.058	0.645	0.757	0.326	0.915	0.624	0.293	0.632	0.645	0.375	0.755	0.636	0.603	0.444	0.273
Na	0.007	0.021	0.011	0.019	0.016	0.016	0.016	0.015	0.006	0.013	0.011	0.012	0.007	0.015	0.017	0.014
K	-	-	-	-	-	0.001	-	-	-	-	-	-	-	-	-	-
P	-	0.006	0.001	0.004	0.004	0.003	0.002	0.003	0.001	0.003	0.002	0.002	-	0.003	0.003	0.001
Nb	-	-	-	-	-	-	-	-	-	-	-	-	-	-	-	-
Sum	8.043	8.007	8.030	8.007	8.012	8.004	8.009	8.014	8.031	8.009	8.011	8.008	8.019	8.006	8.009	8.010
Mg#	0.48	0.55	0.47	0.68	0.58	0.65	0.72	0.80	0.53	0.70	0.78	0.74	0.54	0.73	0.49	0.64
Ca#	0.44	0.50	0.36	0.33	0.17	0.40	0.27	0.12	0.33	0.28	0.15	0.31	0.33	0.26	0.26	0.14

Table C.6 continued

Sample	RV-18	RV-19	RV-20	RV-21	RV-22	RV-23	RV-24	RV-25	RV-26	RV-27	RV-28	RV-29	RV-30	RV-31	RV-32	RV-33
Group	I	I	II _L	I	II _L	I	I	I	I	II _F	-	I	I	I	I	I
$\delta^{18}\text{O}$ (‰)	<i>na</i>	5.37	2.80	6.60	1.79	<i>na</i>	7.59	6.32	<i>na</i>	4.60	<i>na</i>	5.09	6.27	5.75	<i>na</i>	<i>na</i>
N	2	6	51	5	8	4	4	3	4	14	4	5	4	4	2	2
Oxides (wt%)																
SiO ₂	40.07	40.47	40.02	41.18	39.70	40.29	41.21	41.60	41.19	40.00	40.76	40.18	41.02	40.68	40.21	40.21
TiO ₂	0.31	0.43	0.10	0.20	0.16	0.38	0.09	0.21	0.25	0.11	0.30	0.39	0.24	0.37	0.27	0.28
Al ₂ O ₃	21.80	21.89	22.43	23.01	22.19	22.45	23.15	23.01	23.24	22.60	22.46	22.25	22.47	22.08	22.17	22.33
V ₂ O ₃	<i>bdl</i>	0.02	0.03	0.02	0.03	<i>bdl</i>	0.02	<i>bdl</i>	<i>bdl</i>	0.02	0.02	0.02	<i>bdl</i>	<i>bdl</i>	<i>bdl</i>	<i>bdl</i>
Cr ₂ O ₃	0.99	0.04	0.07	0.12	0.05	0.06	0.13	0.30	0.06	0.06	0.05	0.07	0.16	0.20	0.14	0.05
MnO	0.30	0.40	0.31	0.33	0.37	0.31	0.29	0.30	0.22	0.28	0.36	0.17	0.37	0.61	0.39	0.42
FeO	14.79	18.85	16.79	13.58	17.27	14.62	13.55	12.70	10.84	14.31	14.32	10.36	13.84	14.75	16.38	15.55
NiO	0.02	0.02	0.02	<i>bdl</i>	<i>bdl</i>	0.02	0.02	0.01	0.02	<i>bdl</i>	0.01	0.02	<i>bdl</i>	<i>bdl</i>	<i>bdl</i>	<i>bdl</i>
MgO	10.24	13.69	12.25	17.08	8.69	10.51	17.91	18.31	15.56	12.36	13.78	8.17	16.88	15.72	14.63	13.69
CaO	10.96	3.94	7.70	4.07	11.69	11.33	3.34	3.35	8.36	9.56	7.64	17.99	4.11	4.87	4.74	6.55
Na ₂ O	0.13	0.16	0.04	0.08	0.06	0.14	0.05	0.10	0.11	0.04	0.11	0.13	0.10	0.11	0.10	0.12
K ₂ O	<i>bdl</i>	<i>bdl</i>	0.01	0.01	0.01	0.03	<i>bdl</i>	<i>bdl</i>	<i>bdl</i>	<i>bdl</i>	<i>bdl</i>	<i>bdl</i>	0.01	<i>bdl</i>	0.01	<i>bdl</i>
P ₂ O ₅	0.07	0.18	0.02	0.04	0.03	0.05	0.02	0.03	0.06	0.01	0.05	0.03	0.03	0.03	0.04	0.05
Nb ₂ O ₅	<i>na</i>	<i>na</i>	<i>bdl</i>	<i>na</i>	<i>bdl</i>	<i>na</i>	<i>na</i>	<i>na</i>	<i>na</i>	<i>bdl</i>	<i>na</i>	<i>na</i>	<i>na</i>	<i>na</i>	<i>na</i>	<i>na</i>
Sum	99.67	100.10	99.80	99.73	100.26	100.19	99.77	99.91	99.91	99.36	99.86	99.79	99.24	99.42	99.08	99.25
Cations (apfu)																
Si	3.001	3.004	2.985	2.992	2.990	2.994	2.986	2.999	2.985	2.979	3.001	2.997	3.002	2.997	2.992	2.989
Ti	0.017	0.024	0.006	0.011	0.009	0.021	0.005	0.011	0.014	0.006	0.017	0.022	0.013	0.020	0.015	0.016
Al	1.924	1.915	1.971	1.970	1.970	1.966	1.977	1.955	1.985	1.983	1.949	1.956	1.939	1.918	1.944	1.957
V	-	0.001	0.002	0.001	0.002	-	0.001	-	-	0.001	0.001	0.001	-	-	-	-
Cr	0.059	0.002	0.004	0.007	0.003	0.004	0.008	0.017	0.003	0.003	0.003	0.004	0.009	0.012	0.008	0.003
Mn	0.019	0.025	0.019	0.020	0.023	0.020	0.018	0.018	0.014	0.018	0.022	0.011	0.023	0.038	0.025	0.026
Fe	0.926	1.170	1.047	0.825	1.088	0.909	0.821	0.766	0.657	0.891	0.882	0.646	0.847	0.909	1.019	0.967
Ni	0.001	0.001	0.001	-	-	0.001	0.001	0.001	0.001	-	0.001	0.001	-	-	-	-
Mg	1.143	1.515	1.362	1.851	0.976	1.165	1.935	1.968	1.682	1.372	1.512	0.909	1.842	1.727	1.623	1.518
Ca	0.879	0.314	0.615	0.317	0.944	0.902	0.259	0.259	0.649	0.762	0.603	1.438	0.323	0.385	0.378	0.522
Na	0.019	0.024	0.006	0.012	0.008	0.019	0.007	0.014	0.015	0.006	0.015	0.018	0.014	0.016	0.014	0.018
K	-	-	0.001	0.001	0.001	0.003	-	-	-	-	-	-	0.001	-	0.001	-
P	0.005	0.012	0.001	0.003	0.002	0.003	0.001	0.002	0.004	0.001	0.003	0.002	0.002	0.002	0.002	0.003
Nb	-	-	-	-	-	-	-	-	-	-	-	-	-	-	-	-
Sum	7.993	8.007	8.022	8.010	8.016	8.007	8.018	8.008	8.009	8.023	8.009	8.007	8.015	8.023	8.021	8.019
Mg#	0.55	0.56	0.57	0.69	0.47	0.56	0.70	0.72	0.72	0.61	0.63	0.58	0.69	0.66	0.61	0.61
Ca#	0.43	0.17	0.31	0.15	0.49	0.44	0.12	0.12	0.28	0.36	0.29	0.61	0.15	0.18	0.19	0.26

Table C.6 continued

Sample Group	RV-34	RV-35	RV-36	RV-37	RV-38	RV-39	RV-40	RV-41	RV-42	RV-43	RV-44	RV-45	RV-46	RV-47	RV-48	RV-49
$\delta^{18}\text{O}$ (‰)	6.63	na	na	6.20	6.53	na	na	na	6.46	na	na	6.46	6.68	na	6.29	6.27
N	5	4	2	4	4	4	4	2	4	2	3	4	4	7	4	5
Oxides (wt%)																
SiO ₂	41.41	40.06	40.46	40.88	40.66	41.53	40.89	40.59	40.53	40.80	40.73	41.11	40.36	40.79	40.84	40.40
TiO ₂	0.22	0.30	0.35	0.40	0.24	0.48	0.36	0.23	0.39	0.23	0.25	0.21	0.29	0.31	0.33	0.34
Al ₂ O ₃	22.62	21.91	22.58	21.91	22.31	22.39	22.08	22.55	22.02	22.69	22.58	22.64	21.87	22.55	22.25	22.21
V ₂ O ₃	bdl	0.02	bdl	0.03	0.02	0.04	0.02	0.03	0.03	0.04	bdl	bdl	0.03	0.03	bdl	bdl
Cr ₂ O ₃	0.19	0.07	0.15	0.18	0.27	0.03	0.15	0.11	0.15	0.08	0.07	0.15	0.15	0.11	0.15	0.05
MnO	0.29	0.39	0.23	0.56	0.43	0.30	0.51	0.40	0.52	0.34	0.32	0.32	0.85	0.53	0.66	0.36
FeO	13.05	17.52	11.24	15.28	14.95	11.41	15.64	14.49	16.02	13.07	13.01	13.52	17.27	14.82	15.52	14.86
NiO	0.02	bdl	0.02	bdl	0.02	bdl	bdl	0.02	0.02	bdl	bdl	0.02	bdl	0.02	bdl	bdl
MgO	18.46	10.72	14.06	15.68	16.52	18.73	15.39	15.90	14.98	16.40	15.08	16.96	14.40	15.59	15.16	12.07
CaO	3.19	8.71	10.01	4.55	3.81	4.53	4.45	4.82	4.69	5.38	7.12	4.36	4.18	4.65	4.85	9.27
Na ₂ O	0.08	0.09	0.12	0.11	0.09	0.11	0.12	0.10	0.11	0.09	0.11	0.08	0.09	0.10	0.11	0.12
K ₂ O	0.01	bdl	bdl	bdl	0.01	bdl	bdl	bdl	bdl	0.01	bdl	0.01	bdl	bdl	bdl	0.02
P ₂ O ₅	0.02	0.03	0.06	0.03	0.03	0.14	0.03	0.05	0.04	0.06	0.03	0.03	0.03	0.03	0.03	0.05
Nb ₂ O ₅	na															
Sum	99.55	99.83	99.26	99.61	99.37	99.70	99.65	99.28	99.51	99.19	99.31	99.42	99.52	99.53	99.91	99.75
Cations (apfu)																
Si	3.001	3.007	2.978	3.009	2.989	2.994	3.010	2.987	2.998	2.988	2.994	3.000	3.003	2.997	3.003	3.001
Ti	0.012	0.017	0.019	0.022	0.013	0.026	0.020	0.013	0.022	0.013	0.014	0.012	0.016	0.017	0.018	0.019
Al	1.932	1.938	1.958	1.901	1.933	1.903	1.916	1.955	1.920	1.958	1.956	1.947	1.918	1.952	1.928	1.945
V	-	0.001	-	0.001	0.001	0.002	0.001	0.002	0.002	0.002	-	-	0.002	0.002	-	-
Cr	0.011	0.004	0.009	0.010	0.016	0.002	0.009	0.006	0.009	0.005	0.004	0.009	0.009	0.007	0.009	0.003
Mn	0.018	0.025	0.014	0.035	0.027	0.018	0.032	0.025	0.033	0.021	0.020	0.020	0.054	0.033	0.041	0.023
Fe	0.791	1.100	0.692	0.941	0.919	0.688	0.963	0.891	0.991	0.800	0.800	0.825	1.074	0.910	0.954	0.923
Ni	0.001	-	0.001	-	0.001	-	-	0.001	0.001	-	-	0.001	-	0.001	-	-
Mg	1.994	1.199	1.543	1.721	1.810	2.013	1.689	1.744	1.652	1.791	1.652	1.845	1.597	1.708	1.662	1.337
Ca	0.247	0.700	0.789	0.359	0.300	0.350	0.351	0.380	0.372	0.422	0.561	0.341	0.333	0.366	0.382	0.738
Na	0.011	0.013	0.017	0.016	0.013	0.015	0.018	0.014	0.016	0.013	0.016	0.012	0.013	0.014	0.016	0.018
K	0.001	-	-	-	0.001	-	-	-	-	0.001	-	0.001	-	-	-	0.002
P	0.001	0.002	0.003	0.002	0.002	0.009	0.002	0.003	0.003	0.004	0.002	0.002	0.002	0.002	0.002	0.003
Nb	-	-	-	-	-	-	-	-	-	-	-	-	-	-	-	-
Sum	8.020	8.008	8.023	8.017	8.026	8.021	8.012	8.021	8.019	8.018	8.017	8.014	8.021	8.010	8.015	8.012
Mg#	0.72	0.52	0.69	0.65	0.66	0.75	0.64	0.66	0.63	0.69	0.67	0.69	0.60	0.65	0.64	0.59
Ca#	0.11	0.37	0.34	0.17	0.14	0.15	0.17	0.18	0.18	0.19	0.25	0.16	0.17	0.18	0.19	0.36

Table C.6 continued

Sample	RV-50	RV-51	RV-52	RV-53	RV-54	RV-55	RV-56	RV-57	RV-58	RV-59	RV-60	RV-61	RV-62	RV-63	RV-64	RV-65
Group	I	I	I	I	II _L	I	I	I	I	I	II _L	I	II _L	I	I	I
$\delta^{18}\text{O}$ (‰)	<i>na</i>	6.63	<i>na</i>	<i>na</i>	2.27	<i>na</i>	6.34	<i>na</i>	6.61	6.77	<i>na</i>	7.10	2.73	<i>na</i>	<i>na</i>	<i>na</i>
N	3	3	2	3	15	5	4	4	3	3	12	4	31	2	3	3
Oxides (wt%)																
SiO ₂	40.33	40.71	39.97	40.53	39.87	41.21	41.00	39.81	40.31	40.20	39.96	40.90	40.16	40.83	40.74	41.43
TiO ₂	0.33	0.39	0.31	0.32	0.13	0.27	0.25	0.20	0.37	0.31	0.13	0.10	0.11	0.36	0.30	0.23
Al ₂ O ₃	22.21	22.08	22.06	22.23	21.97	22.55	22.59	22.04	21.75	22.29	22.28	22.77	22.46	22.13	22.40	22.83
V ₂ O ₃	<i>bdl</i>	0.02	0.03	0.02	0.03	0.03	0.02	<i>bdl</i>	0.03	<i>bdl</i>	0.02	<i>bdl</i>	0.01	0.02	<i>bdl</i>	0.02
Cr ₂ O ₃	0.14	0.22	0.10	0.15	0.05	0.16	0.15	0.07	0.14	0.06	0.07	0.31	0.06	0.21	0.13	0.05
MnO	0.57	0.57	0.46	0.46	0.35	0.40	0.39	0.53	0.87	0.55	0.29	0.30	0.31	0.51	0.49	0.25
FeO	15.06	15.66	17.03	16.13	18.43	14.22	13.72	18.94	16.06	15.48	16.35	13.09	17.64	14.77	14.46	12.76
NiO	<i>bdl</i>	<i>bdl</i>	0.02	0.02	0.02	0.02	<i>bdl</i>	0.02	<i>bdl</i>	<i>bdl</i>	0.02	<i>bdl</i>	0.02	<i>bdl</i>	0.02	0.03
MgO	13.61	15.10	12.90	15.09	10.20	16.26	15.92	12.46	14.74	13.92	12.04	18.22	11.69	16.40	16.27	18.84
CaO	7.07	4.66	6.21	4.33	9.19	4.65	5.38	5.22	4.95	6.26	8.43	3.39	7.89	4.01	4.51	2.94
Na ₂ O	0.12	0.12	0.11	0.09	0.04	0.10	0.09	0.11	0.11	0.12	0.05	0.04	0.04	0.10	0.10	0.09
K ₂ O	<i>bdl</i>	<i>bdl</i>	<i>bdl</i>	<i>bdl</i>	<i>bdl</i>	0.03	0.13	0.01	0.01	<i>bdl</i>	0.01	<i>bdl</i>	0.01	<i>bdl</i>	<i>bdl</i>	<i>bdl</i>
P ₂ O ₅	0.04	0.03	0.06	0.03	0.01	0.04	0.03	0.04	0.03	0.04	0.01	0.05	0.01	0.03	0.04	0.04
Nb ₂ O ₅	<i>na</i>	<i>na</i>	<i>na</i>	<i>na</i>	<i>bdl</i>	<i>na</i>	<i>na</i>	<i>na</i>	<i>na</i>	<i>na</i>	<i>bdl</i>	<i>na</i>	<i>bdl</i>	<i>na</i>	<i>na</i>	<i>na</i>
Sum	99.48	99.55	99.26	99.40	100.29	99.94	99.68	99.46	99.36	99.21	99.65	99.17	100.41	99.36	99.47	99.50
Cations (apfu)																
Si	2.992	3.005	2.992	2.998	2.996	3.004	2.999	2.993	2.996	2.989	2.986	2.980	2.989	3.001	2.990	2.996
Ti	0.019	0.022	0.017	0.018	0.007	0.015	0.014	0.011	0.021	0.017	0.007	0.006	0.006	0.020	0.017	0.013
Al	1.943	1.920	1.946	1.938	1.945	1.938	1.947	1.953	1.905	1.953	1.962	1.955	1.970	1.917	1.937	1.946
V	-	0.001	0.002	0.001	0.002	0.002	0.001	-	0.002	-	0.001	-	0.001	0.001	-	0.001
Cr	0.008	0.013	0.006	0.009	0.003	0.009	0.009	0.004	0.008	0.003	0.004	0.018	0.003	0.012	0.008	0.003
Mn	0.036	0.035	0.029	0.029	0.023	0.025	0.024	0.034	0.055	0.034	0.018	0.018	0.020	0.032	0.031	0.015
Fe	0.935	0.967	1.066	0.998	1.158	0.867	0.839	1.191	0.998	0.962	1.022	0.798	1.098	0.908	0.888	0.771
Ni	-	-	0.001	0.001	0.001	0.001	-	0.001	-	-	0.001	-	0.001	-	0.001	0.001
Mg	1.506	1.662	1.439	1.664	1.142	1.768	1.736	1.396	1.633	1.543	1.341	1.979	1.296	1.797	1.781	2.031
Ca	0.562	0.369	0.498	0.343	0.740	0.363	0.421	0.421	0.395	0.498	0.675	0.265	0.629	0.316	0.355	0.228
Na	0.017	0.017	0.016	0.013	0.007	0.015	0.012	0.016	0.016	0.017	0.007	0.006	0.005	0.014	0.015	0.013
K	-	-	-	-	-	0.002	0.012	0.001	0.001	-	0.001	-	0.001	-	-	-
P	0.002	0.002	0.004	0.002	0.001	0.002	0.002	0.003	0.002	0.002	0.001	0.003	0.001	0.002	0.002	0.002
Nb	-	-	-	-	-	-	-	-	-	-	-	-	-	-	-	-
Sum	8.019	8.012	8.016	8.014	8.024	8.011	8.018	8.022	8.031	8.021	8.026	8.027	8.020	8.019	8.024	8.020
Mg#	0.62	0.63	0.57	0.63	0.50	0.67	0.67	0.54	0.62	0.62	0.57	0.71	0.54	0.66	0.67	0.72
Ca#	0.27	0.18	0.26	0.17	0.39	0.17	0.20	0.23	0.19	0.24	0.33	0.12	0.33	0.15	0.17	0.10

Table C.6 continued

Sample	RVSA71
Group	I
$\delta^{18}\text{O}$ (‰)	na
N	1
Oxides (wt%)	
SiO ₂	41.53
TiO ₂	0.25
Al ₂ O ₃	23.51
V ₂ O ₃	<i>bdl</i>
Cr ₂ O ₃	0.07
MnO	0.31
FeO	9.97
NiO	<i>bdl</i>
MgO	19.24
CaO	4.27
Na ₂ O	0.07
K ₂ O	<i>bdl</i>
P ₂ O ₅	0.07
Nb ₂ O ₅	na
Sum	99.29
Cations (apfu)	
Si	2.982
Ti	0.014
Al	1.989
V	-
Cr	0.004
Mn	0.019
Fe	0.599
Ni	-
Mg	2.059
Ca	0.329
Na	0.010
K	-
P	0.004
Nb	-
Sum	8.007
Mg#	0.77
Ca#	0.14

Mg# = Mg/(Mg+Fe)

Ca# = Ca/(Ca+Mg)

bdl below detection limit

na not analysed

Table C.7 Average major-element compositions of clinopyroxenes from eclogite xenoliths in this study, reported as oxide wt%. Reported compositions are averages of multiple analyses indicated by N, the number of replicate analyses. All point data are included in Table S2 in the Supplementary Online Dataset. Cations are calculated on the basis of 6 oxygen. All iron is reported as FeO.

Sample Group	RV-1	RV-3	RV-4	RV-5	RV-6	RV-7	RV-8	RV-9	RV-10	RV-11	RV-12	RV-13	RV-14	RV-15	RV-16	RV-17
N	II _L	I	II _F	I	I	I	I	I	II _L	I	I	I	II _L	I	I	I
N	6	4	2	2	1	4	2	2	11	3	1	1	10	2	4	2
Oxides (wt%)																
SiO ₂	54.48	55.35	53.63	54.53	54.93	55.48	55.22	54.79	54.45	55.76	54.72	55.99	54.64	54.61	54.77	54.85
TiO ₂	0.17	0.36	0.22	0.48	0.36	0.33	0.31	0.38	0.17	0.30	0.32	0.28	0.17	0.46	0.39	0.34
Al ₂ O ₃	8.18	16.17	4.15	9.93	5.82	14.69	11.54	3.51	7.35	12.52	3.91	12.72	8.80	7.06	8.04	7.08
V ₂ O ₃	0.06	0.02	0.06	0.03	0.03	0.02	0.02	0.05	0.06	0.02	0.02	0.02	0.04	0.03	0.04	0.03
Cr ₂ O ₃	0.04	0.09	<i>bdl</i>	0.54	0.12	0.04	0.07	0.44	0.05	0.07	0.51	0.07	0.05	0.58	0.11	0.16
MnO	0.02	0.03	0.06	0.03	0.18	0.03	0.03	0.10	0.03	0.03	0.05	0.03	0.03	0.04	0.09	0.11
FeO	5.79	2.14	7.20	2.66	6.22	2.19	2.50	3.38	5.00	2.19	3.01	1.88	4.71	2.68	6.51	5.70
NiO	0.06	0.05	0.05	0.06	0.03	0.04	0.04	0.05	0.07	0.04	0.05	0.04	0.07	0.07	0.04	0.05
MgO	9.64	6.28	12.23	10.30	12.60	7.46	9.61	16.31	10.85	9.05	14.93	9.14	10.12	12.39	10.11	12.50
CaO	15.48	10.76	18.00	14.41	14.92	11.40	13.11	17.50	16.45	12.54	18.86	12.82	15.30	16.64	13.65	13.54
Na ₂ O	4.92	7.26	3.29	5.93	4.12	7.04	6.21	2.61	4.38	6.18	2.80	6.26	5.02	4.50	4.88	4.55
K ₂ O	0.01	0.25	<i>bdl</i>	0.04	0.16	0.10	0.14	0.06	0.03	0.12	0.03	0.12	0.01	0.03	0.19	0.13
P ₂ O ₅	0.02	0.01	<i>bdl</i>	<i>bdl</i>	0.03	0.02	<i>bdl</i>	<i>bdl</i>	<i>bdl</i>	0.03	<i>bdl</i>	<i>bdl</i>	0.01	0.02	0.01	0.01
Nb ₂ O ₅	<i>bdl</i>	<i>na</i>	<i>na</i>	<i>na</i>	<i>na</i>	<i>na</i>	<i>na</i>	<i>na</i>	<i>bdl</i>	<i>na</i>	<i>na</i>	<i>na</i>	<i>bdl</i>	<i>na</i>	<i>na</i>	<i>na</i>
Sum	98.86	98.77	98.88	98.93	99.52	98.83	98.80	99.20	98.90	98.85	99.22	99.36	98.96	99.10	98.84	99.04
Cations (apfu)																
Si	1.988	1.954	1.989	1.961	1.995	1.962	1.972	1.986	1.985	1.978	1.987	1.975	1.980	1.972	1.996	1.988
Ti	0.005	0.009	0.006	0.013	0.010	0.009	0.008	0.010	0.005	0.008	0.009	0.007	0.005	0.013	0.011	0.009
Al	0.351	0.673	0.181	0.421	0.249	0.612	0.485	0.150	0.316	0.523	0.167	0.529	0.376	0.300	0.345	0.302
V	0.002	0.001	0.002	0.001	0.001	0.001	0.001	0.001	0.002	0.001	0.001	0.000	0.001	0.001	0.001	0.001
Cr	0.001	0.002	-	0.015	0.004	0.001	0.002	0.012	0.002	0.002	0.015	0.002	0.001	0.017	0.003	0.005
Mn	0.001	0.001	0.002	0.001	0.005	0.001	0.001	0.003	0.001	0.001	0.002	0.001	0.001	0.001	0.003	0.003
Fe	0.176	0.063	0.223	0.080	0.189	0.065	0.075	0.103	0.152	0.065	0.091	0.055	0.143	0.081	0.198	0.173
Ni	0.002	0.001	0.001	0.002	0.001	0.001	0.001	0.002	0.002	0.001	0.001	0.001	0.002	0.002	0.001	0.001
Mg	0.524	0.331	0.676	0.552	0.682	0.393	0.511	0.881	0.590	0.479	0.808	0.481	0.547	0.667	0.549	0.676
Ca	0.605	0.407	0.715	0.555	0.581	0.432	0.501	0.679	0.642	0.476	0.734	0.484	0.594	0.644	0.533	0.526
Na	0.348	0.497	0.236	0.413	0.290	0.483	0.430	0.183	0.309	0.425	0.197	0.428	0.353	0.315	0.345	0.320
K	0.000	0.011	-	0.002	0.007	0.004	0.006	0.003	0.001	0.005	0.001	0.005	0.000	0.002	0.009	0.006
P	0.001	0.000	-	-	0.001	0.000	-	0.001	-	0.001	-	-	0.000	0.000	0.000	0.000
Nb	-	-	-	-	-	-	-	-	-	-	-	-	-	-	-	-
Sum	4.004	3.952	4.032	4.015	4.016	3.965	3.994	4.014	4.007	3.965	4.013	3.969	4.002	4.014	3.995	4.011
Mg#	0.75	0.84	0.75	0.87	0.78	0.86	0.87	0.90	0.79	0.88	0.90	0.90	0.79	0.89	0.73	0.80
Ca#	0.54	0.55	0.51	0.50	0.46	0.52	0.50	0.44	0.52	0.50	0.48	0.50	0.52	0.49	0.49	0.44

Table C.7 continued

Sample	RV-18	RV-19	RV-20	RV-21	RV-22	RV-23	RV-24	RV-25	RV-26	RV-27	RV-28	RV-29	RV-30	RV-31	RV-32	RV-33
Group	I	I	II _L	I	II _L	I	I	I	I	II _F	-	I	I	I	I	I
N	2	2	24	4	9	2	2	2	3	15	4	4	6	6	2	2
Oxides (wt%)																
SiO ₂	55.12	54.85	54.79	55.34	54.73	55.34	55.12	55.24	55.52	55.12	55.57	55.19	55.62	54.84	54.80	55.33
TiO ₂	0.35	0.59	0.19	0.33	0.20	0.35	0.16	0.32	0.31	0.16	0.34	0.33	0.33	0.38	0.34	0.37
Al ₂ O ₃	11.20	7.25	10.13	8.20	10.55	13.56	5.33	8.56	12.21	8.76	10.72	16.04	7.55	6.78	6.93	10.76
V ₂ O ₃	0.05	0.05	0.04	0.03	0.07	0.06	0.03	0.04	0.03	0.05	0.04	0.02	0.05	0.05	0.05	0.03
Cr ₂ O ₃	1.01	0.03	0.10	0.19	0.05	0.08	0.16	0.21	0.08	0.06	0.05	0.07	0.20	0.20	0.12	0.05
MnO	0.03	0.10	0.03	0.08	0.03	0.04	0.07	0.07	0.03	0.03	0.05	0.02	0.09	0.12	0.10	0.06
FeO	3.50	7.31	4.00	4.28	4.33	3.16	4.16	3.83	2.40	2.54	3.42	1.98	4.67	5.19	5.64	3.94
NiO	0.06	0.02	0.08	0.04	0.05	0.06	0.08	0.06	0.05	0.07	0.04	0.06	0.04	0.03	0.05	0.04
MgO	8.68	11.22	9.45	11.96	9.01	7.64	13.97	11.73	9.35	11.20	9.67	6.52	12.03	12.02	12.13	9.44
CaO	12.92	12.33	14.36	13.53	14.71	11.61	16.77	13.93	12.74	16.75	13.20	11.40	13.87	14.56	14.49	12.70
Na ₂ O	6.25	5.11	5.76	4.78	5.49	7.16	3.49	5.07	6.31	4.40	5.88	7.23	4.62	4.68	4.29	6.09
K ₂ O	0.16	0.11	0.01	0.13	0.01	0.09	0.06	0.15	0.13	0.01	0.14	0.11	0.15	0.11	0.16	0.12
P ₂ O ₅	<i>bdl</i>	0.06	0.02	0.01	0.02	<i>bdl</i>	0.02	<i>bdl</i>	0.01	0.02	0.02	0.01	0.01	0.02	0.02	0.01
Nb ₂ O ₅	<i>na</i>	<i>na</i>	<i>bdl</i>	<i>na</i>	<i>bdl</i>	<i>na</i>	<i>na</i>	<i>na</i>	<i>na</i>	<i>bdl</i>	<i>na</i>	<i>na</i>	<i>na</i>	<i>na</i>	<i>na</i>	<i>na</i>
Sum	99.32	99.05	98.95	98.91	99.23	99.14	99.40	99.23	99.17	99.17	99.13	98.98	99.23	98.98	99.09	98.95
Cations (apfu)																
Si	1.971	1.997	1.975	1.992	1.969	1.966	1.993	1.983	1.970	1.977	1.984	1.947	2.001	1.992	1.989	1.983
Ti	0.009	0.016	0.005	0.009	0.005	0.009	0.004	0.009	0.008	0.004	0.009	0.009	0.009	0.010	0.009	0.010
Al	0.472	0.311	0.430	0.348	0.447	0.568	0.227	0.362	0.511	0.370	0.451	0.667	0.320	0.290	0.296	0.455
V	0.001	0.002	0.001	0.001	0.002	0.002	0.001	0.001	0.001	0.002	0.001	0.001	0.001	0.002	0.001	0.001
Cr	0.029	0.001	0.003	0.005	0.001	0.002	0.005	0.006	0.002	0.002	0.001	0.002	0.006	0.006	0.003	0.001
Mn	0.001	0.003	0.001	0.002	0.001	0.001	0.002	0.002	0.001	0.001	0.001	0.000	0.003	0.004	0.003	0.002
Fe	0.105	0.223	0.121	0.129	0.130	0.094	0.126	0.115	0.071	0.076	0.102	0.058	0.140	0.158	0.171	0.118
Ni	0.002	0.001	0.002	0.001	0.001	0.002	0.002	0.002	0.001	0.002	0.001	0.002	0.001	0.001	0.001	0.001
Mg	0.463	0.609	0.508	0.642	0.483	0.405	0.753	0.628	0.494	0.599	0.515	0.343	0.645	0.651	0.656	0.504
Ca	0.495	0.481	0.555	0.522	0.567	0.442	0.650	0.536	0.484	0.644	0.505	0.431	0.535	0.567	0.564	0.488
Na	0.433	0.361	0.402	0.334	0.383	0.493	0.244	0.353	0.434	0.306	0.407	0.494	0.322	0.330	0.302	0.423
K	0.007	0.005	0.000	0.006	0.000	0.004	0.003	0.007	0.006	0.000	0.006	0.005	0.007	0.005	0.007	0.006
P	-	0.002	0.000	0.000	0.001	-	0.000	-	0.000	0.001	0.001	0.000	0.000	0.000	0.000	0.000
Nb	-	-	-	-	-	-	-	-	-	-	-	-	-	-	-	-
Sum	3.989	4.011	4.004	3.991	3.991	3.988	4.010	4.004	3.984	3.984	3.986	3.959	3.991	4.015	4.005	3.992
Mg#	0.82	0.73	0.81	0.83	0.79	0.81	0.86	0.85	0.87	0.89	0.83	0.85	0.82	0.80	0.79	0.81
Ca#	0.52	0.44	0.52	0.45	0.54	0.52	0.46	0.46	0.49	0.52	0.50	0.56	0.45	0.47	0.46	0.49

Table C.7 continued

Sample	RV-34	RV-35	RV-36	RV-37	RV-38	RV-39	RV-40	RV-41	RV-42	RV-43	RV-44	RV-45	RV-46	RV-47	RV-48	RV-49
Group	I	I	I	I	I	I	I	I	I	I	I	I	I	I	I	I
N	4	4	2	4	4	4	4	2	4	2	4	4	4	6	4	4
Oxides (wt%)																
SiO ₂	55.54	55.21	55.10	55.09	55.40	54.79	55.29	55.51	55.10	55.16	55.55	55.47	55.11	55.38	55.49	55.83
TiO ₂	0.29	0.38	0.40	0.32	0.32	0.35	0.39	0.37	0.39	0.33	0.33	0.35	0.33	0.36	0.37	0.35
Al ₂ O ₃	6.53	8.88	10.08	4.83	6.98	3.49	7.14	8.88	6.79	7.42	9.86	8.07	6.39	8.01	8.39	15.13
V ₂ O ₃	0.03	0.05	0.03	0.07	0.05	0.07	0.06	0.03	0.06	0.06	0.05	0.03	0.06	0.05	0.06	0.04
Cr ₂ O ₃	0.19	0.09	0.17	0.13	0.23	<i>bdl</i>	0.15	0.16	0.12	0.10	0.08	0.17	0.14	0.14	0.15	0.07
MnO	0.11	0.07	0.03	0.14	0.11	0.08	0.12	0.07	0.11	0.09	0.05	0.08	0.20	0.10	0.11	0.03
FeO	4.94	5.41	2.45	5.72	5.22	4.41	5.35	4.27	5.43	4.26	3.19	4.34	6.15	4.53	4.67	2.81
NiO	0.06	0.03	0.06	0.02	0.04	0.05	0.02	0.04	0.03	0.03	0.05	0.04	0.04	0.04	0.03	0.03
MgO	13.72	9.96	10.49	13.65	12.62	15.53	11.88	11.20	12.04	12.11	10.46	11.96	12.16	11.51	11.11	6.76
CaO	13.51	13.67	14.66	15.84	13.67	17.70	13.75	13.35	14.43	14.88	13.80	13.34	14.13	13.95	13.56	10.32
Na ₂ O	4.03	5.13	5.77	3.40	4.28	2.45	4.79	5.27	4.35	4.53	5.41	4.83	4.12	4.76	5.18	7.69
K ₂ O	0.13	0.16	0.04	0.12	0.13	0.08	0.14	0.13	0.16	0.15	0.14	0.13	0.16	0.15	0.13	0.08
P ₂ O ₅	0.02	0.01	0.01	0.01	0.02	0.04	<i>bdl</i>	0.01	0.03	0.02	0.02	0.03	<i>bdl</i>	0.02	<i>bdl</i>	0.02
Nb ₂ O ₅	<i>na</i>	<i>na</i>	<i>na</i>	<i>na</i>	<i>na</i>	<i>na</i>	<i>na</i>	<i>na</i>	<i>na</i>	<i>na</i>	<i>na</i>	<i>na</i>	<i>na</i>	<i>na</i>	<i>na</i>	<i>na</i>
Sum	99.09	99.06	99.30	99.34	99.06	99.04	99.09	99.29	99.04	99.13	98.98	98.85	99.00	99.01	99.24	99.16
Cations (apfu)																
Si	2.001	1.995	1.968	2.002	2.000	1.995	2.001	1.990	1.998	1.990	1.988	1.997	2.004	1.996	1.996	1.969
Ti	0.008	0.010	0.011	0.009	0.009	0.010	0.011	0.010	0.011	0.009	0.009	0.009	0.009	0.010	0.010	0.009
Al	0.277	0.378	0.424	0.207	0.297	0.150	0.305	0.375	0.290	0.316	0.416	0.343	0.274	0.340	0.355	0.629
V	0.001	0.001	0.001	0.002	0.002	0.002	0.002	0.001	0.002	0.002	0.001	0.001	0.002	0.001	0.002	0.001
Cr	0.005	0.003	0.005	0.004	0.007	-	0.004	0.004	0.004	0.003	0.002	0.005	0.004	0.004	0.004	0.002
Mn	0.003	0.002	0.001	0.004	0.003	0.002	0.004	0.002	0.003	0.003	0.002	0.002	0.006	0.003	0.003	0.001
Fe	0.149	0.164	0.073	0.174	0.158	0.134	0.162	0.128	0.165	0.129	0.095	0.131	0.187	0.136	0.140	0.083
Ni	0.002	0.001	0.002	0.001	0.001	0.001	0.001	0.001	0.001	0.001	0.001	0.001	0.001	0.001	0.001	0.001
Mg	0.737	0.536	0.559	0.740	0.679	0.843	0.641	0.599	0.651	0.651	0.558	0.642	0.659	0.618	0.596	0.355
Ca	0.522	0.529	0.561	0.617	0.529	0.690	0.533	0.513	0.561	0.575	0.529	0.515	0.551	0.539	0.522	0.390
Na	0.281	0.360	0.399	0.239	0.300	0.173	0.336	0.366	0.306	0.317	0.375	0.337	0.290	0.332	0.361	0.525
K	0.006	0.008	0.002	0.006	0.006	0.004	0.006	0.006	0.007	0.007	0.006	0.006	0.008	0.007	0.006	0.004
P	0.001	0.000	0.000	0.000	0.001	0.001	-	0.000	0.001	0.001	0.001	0.001	-	0.001	-	0.001
Nb	-	-	-	-	-	-	-	-	-	-	-	-	-	-	-	-
Sum	3.992	3.987	4.006	4.004	3.990	4.006	4.005	3.995	3.999	4.002	3.984	3.990	3.996	3.990	3.997	3.970
Mg#	0.83	0.77	0.88	0.81	0.81	0.86	0.80	0.82	0.80	0.84	0.85	0.83	0.78	0.82	0.81	0.81
Ca#	0.41	0.50	0.50	0.45	0.44	0.45	0.45	0.46	0.46	0.47	0.49	0.45	0.46	0.47	0.47	0.52

Table C.7 continued

Sample	RV-50	RV-51	RV-52	RV-53	RV-54	RV-55	RV-56	RV-57	RV-58	RV-59	RV-60	RV-61	RV-62	RV-63	RV-64	RV-65
Group	I	I	I	I	II _L	I	I	I	I	I	II _L	I	II _L	I	I	I
N	3	3	2	3	11	4	4	2	2	2	9	3	19	2	3	3
Oxides (wt%)																
SiO ₂	55.33	55.13	54.99	54.94	54.70	55.68	55.65	55.41	54.72	55.48	54.70	55.68	54.67	55.37	55.16	55.67
TiO ₂	0.39	0.40	0.35	0.34	0.17	0.36	0.34	0.28	0.32	0.41	0.20	0.17	0.16	0.31	0.36	0.39
Al ₂ O ₃	10.58	6.32	6.42	6.27	9.19	8.40	9.10	10.19	5.75	9.82	10.58	5.79	8.79	7.02	6.95	6.79
V ₂ O ₃	0.04	0.05	0.04	0.06	0.06	0.05	0.05	0.04	0.05	0.07	0.04	0.04	0.04	0.05	0.05	0.03
Cr ₂ O ₃	0.18	0.21	0.14	0.16	0.05	0.16	0.17	0.08	0.13	0.08	0.08	0.34	0.06	0.15	0.20	0.05
MnO	0.08	0.12	0.12	0.11	0.03	0.08	0.08	0.09	0.19	0.08	0.03	0.06	0.03	0.11	0.10	0.08
FeO	3.79	5.65	6.20	5.92	5.75	4.24	3.88	5.70	6.21	3.93	4.12	3.61	4.79	4.74	4.84	4.66
NiO	0.03	0.03	0.03	0.04	0.05	0.04	0.04	0.02	0.03	0.03	0.07	0.03	0.07	0.04	0.04	0.12
MgO	9.46	12.34	12.08	12.72	9.09	11.39	10.87	9.15	12.52	10.30	9.25	13.71	10.06	12.56	12.16	14.07
CaO	12.84	14.70	14.36	14.54	14.45	13.82	13.79	11.64	15.08	13.35	14.34	16.34	15.29	14.69	14.43	13.12
Na ₂ O	6.12	4.40	4.49	4.12	5.40	4.96	5.28	6.70	4.21	5.67	5.71	3.65	4.97	4.26	4.56	4.12
K ₂ O	0.14	0.14	0.14	0.13	0.01	0.14	0.16	0.12	0.13	0.17	0.01	0.08	0.01	0.17	0.13	0.13
P ₂ O ₅	<i>bdl</i>	0.01	0.02	0.02	<i>bdl</i>	0.01	<i>bdl</i>	0.01	0.03	<i>bdl</i>	0.01	<i>bdl</i>	0.02	0.03	0.01	0.02
Nb ₂ O ₅	<i>na</i>	<i>na</i>	<i>na</i>	<i>na</i>	<i>bdl</i>	<i>na</i>	<i>na</i>	<i>na</i>	<i>na</i>	<i>na</i>	<i>bdl</i>	<i>na</i>	<i>bdl</i>	<i>na</i>	<i>na</i>	<i>na</i>
Sum	98.98	99.50	99.36	99.37	98.94	99.34	99.41	99.44	99.35	99.38	99.13	99.49	98.97	99.50	98.98	99.26
Cations (apfu)																
Si	1.984	1.996	1.997	1.992	1.987	1.996	1.991	1.991	1.993	1.985	1.968	2.001	1.981	1.993	1.997	1.997
Ti	0.011	0.011	0.010	0.009	0.005	0.010	0.009	0.007	0.009	0.011	0.005	0.005	0.004	0.008	0.010	0.011
Al	0.447	0.270	0.275	0.268	0.393	0.355	0.384	0.432	0.247	0.414	0.449	0.245	0.375	0.298	0.297	0.287
V	0.001	0.002	0.001	0.002	0.002	0.001	0.001	0.001	0.002	0.002	0.001	0.001	0.001	0.002	0.001	0.001
Cr	0.005	0.006	0.004	0.005	0.001	0.005	0.005	0.002	0.004	0.002	0.002	0.010	0.002	0.004	0.006	0.001
Mn	0.002	0.004	0.004	0.003	0.001	0.002	0.002	0.003	0.006	0.002	0.001	0.002	0.001	0.003	0.003	0.003
Fe	0.114	0.171	0.188	0.180	0.175	0.127	0.116	0.171	0.189	0.117	0.124	0.108	0.145	0.143	0.147	0.140
Ni	0.001	0.001	0.001	0.001	0.002	0.001	0.001	0.001	0.001	0.001	0.002	0.001	0.002	0.001	0.001	0.004
Mg	0.505	0.666	0.654	0.687	0.492	0.609	0.580	0.490	0.680	0.549	0.496	0.735	0.543	0.674	0.657	0.753
Ca	0.493	0.570	0.559	0.565	0.562	0.531	0.528	0.448	0.588	0.512	0.553	0.629	0.594	0.566	0.560	0.504
Na	0.426	0.309	0.316	0.289	0.380	0.345	0.366	0.467	0.297	0.393	0.398	0.255	0.349	0.297	0.320	0.287
K	0.006	0.006	0.006	0.006	0.000	0.007	0.007	0.006	0.006	0.008	0.000	0.004	0.000	0.008	0.006	0.006
P	-	0.000	0.000	0.000	-	0.000	-	0.000	0.001	-	0.000	-	0.001	0.001	0.000	0.001
Nb	-	-	-	-	-	-	-	-	-	-	-	-	-	-	-	-
Sum	3.995	4.012	4.014	4.008	4.001	3.989	3.992	4.020	4.022	3.996	4.000	3.995	3.999	3.998	4.004	3.993
Mg#	0.82	0.80	0.78	0.79	0.74	0.83	0.83	0.74	0.78	0.82	0.80	0.87	0.79	0.83	0.82	0.84
Ca#	0.49	0.46	0.46	0.45	0.53	0.47	0.48	0.48	0.46	0.48	0.53	0.46	0.52	0.46	0.46	0.40

Table C.7 continued

Sample	RVSA71
Group	I
N	1
Oxides (wt%)	
SiO ₂	54.99
TiO ₂	0.29
Al ₂ O ₃	4.75
V ₂ O ₃	<i>bdl</i>
Cr ₂ O ₃	0.09
MnO	0.07
FeO	2.79
NiO	0.05
MgO	15.14
CaO	17.53
Na ₂ O	2.61
K ₂ O	0.30
P ₂ O ₅	0.01
Nb ₂ O ₅	<i>na</i>
Sum	98.62
Cations (apfu)	
Si	1.994
Ti	0.008
Al	0.203
V	-
Cr	0.003
Mn	0.002
Fe	0.085
Ni	0.001
Mg	0.819
Ca	0.681
Na	0.184
K	0.014
P	0.000
Nb	-
Sum	3.993
Mg#	0.91
Ca#	0.45

Mg# = Mg/(Mg+Fe)

Ca# = Ca/(Ca+Mg)

bdl below detection limit

na not analysed

Table C.8 Average trace-element compositions of garnets from eclogite xenoliths in this study, reported as ppm. Compositions are single spot analyses unless the number of spot analyses (N) is greater than one, in which case the reported composition is an average. All point data are included in Table S2 in the Supplementary Online Dataset. The oxygen isotope compositions ($\delta^{18}\text{O}$) for different garnet grains from the same sample are reported, as determined by SIMS (see Table C.5).

Sample Group	RV-1	RV-3	RV-4	RV-5	RV-6	RV-7	RV-8	RV-9	RV-10	RV-11	RV-12	RV-13	RV-14	RV-15	RV-16	RV-17	RV-18
$\delta^{18}\text{O}$ (‰)	II _L	I	II _F	I	I	I	I	I	II _L	I	I	I	II _L	I	I	I	I
N	1	1	1	1	1	2	1	1	1	1	1	1	1	1	2	1	1
Na	332.1	959.5	478.8	891	848.1	795.3	764.5	829.7	319.5	594.5	646	604.8	335.4	794.5	868.6	610.5	883.9
Ti	928.8	2129	2684	2394	2411	1878	1673	3205	954.9	1065.7	2167	1289.1	2730	2370	2244	1573.2	2073.6
Ni	35.14	73.53	28.55	57.79	38.05	53.93	60.37	61.77	39.72	66.73	53.94	73.16	39.42	63.36	38.30	51.35	77.78
Sr	0.0899	7.48	0.1558	0.52	1.024	4.448	2.72	0.346	0.0598	2.149	0.251	2.993	0.258	0.418	0.966	1.248	2.027
Y	23.21	21.94	39.82	17.38	24.86	6.839	9.911	26.47	33.38	5.304	12.21	3.685	30.44	17.93	37.46	12.03	28.67
Zr	0.474	83.93	10.98	62.14	19.13	22.47	21.57	57.95	2.871	12.65	25.94	12.82	3.91	72.36	19.04	10.66	60.96
Nb	0.00057	0.0137	<i>bdl</i>	0.108	0.0333	0.0062	0.0943	0.0454	0.00051	0.079	0.0446	0.00277	0.00284	0.0605	0.0055	0.0872	0.0083
Ba	<i>bdl</i>	2.98	0.0004	0.0114	0.64	0.0042	4.6	0.371	<i>bdl</i>	3.26	<i>bdl</i>	0.009	2.68	<i>bdl</i>	<i>bdl</i>	4.62	0.026
La	<i>bdl</i>	0.27	0.00046	0.0185	0.067	0.0281	0.1647	0.0202	0.0012	0.144	0.0102	0.0176	0.041	0.0128	0.0164	0.1241	0.0267
Ce	0.00011	1.534	0.0291	0.2464	0.262	0.3557	0.476	0.1185	0.00078	0.516	0.1537	0.2161	0.0639	0.1808	0.2169	0.288	0.2485
Pr	0.00049	0.554	0.0248	0.1139	0.0801	0.1626	0.1286	0.0485	0.00273	0.152	0.0613	0.1171	0.0083	0.0819	0.0946	0.0542	0.1179
Nd	0.0633	5.889	0.522	1.502	0.846	1.673	1.218	0.537	0.125	1.511	0.616	1.508	0.132	0.893	1.124	0.476	1.848
Sm	0.369	3.991	1.001	1.587	0.717	1.004	0.986	0.55	0.612	1.086	0.502	0.74	0.538	1.063	1.235	0.413	2.664
Eu	0.369	1.615	0.674	0.817	0.36	0.689	0.472	0.285	0.479	0.535	0.301	0.471	0.415	0.587	0.6515	0.239	1.273
Gd	1.556	4.789	3.143	2.859	1.615	1.312	1.741	1.45	2.349	1.424	1.22	0.73	2.033	2.455	3.298	0.933	4.722
Tb	0.403	0.697	0.715	0.492	0.3638	0.1998	0.3057	0.358	0.578	0.1915	0.2557	0.1102	0.498	0.4983	0.738	0.2316	0.811
Dy	3.543	4.266	6.128	3.268	3.414	1.309	2.11	3.498	4.951	1.12	2.105	0.724	4.443	3.579	6.008	1.951	5.317
Ho	0.868	0.798	1.474	0.663	0.907	0.2517	0.3697	0.934	1.199	0.196	0.458	0.1379	1.112	0.699	1.366	0.446	1.054
Er	2.88	2.19	4.852	1.938	3.392	0.732	0.911	3.52	4.037	0.527	1.42	0.37	3.777	1.934	4.250	1.438	3.021
Tm	0.406	0.2867	0.703	0.2602	0.569	0.0960	0.1129	0.56	0.601	0.0766	0.2049	0.0525	0.561	0.2573	0.6105	0.2146	0.389
Yb	3.02	1.956	5.205	1.841	4.506	0.735	0.7	4.391	4.332	0.562	1.401	0.395	4.31	1.818	4.405	1.501	2.679
Lu	0.446	0.2728	0.789	0.2711	0.709	0.1134	0.0978	0.718	0.659	0.0896	0.1991	0.0628	0.666	0.2574	0.651	0.2224	0.3611
Hf	0.0159	1.333	0.333	0.906	0.382	0.4145	0.409	1.186	0.0768	0.222	0.359	0.256	0.134	1.121	0.3255	0.197	1.034

Table C.8 continued

Sample	RV-19	RV-20	RV-21	RV-22	RV-23	RV-24	RV-25	RV-26	RV-27	RV-28	RV-29	RV-30	RV-31	RV-32	RV-33	RV-34	RV-36
Group	I	II _L	I	II _L	I	I	I	I	II _F	-	I	I	I	I	I	I	I
$\delta^{18}\text{O}$ (‰)	5.37	2.80	6.60	1.79	<i>na</i>	7.59	6.32	<i>na</i>	4.60	<i>na</i>	5.09	6.27	5.75	<i>na</i>	<i>na</i>	6.63	<i>na</i>
N	2	2	2	1	1	1	1	1	1	1	2	1	1	1	1	1	1
Na	1266	330.0	631.5	<i>na</i>	<i>na</i>	<i>na</i>	<i>na</i>	<i>na</i>	<i>na</i>	<i>na</i>	593.1	<i>na</i>	<i>na</i>	<i>na</i>	<i>na</i>	<i>na</i>	<i>na</i>
Ti	2998	859.1	1289	1044.6	2422	666.2	1434.6	1662	741.7	1978.8	2606	1742.7	2731	2045	2167	1758	2591
Ni	22.04	55.66	59.05	21.97	73.03	52.53	67.95	74.27	39.55	56.3	72.76	56.7	36.86	59.7	58.27	86.2	68.67
Sr	0.5865	0.0997	0.6795	0.1212	5.87	0.2958	1.879	1.121	0.3	2.598	6.078	1.419	1.042	0.532	0.968	0.463	1.81
Y	73.65	30.7	8.079	49.88	25.96	7.018	7.485	9.437	16.389	17.34	8.453	6.748	27.43	25.29	28.87	6.194	16.6
Zr	59.37	2.878	8.099	2.337	33.83	4.427	10.206	19.99	2.612	18.72	16.94	14.65	86.78	14.79	18.27	13.53	47.15
Nb	0.00198	0.0031	0.0175	0.00026	0.193	0.00041	0.0742	0.0116	0.0621	0.141	0.0308	0.0656	0.0454	0.0063	0.0105	0.0056	0.172
Ba	<i>bdl</i>	1.255	<i>bdl</i>	<i>bdl</i>	12.9	<i>bdl</i>	3.04	0.0007	0.23	6.49	1.505	2.84	0.042	<i>bdl</i>	0.0024	0.004	5.62
La	0.0383	0.0542	0.0516	0.0024	0.526	0.0098	0.1446	0.018	0.0135	0.216	0.1049	0.0894	0.0287	0.0045	0.015	0.0036	0.1239
Ce	0.4815	0.0455	0.1736	0.0042	1.195	0.1166	0.32	0.2224	0.0545	0.626	0.684	0.238	0.3603	0.0952	0.1971	0.0357	0.391
Pr	0.2072	0.0057	0.0523	0.0076	0.2534	0.0532	0.0638	0.1056	0.02	0.1411	0.253	0.0624	0.1573	0.0559	0.0902	0.0164	0.1136
Nd	2.468	0.0975	0.5515	0.235	2.278	0.552	0.511	1.193	0.299	1.291	2.391	0.623	1.881	0.773	1.057	0.195	1.302
Sm	2.471	0.4165	0.45	0.72	1.653	0.45	0.43	0.983	0.461	0.985	1.168	0.492	1.365	0.84	0.949	0.25	1.319
Eu	1.18	0.4115	0.2665	0.488	0.808	0.2297	0.2345	0.503	0.355	0.499	0.951	0.307	0.631	0.424	0.498	0.229	0.717
Gd	5.805	1.845	0.881	2.824	3.098	0.869	0.894	1.823	1.281	1.955	1.521	0.858	2.521	2.1	2.16	0.549	2.593
Tb	1.276	0.4945	0.1721	0.744	0.603	0.1571	0.1718	0.3305	0.2942	0.4152	0.2527	0.157	0.522	0.447	0.52	0.1122	0.491
Dy	10.81	4.422	1.329	6.949	4.57	1.216	1.316	2.108	2.548	3.119	1.677	1.194	4.304	3.931	4.686	1.004	3.24
Ho	2.615	1.1385	0.3052	1.781	0.974	0.2631	0.2787	0.3438	0.619	0.669	0.3295	0.253	1.032	0.916	1.065	0.233	0.63
Er	8.88	3.787	0.975	6.158	2.946	0.794	0.826	0.805	2.085	1.906	0.924	0.807	3.553	3.094	3.451	0.748	1.812
Tm	1.346	0.582	0.1419	0.934	0.4111	0.1085	0.119	0.0909	0.3145	0.269	0.1167	0.1223	0.524	0.449	0.462	0.1244	0.2414
Yb	10.24	4.283	1.125	7.148	2.929	0.824	0.878	0.568	2.386	1.78	0.797	0.929	4.032	3.501	3.093	0.97	1.768
Lu	1.585	0.657	0.1784	1.088	0.422	0.1163	0.1406	0.0803	0.3544	0.235	0.1078	0.1476	0.613	0.538	0.426	0.1601	0.239
Hf	0.789	0.0824	0.1395	0.0909	0.624	0.0518	0.189	0.402	0.051	0.36	0.364	0.235	1.815	0.242	0.352	0.2	0.674

Table C.8 continued

Sample	RV-37	RV-38	RV-39	RV-40	RV-41	RV-42	RV-43	RV-44	RV-45	RV-46	RV-47	RV-48	RV-49	RV-50	RV-51	RV-52	RV-53
Group	I	I	I	I	I	I	I	I	I	I	I	I	I	I	I	I	I
$\delta^{18}\text{O}$ (‰)	6.20	6.53	na	na	na	6.46	na	na	6.46	6.68	na	6.29	6.27	na	6.63	na	na
N	1	1	1	1	1	1	1	1	1	1	3	1	1	1	1	1	1
Na	na	na	na	na	na	na	na	na	na	na	916.9	na	na	na	na	na	na
Ti	2871	1817	3911	2878	1913	3346	1919	1996.8	1401.6	2599	2277	2734	2444	2562	2728	2295	2476
Ni	30.59	55.42	40.97	39.04	58.53	40.66	53.45	62.04	61.58	44.67	41.97	46.86	54.54	46.53	40.23	39.13	54
Sr	2.69	1.083	0.551	1.97	1.56	3.6	0.749	3.05	2.32	1.8	2.987	4.06	3.14	1.145	0.86	0.89	0.65
Y	31.75	12.39	30.23	24.73	13.98	26.45	9.332	14.995	7.132	26.67	19.373	20.33	17.72	30.87	24.4	45.51	22.2
Zr	55.25	10.17	36.79	36.06	14.57	58.45	17.5	16.95	9.27	16.05	40.47	28.26	28.63	30.76	37.44	37.34	26.61
Nb	0.214	0.0513	0.00232	0.1	0.104	0.198	0.0088	0.0629	0.165	0.0623	0.1220	0.472	0.128	0.0213	0.029	0.0161	0.0184
Ba	5.39	2.31	0.0013	3.01	1.53	8.3	0.0227	59.4	5.91	1.042	6.857	13.19	8.3	bdl	0.236	0.0007	0.095
La	0.1135	0.1342	0.01	0.146	0.0479	0.216	0.0091	0.1	0.439	0.102	0.3203	0.275	0.293	0.0176	0.0286	0.0167	0.0194
Ce	0.401	0.3067	0.1597	0.484	0.185	0.651	0.1141	0.346	0.93	0.292	0.719	0.747	0.751	0.2541	0.2081	0.2135	0.1338
Pr	0.1096	0.0627	0.0856	0.1125	0.0589	0.128	0.0589	0.1062	0.141	0.0773	0.1265	0.151	0.1543	0.1141	0.084	0.0995	0.0556
Nd	1.089	0.621	1.128	1.065	0.582	1.16	0.696	1.058	0.891	0.768	1.006	1.222	1.264	1.351	1.032	1.299	0.639
Sm	0.857	0.495	1.154	0.827	0.564	0.857	0.595	0.887	0.549	0.628	0.75	0.816	1	1.139	0.869	1.877	0.617
Eu	0.434	0.263	0.645	0.425	0.283	0.421	0.324	0.465	0.33	0.345	0.3853	0.405	0.525	0.568	0.428	0.977	0.306
Gd	2.038	1.06	2.527	1.822	1.209	1.909	1.166	1.758	0.795	1.58	1.588	1.701	1.962	2.507	1.926	4.61	1.4
Tb	0.494	0.2258	0.543	0.422	0.272	0.444	0.223	0.351	0.1497	0.392	0.3553	0.359	0.415	0.567	0.417	0.945	0.328
Dy	4.467	1.994	4.715	3.723	2.228	3.995	1.69	2.665	1.128	3.714	3.021	3.089	3.095	4.914	3.67	7.42	3.201
Ho	1.191	0.465	1.124	0.932	0.525	1.011	0.355	0.569	0.2567	0.966	0.7323	0.759	0.695	1.139	0.904	1.649	0.81
Er	4.392	1.534	3.834	3.335	1.731	3.597	1.072	1.709	0.896	3.627	2.428	2.757	2.007	3.764	3.188	5.312	3.046
Tm	0.727	0.2164	0.573	0.52	0.2463	0.536	0.1414	0.2275	0.1386	0.55	0.3586	0.431	0.281	0.536	0.5	0.752	0.471
Yb	5.87	1.628	4.691	4.219	1.816	4.269	1.061	1.538	1.075	4.3	2.718	3.4	2.019	3.714	4.06	5.45	3.783
Lu	0.959	0.249	0.673	0.67	0.26	0.659	0.1492	0.2147	0.1682	0.651	0.407	0.519	0.292	0.534	0.604	0.788	0.573
Hf	1.176	0.192	0.72	0.883	0.296	1.406	0.356	0.323	0.14	0.353	0.9717	0.683	0.622	0.601	0.785	0.634	0.536

Table C.8 continued

Sample Group	RV-54	RV-55	RV-56	RV-57	RV-58	RV-59	RV-60	RV-61	RV-62	RV-63	RV-64	RV-65	RVSA71
$\delta^{18}\text{O}$ (‰)	II _L	I	I	I	I	I	II _L	I	II _L	I	I	I	I
N	2.27	na	6.34	na	6.61	6.77	na	7.10	2.73	na	na	na	na
	1	1	1	1	1	1	1	1	1	1	1	1	1
Na	na	na	na	na	na	na	na	na	na	na	na	na	695.7
Ti	990.5	2050	1793	1508.6	2945	2402	1006.6	885.7	877.4	2668	2319	1829	1932
Ni	34.29	50.03	60.61	38.96	30.74	32.84	58.98	37.66	43.65	46.67	51.44	164.3	63.09
Sr	0.0778	0.887	0.823	1.449	2.13	1.482	0.0583	0.455	1.67	0.715	1.859	0.426	1.444
Y	32.57	10.604	8.61	32.65	28.46	24.36	30.72	11.62	25.45	19.08	17.06	19.99	19.54
Zr	0.751	22.45	17.49	16.5	95.57	20.43	3.311	6.549	2.771	29.93	49.05	30.11	71.56
Nb	0.00149	0.0285	0.0132	0.0164	0.0978	0.0158	bdl	0.00137	bdl	0.0196	0.0741	bdl	0.0063
Ba	0.0006	0.955	0.16	bdl	12.52	0.214	bdl	bdl	4.55	0.225	2.26	0.0023	0.01535
La	0.00124	0.0408	0.0169	0.0294	0.15	0.0262	bdl	0.0199	0.0654	0.0328	0.1193	0.0054	0.0363
Ce	0.0083	0.1651	0.1629	0.374	0.585	0.263	0.00038	0.2285	0.0951	0.1639	0.416	0.0417	0.3074
Pr	0.00254	0.0539	0.0668	0.1477	0.1861	0.1105	0.00223	0.0825	0.0121	0.0557	0.1235	0.0256	0.1186
Nd	0.071	0.589	0.857	1.557	2.034	1.234	0.101	0.904	0.146	0.679	1.162	0.462	1.106
Sm	0.388	0.57	0.662	1.286	1.481	1.015	0.512	0.846	0.581	0.68	0.876	0.817	0.8525
Eu	0.425	0.288	0.378	0.722	0.692	0.488	0.473	0.431	0.461	0.344	0.406	0.564	0.4363
Gd	1.875	1.176	1.188	2.8	2.72	1.987	2.014	1.421	2.205	1.51	1.661	2.243	1.729
Tb	0.504	0.2339	0.22	0.605	0.562	0.426	0.506	0.261	0.5	0.325	0.337	0.496	0.3722
Dy	4.87	1.786	1.62	5.15	4.529	3.661	4.646	1.957	4.163	2.872	2.797	3.669	2.986
Ho	1.209	0.403	0.313	1.187	1.086	0.923	1.112	0.418	0.963	0.726	0.655	0.76	0.6801
Er	4.133	1.251	0.933	3.824	3.624	3.199	3.68	1.37	2.944	2.534	2.15	2.048	2.1508
Tm	0.629	0.1799	0.1386	0.552	0.553	0.497	0.562	0.2075	0.419	0.392	0.33	0.267	0.3064
Yb	4.813	1.395	0.929	3.953	4.48	3.78	4.222	1.624	3.154	3.182	2.403	1.776	2.229
Lu	0.712	0.2096	0.1432	0.596	0.671	0.571	0.64	0.251	0.44	0.503	0.373	0.253	0.3320
Hf	0.0287	0.468	0.307	0.257	2.054	0.39	0.087	0.098	0.084	0.656	1.11	0.396	1.442

bdl below detection limit

na not analysed

Table C.9 Average trace-element compositions of clinopyroxenes from eclogite xenoliths in this study, reported as ppm. Compositions are single spot analyses unless the number of spot analyses (N) is greater than one, in which case the reported composition is an average. All point data are included in Table S2 in the Supplementary Online Dataset.

Sample Group	RV-1	RV-3	RV-4	RV-5	RV-6	RV-7	RV-8	RV-9	RV-10	RV-11	RV-12	RV-13	RV-14	RV-15	RV-16	RV-17	RV-18
	II _L	I	II _F	I	I	I	I	I	II _L	I	I	I	II _L	I	I	I	I
N	1	1	1	1	1	2	1	1	1	1	1	1	1	1	2	1	1
Na	32280	48050	20530	37470	28530	42900	42170	18530	28330	43060	21250	43940	34410	30220	32530	29100	41890
Ti	1100.9	2438	1417.8	3254	2203	2185	2050	2419	1034.3	2025	2095	1959	1134.7	2992	2760	2164.8	2512
Ni	495.1	384	428.3	427.3	265.7	343.4	276.3	392.3	573.9	311.9	415.3	375.9	494.7	491.2	299.1	363.9	514.3
Sr	19.48	233.9	89.86	114.04	305.1	141.9	178.8	150.8	28.6	175.4	314.1	180	23.64	112.23	241.05	217	163.4
Y	0.636	0.291	2.159	0.758	2.421	0.266	0.41	5.83	1.208	0.481	1.798	0.2285	0.984	1.034	2.857	1.83	0.887
Zr	1.06	38.75	9.98	39.07	21.18	9.579	11.26	37.13	6.444	9.324	36.17	8.951	5.21	62.39	24.07	14.93	27.35
Nb	<i>bdl</i>	0.00148	0.00008	0.1923	0.0246	0.015	0.0243	0.1007	0.00002	0.0199	0.1769	0.0746	0.00007	0.1817	0.013	0.0208	0.336
Ba	0.35	0.0523	0.0122	0.131	0.467	262.6	0.19	0.503	0.0007	272	0.58	52.3	<i>bdl</i>	0.178	0.529	2.9	3.19
La	0.00229	0.745	0.167	0.883	1.607	0.306	0.669	2.794	0.0012	0.5	4.55	0.592	0.00084	1.427	1.363	1.166	0.593
Ce	0.00458	2.56	0.976	3.715	6.625	1.350	2.696	9.225	0.0207	2.088	17.83	2.153	0.0183	4.879	5.271	4.582	2.224
Pr	0.00435	0.486	0.2769	0.669	1.23	0.2817	0.5058	1.541	0.0245	0.41	2.76	0.3919	0.0181	0.797	0.964	0.844	0.4048
Nd	0.134	2.813	2.174	3.509	6.596	1.602	2.713	7.975	0.452	2.26	12.42	2.11	0.361	4.164	5.28	4.497	2.297
Sm	0.15	0.592	0.947	0.862	1.451	0.379	0.553	1.966	0.469	0.51	2.081	0.439	0.333	1.196	1.341	1.023	0.694
Eu	0.0913	0.1597	0.3617	0.2509	0.408	0.1201	0.1722	0.59	0.1957	0.1514	0.575	0.138	0.155	0.3852	0.4115	0.341	0.2231
Gd	0.239	0.293	1.001	0.596	1.086	0.245	0.349	1.788	0.555	0.32	1.327	0.24	0.443	0.892	1.194	0.815	0.567
Tb	0.0333	0.0298	0.1214	0.0601	0.1254	0.0251	0.0346	0.2351	0.0664	0.0349	0.1415	0.0205	0.0555	0.0921	0.155	0.1009	0.0587
Dy	0.172	0.107	0.599	0.243	0.658	0.1016	0.149	1.296	0.348	0.145	0.591	0.0909	0.269	0.37	0.791	0.518	0.271
Ho	0.0257	0.0126	0.0847	0.0308	0.1001	0.0127	0.0199	0.2086	0.0487	0.0189	0.0759	0.0094	0.0379	0.0459	0.1176	0.0816	0.036
Er	0.0571	0.0249	0.1767	0.0573	0.22	0.0224	0.0333	0.489	0.1043	0.042	0.137	0.0129	0.0776	0.076	0.259	0.1733	0.0741
Tm	0.00654	0.00257	0.0177	0.00488	0.0236	0.0016	0.00283	0.0509	0.009	0.00338	0.0127	0.00064	0.0071	0.0071	0.0274	0.0191	0.0062
Yb	0.0291	0.0094	0.0884	0.0247	0.1292	0.0074	0.0133	0.287	0.0497	0.016	0.0535	0.0057	0.0435	0.0327	0.1418	0.0976	0.0362
Lu	0.00274	0.0007	0.0103	0.0028	0.0153	0.00119	0.00199	0.0327	0.00495	0.0008	0.00559	0.00081	0.00449	0.00197	0.0162	0.0118	0.00465
Hf	0.1308	1.83	0.81	1.882	1.276	0.56	0.609	2.119	0.553	0.499	1.729	0.508	0.419	3.103	1.279	0.751	1.403

Table C.9 continued

Sample Group	RV-19	RV-20	RV-21	RV-22	RV-23	RV-24	RV-25	RV-26	RV-27	RV-28	RV-29	RV-30	RV-31	RV-32	RV-33	RV-34	RV-35
N	I	II _L	I	II _L	I	I	I	I	II _F	-	I	I	I	I	I	I	I
	2	2	2	1	1	1	1	1	1	1	1	1	2	1	1	1	1
Na	37460	36410	32620	na	na	na	na	na	na	na	na	na	na	na	na	na	na
Ti	3892	1433	2210	1244.8	2375	1005.3	2080	2139	1093	2258	2296	2224	2444	2220	2547	1797	2557
Ni	141.6	615.1	362.3	310.7	471.1	598.1	421.3	423.5	549	330.3	437.9	335.9	234.0	428.6	374.3	600.1	218.3
Sr	214.55	16.86	247.7	18.19	120.35	496.9	268.5	161.31	54.45	168.47	103.77	245.7	362	192.96	184.8	284.9	212.46
Y	11.56	0.944	1.288	1.063	0.582	0.756	1.299	0.511	0.4339	0.785	0.1883	1.262	2.315	2.64	1.382	1.371	1.529
Zr	91.54	5.186	14.78	3.462	12.72	11.661	11.803	10.07	4.023	12.112	7.858	15.1	66.50	28.6	13.97	15.77	12.6
Nb	0.0082	0.00017	0.02415	0.00048	0.0161	0.00163	0.0162	0.0138	0.00138	0.0398	0.0214	0.023	0.0861	0.0144	0.0195	0.0241	0.0179
Ba	5.927	bdl	0.265	0.0049	0.437	0.327	0.353	0.152	0.305	0.228	44	0.343	0.6055	0.522	0.216	0.457	0.35
La	5.871	0.0017	1.031	0.00235	0.338	6.885	1.202	0.575	0.1913	0.5823	0.2953	1.205	3.071	0.828	0.67	1.624	1.108
Ce	23.7	0.0176	4.428	0.0298	1.45	20.6	4.721	2.412	0.5873	2.361	1.179	5.127	13.58	4.144	2.862	6.388	4.235
Pr	4.068	0.0119	0.8415	0.0187	0.2984	2.711	0.8863	0.4573	0.1184	0.469	0.2258	0.928	2.403	1.005	0.5337	0.988	0.747
Nd	22.38	0.213	4.632	0.277	1.705	11.471	4.788	2.458	0.782	2.608	1.212	4.924	12.34	7.014	2.896	4.87	3.83
Sm	5.757	0.252	1.027	0.219	0.4	1.788	1.077	0.529	0.282	0.632	0.265	1.037	2.197	1.928	0.696	1.056	0.841
Eu	1.587	0.131	0.3234	0.0899	0.1304	0.4906	0.3338	0.1648	0.1195	0.1885	0.0857	0.3269	0.575	0.526	0.226	0.424	0.2668
Gd	4.691	0.345	0.714	0.315	0.314	1.011	0.739	0.37	0.223	0.445	0.167	0.734	1.363	1.326	0.54	0.714	0.632
Tb	0.5645	0.0482	0.0815	0.0459	0.0349	0.091	0.0817	0.0384	0.0257	0.0528	0.0173	0.081	0.1476	0.147	0.068	0.0787	0.0871
Dy	2.861	0.247	0.398	0.245	0.161	0.352	0.392	0.162	0.1305	0.239	0.0626	0.381	0.703	0.708	0.374	0.384	0.423
Ho	0.4378	0.0396	0.0585	0.0412	0.0204	0.0433	0.0537	0.0193	0.0173	0.0334	0.0076	0.0555	0.1047	0.1118	0.0554	0.0565	0.0632
Er	1.008	0.0824	0.1221	0.0902	0.046	0.0808	0.1071	0.0327	0.0358	0.0668	0.0146	0.1211	0.2305	0.229	0.1184	0.1203	0.1513
Tm	0.1054	0.0084	0.0124	0.0109	0.0053	0.0076	0.01	0.00339	0.00342	0.00574	0.00164	0.0122	0.0238	0.0249	0.0108	0.0147	0.0172
Yb	0.581	0.0463	0.0717	0.0586	0.0217	0.0327	0.0543	0.0155	0.0163	0.0326	0.0055	0.0657	0.1331	0.149	0.0565	0.0666	0.0843
Lu	0.0662	0.0039	0.0079	0.0071	0.00223	0.00345	0.0054	0.0015	0.00156	0.00327	0.00031	0.0075	0.0135	0.0159	0.0053	0.0075	0.0106
Hf	3.456	0.45	0.7925	0.373	0.72	0.509	0.609	0.614	0.271	0.684	0.457	0.847	4.150	1.147	0.758	0.706	0.717

Table C.9 continued

Sample	RV-36	RV-37	RV-38	RV-39	RV-40	RV-41	RV-42	RV-43	RV-44	RV-45	RV-46	RV-47	RV-48	RV-49	RV-50	RV-51	RV-52
Group	I	I	I	I	I	I	I	I	I	I	I	I	I	I	I	I	I
N	1	1	1	1	1	1	1	1	1	1	1	4	1	1	1	1	1
Na	<i>na</i>	35840	<i>na</i>	<i>na</i>	<i>na</i>	<i>na</i>	<i>na</i>										
Ti	2707	2117.8	2183	2002	2547	2468	2486	2115	2218.4	2262.9	2108.7	2538	2450	2454	2640	2523	2302
Ni	464.9	190.6	342.2	305.5	195.8	348.3	240.5	320.9	349.9	340.5	284.6	306.1	277	235.6	261.6	286.2	239
Sr	114.65	290.5	231.6	310.3	273.3	199.61	265.4	254.6	194.3	229.66	252.1	299.55	233.7	121.9	198.6	293	291.9
Y	0.529	3.153	1.556	3.77	2.484	1.418	2.452	1.027	0.54	1.332	1.97	1.569	1.29	0.2795	1.199	2.729	2.761
Zr	23.38	41.98	13.82	15.63	29.54	14.96	22.31	18.09	12.33	15.46	15.67	25.04	19.81	9.28	16.9	36.09	39.85
Nb	0.147	0.0452	0.0259	0.00389	0.0412	0.0259	0.0251	0.0253	0.0185	0.0268	0.0233	0.0381	0.0356	0.0207	0.0247	0.0433	0.0526
Ba	0.096	0.621	0.36	0.583	0.434	0.252	0.39	0.314	2.22	0.281	0.391	1.300	0.354	99	0.189	0.485	0.767
La	0.554	2.369	1.279	2.409	1.767	0.895	1.486	1.03	0.671	1.049	1.235	1.440	1.212	0.454	0.733	1.998	2.237
Ce	2.253	10.171	5.299	12.9	7.818	3.799	6.873	4.548	2.885	4.468	5.233	6.123	5.31	1.565	3.152	8.656	9.854
Pr	0.4452	1.779	0.927	2.29	1.34	0.707	1.208	0.873	0.553	0.83	0.963	1.121	0.926	0.271	0.573	1.529	1.712
Nd	2.611	9.19	4.932	12.46	6.96	3.833	6.287	4.982	3.035	4.423	5.21	6.01	4.93	1.41	3.096	7.98	8.704
Sm	0.655	1.817	1.061	2.903	1.475	0.832	1.315	1.046	0.705	0.948	1.175	1.227	1.051	0.3	0.697	1.721	1.732
Eu	0.1964	0.488	0.3312	0.962	0.444	0.27	0.396	0.312	0.2109	0.3027	0.336	0.3571	0.2962	0.1032	0.2072	0.464	0.466
Gd	0.421	1.268	0.783	1.984	1.105	0.63	0.997	0.707	0.477	0.666	0.865	0.821	0.733	0.185	0.534	1.216	1.199
Tb	0.0429	0.1615	0.0876	0.2206	0.134	0.0771	0.1255	0.0715	0.0475	0.0808	0.1064	0.0940	0.0799	0.0174	0.0615	0.1456	0.1392
Dy	0.176	0.842	0.451	1.086	0.677	0.395	0.659	0.33	0.225	0.386	0.55	0.458	0.381	0.083	0.318	0.742	0.753
Ho	0.0218	0.1345	0.0655	0.1593	0.1108	0.0586	0.1027	0.0479	0.0271	0.0575	0.0876	0.069	0.0627	0.0104	0.0476	0.1175	0.1159
Er	0.044	0.328	0.137	0.339	0.24	0.1347	0.227	0.0944	0.0557	0.1237	0.197	0.1527	0.139	0.0199	0.1073	0.264	0.27
Tm	0.00364	0.0344	0.0143	0.0315	0.0267	0.0125	0.0257	0.0102	0.00499	0.0123	0.021	0.0147	0.0133	0.00241	0.0106	0.0291	0.0305
Yb	0.0178	0.206	0.0744	0.185	0.155	0.0695	0.1376	0.0541	0.0312	0.0709	0.1236	0.0858	0.084	0.0135	0.046	0.165	0.154
Lu	0.00296	0.025	0.0114	0.0226	0.0201	0.0064	0.0148	0.0057	0.00312	0.0077	0.0129	0.0098	0.0087	0.00147	0.0066	0.0191	0.0169
Hf	1.1	2.53	0.722	0.881	1.992	0.836	1.212	1.081	0.702	0.859	0.875	1.4208	1.081	0.458	0.949	2.349	2.296

Table C.9 continued

Sample	RV-53	RV-54	RV-55	RV-56	RV-57	RV-58	RV-59	RV-60	RV-61	RV-62	RV-63	RV-64	RV-65	RVSA71
Group	I	II _L	I	I	I	I	I	II _L	I	II _L	I	I	I	I
N	1	1	1	1	1	1	1	1	1	1	1	1	1	1
Na	<i>na</i>	<i>na</i>	<i>na</i>	<i>na</i>	<i>na</i>	<i>na</i>	<i>na</i>	<i>na</i>	<i>na</i>	<i>na</i>	<i>na</i>	<i>na</i>	<i>na</i>	18429
Ti	2263	1690	2349	2175	1990.9	1896	2705	1274.6	1055.6	1156.3	2011.5	2323	2602	1700
Ni	374.9	436.1	356.7	343.2	196.6	214.3	216.5	615.8	354.1	547.5	294.7	319.7	1082	358.7
Sr	217.4	15.49	222.9	232.2	312.4	336.4	293.2	13.802	669.8	25.41	249.13	311.6	247.4	1142.94
Y	2.9	0.782	1.188	1.016	1.37	2.853	1.165	0.828	1.159	0.813	1.528	1.73	4.254	3.321
Zr	29.78	1.345	16.2	13.73	37.15	65.58	15.53	4.786	15.65	5.627	11.71	40.24	50.31	53.00
Nb	0.0305	0.00056	0.0684	0.0224	0.0525	0.411	0.0183	0.00045	0.00231	0.00056	0.0166	0.113	0.00135	0.0107
Ba	0.343	0.057	10.6	2.5	0.378	67	0.34	0.0211	3.586	0.0208	0.372	3.07	0.33	2.008
La	1.188	0.0166	1.156	1.034	1.961	3.955	1.155	0.00094	11.958	0.0011	1.126	2.132	0.3941	9.980
Ce	5.536	0.038	4.674	4.372	7.955	15.2	4.643	0.0093	36.7	0.0194	4.645	9.371	2.451	41.58
Pr	1.027	0.0079	0.841	0.811	1.421	2.562	0.829	0.0109	4.556	0.0188	0.864	1.669	0.815	5.304
Nd	5.782	0.134	4.389	4.365	7.205	13.03	4.332	0.22	18.64	0.374	4.693	8.86	7.191	19.99
Sm	1.382	0.166	0.93	0.947	1.403	2.452	0.858	0.24	3.131	0.361	1.069	1.717	3.127	3.034
Eu	0.404	0.1057	0.289	0.266	0.388	0.606	0.2469	0.1303	0.87	0.1571	0.3258	0.437	1.18	0.9245
Gd	1.063	0.263	0.657	0.625	0.895	1.461	0.546	0.328	1.617	0.419	0.797	1.035	2.897	2.1102
Tb	0.1414	0.0413	0.0747	0.065	0.0935	0.1586	0.0605	0.0455	0.1436	0.0499	0.092	0.1103	0.3238	0.2303
Dy	0.738	0.196	0.37	0.32	0.443	0.819	0.344	0.216	0.529	0.248	0.46	0.535	1.38	1.062
Ho	0.1193	0.0326	0.0507	0.0427	0.0621	0.1234	0.0496	0.0344	0.0627	0.0321	0.068	0.0791	0.1636	0.14615
Er	0.277	0.0664	0.1072	0.0954	0.116	0.275	0.1196	0.0668	0.1286	0.0661	0.1389	0.177	0.313	0.2808
Tm	0.0279	0.0062	0.0116	0.0089	0.0112	0.0284	0.0118	0.0072	0.0123	0.0057	0.0153	0.0154	0.0253	0.02611
Yb	0.168	0.0401	0.0544	0.0542	0.06	0.177	0.0662	0.0453	0.0631	0.0352	0.0762	0.101	0.137	0.1326
Lu	0.0178	0.0048	0.0058	0.0073	0.0073	0.021	0.0073	0.0048	0.0065	0.0033	0.0088	0.011	0.0136	0.0121
Hf	1.754	0.154	1.017	0.762	1.695	3.982	0.891	0.34	0.67	0.467	0.636	2.763	1.856	3.1201

bdl below detection limit

na not analysed

Table C.10 Average $\pm 2\sigma$, minimum, and maximum garnet $\delta^{18}\text{O}$, whole-rock molar Mg# and Ca#, and whole-rock trace-element compositions (ppm) for the eclogite Groups defined in this study. Whole-rock compositions are reconstructed from mineral chemistry and mineral modes where available. Garnet to clinopyroxene modes of 50:50 are assumed when modes are not given. Data are a combination of new data from this study (Table S2 in the Supplementary Online Dataset) and published literature (Table S6 in the Supplementary Online Dataset).

	Group I				Group II _{No}				Group II _F				Group II _L			
	Ave	$\pm 2\sigma$	Min	Max	Ave	$\pm 2\sigma$	Min	Max	Ave	$\pm 2\sigma$	Min	Max	Ave	$\pm 2\sigma$	Min	Max
Major-elements																
N	133				4				5				25			
Mg#	0.70	0.11	0.56	0.84	0.79	0.12	0.71	0.84	0.64	0.11	0.60	0.74	0.60	0.07	0.54	0.65
Ca#	0.38	0.15	0.26	0.65	0.37	0.19	0.31	0.51	0.48	0.26	0.35	0.69	0.46	0.14	0.27	0.57
$\delta^{18}\text{O}$																
N	70				4				2				19			
Garnet (‰)	6.35	1.39	4.95	9.08	5.38	1.69	4.67	6.60	2.85	4.94	1.11	4.60	2.81	1.04	1.79	3.62
Trace-elements																
N	99				4				5				25			
Ti	2141	949	690	3571	1145	1612	112	2053	1220	985	765	1949	1142	462	758	1903
Y	10.625	11.232	2.130	36.394	3.881	6.367	1.053	7.940	17.898	16.750	6.816	26.852	19.128	14.754	9.263	34.859
Zr	26.823	34.055	5.920	79.675	10.049	21.183	1.041	25.305	7.009	7.468	2.896	10.839	2.806	3.467	0.471	5.862
La	0.872	2.030	0.098	5.989	2.510	5.943	0.082	6.709	0.059	0.121	0.003	0.120	0.011	0.027	0.001	0.045
Ce	3.556	7.589	0.590	22.535	7.790	18.090	0.236	20.307	0.310	0.471	0.040	0.597	0.028	0.044	0.003	0.075
Pr	0.646	1.113	0.147	3.472	1.007	2.275	0.037	2.550	0.107	0.136	0.025	0.176	0.012	0.020	0.001	0.043
Nd	3.612	4.946	0.998	15.065	4.731	10.122	0.208	11.271	1.137	1.187	0.440	1.798	0.202	0.270	0.025	0.623
Sm	1.169	1.146	0.408	4.442	0.904	1.701	0.055	1.699	0.947	1.032	0.354	1.552	0.389	0.392	0.138	1.030
Eu	0.472	0.387	0.274	1.424	0.348	0.404	0.100	0.523	0.484	0.470	0.214	0.754	0.275	0.189	0.150	0.592
Gd	1.430	1.397	0.502	5.136	0.780	1.373	0.094	1.519	1.846	1.893	0.646	2.943	1.270	1.100	0.589	3.155
Tb	0.249	0.247	0.070	0.849	0.104	0.181	0.019	0.213	0.376	0.385	0.133	0.584	0.316	0.255	0.162	0.715
Dy	1.849	1.833	0.439	6.039	0.766	1.285	0.186	1.575	2.951	2.789	1.098	4.347	2.839	2.169	1.357	5.596
Ho	0.407	0.419	0.080	1.309	0.184	0.247	0.064	0.310	0.683	0.650	0.258	1.046	0.722	0.586	0.360	1.484
Er	1.264	1.398	0.209	4.157	0.473	0.784	0.132	0.993	2.074	1.786	0.855	3.138	2.393	1.909	1.170	4.509
Tm	0.181	0.207	0.029	0.602	0.065	0.105	0.018	0.134	0.306	0.271	0.128	0.477	0.366	0.311	0.184	0.704
Yb	1.355	1.682	0.220	4.445	0.484	0.792	0.132	1.020	2.210	1.922	0.964	3.429	2.845	2.357	1.375	5.226
Lu	0.199	0.257	0.035	0.674	0.070	0.113	0.021	0.147	0.326	0.294	0.143	0.524	0.427	0.367	0.202	0.803
Rb	0.196	0.627	0.011	1.089	-	-	-	-	-	-	-	-	0.048	0.075	0.008	0.086
Nb	0.0532	0.1152	0.0010	0.3448	0.0767	0.1752	0.0138	0.1996	-	-	0.0257	0.0257	0.0062	0.0154	0.0002	0.0252
Pb	1.406	10.132	0.093	24.043	1.854	6.110	0.051	5.381	0.007	-	0.007	0.007	0.068	0.108	0.009	0.148
Sr	143.47	183.14	16.00	572.19	176.42	327.74	9.37	388.71	32.95	35.71	5.40	53.98	9.18	7.34	2.78	15.76
Hf	0.929	1.194	0.137	3.216	0.261	0.504	0.037	0.616	0.436	0.487	0.183	0.722	0.210	0.210	0.061	0.420
V	234	174	33	420	135	216	48	289	248	142	200	330	300	151	180	458
Cr	1226	3282	189	8630	984	987	349	1453	539	697	145	810	517	785	194	1563
Ni	201	152	81	623	405	539	203	783	289	233	100	408	225	175	82	365

Table C.10 continued

	Group II _H			
	Ave	±2σ	Min	Max
Major-elements				
N	4			
Mg#	0.80	0.02	0.79	0.81
Ca#	0.43	0.16	0.33	0.53
δ¹⁸O				
N	2			
Garnet (‰)	4.75	0.21	4.67	4.82
Trace-elements				
N	4			
Ti	440	404	146	598
Y	3.583	3.712	1.129	5.593
Zr	0.662	1.154	0.152	1.490
La	0.081	0.201	0.001	0.194
Ce	0.124	0.309	0.002	0.330
Pr	0.019	0.024	0.005	0.026
Nd	0.104	0.149	0.010	0.187
Sm	0.132	0.015	0.124	0.138
Eu	0.086	0.089	0.020	0.119
Gd	0.270	0.259	0.078	0.364
Tb	0.076	0.022	0.066	0.087
Dy	0.724	0.313	0.591	0.896
Ho	0.136	0.143	0.040	0.210
Er	0.468	0.516	0.132	0.754
Tm	0.069	0.077	0.020	0.113
Yb	0.528	0.583	0.152	0.856
Lu	0.076	0.089	0.022	0.130
Rb	0.084	0.011	0.081	0.088
Nb	0.0547	0.0972	0.0193	0.1101
Pb	0.048	0.124	0.004	0.092
Sr	7.79	11.66	0.56	14.17
Hf	0.027	0.033	0.008	0.049
V	160	112	128	244
Cr	971	1090	169	1367
Ni	375	238	244	489

Table C.11 Strontium isotopic compositions of garnets and clinopyroxenes from Roberts Victor eclogites in this study, as well as for standards BHVO-2 and NIST SRM 987

	Group	Sr (ppm) ^a	⁸⁴ Sr	⁸⁶ Sr	⁸⁷ Sr	⁸⁸ Sr	⁸⁷ Sr/ ⁸⁶ Sr	±2σ	⁸⁸ Sr/ ⁸⁶ Sr	±2σ	⁸⁴ Sr/ ⁸⁶ Sr	±2σ
<i>Garnets</i>												
RV-1	II _L	0.0899	0.04065	0.72171	0.51248	6.06081	0.70910	0.00009	8.39878	0.05222	0.05649	0.00004
RV-10	II _L	0.0598	0.01462	0.26035	0.18504	2.19336	0.70845	0.00016	8.42761	0.02369	0.05648	0.00008
RV-14	II _L	0.258	0.03006	0.53160	0.37683	4.44874	0.70913	0.00011	8.36594	0.03617	0.05650	0.00005
RV-20	II _L	0.0997	0.03523	0.62432	0.44273	5.23478	0.70846	0.00011	8.38617	0.07314	0.05649	0.00005
RV-22	II _L	0.1212	0.04337	0.77627	0.55397	6.57257	0.70972	0.00009	8.47337	0.08036	0.05649	0.00004
RV-27	II _F	0.3	0.01202	0.20961	0.14762	1.73004	0.70946	0.00023	8.24250	0.07719	0.05651	0.00015
RV-54	II _L	0.0778	0.05663	1.00522	0.71448	8.43949	0.70987	0.00007	8.39463	0.06248	0.05648	0.00003
RV-60	II _L	0.0583	0.04519	0.79832	0.56506	6.67235	0.70853	0.00014	8.35328	0.06415	0.05649	0.00005
RV-62	II _L	1.67	0.03497	0.61806	0.43780	5.16852	0.70885	0.00012	8.35953	0.01587	0.05649	0.00005
<i>Clinopyroxenes</i>												
RV-10	II _L	28.6	0.13253	2.28503	1.58564	18.65340	0.70292	0.00005	8.16388	0.07011	0.05650	0.00002
RV-14	II _L	23.64	0.26380	4.65164	3.26604	38.81133	0.70346	0.00004	8.34188	0.02359	0.05649	0.00009
RV-22	II _L	18.19	0.01681	0.29878	0.21124	2.51222	0.70562	0.00016	8.40891	0.01870	0.05649	0.00009
RV-27	II _F	54.45	0.23035	4.02665	2.80567	33.31404	0.70108	0.00005	8.27415	0.02014	0.05650	0.00002
<i>BHVO-2</i>												
1	-	-	0.11789	2.08390	1.46492	17.42781	0.70348	0.00005	8.35928	0.02682	0.05649	0.00002
2	-	-	0.02230	0.38928	0.27193	3.21494	0.70349	0.00017	8.25901	0.00255	0.05648	0.00012
3	-	-	0.07936	1.38659	0.96921	11.46674	0.70346	0.00008	8.26963	0.00289	0.05650	0.00003
4	-	-	0.03305	0.58026	0.40657	4.82136	0.70347	0.00011	8.30898	0.00376	0.05649	0.00005
5	-	-	0.03618	0.63036	0.43998	5.19792	0.70346	0.00012	8.24809	0.01298	0.05649	0.00005
<i>NIST SRM 987</i>												
1	-	-	0.03464	0.61289	0.43523	5.13149	0.71023	0.00010	8.37255	0.04205	0.05649	0.00005
2	-	-	0.04305	0.75880	0.53777	6.32767	0.71026	0.00010	8.33905	0.00320	0.05649	0.00004
3	-	-	0.11358	2.00502	1.42201	16.74339	0.71027	0.00005	8.34981	0.01095	0.05648	0.00002
4	-	-	0.13285	2.35219	1.67079	19.70239	0.71027	0.00005	8.37786	0.00717	0.05648	0.00002

^aSr (ppm) for garnet and clinopyroxene in this study determined by LA-ICP-MS (Tables C.8 and C.9, respectively).

Published BHVO-2 average ⁸⁷Sr/⁸⁶Sr = 0.703435 (Raczek *et al.* 2003).

Published NIST SRM 987 average ⁸⁷Sr/⁸⁶Sr = 0.710246 (Jochum *et al.* 2005)